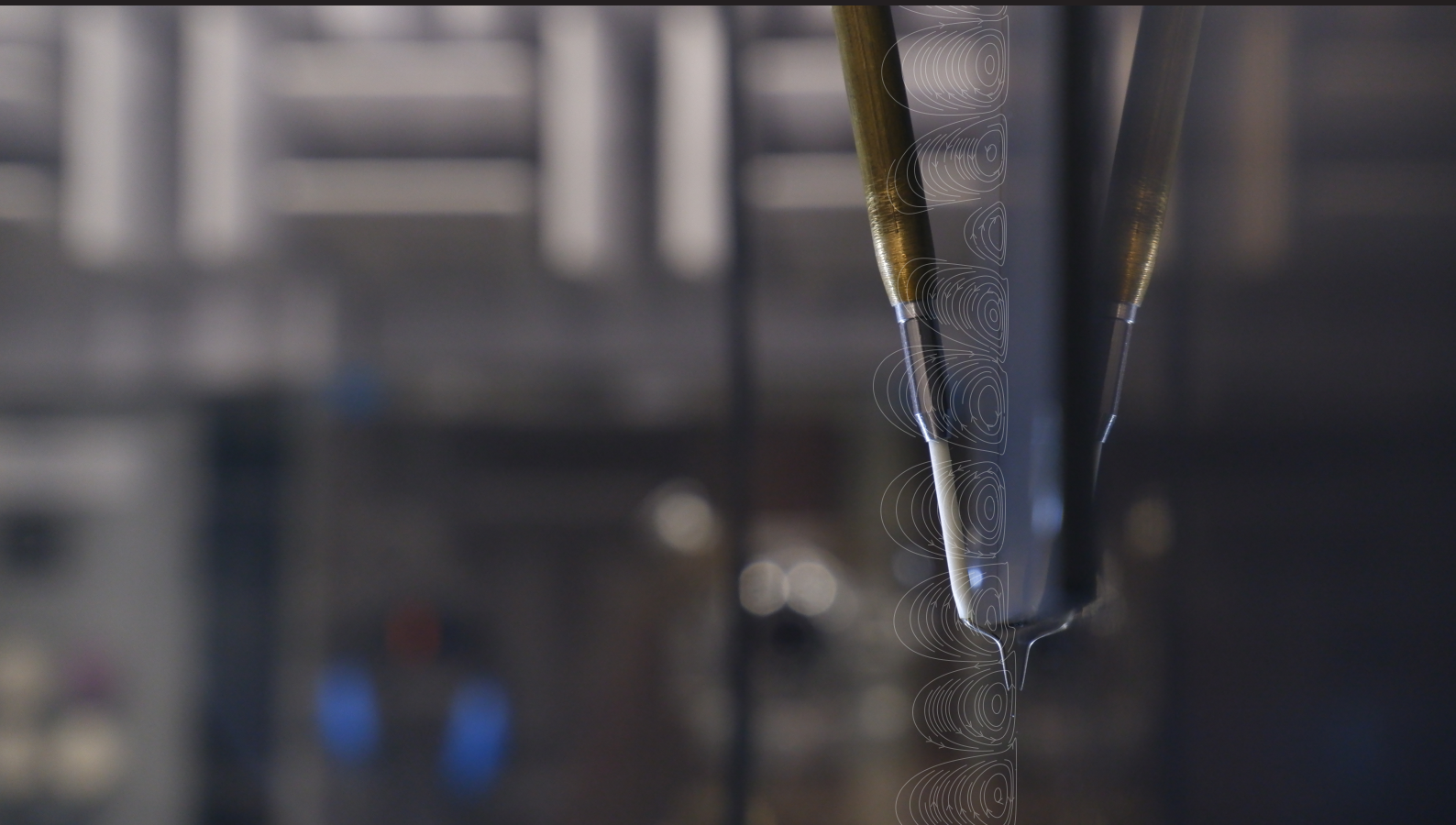


# Experimental Study on Tollmien-Schlichting Waves over Forward- Facing Steps

Comparison with Direct Numerical Simulations in Collabora-  
tion with DLR

Marina Barahona





# Experimental Study on Tollmien-Schlichting Waves over Forward- Facing Steps

**Comparison with Direct Numerical  
Simulations in Collaboration with DLR**

by

Marina Barahona

to obtain the degree of Master of Science  
at the Delft University of Technology,  
to be defended publicly on Tuesday May 17th, 2022 at 10:00 AM.

Student number:	5005043	
Project duration:	April 15th, 2021 – May 17th, 2022	
Thesis committee:	Dr. M. Kotsonis,	Aerodynamics
	Dr. D. Ragni,	Wind Energy
	Dr. T. Michelis,	Propulsion & Power
	Ir. A. F. Rius-Vidales,	Aerodynamics
	Ir. F. Tocci,	Aerodynamics

An electronic version of this thesis is available at <http://repository.tudelft.nl/>.



# Acknowledgments

I write this from my garden, away from my desktop, because I want this part of the thesis to be completely different, personal. It has been six years since I decided that I wanted to study Aerodynamics. Now, when I remember that homemade sloppy wind tunnel that I built for my final high-school project, I can't help but smile. That Marina would have never imagined that she would be working for 5 weeks almost alone in a wind tunnel so big that you can sleep inside (not that I have done it!). However, I know that I would have never been able to reach this point without any help. This is why I would like to devote this page to acknowledging those persons which have helped me during the time of my thesis and those who have always been there.

I would like first and foremost to thank my two supervisors, Marios and Beto, without whom this work would have probably resembled a bit more my old sloppy high-school wind-tunnel project. Marios is an incredible professional. His ability to simplify things has saved me lots of time during the thesis when, in my head, everything was a bit of a disaster. However, if I have to thank him for something in particular, this would be for helping out when things get messy in life. Special thanks to Beto, for his immense patience with me and the countless number of lessons he taught me in so many different fields ranging from bolts, transition, and PhD-related matters! His eye for detail and neat work are already in my *things-to-accomplish* list during my future Ph.D. I would also like to thank Jordi, particularly for his revealing discussions on non-modal growth. His passion for science and his hard work are a source of inspiration to me. Finally, huge thanks to the people from the Ph.D. room (Giulia, Sven, Theo, Giulio, Kaisheng, Ale, Kristie, Nivi, and Aaron), which were always ready to help out when needed and became my social support during the weeks of campaign. Special thanks to Ale, whose cheerful aura and fancy coffees lightened up my days in the wind tunnel.

I would like to thank Emiel and Stefan for their help and valuable advice during my experimental campaign. Especially to Emiel, for having had so much patience with me during the first campaign while I was getting familiar with almost everything. I would also like to acknowledge the work and advice provided by Francesco, Stefan, and Paul from DLR. Special thanks to Francesco for his interesting insights and discussions on the topic.

My thesis period has become very special thanks to the many wonderful people I met in Delft after the pandemic. First of all, I cannot thank enough the people from Room 2.44 for literally being my Little Portion of South in the Aerospace Faculty. The cakes and parties made my thesis period worth it. I would also like to thank the people from *Latitud*, especially Caro and Miri, with whom I felt more like in the Bahamas and less in the rainy NL when I was anywhere near them. Special thanks to Xavi, Chris, and Lidia, for always being able to listen and help out when things get complicated. Last but not least, I would like to thank my dearest friends Marina, Sandra, Ester, and Judith who, despite not having a clue of what I am doing one thousand km away from home, keep being as supportive as ever.

I am not sure I can express in some lines how grateful I am to Oscar. His technical insight resulted extremely useful sometimes during our casual discussions at home and helped me to see the big picture of the problem. However, most important to me is his support in all aspects of my life. I do not know how would I have managed all this time without his cheerful presence and love. Finally, I am deeply thankful to my family, Montse, Roman, and my little brother, Fran, for always believing in me and my dreams until the end.

*Marina Barahona  
Delft, May 2022*



# Abstract

Current manufacturing techniques in the aviation industry result in a number of two-dimensional surface irregularities (e.g. panel joints, seals, seams) which can lead to an increase in skin friction due to premature boundary layer transition. Panel joints are commonly modeled in the form of two-dimensional steps. Prior studies have shown that Backward-Facing Steps (BFS) promote transition earlier than Forward-Facing Steps (FFS). Therefore, in the design of laminar flow components, FFS are preferred over BFS. However, the understanding of which mechanisms are responsible for the larger growth experienced by Tollmien-Schlichting (TS) waves in the presence of FFS remains unknown. Prior experimental works focused on parametric studies on transition location with limited measurements close to the step. In addition, studies using Direct Numerical Simulations (DNS) assume two-dimensional flow and consequently do not capture transition location. All of this makes comparison between existing experimental and numerical data rather cumbersome, hindering the problem understanding.

In light of this, the present study aims to close-examine the TS waves at the step to identify which are the relevant mechanisms that modify their growth and move transition upstream. To do so, this work presents an experimental and numerical investigation jointly conducted by TU Delft and the German Aerospace Center (DLR) on Tollmien-Schlichting (TS) waves interaction with a Forward-Facing Step (FFS). Experiments are conducted at the TU Delft low-turbulence anechoic wind tunnel (A-tunnel) on an unswept flat plate model. Single-frequency disturbances are introduced using controlled acoustic excitation. The temporal response of the flow in the vicinity of the step is measured using Hot-Wire Anemometry (HWA). In addition, the global effect of the step on laminar-turbulent transition is captured using Infrared Thermography (IR). Two-dimensional (2D) Direct Numerical Simulations (DNS) performed at DLR provide detailed information at the step. Experimental and numerical comparison is performed in subcritical step conditions ( $h/\delta^* = 0.775$ ). At larger step heights only experimental data is provided.

Experimental and DNS results in clean and subcritical step conditions present very good agreement. Both methods predict large distortion of the TS wave downstream of the step, where DNS results present different growth trends between streamwise and wall-normal components of the fundamental mode. Furthermore, while upstream of the step the TS waves exhibit exponential growth, downstream of it they present a complex growth behavior followed by regions where the perturbation energy production term changes sign along the streamwise direction. Finally, regions of highly negative and positive production seem to correlate with the tilting of TS waves in and against the mean shear direction, respectively. These findings point towards the presence of different growth mechanisms triggered by the step which could modify the level of amplification of disturbances far downstream.



# Contents

<b>Preface</b>	<b>3</b>
<b>List of Figures</b>	<b>9</b>
<b>List of Tables</b>	<b>15</b>
<b>1 Introduction</b>	<b>1</b>
1.1 Motivation . . . . .	1
1.2 Stability of boundary layer flows . . . . .	2
1.2.1 Modal growth . . . . .	3
1.2.2 Non-modal growth . . . . .	7
1.2.3 Paths to transition . . . . .	8
1.3 Effect of roughness elements on transition: forward-facing steps . . . . .	10
1.3.1 Transition prediction with TS-FFS: numerical and experimental progress . . . . .	11
1.3.2 Close-examination of the flow features and growth mechanisms with FFS . . . . .	13
1.4 Acoustic forcing of Tollmien-Schlichting waves . . . . .	14
1.5 Discussion and outline . . . . .	15
1.6 Research questions and objectives . . . . .	17
<b>2 Methodology</b>	<b>19</b>
2.1 Design of the experimental test matrix . . . . .	19
2.1.1 Step heights . . . . .	19
2.1.2 Disturbance frequencies and amplitudes . . . . .	20
2.1.3 Test cases . . . . .	22
2.2 Numerical methods . . . . .	22
2.2.1 Boundary layer and Orr-Sommerfeld solver . . . . .	23
2.2.2 Direct numerical simulations . . . . .	23
2.3 Flow diagnostics . . . . .	24
2.3.1 Infrared thermography . . . . .	25
2.3.2 Hot-wire anemometry . . . . .	26
2.3.3 Planar particle image velocimetry . . . . .	27
2.4 Data analysis . . . . .	28
2.4.1 Differential infrared thermography . . . . .	29
2.4.2 Wall-finding in HWA velocity profiles . . . . .	29
2.4.3 Welch's modified periodogram . . . . .	30
2.4.4 Proper orthogonal decomposition . . . . .	30
2.5 Uncertainty analysis . . . . .	31
2.5.1 Pressure coefficient . . . . .	32
2.5.2 IR transition fronts . . . . .	32
2.5.3 HWA profiles . . . . .	33
2.5.4 PIV flowfields . . . . .	34
<b>3 Experimental Protocol</b>	<b>37</b>
3.1 Experimental set-up . . . . .	37
3.1.1 Infrared thermography . . . . .	38
3.1.2 Hot-wire anemometry . . . . .	38
3.1.3 Particle image velocimetry . . . . .	39
3.1.4 Static pressure measurements . . . . .	40
3.1.5 FFS height adjustment . . . . .	41

3.2	Pulsed and continuous acoustic excitation of TS waves . . . . .	41
3.2.1	Working principle of the pulsed acoustic forcing . . . . .	41
3.2.2	Acoustic set-up . . . . .	43
<b>4</b>	<b>Baseline Results: Clean Case</b>	<b>45</b>
4.1	Spanwise flow uniformity . . . . .	45
4.2	Freestream turbulence and background noise . . . . .	46
4.3	Boundary layer stability . . . . .	48
4.4	Laminar-to-turbulent transition . . . . .	49
4.5	Forced and unforced disturbances . . . . .	49
<b>5</b>	<b>Results with Forward-Facing Steps</b>	<b>53</b>
5.1	Transition front movement . . . . .	53
5.2	Meanflow modulation at the step . . . . .	56
5.3	Growth of the fundamental mode and harmonics over the step . . . . .	59
5.4	The perturbation field at the step . . . . .	64
5.4.1	Amplitude and phase modification of the fundamental mode . . . . .	64
5.4.2	Production of perturbation energy . . . . .	67
5.5	Phase-locked fields: TS waves motion over the step . . . . .	70
5.6	Disturbance energy spectra over an FFS . . . . .	72
5.6.1	The subharmonic content . . . . .	74
5.7	Effect of disturbance frequency . . . . .	76
<b>6</b>	<b>Conclusions and Recommendations</b>	<b>81</b>
6.1	Conclusions . . . . .	81
6.2	Recommendations . . . . .	82
<b>A</b>	<b>Extra figures</b>	<b>85</b>
	<b>Bibliography</b>	<b>87</b>

# List of Figures

1.1	(a) Spatial stability neutral curve from analytical (lines) and experimental (symbols) data. Figure reproduced from White and Corfield (2006). (b) Evolution of a local perturbation on a boundary layer depicting an absolute and a convective instability. . . . .	5
1.2	Eigenfunction of the primary instability in a Blasius boundary layer. (a) normal and (b) streamwise perturbation velocity components at $\alpha = 0.2$ and $Re = 500$ . The thick lines represent the absolute value while the thin lines are the imaginary and real contributions. Figure reproduced from Schmid and Henningson (2012). . . . .	6
1.3	Sketch representing the mechanisms which explain the existence of a viscous instability by means of the build-up of a Reynolds stress across the boundary layer. Inspired on the illustration shown in Baines et al. (1996) work. . . . .	7
1.4	Sketch of the Orr-mechanism on the plane x-y (a) and the lift-up effect on the plane y-z (b) reproduced from Jiménez (2013). . . . .	8
1.5	Possible transition scenarios as described in Morkovin (1994). Figure reproduced from Reshotko (2008). . . . .	9
1.6	(a) Different patterns of $\Lambda$ vortices depicting K- and H-type transition, reproduced from Schlichting (1933). (b) Spectra of velocity fluctuations measured with a hot-wire probe in the H-type transition region during Kachanov and Levchenko (1984a) experiments. . . . .	9
1.7	(a) Wall-pressure, streamwise curvature and separated flow (dashed lines) around an FFS of $h/\delta^* \approx 0.94$ . Image reproduced from the work of Edelmann and Rist (2014). (b) Sketch of the effect of a surface defect on the N-factor when the defect is subcritical and critical. Note that Methel et al. (2021) definition of critical and subcritical step differs from this work definition, see section 2.1. Main parameters used in the N-factor method indicated. Figure reproduced from Methel et al. (2021). . . . .	11
1.8	(a) $\Delta N$ for different TS wave frequencies ( $F = 60$ and $F = 100$ corresponding to Branch I and Branch II respectively) along the streamwise direction. The step is located at $x = 220$ and the step heights depicted are (a) $h/\delta^* = 0.7$ and (b) $h/\delta^* = 1.4$ . (b) Streamwise velocity (left) and phase (right) of the primary mode for $h/\delta^* = 1.4$ at the most unstable frequency ( $F = 80$ ). Note the opposite phase of the lower and upper structure immediately after the step. Figure reproduced from Shahzad (2020). . . . .	14
1.9	(a) Time-signal of a hot-wire probe placed inside the boundary layer and on the freestream when a sound pulse is sent. Figure reproduced from Saric and White (1998). (b) Global stability results of Chauvat (2020) near the LE where receptivity to a travelling acoustic wave takes place. Contours of $u$ . . . . .	15
2.1	Change of transition location for different FFS heights. Data from experiments of Perraud and Seraudie (2000) ( $\square$ ) and Wang and Gaster (2005) ( $\Delta$ ). The dashline (---) indicates the critical $h/\delta^*$ and $Re_h$ where the boundary layer trips. . . . .	20
2.2	Step parameters used in different works from literature. ( $\diamond$ ) Shahzad (2020), ( $*$ ) Zh and Fu (2017), ( $\Delta$ ) Wang and Gaster (2005), ( $\circ$ ) Edelmann and Rist (2015), ( $\square$ ) Perraud and Seraudie (2000), ( $\blacksquare$ ) Campaign I and ( $\blacksquare$ ) Campaign II test cases. Filled symbols indicate the step cases for which a second recirculating region is expected during the experiments based on the numerical results from Edelmann and Rist (2015) ( $\bullet$ ) and Shahzad (2020) ( $\blacksquare$ ). The dashlines (---) indicate the critical $h/\delta^*$ and $Re_{hh}$ where the boundary layer might trip. . . . .	21
2.3	(a) Stability diagram from OS solver showing the growth rate (—) and N-factor isolines (---) with conditions from Campaign I and growth rate from Campaign II (-·-·). (b) N-factor development in streamwise direction for frequencies $f = 300$ Hz (green), $f = 450$ Hz (blue) and $f = 550$ Hz (magenta) at Campaign I conditions (—) and Campaign II (-·-·). . . . .	21

2.4	(a) Integral parameters from DNS (—), BL solver (- - -) and experiments (◦). (a) N-factor development along $x$ for the three different frequencies tested: $f = 300$ Hz (green), $f = 450$ Hz (blue) and $f = 550$ Hz (magenta). Results from DNS (—), OS solver fed with baseflow from BL solver (- - -), OS solver fed with DNS baseflow (- · - ·) and experimental results (◦). All results presented are in clean conditions, $h = 0 \mu\text{m}$ . . . . .	25
2.5	(a) Schematic of double-frame mode with later cross-correlation of the interrogation windows from both frames. (b) Pre-processing of the raw frame. . . . .	28
2.6	Schematic of the post-processing procedure used to extract the transition front location from the IR images. . . . .	30
2.7	(a) Blasius profile (—) and mean velocity profile from HW measurements (◦) with error bars indicating uncertainty in velocity and wall-normal direction. (b) Pressure coefficient $C_p$ with uncertainties. . . . .	34
2.8	(a) Convergence of meanflow U-component at point (+) with errorbars denoting standard deviation. (b) Contours of $\varepsilon_u$ with $N = 1944$ averaged vector fields. . . . .	34
3.1	Sketch of the experimental set-up featuring the unswept flat plate, the FFS mechanism, the acoustic forcing system and the different measurement techniques used. Numbers indicate the subsections within this section where the details of the different measurement techniques are presented. . . . .	37
3.2	Sketch of the IR system illustrating the materials used and the flux of the different heat transfer mechanisms across the layout. . . . .	38
3.3	Sketch of the 55P15 Dantec hot-wire probe with predominant heat transfer exchange terms indicated. The annotation indicates the minimum distance to which the wire could be placed upstream of the step to avoid the wire prongs touching the step edge. . . . .	39
3.4	Location of HWA profiles and PIV field of view (FoV) with respect to the FFS location. Drawing has scale 2:1. . . . .	39
3.5	Schematic of the PIV set-up used during Campaign II. The sketch includes a realistic layout of optics, gadgets used (laser, camera, etc.), and the signal path (acoustic and laser trigger, etc.). . . . .	40
3.6	Sketch of pressure taps distribution along the model and insert (not to scale). Horizontal direction is $x$ and vertical direction is $z$ . . . . .	41
3.7	FFS mechanism: (a) CAD model, (b) real model and (c) sketch of the working principle. . . . .	42
3.8	Schematic of the working principle of the <i>pulsing technique</i> . The right figure illustrates the position of the speaker w.r.t the A-tunnel cross-section. The left figure is a space-time diagram illustrating the propagation of the acoustic and TS waves during the pulse duration. Below the diagram, the time intervals where one would find an individual or combined Stokes and TS waves within the RoI are indicated. . . . .	43
3.9	(a) Frequency response of speaker (black plot), ideal frequency response (gray plot) and frequencies of interest (dash-lines). (b) Correlation of input voltage to acoustic amplitude measured by the microphone at the LE for frequencies 550 Hz (*), 450 Hz (+) and 300 Hz (◦). . . . .	44
4.1	(a) Chordwise pressure coefficient distribution $C_p$ from pressure taps at $z = 120$ mm (red) and $z = -120$ mm (blue). (b) Spanwise pressure coefficient distribution from taps at $x = 60$ mm (blue) and $x = 360$ mm (black). . . . .	46
4.2	(a) Surface profiles in $xy$ as read from laser scanner at $z = -40$ mm (blue), $z = 0$ mm (black) and $z = 40$ mm (red) in no-step case. (b) Spanwise variation of the step height in no-step case. . . . .	46
4.3	(a) Displacement thickness ( $\delta^*$ ) measured with PIV at different spanwise locations, $z = -40$ mm (blue), $z = 0$ mm (black) and $z = 40$ mm (red) in no-step conditions. Black-dashed line (- - -) is $\delta^*$ as predicted from the BL solver at PIV conditions. Magenta lines indicate $\delta^*$ at the centerline and the deviation from this value at $z = \pm 40$ mm. XY contour planes of the streamwise (b) and wall-normal (c) meanflow velocity components measured by PIV at different spanwise locations. . . . .	47
4.4	(a) Frequency spectrum of pressure fluctuations read by microphone in SPL (black plot) and velocity fluctuations of the HWA at $y = 0.5$ mm away from the wall (gray plot). (b) Coherence between pressure and velocity fluctuations. Red patch denotes the frequency band of amplified TS waves in clean case conditions. . . . .	47

4.5	Flow diagnostics without step at $x = 0.38$ m as computed with DNS (—), BL solver + OS (- - -) and measured with HWA (◦). (a) BL velocity profile. TS wave shape at forcing frequency $f = 300$ Hz (a), $f = 450$ Hz (b) and $f = 550$ Hz (c). . . . .	48
4.6	(a) PSD of HWA velocity fluctuations measured at the TS wave maximum. (b) N-factor spectrum from OS solver. Note how OS instability bounds agree with experimental results. . . . .	49
4.7	(a) N-factor envelope from OS solver at the test conditions specified in table 2.1 (low-Reynolds, thick black line) and at high Reynolds number (thick red line) for which the transition front is observed in (b). $N_T$ denotes the N-factor where laminar-to-turbulent transition is expected to happen based on the freestream turbulence, $Tu \leq 0.06$ . (b) DIT image in no-step and no-forcing conditions at low-Reynolds, $Re = 1.32 \times 10^6$ and high-Reynolds number, $Re = 1.45 \times 10^6$ . Dashed magenta lines in (a) and (b) indicate the IR FoV. Blue lines indicate the transition location and corresponding N-factor at high Re conditions. . . . .	50
4.8	Normalized POD modes from $u$ -component under pulsed acoustic forcing conditions. . . . .	50
4.9	(a) Energy fraction per mode from POD cases. (b) Root mean square of reconstructed flowfield of $u$ -component from POD modes (b) 1, (c) 2, (d) {1, 2} and (e) {3, 4}. No acoustic forcing case (black), pulsed forcing (blue) and continuous forcing (red). . . . .	51
4.10	(a) PSD from HW signal in no-step and no-forcing conditions at $x = 420$ mm at different $y$ stations. Colored areas indicate the frequency bands where the signal was bandpass to retrieve the disturbance profiles in figure 4.11. (b) Contours of PSD at same conditions and streamwise location as (a). . . . .	51
4.11	Wall-normal profiles of the resulting disturbances from bandpassing the PSD signal at the frequency bands indicated in figure 4.10 (a) with the same color notation used herein for the profiles. In (a) the magenta line represents the mean shear ( $\partial U/\partial y$ ) obtained from derivating the HWA meanflow velocity profile along $y$ . . . . .	52
5.1	Transition front identification using DIT for different step heights with forcing frequency $F = 90$ . Green dots indicate the transition front, dashed and solid magenta lines illustrate the variance and the linear fit to the front, respectively. Yellow dashed lines indicate the location of the step edge, $x = 380$ mm. Flow comes from left to right. . . . .	54
5.2	Transition front movement along the heating plate for increasing step height at different forcing conditions, as specified in table 2.3. Flow comes from left to right. Increasing color intensity indicates increasing step height, i.e. blue denotes clean case while brown indicates the highest step case ( $h/\delta^* = 1.950$ ). . . . .	54
5.3	(a) Reynolds transition ( $Re_{x_T}$ ) as a function of the relative step height ( $h/\delta^*$ ). Data digitized from Fig.4 in Wang and Gaster (2005) (□) and these experiments (◦). (b) N-factor decrease at transition, $\Delta N$ , as a function of the relative step height. Data fit digitized from Fig. 7 in Wang and Gaster (2005) (- - -), Fig. 6.4.2.1 (d) in Costantini (2016) (—), $\Delta N = 1.6h/\delta^*$ model from Crouch et al. (2006) (⋯⋯⋯) and the present experiments (◦). Unforced (black) and forced conditions at $F = 60$ (blue), $F = 90$ (green) and $F = 110$ (magenta). Confidence bands indicate uncertainty on the transition front measurements. . . . .	55
5.4	(a) Pressure coefficient at the wall, (b) displacement thickness ( $\delta^*$ ), (c) shape factor ( $H$ ) and (d) momentum thickness ( $\theta$ ). Symbols denote experimental data and full lines DNS. Clean (black), subcritical (blue), critical (green) and supercritical (orange) step cases. Confidence bands for experimental data are included. Note that DNS data is only provided in clean and subcritical step cases. Step is at $x = 380$ mm. . . . .	56
5.5	Normalized wall-normal velocity profiles of $Q$ (with $Q = \sqrt{U^2 + V^2}$ ) (—) and $\partial U/\partial y$ (- - -). Lines denote DNS data and symbols (◦) HWA results. Subcritical (a), critical (b) and supercritical (c) step cases, represented in colors. Clean case results are included in all step cases and represented in black. The streamwise locations plotted are at (from left to right) $x = [341, 361, 374, 381, 383, 391, 401, 421]$ mm with the step at $x = 380$ mm. The horizontal spacing between profiles is set to $\Delta = 1.2$ for legibility. . . . .	57
5.6	Contours of meanflow $U$ ((a) and (c)) and $V$ ((b) and (d)) components from PIV ((a) and (b)) and DNS ((c) and (d)) for $h/\delta^* = 0.775$ . Streamlines (gray —), recirculating regions (white - - -) and inflection points (- - -) are also indicated. . . . .	58

- 5.7 Contours of meanflow  $U$  ((a) and (c)) and  $V$  ((b) and (d)) components from PIV ((a) and (b)) and DNS ((c) and (d)) for  $h/\delta^* = 1.462$ . Streamlines (gray —), recirculating regions (white - - -) and inflection points (- - -) are also indicated. . . . . 58
- 5.8 Contours of meanflow  $U$  (a) and  $V$  (b) components from PIV for  $h/\delta^* = 1.950$ . Streamlines (gray —), recirculating regions (white - - -) and inflection points (- - -) are also indicated. . . . . 58
- 5.9 N-factor evolution of the  $|\hat{u}|$  maximum from the fundamental mode (a), subharmonic mode (b), second (c) and third (d) harmonics. Full lines denote DNS data (in clean and subcritical step cases) and symbols HWA measurements. Clean case ( $h = 0$  mm, black), subcritical ( $h = 0.775$  mm, blue), critical ( $h = 1.462$  mm, green) and supercritical ( $h = 1.950$  mm, orange) step cases. The frequency of the fundamental mode is  $F = 90$ . Note that dashed lines are not numerical data but just have the purpose of tracing the HWA points. . . . . 60
- 5.10 Absolute amplitude for different step heights: clean case (a), subcritical (b), critical (c) and supercritical (d) step conditions. Full lines denote DNS data (in clean and subcritical step cases) and symbols HWA measurements. Fundamental mode ( $F = 90$ , black), subharmonic mode ( $n = 0.5$ , gray), second harmonic ( $n = 2$ , blue) and third harmonic ( $n = 3$ , orange). Note that lines between experimental points are only for indicative purposes on the data trend. . . . . 60
- 5.11 Wall-normal profiles of the fundamental mode ( $F = 90$ ) in terms of  $|\hat{u}|$  (black) and  $\partial U/\partial y$  (gray). Full lines denote DNS data and symbols (o) HWA results. Clean (a), subcritical (b), critical (c) and supercritical (d) step cases. The streamwise locations plotted are at (from left to right)  $x = [341, 361, 374, 381, 383, 391, 401, 421]$  mm with the step at  $x = 380$  mm. The horizontal spacing between profiles is set to  $\Delta = 1.2$  for legibility. Note that the dashed-dotted lines in (c) and (d) are not numerical data but just intend to trace the experimental data points for easier interpretability. . . . . 61
- 5.12 (a) N-factor of the different peaks in the fundamental mode ( $F = 90$ ) shape function from DNS in subcritical step case conditions. Full lines indicate the maxima of  $|\hat{u}|$  (black) and  $|\hat{v}|$  (red) while dashed lines indicate the secondary peaks different from the maxima. (b) N-factor based on the maxima of  $|\hat{u}|$  (black) and  $|\hat{v}|$  (red) from DNS for the fundamental mode ( $F = 90$ ) in subcritical step case conditions. Equivalent results from the OS solver computed with the DNS baseflow are indicated in blue. The green patch indicates the maximum streamwise extent of the secondary peak. . . . . 62
- 5.13 Shape function of the fundamental mode from DNS (full lines) and OS (dashed lines) results in clean (a) and subcritical (b) step conditions. Shape function of  $|\hat{u}|$  in black and  $|\hat{v}|$  in red. . . . . 63
- 5.14 N-factor evolution of the disturbance components orthogonal to the baseflow,  $|\hat{u}_\perp|$  (black) and  $|\hat{v}_\perp|$  (red), as obtained from equation (5.2). Clean case (dashed lines) and subcritical step case (full lines) from DNS results. (a) N-factor defined in terms of the disturbance energy integrated along  $y$ , i.e.  $\int_0^{h_{\text{DNS}}} |\hat{u}_\perp|^2 dy$ . (b) N-factor defined based on the maxima of  $|\hat{u}_\perp|$  and  $|\hat{v}_\perp|$ . . . . . 64
- 5.15 Contours of the fundamental mode ( $F = 90$ ) amplitude in terms of  $|\hat{u}|$  (a, c, e, g, i) and  $|\hat{v}|$  (b, d, f, h, j) components from DNS (a)-(d) and PIV (e)-(j) results. Contour lines of the inflection points from  $\partial U/\partial y$  (- - -),  $|\hat{u}|$  (black —) and  $|\hat{v}|$  (yellow —) are also shown. Clean case (a)-(b), subcritical step (c)-(f), critical step (g)-(h) and supercritical step case (i)-(j). The colorbar legend corresponds to  $|\hat{u}|/U_{\text{ref}}(\%)$ . Note:  $|\hat{v}|$  is multiplied by two to fit it within the colorbar of  $|\hat{u}|$ . The wall-normal coordinate has been scaled by 1.35 for visualization purposes. . . . . 66
- 5.16 Contours of the fundamental mode ( $F = 90$ ) phase in terms of  $\varphi_{\hat{u}}$  (a, c, e, g, i) and  $\varphi_{\hat{v}}$  (b, d, f, h, j) components from DNS (a)-(d) and PIV (e)-(j) results. Contour lines of the inflection points from  $\partial U/\partial y$  (- - -),  $|\hat{u}|$  (black —) and  $|\hat{v}|$  (yellow —) are also shown. Clean case (a)-(b), subcritical step (c)-(f), critical step (g)-(h) and supercritical step case (i)-(j). The wall-normal coordinate has been scaled by 1.35 for visualization purposes. . . . . 67
- 5.17 (a) Contours of the production term ( $\tilde{P}$ ) as defined in equation (5.3). In addition, streamlines from DNS for the fundamental mode ( $F = 90$ ) at phase  $\phi = \pi$  rad are shown. (b) Streamwise evolution of the production term and its different contributions:  $\hat{P}_{11}$  (magenta),  $\hat{P}_{12}$  (red),  $\hat{P}_{22}$  (blue),  $\hat{P}_{21}$  (green) and total production (black). A dashed line indicates the zero in the  $y$ -axis. (c) Streamwise evolution of the disturbance kinetic energy ( $\tilde{E} = |\hat{u}|^2 + |\hat{v}|^2$ ) integrated in wall-normal direction and multiplied by the TS frequency ( $\omega = 2\pi f$ ). Contributions of  $|\hat{u}|$  (black-dashed line) and  $|\hat{v}|$  (red-dashed line) to the energy are also represented. The wall-normal coordinate has been scaled by 1.35 for visualization purposes. . . . . 69

- 5.18 Contours of the production term ( $\tilde{P}$ ) as defined in equation (5.3) at different step heights. Contour lines represent the inflection points from  $\partial U/\partial y$  (---),  $|\hat{u}|$  (black —) and  $|\hat{v}|$  (yellow —). Subcritical step (a)-(b), critical step (c) and supercritical step case (d). Results in (a) correspond to DNS. The wall-normal coordinate has been scaled by 1.35 for visualization purposes. . . . . 70
- 5.19 Contour fields of the disturbance  $u$  component from DNS results at three different phases of the TS wave cycle:  $\phi = 0^\circ$  (a),  $\phi = 60^\circ$  (b) and  $\phi = 120^\circ$  (c). Subcritical step conditions ( $h/\delta^* = 0.775$ ) with fundamental mode frequency being  $F = 90$ . Disturbance streamlines are also included at the corresponding phase. Green dash-dotted lines indicate the streamwise positions where production changes sign in figure 5.18 (b). The wall-normal coordinate has been scaled by 1.35 for visualization purposes. . . . . 71
- 5.20 Contours of the normalized spanwise vorticity ( $\omega_z$ ) and disturbance streamlines around the step corner from DNS results at three different phases of the TS wave cycle:  $\phi = 0^\circ$  (a),  $\phi = 60^\circ$  (b) and  $\phi = 120^\circ$  (c). Subcritical step conditions and forcing frequency at  $F = 90$ . Wall-normal axis is scaled by 1.35 for visualization purposes. . . . . 71
- 5.21 Velocity contours ( $u$ ) and disturbance streamlines for a critical step,  $h/\delta^* = 1.462$  from PIV phase-locked frames. The different images correspond to the different phases measured:  $\phi = 0^\circ$  (a),  $\phi = 60^\circ$  (b),  $\phi = 120^\circ$  (c),  $\phi = 180^\circ$  (d),  $\phi = 240^\circ$  (e) and  $\phi = 300^\circ$  (f). Wall-normal axis is scaled by 1.35 for visualization purposes. . . . . 72
- 5.22 Velocity contours ( $u$ ) and disturbance streamlines for a supercritical step,  $h/\delta^* = 1.950$  from PIV phase-locked frames. The different images correspond to the different phases measured:  $\phi = 0^\circ$  (a),  $\phi = 60^\circ$  (b),  $\phi = 120^\circ$  (c),  $\phi = 180^\circ$  (d),  $\phi = 240^\circ$  (e) and  $\phi = 300^\circ$  (f). Wall-normal axis is scaled by 1.35 for visualization purposes. . . . . 72
- 5.23 Power Spectral Density results from HWA measurements for different step heights with acoustic forcing at  $F = 90$ . Streamwise locations shown:  $x = 341$  mm (a),  $x = 361$  mm (b),  $x = 374$  mm (c),  $x = 383$  mm (d),  $x = 396$  mm (e) and  $x = 421$  mm (f). Step is located at  $x = 380$  mm. Clean case ( $h/\delta^* = 0$ , black), subcritical step ( $h/\delta^* = 0.775$ , blue), critical step ( $h/\delta^* = 1.462$ , green) and supercritical step ( $h/\delta^* = 1.950$ , orange). The x-axis corresponds to reduced frequency,  $F = (2\pi f U_{ref}^2/\nu) \times 10^6$ . Full vertical lines denote fundamental and higher harmonics (black) and subharmonic (magenta) of the forced frequency. Dashed black lines indicate the limits of the naturally forced TS waves. Dashed magenta lines denote the subharmonic corresponding to the band of unstable TS waves. . . . . 73
- 5.24 PSD contours from HWA measurements in critical step case conditions ( $h/\delta^* = 1.462$ ) with acoustic forcing at  $F = 90$ . Streamwise locations shown:  $x = 341$  mm (a),  $x = 361$  mm (b),  $x = 374$  mm (c),  $x = 383$  mm (d),  $x = 396$  mm (e) and  $x = 421$  mm (f). Step is located at  $x = 380$  mm. The x-axis corresponds to reduced frequency,  $F = (2\pi f U_{ref}^2/\nu) \times 10^6$ . Full vertical lines denote fundamental and higher harmonics (black) and subharmonic (magenta) of the forced frequency. Dashed black lines indicate the limits of the naturally forced TS waves. Dashed magenta lines denote the subharmonic corresponding to the band of unstable TS waves. . . . . 74
- 5.25 POD results for a critical step ( $h/\delta^* = 1.462$ ) with acoustic forcing at  $F = 90$ . First five normalized POD modes from the  $u$ -component of the disturbance (a, b, c, d, e) and energy fraction per mode from both  $u$ - (black bars) and  $v$ - (red bars) components. . . . . 75
- 5.26 Wall-normal profiles of the subharmonic modes as extracted from HWA spectral data bandpass at  $30 \leq F \leq 57$  (black symbols) and from the RMS of the reconstructed flow from POD modes 5-6 for a subcritical step and 4-5 for a critical step (red symbols). Subcritical step results (top figure) and critical step results (bottom figure). Streamwise locations shown (from left to right):  $x = [371, 382, 386, 391, 401]$  mm. . . . . 76
- 5.27 N-factor of the fundamental mode for different forcing frequencies:  $F = 60$  (blue),  $F = 90$  (green) and  $F = 110$  (magenta). Clean case (a), subcritical step (b), critical step (c) and supercritical step (d) conditions. Symbols denote HWA measurements, full lines represent DNS results in clean (a) and subcritical step conditions (b). Dashed lines in (a), (b) and (c) denote the clean case results from DNS. Note that the dashed-dotted lines between HWA data points are not numerical data but are just included for easier interpretability of the experimental data trend. . . . . 77

5.28	Wall-normal profiles of the fundamental mode ( $F = 110$ ) in terms of $ \hat{u} $ (black) and $\partial U/\partial y$ (gray). Full lines denote DNS data and symbols ( $\circ$ ) HWA results. Clean (a), subcritical (b), critical (c) and supercritical (d) step cases. The streamwise locations plotted are at (from left to right) $x = [341, 361, 374, 381, 383, 391, 401, 421]$ mm with the step at $x = 380$ mm. The horizontal spacing between profiles is set to $\Delta = 1.2$ for legibility. Note that the dashed-dotted lines in (c) and (d) are not numerical data but just intend to trace the experimental data points for easier interpretability. . . . .	79
5.29	Wall-normal profiles of the fundamental mode ( $F = 60$ ) in terms of $ \hat{u} $ (black) and $\partial U/\partial y$ (gray). Full lines denote DNS data and symbols ( $\circ$ ) HWA results. Clean (a), subcritical (b), critical (c) and supercritical (d) step cases. The streamwise locations plotted are at (from left to right) $x = [341, 361, 374, 381, 383, 391, 401, 421]$ mm with the step at $x = 380$ mm. The horizontal spacing between profiles is set to $\Delta = 1.2$ for legibility. Note that the dashed-dotted lines in (c) and (d) are not numerical data but just intend to trace the experimental data points for easier interpretability. . . . .	80
6.1	Schematic of main flow features and growth trends found in this work for a FFS with an incoming TS wave. . . . .	82
A.1	Velocity contours ( $u$ ) and disturbance streamlines for a subcritical step, $h/\delta^* = 0.775$ at forcing frequency $F = 90$ . PIV (a, c, e, g, i, k) and DNS (b, d, f, h, j, l) results. $\phi = 0^\circ$ (a, b), $\phi = 60^\circ$ (c, d), $\phi = 120^\circ$ (e, f), $\phi = 180^\circ$ (g, h), $\phi = 240^\circ$ (i, j) and $\phi = 300^\circ$ (k, l). Wall-normal axis is scaled by 1.35 for visualization purposes. . . . .	85
A.2	POD results for a subcritical step ( $h/\delta^* = 0.775$ ) with acoustic forcing at $F = 90$ . First five normalized POD modes from the $u$ -component of the disturbance (a, b, c, d, e) and energy fraction per mode from both $u$ - (black bars) and $v$ - (red bars) components. . . . .	86
A.3	POD results for a supercritical step ( $h/\delta^* = 1.950$ ) with acoustic forcing at $F = 90$ . First five normalized POD modes from the $u$ -component of the disturbance (a, b, c, d, e) and energy fraction per mode from both $u$ - (black bars). . . . .	86

# List of Tables

2.1	Test cases using Hot-Wire Anemometry (HWA). . . . .	22
2.2	Test cases using Particle Image Velocimetry (PIV). . . . .	22
2.3	Test cases using Infrared Thermography (IR). . . . .	23
2.4	Numerical parameters used for the BL and OS solvers. . . . .	24
2.5	Numerical parameters used for DNS. . . . .	25
2.6	Uncertainties from experimental instrumentation and calibration. . . . .	34
2.7	Maximum systematic uncertainty in velocity and wall-normal coordinate found amongst all HW profiles. . . . .	34
2.8	Uncertainty of the U meanflow component in PIV. . . . .	35
3.1	Main PIV parameters during the experiments. . . . .	40



# Nomenclature

## Abbreviations, Acronyms

APG	Adverse Pressure Gradient
BFS	Backward-Facing Step
BL	Boundary Layer
DNS	Direct Numerical Simulation
FFS	Forward-Facing Step
FPG	Favorable Pressure Gradient
HWA	Hot-Wire Anemometry
IR	Infrared Thermography
LE	Leading Edge
PIV	Particle Image Velocimetry
POD	Proper Orthogonal Decomposition
PSD	Power Spectral Density
SPL	Sound Pressure Level [dB]
TE	Trailing Edge
TS	Tollmien-Schlichting
ZPG	Zero Pressure Gradient

## Dimensionless Parameters

$Re_{\delta^*}$	Reynolds number based on displacement thickness	[-]
$Re_{h,crit}$	Critical Reynolds step height, $Re_{h,crit} = h_{crit}U/\nu$	[-]

$Re_{hh}$  Reynolds number based on the step height,  $Re_{hh} = hU_h/\nu$  [-]

$Re_h$  Reynolds number based on the step height,  $Re_h = hU_e/\nu$  [-]

$Re_u$  Unit Reynolds number [-]

$Re_{x_s}$  Reynolds number based on the step location [-]

$Re_{x_T}$  Reynolds number based on the transition location,  $Re_{x_T} = x_T U_\infty/\nu$  [-]

$Re_x$  Reynolds number based on streamwise coordinate [-]

$C_f$  Skin friction coefficient,  $\frac{\tau_w}{1/2\rho U_\infty^2}$  [-]

$C_p$  Pressure coefficient [-]

$s$  Relative transition location,  $s = (x_T - x_h)/(x_{T, clean} - x_h)$  [-]

$Tu$  Turbulence intensity,  $Tu = \sqrt{\bar{u}^2}/U_\infty$  [-]

$F$  Non-dimensional frequency,  $F = (2\pi\omega f\nu/U_\infty^2) \times 10^6$  [-]

$H = h/\delta^*$  Relative step height [-]

$N$  N-factor [-]

## Physical Variables

$\alpha$  Streamwise wavenumber [1/m]

$\beta$  Spanwise wavenumber [1/m]

$\delta^*$  Displacement thickness [m]

$\delta_{99}$  Boundary layer thickness [m]

$(U, V, W)$  Velocity components of the base flow [m/s]

$(u, v, w)$  Velocity components of the perturbation [m/s]

$\tau_w$  Wall shear stress [Pa]

$\theta$	Momentum thickness	[m]	$U_e$	External velocity	[m/s]
$c$	Phase speed	[m/s]	$u_{rev}$	Reversed velocity	[m/s]
$E_V$	Kinetic energy of the perturbation	[m <sup>2</sup> /s <sup>2</sup> ]	$x_T$	Transition location	[m]
$f$	Frequency	[Hz]	h	Step height	[m]

# Introduction

## 1.1. Motivation

In recent years, the EU has increased its efforts towards reducing Greenhouse Gas (GHG) emissions in aviation. However, the constant growth of air traffic makes it challenging to fulfill the Flightpath 2050 program goals (Krein and Williams, 2012). In this context, Natural Laminar Flow (NLF) technologies are a promising field due to their effectiveness in decreasing the skin-friction drag component (Arnal and Archambaud, 2008).

The emergence of electric-powered aircraft within commercial air transport has drawn the attention of NLF on unswept wings where transition is primarily driven by Tollmien-Schlichting (TS) waves. However, surface discontinuities remain the main concern towards achieving NLF since they can move transition upstream. The high surface quality requirements to achieve NLF call into question whether this could be accomplished within conventional production standards (Hansen, 2010). This stressed the need to understand the effects of surface imperfections on flow transition.

In the last twenty years, important research efforts have focused on panel discontinuities (modeled as two-dimensional steps across the wingspan) since these constitute one of the most ubiquitous surface imperfections<sup>1</sup> which rapidly move transition upstream. Prior studies have shown that Backward-Facing Steps (BFS) promote transition earlier than Forward-Facing Steps (FFS) (Wang and Gaster, 2005). Therefore, in the design of laminar flow components, FFS are preferred over BFS. This is why this work will focus on the effect of FFS on laminar-turbulent transition.

First research efforts concerning FFS-induced transition aimed at finding critical Reynolds heights ( $Re_{h,crit}$ ) to provide manufacturers with a rapid estimate of the transition location and the maximum permissible height between panel discontinuities. However, it was soon proved by the experiments of the Northrop Grumman Corporation (Drake et al., 2008a,b, 2010) that the large dependency of FFS-induced transition to the specific test conditions makes  $Re_{h,crit}$  alone not sufficient to determine when FFS become critical.

The experimental results of Wang and Gaster (2005) suggested that transition with FFS could be largely described by the exponential growth of disturbances downstream. Their results were in agreement with observations from other authors, whose focus was on developing a semi-empirical model inspired on the  $e^N$ -method to predict transition location (Crouch et al., 2006; Perraud et al., 2014). These models attempt to isolate the effect that the step has on transition in one single parameter,  $\Delta N$ . Large discrepancies are observed when the data fits and models proposed by different authors are compared, as noticed in Costantini (2016). The outcomes of the aforementioned studies raise the question of whether the effect of an FFS on transition can be uniquely described by  $\Delta N$ .

Recent DNS and experiments in 3D boundary layers dominated by Crossflow Instabilities (CFI) in the presence of FFS point to different growth mechanisms at the step. These could explain the observed delay on transition for some step heights (Rius-Vidales and Kotsonis, 2021), the unsteadiness of the shear layer downstream (Eppink, 2020) or the onset of near-wall vortices immediately after the step (Casacuberta et al., 2021). Despite the different incoming instability in these works, compared to TS waves, their findings emphasize the importance of close-examining the disturbances evolution in the vicinity of a FFS to understand how this could influence transition downstream.

---

<sup>1</sup>Hansen (2010) argues that a continuous surface between the wing box and the Leading Edge (LE) makes repair and system integration very difficult.

From the aforementioned works the mechanisms governing the growth of disturbances at the step remain not fully understood. In turn, the lack of comparison between numerical and experimental data further hinders the problem understanding. On the one hand, existing experimental works on TS-FFS dominated transition were mainly concerned with transition prediction, providing limited measurements in the vicinity of the step. On the other hand, previous numerical studies were not designed to match other experimental works. In light of this, this study offers for the first time detailed comparison on numerical and experimental results concerned with FFS-TS dominated transition.

The remaining of this section aims to study in detail relevant literature on FFS-TS transition. The first part of this chapter (section 1.2) revises some concepts of boundary layer stability that are key to understand the main findings from literature: modal, non-modal growth, transition paths, etc. Section 1.3 briefly discusses the main findings on two-dimensional roughness elements, focusing on literature regarding TS-FFS transition. Section 1.4 presents an overview of previous works concerned with the acoustic forcing of TS waves to justify the excitation approach used in these experiments. Finally, in section 1.5 the main literature findings are summarized and in section 1.6 the main research questions and the final objective of this work are presented

## 1.2. Stability of boundary layer flows

Boundary layer flows are sensitive to disturbances present in the environment or introduced directly into the flow. Likewise a system of resonators, the boundary layer amplifies certain disturbance frequencies. Some of these frequencies are amplified at several streamwise locations and later on damped. In this case, the flow is said to be stable. When the disturbances go on amplifying, at some point the energy of the most amplified frequencies is poured onto its harmonic modes and so forth, increasing the energy contained at higher frequencies. This process is governed by the non-linear term of the Navier-Stokes equations. Once the spectral energy content reaches the Kolmogorov equilibrium, the boundary layer is said to become turbulent.

Hydrodynamic stability studies the growth or decay of small amplitude disturbances in the boundary layer by adding an initial perturbation  $(u_i, p)$  on top of the initially undisturbed flow  $(U_i, P)$ , i.e. base flow. The evolution of the perturbation can be studied from the modified incompressible non-linear Navier Stokes (N-S) equations (Schmid and Henningson, 2012).

$$\frac{\partial u_i}{\partial t} = -U_j \frac{\partial u_i}{\partial x_j} - u_j \frac{\partial U_i}{\partial x_j} - \frac{\partial p}{\partial x_i} + \frac{1}{\text{Re}} \nabla^2 u_i - u_j \frac{\partial u_i}{\partial x_j}, \quad (1.1)$$

$$\frac{\partial u_i}{\partial x_i} = 0. \quad (1.2)$$

This set of equations is commonly known as the Nonlinear Disturbance Equations. The question that remains to be answered is whether a mode will decay or grow. Two different approaches exist to answer this question: the energy method and the method of small disturbances or most commonly known as Linear Stability Theory (LST). The latter has proved more successful in the study of convective instabilities given the rather conservative estimates that the energy approach provides (Schlichting and Gersten, 2016). Nevertheless, the energy method provides intuitive insight into the mechanisms responsible for the growth of disturbances.

### The energy approach

A natural choice to study the stability of the flow is to analyze the temporal evolution of the perturbation kinetic energy. If the energy of the perturbation increases unconstrained in time, the flow is unstable. Although this distinction is more difficult to make when studying a spatially unstable wave<sup>2</sup>, it is also intuitive to define spatially unstable disturbances as those whose kinetic energy grows unbounded in space. The evolution of the perturbation kinetic energy can be obtained by multiplying equation (1.1) by  $u_i$  and integrating on a certain volume  $V$ . Assuming the disturbance is localized in space, i.e.  $\partial E_V / \partial x_i = 0$  (Schmid and Henningson, 2012):

$$\frac{dE_V}{dt} = - \int_V u_i u_j \frac{\partial U_i}{\partial x_j} dV - \frac{1}{\text{Re}} \int_V \left( \frac{\partial u_i}{\partial x_j} \right)^2 dV, \quad (1.3)$$

<sup>2</sup>Mathematically, the temporal stability of a disturbance can be defined in terms of energy by comparing the kinetic energy within a volume of the disturbance at different instants. However, this criteria is more challenging to define in spatially developing disturbances since there can be planes in which energy can be equal to zero (since the disturbance is oscillating in streamwise direction) while the disturbance can still be growing downstream.

where  $E_V = 1/2 \int_V u_i u_i dV$ . The above expression is commonly known as Reynolds-Orr equation (Orr, 1907; Reynolds, 1895). Notice that all non-linear terms dropped given the conservative nature of the N-S equations. From this equation one can demonstrate that the mechanisms through which disturbances initially amplify are linear while non-linear terms (last term in equation (1.1)) redistribute the energy between modes.

From equation (1.3) two main linear sources of disturbance growth or decay can be identified. The first term on the right-hand side describes the transfer of energy between the disturbance and the base flow while the second term defines the dissipation of energy through viscosity (Henningson, 1996).

The energy approach can determine if a flow is stable or unstable under all possible perturbations. However, it is insufficient to study the stability of the flow under certain disturbances (individual frequencies). For this, it is necessary to introduce Linear Stability Theory (LST) (Drazin, 2002).

### Linear Stability of parallel flows

The assumption of parallel flow is generally a suitable one for a Blasius boundary layer, i.e. the flow in the  $x$ -direction only changes in wall-normal direction,  $y$ . Saric and Nayfeh (1975) solved the non-parallel equations for a Blasius flow and compared its neutral curve with the one assuming parallel flow. They observed that non-parallel terms in the resulting stability equations did not contribute much except for small boundary layers (small  $\delta^*$ ) or low Reynolds numbers. Note that these conditions usually occur at the LE of a flat plate.

It can be assumed that the velocity profile depends uniquely on the  $y$ -coordinate such that  $U_i = U(y)$  and  $V = W = 0$ . In addition, if the perturbations are assumed small, all quadratic terms in the equations drop. When these assumptions are introduced in equation (1.1) and 2D flow is further assumed, the Linearized N-S equations (LNSE) for 2D parallel flows are obtained (Schmid and Henningson, 2012):

$$\frac{\partial u}{\partial t} + U \frac{\partial u}{\partial x} + v \frac{\partial U}{\partial y} = -\frac{\partial p}{\partial x} + \frac{1}{\text{Re}} \nabla^2 u, \quad (1.4)$$

$$\frac{\partial v}{\partial t} + U \frac{\partial v}{\partial x} = -\frac{\partial p}{\partial y} + \frac{1}{\text{Re}} \nabla^2 v, \quad (1.5)$$

$$\frac{\partial u}{\partial x} + \frac{\partial v}{\partial y} = 0. \quad (1.6)$$

Since the non-linear terms disappeared, the resulting PDEs are in separable form such that normal mode solutions can be sought, i.e. eigenvalue problem (Mack, 1984). This set of equations can be simplified to an expression based on  $v^3$ :

$$\left[ \left( \frac{\partial}{\partial t} + U \frac{\partial}{\partial x} \right) \nabla^2 - U'' \frac{\partial}{\partial x} - \frac{1}{\text{Re}} \nabla^4 \right] v = 0, \quad (1.7)$$

where  $U'' = \frac{\partial^2 U}{\partial y^2}$ .

#### 1.2.1. Modal growth

Wave-like or modal functions are solution of equation (1.7). In a 2D approach, they represent a wave traveling in the  $x$  direction with its amplitude growing in exponential form along  $x$ . Hence, fluctuations in  $v$  can be expressed as:

$$v(x, y, t) = \tilde{v}(y) e^{i(\alpha x - \omega t)}, \quad (1.8)$$

where the phase speed is  $c = \omega/\alpha$ . Introducing this solution in equation (1.7), a fourth order differential equation results that describes the evolution of the perturbation amplitude (Schlichting and Gersten, 2016):

$$\left[ (-i\omega + i\alpha U) (\mathcal{D}^2 - \alpha^2) - i\alpha U'' - \frac{1}{\text{Re}} (\mathcal{D}^2 - \alpha^2) \right] \tilde{v} = 0, \quad (1.9)$$

where  $\mathcal{D} = \partial/\partial y$  and the boundary conditions are  $\tilde{v} = \mathcal{D}\tilde{v} = 0$  at  $y = 0$  and  $y = \infty$ . This equation is the well-known Orr-Sommerfeld (Orr, 1907; Sommerfeld, 1908) equation for a 2D boundary layer. Most of the research done on the stability of incompressible flows revolves around this equation (Mack, 1984).

<sup>3</sup>The reader is referred to Saric for further details into the mathematical steps followed to obtain this equation.

Two approaches can be adopted in stability theory at this point. On the one hand, one can assume that  $\alpha$  is real and  $\omega$  is complex such that the amplitude of the wave grows in time. This approach is called temporal stability and was widely used in the past because of its lower mathematical complexity. On the other hand, the spatial approach assumes  $\alpha$  complex and  $\omega$  real. From equation (1.9) one can distinguish the added complexity of the spatial approach: the eigenvalue problem is now of fourth-order. However, the stability of conventional<sup>4</sup> boundary layer problems are well-represented by the spatial approach, where the amplitude of the wave grows in streamwise direction while it remains constant in time.

### Neutral stability

The most common way of studying the spatial stability of a flow is using the so-called neutral stability curves. The solid black line in figure 1.1 (a) encompasses the streamwise locations where perturbations grow in a Blasius BL. The curve can be understood as follows. Let a disturbance with non-dimensional frequency  $F = (\omega v/U_0) \times 10^6 = 200$  be introduced at the LE of the flat plate. This perturbation will experience exponential growth at streamwise positions  $500 \lesssim Re_{\delta^*} \lesssim 700$  and will decay otherwise. In quasi-parallel theory wavenumbers and frequencies are allowed to depend on the streamwise location assuming that the baseflow varies on a larger length scale. The disturbances are expressed as

$$\psi(x, y, t) = \varphi(y) e^{-\int^x \alpha_i dx} e^{i(\int^x \alpha_r dx - \omega t)}, \quad (1.10)$$

so that the total amplitude of the wave at a given streamwise location results in:

$$\frac{1}{A} \frac{dA}{dx} = -\alpha_i, \quad (1.11)$$

$$N = \ln\left(\frac{A}{A_0}\right) = -\int_{x_0}^x \alpha_i dx, \quad (1.12)$$

where  $\alpha_i$  and  $\alpha_r$  are the complex and real terms of the streamwise wavenumber (Mack, 1984). The indifference Re number is defined from the neutral stability curve as that Reynolds number below which all perturbations decay. In figure 1.1 (a) this corresponds to  $Re_{\delta^*} \approx 400$ . In experiments, the critical and the indifference Reynolds numbers are seen to be different. This demonstrates the existence of a region before transition in which disturbances grow enough until turbulence breakdown: the transition region.

### Absolute and Convective Instabilities

When a local perturbation is introduced in the flow, the boundary layer can behave as a noise amplifier or as an oscillator (Chomaz, 2005). In the first, the local instabilities are overcome by advection and are transported away from the perturbation source. These are denoted as convective instabilities. In the second, if the local instability experiences a large growth in a small time-lapse, self-sustained oscillations can take place and contaminate the entire flowfield. The last are absolute instabilities and when they take place the flow is said to *suddenly* experience transition (see figure 1.1 (b)). A clear example of absolute instability is the wake of a cylinder over a critical Re number. Conversely, flat plate boundary layers exhibit convective instabilities which allow for a sustained unstable development downstream.

### Inviscid Instabilities

The Orr-Sommerfeld equation (equation (1.9)) can be largely simplified if viscosity effects are assumed to affect only the baseflow but not the development of the instability. Thus, the fourth-order term disappears and the resulting equation is the so-called Rayleigh equation:

$$(U - c)(\varphi'' - \alpha^2 \varphi) - U'' \varphi = 0, \quad (1.13)$$

a second order differential equation with boundary conditions  $\varphi(0) = 0$  and  $\varphi(y) \rightarrow 0$  as  $y \rightarrow \infty$ . The Rayleigh equation describes the amplitude evolution of an inviscid disturbance. After some mathematical alterations and assuming a 2D temporal instability, the following expression can be derived from equation (1.13) (Mack, 1984):

<sup>4</sup>Conventional here denotes no presence of roughness elements or other devices which largely increase the complexity of the flow stability.

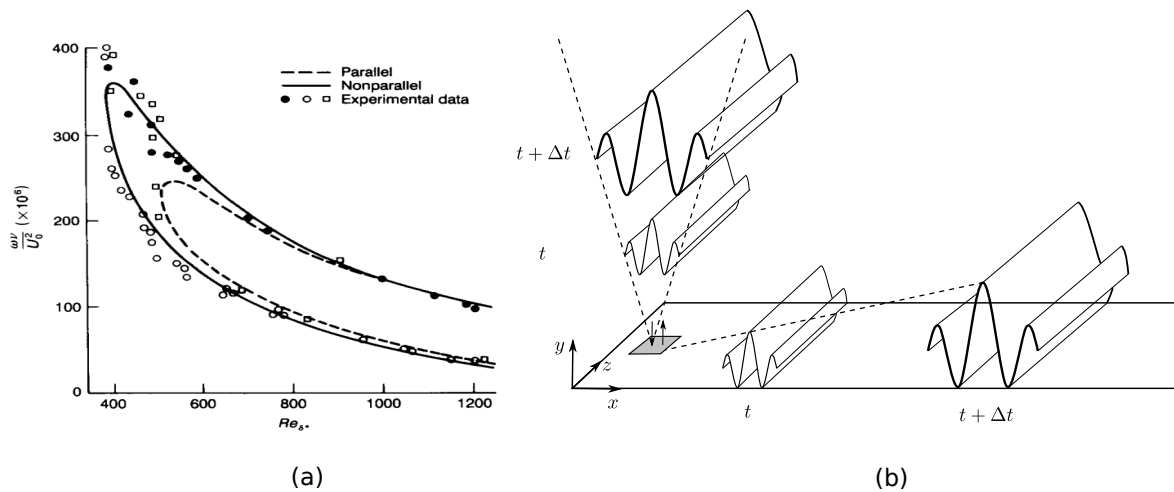


Figure 1.1: (a) Spatial stability neutral curve from analytical (lines) and experimental (symbols) data. Figure reproduced from White and Corfield (2006). (b) Evolution of a local perturbation on a boundary layer depicting an absolute and a convective instability.

$$\omega_i \int_0^{\delta_{99}} \frac{\{\varphi^2\} U''}{|\alpha U - \omega|^2} dy = 0. \quad (1.14)$$

From this equation, it can be observed that when  $\omega_i \neq 0$ ,  $U''$  must change sign somewhere along  $y$ . This demonstrates that inviscid unstable waves can only take place when there is an inflection point across the velocity profile.

A very important characteristic of the Rayleigh equation is the singular point at  $\omega/\alpha = U$  (group velocity equal to base flow streamwise component) which takes place at the so-called critical layer. At this critical point, if there is no inflection point ( $U'' \neq 0$ ),  $\varphi$  becomes infinitely large. This nonphysical result of the Rayleigh equation demonstrates that at the critical point viscosity should play an important role to explain the disappearance of this singularity (Schlichting and Gersten, 2016). Indeed, in 1929 Tollmien demonstrated the existence of two regions where viscous effects should play an important role even if  $Re \rightarrow \infty$ . These regions correspond to the near wall and the region around the critical layer. The findings of Tollmien shed light on the possible existence of instabilities triggered by viscosity.

### Viscous Instabilities

The finding of viscous instabilities implies solving a complex fourth-order eigenvalue problem (equation (1.9)). In addition, for large Reynolds numbers, the Orr-Sommerfeld equation presents a stiff behavior, i.e. numerical methods become unstable if the step size is not sufficiently small. This is why the first complete solutions to the viscous stability problem date from the first decade of the twenty-first century.

The most widely accepted hypothesis before Schubauer and Skramstad (1947) experiments was that viscosity only acted to damp instabilities. Taylor (1915) and Prandtl (1921) were the first authors who adventured that instability waves could also exist without inflection points. They tried to explain the role of viscosity through the Reynolds stresses. This will be described in the next section.

Later, Tollmien (1929) and Schlichting (1933) mathematically demonstrated that the primary instability mode in a Blasius boundary layer is a convective wave which can only be explained accounting for viscosity, i.e. Tollmien-Schlichting (TS) waves. This could not be proven until 1940 when Schubauer and Skramstad (1947) performed a low-turbulence ( $Tu = 0.02\%$  of  $U_\infty$ ) experiment where they could observe the growth of TS waves and determine the neutral curve (presented in figure 1.1 (a)) for a Blasius boundary layer. They also measured the critical Reynolds number of the boundary layer<sup>5</sup>, which resulted to be four orders of magnitude larger than the indifference Reynolds number. Hence, a wave starts to grow at the region where  $Re \geq Re_{ind}$  until the complete transition to turbulent flow takes place at  $Re \approx Re_c$ . This concept is what is nowadays behind one of the most widely used methods to predict transition in the industry, the  $e^N$ -method, developed in parallel by Smith and Gamberoni (1956) and Van Ingen (1956). Assuming LST, each perturbation grows at an

<sup>5</sup>Other authors also measured this quantity but they were not able to determine the correct value for TS-dominated transition since the turbulence intensity of their experiments was too large and no selective amplification was observed (Schlichting and Gersten, 2016).

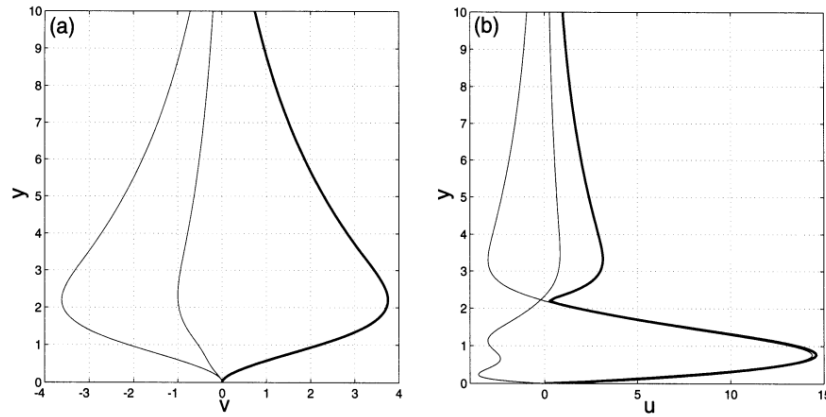


Figure 1.2: Eigenfunction of the primary instability in a Blasius boundary layer. (a) normal and (b) streamwise perturbation velocity components at  $\alpha = 0.2$  and  $Re = 500$ . The thick lines represent the absolute value while the thin lines are the imaginary and real contributions. Figure reproduced from Schmid and Henningson (2012).

exponential rate within the unstable region. These authors compared the amplification factor of the unstable waves at  $Re_c$  to that at  $Re_{ind}$ . Based on experimental data, they could prove that the N-factor was generally constant, ranging from 8 to 11 depending on the levels of the turbulence intensity.

### The nature of Tollmien-Schlichting waves

From the solutions of the Orr-Sommerfeld equation for a Blasius boundary layer one can obtain the eigenfunctions of the TS waves (see figure 1.2). Some of the most particular features of TS waves are their long wavelengths, which are approximately six times the boundary layer thickness. Moreover, due to their low phase speeds, they have their maxima very close to the wall, i.e. they advance with the slow region of the boundary layer (Schmid and Henningson, 2012). Another important characteristic is its dual-peak on the streamwise velocity component, indicating a  $180^\circ$  phase shift on  $u$  at the critical layer, where the wave phase speed equals the baseflow streamwise velocity (Reed and Saric, 2008).

Finally, although in this work only TS waves were mentioned as the primary growth modes for Blasius BL flows, when different baseflows are considered, other instabilities can be found from the Orr-Sommerfeld equation. Two important examples are Crossflow (CF) and Görtler instabilities which take place when 3D boundary layers or concave walls are considered, respectively.

The computation of TS waves has been widely discussed over the last 60 years. However, if one wants to understand the nature of their existence, the early works of Prandtl (1921), Taylor (1915) and Lin (1954) are most useful. Already in 1915 Taylor was the first author to envisage that, in a non-inflectional boundary layer, the only way an instability could exist is if viscosity builds up a positive Reynolds stress near the wall such that energy is removed from the mean flow to make the disturbance grow. Later, Prandtl (1921) and Lin (1954) presented similar conclusions.

Figure 1.3 depicts a simplified sketch illustrating the original derivation of Prandtl (1921). The Reynolds number is assumed to be  $Re \rightarrow \infty$  such that the viscous sublayer is confined at a region very close to the wall where the velocity is very small,  $U \approx 0$ . Outside the viscous sublayer, an inviscid instability exists. Since  $u_i$  and  $v_i$  are  $90^\circ$  out of phase in this region, the Reynolds stresses are zero,  $\langle u_i v_i \rangle = 0$ . To satisfy the no-slip condition at the wall, a viscous instability must exist within the viscous sublayer which counteracts the inviscid instability, i.e.  $u_i + u_v = 0$  at the wall. However, when deriving the  $u$  and  $v$  components of the viscous instability, it is observed that they are correlated with a phase-shift of  $135^\circ$ , i.e.  $\langle u_v v_v \rangle \neq 0$ . Outside of the viscous sublayer,  $u$  decays to zero while  $v$  persists further up, building a non-zero Reynolds stress with the inviscid instability, i.e.  $\langle u_i v_v \rangle \neq 0$ . At the critical layer, both  $\langle u_v v_v \rangle$  and  $\langle u_i v_v \rangle$  are equal. The overall mechanism presented here was perfectly summarized by Taylor (1915): "Viscosity acts to permit the momentum of the disturbance to be absorbed at the wall".

<sup>6</sup>The expressions describing both inviscid and viscous instabilities can be found in Mack (1984)

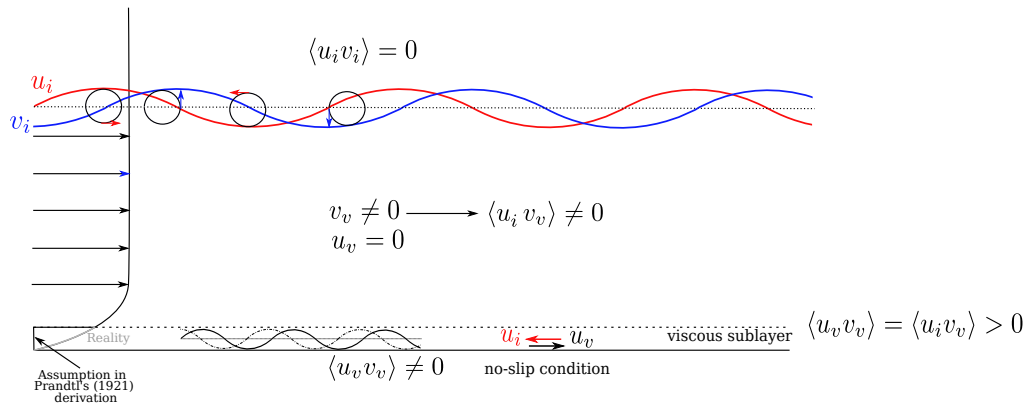


Figure 1.3: Sketch representing the mechanisms which explain the existence of a viscous instability by means of the build-up of a Reynolds stress across the boundary layer. Inspired on the illustration shown in Baines et al. (1996) work.

### 1.2.2. Non-modal growth

Some flows such as Pipe, Couette, channel flows, or flat plate boundary layers under high or moderate levels of turbulence intensity present critical Reynolds numbers which do not agree with linear stability theory. The first hypothesis resorted to non-linearities to explain this behavior. However, it was later confirmed that are indeed linear mechanisms the ones responsible for earlier transition in these cases. Ellingsen and Palm (1975) identified the possible existence of a linear mechanism different from a TS wave able to amplify disturbances when no inflection point is present. Over the last 30 years, it could be mathematically demonstrated that, due to the non-normality of the Orr-Sommerfeld equation, algebraic (rather than exponential) growth can happen at earlier times (or streamwise positions) due to the non-orthogonal superposition of asymptotically stable modes, i.e. the solution at  $t \rightarrow \infty$  ( $x \rightarrow \infty$ ) corresponds to the one predicted by LST (Reshotko, 2008). This earlier growth can lead to sudden breakdown. In Blasius boundary layers two types of linear mechanisms have been observed to enhance non-modal growth: the lift-up effect and the Orr mechanism.

The Orr-mechanism (Orr, 1907) enhances the amplification of disturbances whose streamlines are tilted with respect to the mean shear. In figure 1.4 (a) the mean shear is parallel to the lower solid line and it tilts the perturbation structures to the right as the right-pointing arrow shows. Since their horizontal spacing does not change but the vertical distance has increased, the normal velocity needs to raise due to continuity. When the perturbations align with the mean shear, they start to lose energy to finally decay (Jiménez, 2013).

The second mechanism is the so-called lift-up effect. It takes place when small perturbations push (or lift-up) horizontal momentum to different  $y$ -levels and create large perturbations in the streamwise velocity (Brandt, 2014). Ellingsen and Palm (1975) mathematically demonstrated that disturbances in the cross-stream velocity components ( $v, w$ ) which are independent of the streamwise direction would linearly change the streamwise momentum of the perturbation in time as

$$u = u(0) - v \frac{dU}{dy} t, \quad (1.15)$$

where the flow is assumed parallel and inviscid such that  $v$  does not decay in time.

The lift-up effect is commonly observed in Blasius flows with moderate to large levels of freestream turbulence. Counterrotating vortices in the streamwise direction enhance the lift-up effect and create uneven regions of streamwise momentum which give rise to near-wall streaks, see figure 1.4 (b) (Brandt, 2014).

The study of non-modal growth is of interest in this work since local geometrical discontinuities could trigger transient growth of the convective instabilities. The most recent work related to this is the one performed by Blackburn et al. (2008). The authors studied the transient growth (no assumption of eigenmodal behavior) of linear optimal<sup>7</sup> perturbations around BFS on channel flows driven by the presence of large non-parallel effects at the step. Non-parallel effects are seen to enhance algebraic growth (Hack and Moin, 2017). The authors studied the modes which triggered maximum energy growth along time and showed that the same modes appeared downstream of a BFS in DNS simulations when white noise was included at the inflow.

<sup>7</sup>If the reader is interested in the study of transient growth through optimal disturbances she/he can refer to Schmid and Henningson (2012).

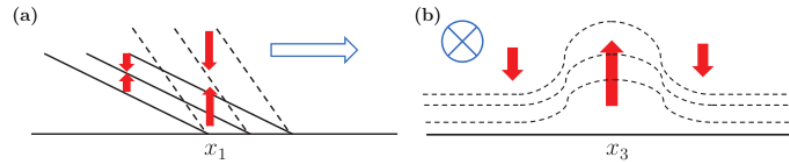


Figure 1.4: Sketch of the Orr-mechanism on the plane  $x$ - $y$  (a) and the lift-up effect on the plane  $y$ - $z$  (b) reproduced from Jiménez (2013).

Although Blackburn et al. (2008) did not observe transition, their findings demonstrate that BFS can trigger large transient growth even in the presence of low turbulence intensity.

### 1.2.3. Paths to transition

The most likely transition scenario depends on the freestream turbulence intensity. Recently, mostly all works regarded the modal transition scenario as the predominant one in laminar-turbulent transition. This transition scenario is path A in figure 1.5.

In path A, freestream disturbances are firstly entrained into the boundary layer through a receptivity process at the LE and later the primary modes are excited. These convective instabilities (T-S waves, crossflow, or Görtler vortices, depending on the base flow) undergo exponential growth downstream. When they amplify above approximately 1% of  $U_\infty$  (in the case of TS waves), they start to modulate the baseflow. The previous mode saturates, i.e. stops the efficient extraction of energy from the mean flow, and a new quasi-steady base flow gives rise to the growth of a secondary instability (Schmid and Henningson, 2012). Later, modes that have acquired enough amplification start a triadic interaction process, i.e. two different modes prompt the amplification of fluctuations at their frequency and their harmonics and also at the sum and difference of their frequencies and harmonics (Klebanoff et al., 1962). The flow achieves its turbulent state when the energy, first concentrated on the initially unstable modes, is redistributed over a broad range of frequencies. This is a very fast process compared to the linear growth of instabilities.

The transition path described above is widely accepted under low levels of freestream turbulence and smooth surfaces. However, the experiments of Klebanoff et al. (1962) showed that for higher levels of freestream turbulence, other structures in the form of streaks showing non-exponential growth play an important role in the onset of transition. Morkovin (1994) denoted these different transition scenarios as bypass transition. In his work Morkovin (1994) carefully delineated five possible transition scenarios depending on the free-stream turbulence (see figure 1.5).

During flight only paths A-C become relevant. Path A was already described above as the *traditional* transition scenario. This path is the one expected in these experiments due to the low turbulence of the wind tunnel facility used ( $Tu \leq 0.07\%$ ). Already in 1962 Klebanoff et al. (1962) demonstrated with a set of experiments that when TS waves reach an amplitude above  $\geq 1\%$  of  $U_\infty$  they become three-dimensional and present a spanwise modulation with a wavelength of the same order of the streamwise wavelength of TS waves. In the late stages of transition, the peaks in the spanwise modulation display high-frequency and large amplitude velocity fluctuations (spikes) which double, triple, etc. downstream. These spikes are directly associated with the high wall-normal shear present above the *head* of  $\Lambda$ -shaped vortices where inflectional instabilities are generated. Finally, the spike stage and later breakdown to turbulence quickly develop, within approximately one TS wavelength. The above-presented transition scenario is commonly known as K-type transition.

Different patterns of  $\Lambda$ -shaped vortices (see figure 1.6 (a)) were observed during Knapp and Roache (1968) experiments, which indicated the existence of a second transition scenario. The staggered  $\Lambda$  pattern observed is related to the role of the subharmonic mode. A detailed analysis of this type of transition scenario was performed by Kachanov and Levchenko (1984a) where broadband-like, high-amplitude fluctuations were observed at low frequencies in the hot-wire spectra when TS waves started to display the spanwise modulation also observed in the K-type transition, see figure 1.6 (b). This low-frequency regime is amplified due to the *resonant interaction of quasi-subharmonic 3D disturbances with the 2D fundamental wave* (Kachanov, 1994). This transition scenario is commonly known as N- or H-type and, conversely to K-type transition, no turbulent spots are observed (Sayadi et al., 2013).

From computations, it is usually concluded that H-type transition should predominate before K-type since subharmonics are the most unstable secondary instability. However, the presence of low-amplitude streamwise

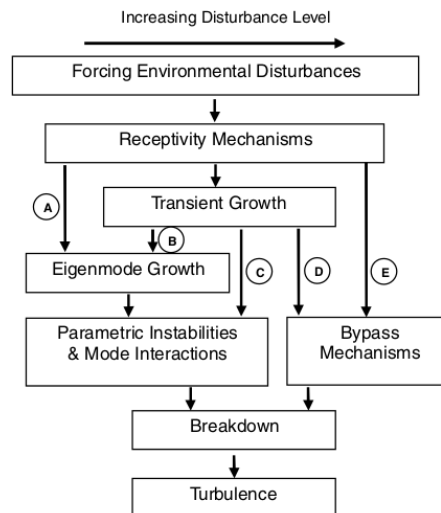


Figure 1.5: Possible transition scenarios as described in Morkovin (1994). Figure reproduced from Reshotko (2008).

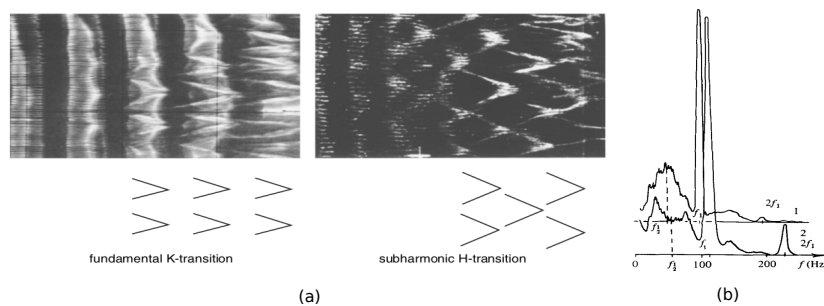


Figure 1.6: (a) Different patterns of  $\Lambda$  vortices depicting K- and H-type transition, reproduced from Schlichting (1933). (b) Spectra of velocity fluctuations measured with a hot-wire probe in the H-type transition region during Kachanov and Levchenko (1984a) experiments.

vortices (free-stream turbulence) enhances a different secondary instability, triggering K-type transition more often during experiments (Schmid and Henningson, 2012).

Conversely to path A, path B is still today for most researchers difficult to understand. In this path, it is thought that both modal and non-modal transition play an important role. The complexity of this scenario lies in the fact that it is not clear how a stationary streamwise disturbance (likewise streaks) will interact with traveling and exponentially growing disturbances (likewise TS waves) in the evolution to transition (Reshotko, 2008). Very interesting findings have been observed related to this path. For instance, Brandt et al. (2011) observed that streamwise streaks were a *stronger process* than modal growth of TS waves, i.e. they prevailed under large modifications of the base flow. The authors also observed that streaks can stabilize T-S waves, and these at the same time acquire different wall-normal profiles along the span due to the streak spanwise modulation. Hence, it is yet unclear which of the instabilities trigger transition when both streaks and wave-like disturbances take place.

Finally, path C is governed by transient growth. These instabilities grow algebraically in streamwise direction. The most striking example of this path is the Blunt-Body Paradox, where transition takes place in a region where perturbations are stable for LST. Several authors have worked towards developing models to predict the transition Reynolds number in the presence of path C. In the specific case of boundary layer flows, Klebanoff (1971) identified different modes present in the boundary layer when the freestream turbulence reaches moderate to high levels,  $Tu \geq 1\%$ . The author noticed the existence of a *breathing mode* in the boundary layer which manifested as temporal fluctuations of its thickness. In addition, low and high longitudinal velocity fluctuations at a much lower frequency than the TS waves were generated inside the boundary layer. These streaks are nowadays known as Klebanoff modes. Later, several authors as Kendall (1985) or Matsubara and Alfredsson (2001) showed that the boundary layer entrains and amplifies the low-frequency content of the vortex motion present in the freestream and gives rise to the modes observed by Klebanoff (1971).

### 1.3. Effect of roughness elements on transition: forward-facing steps

The study of the effect of roughness elements on transition can be split into two distinguished fields: 2D roughness elements and distributed (3D) roughness elements. The transition mechanisms of distributed and spanwise roughness elements are very different.

In distributed roughness elements the flow wraps along its spanwise direction, creating an initial spanwise vorticity component that later is shed in streamwise direction along the sides of the element. These counter-rotating vortices transport high- and low-momentum flow to the wall region in the wake creating streamwise velocity streaks through a lift-up process (Landahl, 1980). In the center of the wake, a low-speed recirculation region takes place. The large modulation of the flow in wall-normal and spanwise directions leads to the presence of inflection points which enhances the growth of inviscid instabilities (Ye, 2017).

The findings of Loiseau et al. (2014) suggest that the dominant effect on transition with distributed roughness highly depends on the aspect ratio of the element (frontal area) which modifies the blockage effect that the element exerts on the incoming flow and hence the vorticity of the horseshoe vortex system shed downstream. Later, Ye (2017) experimentally studied the stability of micro-ramp roughness elements (zero frontal area) and successfully proved the delay in transition of these elements compared to blunt front bodies where the upstream separation region enhances the transition dynamics at the wake.

In 2D roughness elements the frontal area is infinitely large and no horseshoe vortex would wrap around it. Hence, the flow instabilities that enhance early transition in this type of roughness element might be different.

Most of the existing research on TS transition subject to roughness elements explain their sudden amplification close to the element vicinity resorting to the base flow modification at the surface defect. Initially, Klebanoff and Tidstrom (1972) postulated that transition is driven by absolute instabilities triggered by the inflectional points developed from the strong modulation that the element incurs on the meanflow. This could explain the immediate transition after large step heights. However, it does not explain the progressive transition movement observed at moderate step heights, where the TS wave still exhibits exponential growth after the roughness element (Wang and Gaster, 2005).

Based on the different transition behavior observed for different roughness heights, Tani (1961) made the distinction between critical<sup>a</sup> and subcritical surface defect. The authors performed a series of experiments on wires and defined subcritical roughness as one in which transition occurs far from the discontinuity position and where TS waves are exponentially amplified. Conversely, a critical roughness is such that transition is triggered very close to or at the defect location. Inspired by the seemingly linear growth of instabilities around subcritical 2D roughness elements, first efforts were focused on either quantifying the reduction of the critical Reynolds number or on finding correlations of non-dimensional parameters to obtain an estimate of the transition location. Concerning the first, Goldstein (1985) and Tani (1961) studied the critical height of cylindrical wires which would trigger transition immediately downstream. On the other hand, Dryden (1953) compared different experimental data and noticed that all subcritical cases laid on a single curve ( $U_e h/\nu \approx 900$ ), but critical and supercritical cases resulted less predictable. The main non-dimensional parameters used within the literature to obtain correlation laws on TS transition in the presence of roughness elements consist of:

$$\begin{aligned} \text{Re}_{x_s} &= \frac{U_e x_s}{\nu} & \text{Re}_h &= \frac{U_e h}{\nu} & \text{Re}_{hh} &= \frac{U_{h,\text{clean}} h}{\nu} \\ \mathcal{H} &= \frac{h}{\delta^*} & s &= \frac{x_T - x_h}{x_{T,\text{clean}} - x_h} & \text{Re}_{x_T} &= \frac{U_e x_T}{\nu} \end{aligned}$$

where  $U_h$  denotes the streamwise velocity at a wall-normal position equal to the step height,  $y = h$ , and  $x_h$  is the position of the step. These quantities will be widely used during this work, especially when comparing transition location results with existing literature.

Backward and Forward Facing Steps (BFS and FFS) constitute a type of 2D roughness elements which are of major relevance within the industry given their ubiquitousness in the design of laminar components, e.g. panel joints, and seals, seams, etc. Similar to wires, steps also move transition upstream when the roughness height is increased. However, large differences have been observed between transition driven by FFS and BFS. In terms of meanflow distortion, while BFS present one large recirculating region downstream of the step (of approximately 30 step heights length), FFS present two recirculating regions, one upstream of the step (2 to 6 step heights length) and, for higher step heights, a second after the step edge (lengths from 6 to 12 step

<sup>a</sup>Sometimes *critical* is also denoted as *supercritical* within literature.

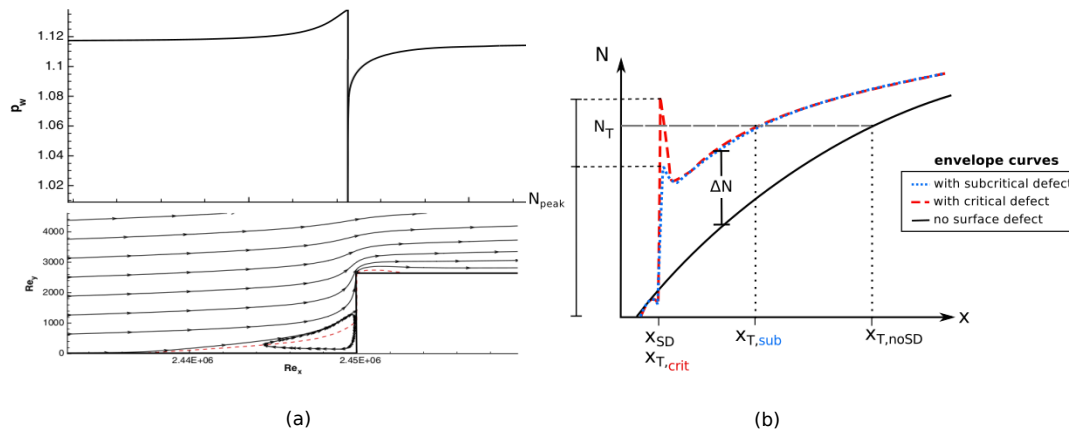


Figure 1.7: (a) Wall-pressure, streamwise curvature and separated flow (dashed lines) around an FFS of  $h/\delta^* \approx 0.94$ . Image reproduced from the work of Edelmann and Rist (2014). (b) Sketch of the effect of a surface defect on the N-factor when the defect is subcritical and critical. Note that Methel et al. (2021) definition of critical and subcritical step differs from this work definition, see section 2.1. Main parameters used in the N-factor method indicated. Figure reproduced from Methel et al. (2021).

heights) (Edelmann and Rist, 2014; Perraud et al., 2014). Wang and Gaster (2005) experimentally observed that BFS induce earlier transition than FFS for the same test conditions. Perraud et al. (2014) argue that the reason why BFS are more unstable than FFS is due to the thicker BL present downstream of a BFS compared to an FFS, which makes the former more susceptible to the amplification of low frequencies which grow over longer distances compared to high frequencies, which are rapidly damped. Therefore, in the design of laminar flow components, FFS are preferred over BFS.

Figure 1.7 (a) shows the flow topology and pressure change around critical FFS, where a second separation bubble starts to be present. The flow around an FFS is characterized by a sharp adverse pressure gradient upstream of the step which drastically reduces the streamwise velocity component, increasing the wall-normal velocity at the step region, i.e. lifting the flow in front of the step. Immediately after the step, a very sharp and localized favorable pressure gradient exists and finally, a smooth adverse pressure gradient develops downstream of the step until the flat plate pressure is recovered (Edelmann and Rist, 2014). In general, recent research efforts on FFS can be distinguished in two different directions. On the one hand, the first branch of research concerns those studies aimed to find a model inspired on the  $e^N$ -method, given the presumably linear amplification of TS waves, to predict transition location (Crouch et al., 2006; Perraud et al., 2014; Wang and Gaster, 2005). On the other hand, the second branch of research is concerned with the stability characteristics in the vicinity of the step, with some results suggesting the presence of different growth mechanisms in this region (Casacuberta et al., 2021; Eppink and Casper, 2019; Shahzad, 2020).

### 1.3.1. Transition prediction with TS-FFS: numerical and experimental progress

First research efforts on TS-FFS transition focused on obtaining critical Reynolds heights to provide manufacturers with a rapid estimate of the transition location or the maximum permissible height between panel discontinuities. The first experimental investigation to provide a critical Reynolds number for FFS was the one of Gluyas and Nenni (1966) with an estimated  $Re_{h,crit} = 1800$  for FFS. A series of recent experiments conducted by the Northrop Grumman Corporation (Drake et al., 2008a, 2010) using a propelled-model facility showed that even larger defect heights (herein denoted as  $Re_{hh}$ ) could be achieved without severely moving transition forward. In addition, Drake et al. (2010) observed that favorable pressure gradients help to increase  $Re_{h,crit}$  beyond previous values with zero pressure gradient.

A different strategy to characterize transition with FFS was used in Perraud and Seraudie (2000). The authors developed a semi-empirical method ( $\Delta N$  method) inspired by the well-known  $e^N$  method for transition prediction. Perraud and Seraudie (2000) argued that, from experiments, it could be observed that the N-factor undergoes a total amplification at the step which can be split into two:  $N_{peak}$  takes place at the step location and  $\Delta N$  which moves upwards all the values of  $N$  for the clean case downstream the step (see figure 1.7). The authors postulated that when  $N_{peak}$  was above  $N_T$  (the N-factor for which transition will take place based on the  $e^N$  method), transition takes place at the step, i.e. the defect is critical. Conversely, if the discontinuity is subcritical, the transition location will be determined by the intersection of  $(N_{clean} + \Delta N)$  and  $N_T$  in  $x$ .

Crouch et al. (2006) proposed a  $\Delta N$ -model for BFS and FFS in the presence of adverse and favorable pressure

gradients. The authors observed that their experimental data presented a linear relationship when it was described in terms of  $\Delta N$  against  $h/\delta^*$ . Later Perraud et al. (2014) proposed a more elaborate  $\Delta N$ -model for FFS with zero pressure gradient to represent the streamwise evolution of  $\Delta N$ .

The numerical results of Edelmann and Rist (2015) provided a detailed examination of the instability in the vicinity of a step. The authors observed a complex growth behavior after the step which could not be captured with LST. Additionally, Edelmann and Rist (2015) compared the N-factor envelopes obtained from their DNS with existing  $\Delta N$  models, depicting promising results in the case of Perraud et al. (2014) model. Nevertheless, the authors emphasize that none of the  $\Delta N$  models was able to accurately capture the amplification downstream of the step, which was in turn highly dependent on other parameters such as the step location and the Mach number. Recently, the findings of Crouch and Kosorygin (2020) experiments show that Crouch et al. (2006)  $\Delta N$  model is also applicable for different step locations. Furthermore, the authors clarify that the  $\Delta N$  model is not meant to describe the growth evolution around the step (as performed in Edelmann and Rist (2015) comparison) but to provide an estimate of the transition location.

The most comprehensive set of experiments on FFS is the one performed by Wang and Gaster (2005). Transition at low freestream turbulence in a flat plate at ZPG was studied in the presence of spanwise invariant FFS and BFS. TS waves were generated by receptivity from the LE to background wind tunnel disturbances. Wang and Gaster (2005) tested different step heights ( $0.4 \leq h/\delta^* \leq 1.6$ ) and computed the  $\Delta N$  factor as  $\Delta N = N_{\text{clean}} - N_{\text{step}}$  to plot it against the relative step height,  $h/\delta^*$ . Similar to Crouch et al. (2006) findings, the authors note that when results based on  $\Delta N$  are plotted against  $h/\delta^*$ , excellent correlation is observed except at large step heights. Nevertheless, the fit found by the authors presented differences from the linear one proposed by Crouch and Kosorygin (2020); Crouch et al. (2006), with small step heights having almost no effect on transition.

Following the need for experiments to assess the effect of the Mach number, pressure gradient, and wall temperature on TS-FFS transition, Costantini (2016) performed an extensive experimental study assessing the effect of changing the step height under different flow conditions. The authors observed large discrepancies between their transition location results and the data and models reported from previous experimental works of Wang and Gaster (2005) and Crouch et al. (2006). The author attributes the observed disagreement to differences in the step geometry, the step location, the nature of the clean transition, and the transition detection techniques used in each experiment.

Local Stability Theory (LST) or Parabolized Stability Equations (PSE) are the most widely used numerical tools to quantify the amplification of disturbances within the boundary layer and predict transition location without resorting to DNS. Park and Park (2013) studied the applicability of PSE and LST in the case of humps where the streamwise pressure gradients remain smooth and a PSE approach holds. As expected, the authors observed large discrepancies between PSE and LST results. More interesting is their comparison between NPSE and PSE where their findings suggest that the hump acts towards enhancing early non-linear development even for very small initial disturbance amplitudes. Furthermore, Park and Park (2013) observe that the subharmonic mode appears highly amplified in the presence of a hump, with a wide range of spanwise wavenumbers becoming unstable. However, in the presence of an FFS, the problem cannot be fully solved using LST or PSE given the large streamwise gradients close to the step region which make the basic flow to be highly non-parallel, causing the disturbance to change rapidly in  $x$ .

Other numerical methods which require less computational efforts than DNS have also been exploited to study the effect of FFS on stability, when PSE methods result insufficient. One example of this is the work of Dong and Zhang (2018) where, using a local scattering approach (LSA) based on triple-deck theory the authors could describe the evolution of disturbances around an FFS. Although the numerical approach of Dong and Zhang (2018) is extremely more efficient than DNS, the height of the steps that they could simulate is limited to the first deck ( $\text{Re}_h \leq \text{Re}^{-5/8}$ ).

The work of Franco et al. (2020) circumvents the limitations of PSE by solving the Adaptive Harmonic Linearized N-S (AHLNS) equations, where large pressure gradients are withstood. In addition, this method does not present any limitations regarding the step height as in LSA. AHLNS assumes linear behavior of the NS equations and a modal growth of convective instabilities. This novel approach shows remarkably good agreement with N-factor results obtained in Edelmann and Rist (2014) DNS (Franco et al., 2020). A more detailed comparison between this approach with PSE, LST, and DNS is given in Tocci et al. (2020) where the authors also observe very good agreement between AHLNS and DNS. The biggest advantage of this approach is that, conversely to DNS, an extended database could be performed to design general transition correlations for the case of different two-dimensional roughness elements. However, some of the assumptions made in AHLNS could be called into question for surface irregularities such as FFS where it is not yet well-established

that disturbances can be fully described in modal form. In addition, AHLNS is limited to moderate FFS heights, where non-linear effects are negligible. For cases in which the latter cannot be ensured, DNS remains the best option.

### 1.3.2. Close-examination of the flow features and growth mechanisms with FFS

The work of Edelmann (2014) constitutes one of the most comprehensive numerical investigations on the flow mechanisms developing at the step region. The author focused on the disturbance growth in subsonic and supersonic regimes. Within this work, Edelmann (2014) compared DNS with LST results in the presence of a step. The author observed that far downstream of the step, within a region where non-parallel effects are no longer relevant, both LST and DNS predicted different growth rates. This, together with the author's observations regarding the different growth trends that the N-factor presented when it was defined based on the  $|u|$  maximum or the energy norm, motivated the exploration of transient growth in Edelmann (2014) work. The author performed a simplified non-modal analysis by superposition of four LST modes and observed that the growth predicted in this case by LST presents better agreement with DNS results. In light of this, the author concludes that, within a region behind the step, non-modal growth could play an important role in the amplification of the disturbance.

Further details on the flowfield in the vicinity of the step were provided in Shahzad (2020). The author performed DNS simulations on FFS subject to single-frequency TS waves. Similar to Edelmann (2014) findings, Shahzad (2020) observed that the amplification of disturbances upstream and far downstream of the step can be largely explained by the baseflow distortion. However, immediately after the step, in a region where LST and DNS show good agreement in terms of  $\alpha_i$  (growth rate), PSE and LST show large disagreement, similar to what Edelmann (2014) also observed. Interestingly, the author observed a vortical structure immediately after the step edge counterrotating the incoming TS wave which is manifested as a new near-wall peak in the TS shape function. The findings of Shahzad (2020) point out the presence of complex flow features taking place at the step region. The emergence of these features could help to explain the differences observed in the amplification of TS waves for different step heights.

A different line of work is the one conducted by Tufts et al. (2017), Eppink (2020), Rius-Vidales and Kotsonis (2021) or Casacuberta et al. (2021), where the effect of FFS is studied in crossflow dominated transition. Tufts et al. (2017) also observed two recirculating regions upstream and downstream of the step. In addition, they noticed a secondary near-wall lobe in the crossflow shape function (similar to observations in Shahzad (2020)). The authors postulated that a constructive or destructive interaction between the downstream recirculating region and the crossflow instability was causing the growth of the disturbance after the step. Eppink (2020) also found this secondary lobe at the step but they could not confirm that the crossflow amplification was due to the interaction proposed by Tufts et al. (2017). Instead, the authors identified that crossflow undergoes two regions of growth. First, upstream of the step, disturbance amplification is explained by the modification of the baseflow by the adverse pressure gradient (again, similar to findings in Shahzad (2020)). Secondly, downstream of the step, due to the non-linear interaction with streamwise vortices presumably produced by the secondary recirculating region. Similar results were drawn by Rius-Vidales and Kotsonis (2020, 2021). In addition, Rius-Vidales and Kotsonis (2021) characterized in detail the change in the trajectory of the crossflow vortices as they interact with the FFS, which could potentially play an important role in the amplification of the crossflow vortices at the step location. Moreover, an unprecedented transition delay effect was measured for the smallest FFS, opening the possibility of passive flow control using surface irregularities.

The DNS of Casacuberta et al. (2021) offers detailed observations on crossflow instability development close to an FFS. Similar to Eppink (2020), the authors observe streaky features upstream and downstream of the step for the first Fourier mode (0,1) and link their presence to the secondary peak observed on the crossflow shape function. Casacuberta et al. (2021) discuss that the growth of perturbations observed immediately after the step could be related to, as Eppink (2020) suggested, the inflectional points induced by the first recirculating region which destabilize crossflow. However, they also propose that transient growth could explain the amplification observed after the step and the presence of streaks. Finally, the authors suggest a different approach to determining the growth of crossflow with FFS. The authors point to misleading interpretations when the maximum of the perturbation across  $y$  is taken to define the amplification at the step since, unintentionally, also the growth of additional peaks (related to the near-wall structures observed) is accounted for.

It remains unclear whether the emerging structures after the step observed in Eppink (2020), Rius-Vidales and Kotsonis (2021) or Casacuberta et al. (2021) are generated by non-modal mechanisms or from the non-linear interaction with the secondary bubble as Eppink (2020) suggests. In line with the latter, the work of Rodríguez et al. (2013, 2021) might appear useful given the observation of three-dimensional structures taking

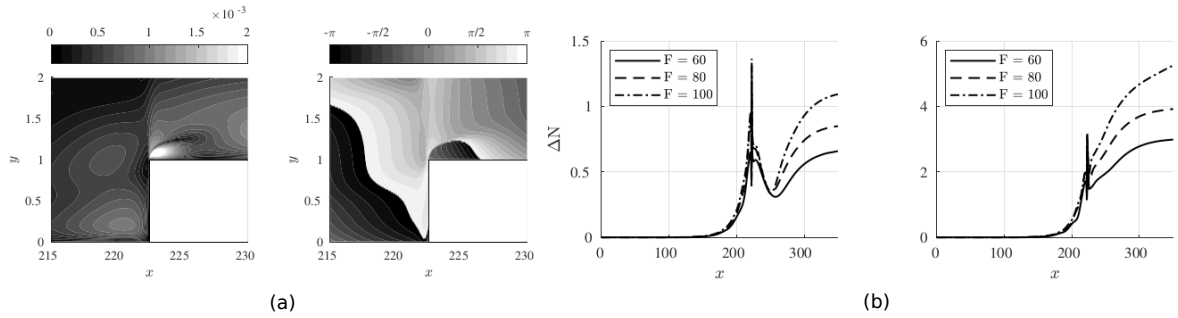


Figure 1.8: (a)  $\Delta N$  for different TS wave frequencies ( $F = 60$  and  $F = 100$  corresponding to Branch I and Branch II respectively) along the streamwise direction. The step is located at  $x = 220$  and the step heights depicted are (a)  $h/\delta^* = 0.7$  and (b)  $h/\delta^* = 1.4$ . (b) Streamwise velocity (left) and phase (right) of the primary mode for  $h/\delta^* = 1.4$  at the most unstable frequency ( $F = 80$ ). Note the opposite phase of the lower and upper structure immediately after the step. Figure reproduced from Shahzad (2020).

place in weak (i.e. with low reversed velocities) laminar separation bubbles (LSB). In Rodríguez et al. (2013) the authors observe different types of self-sustained<sup>9</sup> linear global instabilities in LSB. The first is related to an absolute instability due to the presence of an inflection point below the separated region (Rodríguez et al., 2013). In this case, a global mechanism exists that gives rise to synchronized oscillations which explains the vortex shedding observed downstream. The second self-sustained instability of LSB consists of a centrifugal one which gives rise to “*steady three-dimensionalization of the bubble*” (Rodríguez et al., 2013) which takes place for reversed velocities as low as 4%. In (Rodríguez et al., 2021) the authors suggest that the global oscillator frequency observed in previous experiments is in agreement with the one predicted from their simulations, indicating that this second self-sustained instability, leading to the three-dimensionalization of the LSB, is also present in experiments.

Non-modal growth (suggested in Casacuberta et al. (2021) as a possible mechanism behind the formation of streaks behind the FFS) has already been proposed in other works concerned with channel flows and FFS at very low Reynolds numbers. Interestingly, similar streaky structures as the ones reported in Eppink (2020) and Casacuberta et al. (2021) have been also observed during the experiments of Stürer et al. (1999) in a channel flow subject to white noise. Lanzerstorfer and Kuhlmann (2012) performed a temporal global stability analysis to study the physical nature of the structure observed during Stürer et al. (1999) experiments. The authors observe that the critical mode consists of streamwise streaks (similar to the ones observed in the experiments of Stürer et al. (1999)) which are confined within the secondary separation bubble. This instability is seen to gain its energy from a balanced contribution of the lift-up effect (non-modal growth) and the base flow deceleration. Immediately downstream of the step, the lift-up effect energizes the streaks while the flow deceleration has a stabilization effect. The opposite takes place downstream when the flow accelerates and the lift-up effect incurred by the step is reduced. The total effect of both contributions reveals an initial amplification of the streaks and their later decay. However, the large initial amplification of the streaks could lead to non-linearities and hence transition immediately after the step during experiments. Despite the clear differences between these works (channel-flow at low Re numbers) and the one concerned herein (boundary layer at high Re numbers), it is nevertheless surprising the similarity of the features observed at the step.

## 1.4. Acoustic forcing of Tollmien-Schlichting waves

Most of the experimental works concerned with TS waves use plasma actuators (e.g. Kotsonis et al. (2015)) or vibrating ribbons (e.g. Schubauer and Skramstad (1947)) to excite them in the boundary layer. However, some of these techniques present inherent disadvantages: they are intrusive or, in the case of plasma actuators, present poor repeatability. This is why in this work acoustic waves will be instead used to force TS waves. This technique is non-intrusive, easy to set up, presents good repeatability, and there is extensive research related to it. In particular, the investigations on LE and roughness receptivity from (Saric and White, 1998; White et al., 2000a) provide useful practical and physical insight into this technique.

Acoustic waves can force TS waves within the boundary layer. While the growth of TS waves is well-understood, the receptivity process giving rise to TS waves is generally more complex and difficult to quantify in experiments (Chauvat, 2020; Saric and White, 1998; White et al., 2000a). When an acoustic wave meets the LE, a wavelength conversion process takes place which transforms the long wavelengths of acoustic waves into

<sup>9</sup>Herein self-sustained means that the instability exists without the presence of external disturbances

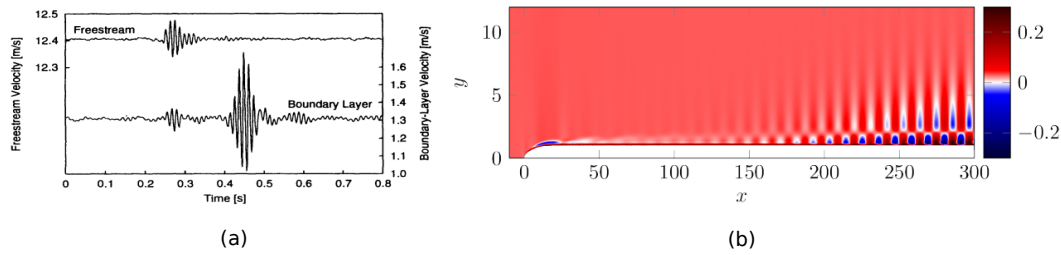


Figure 1.9: (a) Time-signal of a hot-wire probe placed inside the boundary layer and on the freestream when a sound pulse is sent. Figure reproduced from Saric and White (1998). (b) Global stability results of Chauvat (2020) near the LE where receptivity to a travelling acoustic wave takes place. Contours of  $u$ .

short-wavelength hydrodynamic disturbances convected within the BL. This process is denoted as receptivity. Goldstein (1983) was the first to suggest that this process takes place due to the non-parallel growth of the boundary layer. Hence, receptivity commonly takes place across the LE or in regions where the boundary layer is very thin compared to surface roughness, enhancing non-parallel effects.

An immediate consequence of having an acoustic wave traveling across the boundary layer is that a Stokes layer (SL) is created (Stokes second problem). Since the TS wave and the SL share the same frequency, it is very difficult to decouple one from the other experimentally. An example of this are the experiments of Saric et al. (1995), where TS waves were forced using a continuous acoustic field to measure the receptivity of a modified super-ellipse (MSE) LE with  $\mathcal{R}$  20:1. The final results were misleading due to the impossibility of separating the amplitude of the TS wave from the Stokes wave when measuring with a hot-wire probe inside the boundary layer.

Later, Saric and White (1998) developed a technique to circumvent this issue based on the different phase speeds between TS and Stokes waves. Instead of applying a continuous acoustic tone in time, a sinusoidal pulse was forced with frequency  $f_{\text{pulse}}$ . Since TS waves travel much slower than the Stokes wave, their signal on the hot-wire appeared delayed compared to the SL<sup>10</sup>, see figure 1.9 (a). An added advantage of using a pulsed-sound technique is that reflections could also be distinguished. Saric and White (1998) used this technique to measure the receptivity of the same elliptic LE used in Saric et al. (1995) and their results agreed with the ones of the DNS performed by Wanderley and Corke (2001), confirming the feasibility of a pulsed technique to measure the TS waves amplitude. In section 3.2 the methodology used to implement the pulsed technique to measure the TS waves amplitude in these experiments is discussed.

A recent work performed by Chauvat (2020) introduced a less resourceful approach than DNS to study receptivity across the LE. The authors performed a global stability analysis close to the LE to study the receptivity process and switch the computation to a conventional PSE towards the end of the LE, where non-parallel effects can be neglected. Figure 1.9 (b) shows the generation of TS waves through the receptivity of travelling acoustic waves. The authors indicate that wall-normal velocity fluctuations of the perturbation are a more reliable means of retrieving the actual TS wave growth since the Stokes wave mainly contributes to the stream-wise velocity fluctuations. This appears useful for this work in the case of PIV measurements, where  $u$  and  $v$  can be measured separately.

## 1.5. Discussion and outline

The literature of the previous sections frames the research gap of this work. In general, it has been observed that there exists no unique consensus to explain which are the growth mechanisms that amplify instabilities after the step. In turn, the lack of comparison between numerical and experimental data furtherly hinders the problem understanding. This section aims to summarize the main findings and limitations found within the literature. Finally, the approach adopted in this work is justified.

Edelmann (2014) observed downstream of the step large differences between describing the N-factor based on the maximum of  $|\hat{u}|$  or on the energy norm (defined in Eq. 4.6 in Edelmann (2014)). This exemplifies that it is still not certain whether the growth of TS waves after the step can be uniquely described by exponential growth, as inherently assumed in the  $\Delta N$  methods (e.g. Crouch et al. (2006); Perraud et al. (2014)).

Detailed flow visualizations in the vicinity of the step have been presented in 2D DNS simulations like the ones performed by Edelmann and Rist (2014) and Shahzad (2020). There, different features were observed

<sup>10</sup>Stokes waves travel at the speed of sound while TS waves travel at a much lower phase speed,  $c = 2\pi f / \alpha_\tau$ .

which might point to a key role of the second recirculating region in modulating TS waves, similar to what also Eppink (2020), Rius-Vidales and Kotsonis (2021) and Casacuberta et al. (2021) noticed for crossflow instabilities. In particular, Shahzad (2020) reports the emergence of a vortical structure counterrotating the incoming TS wave at the step edge which could have a stabilization effect on the TS wave. Nevertheless, it remains unknown which are the mechanisms that give rise to this structure.

In short, it has been observed that there is little or no work concerned with the comparison between numerical and experimental findings, making it difficult to relate the phenomena described in each case. Since existing experimental works on TS-FFS dominated transition are mainly concerned with transition prediction, providing limited measurements in the vicinity of the step, it is difficult to compare this data with numerical works, where limited streamwise domain is computed given the high computational cost and transition is usually not captured.

In general, it has been observed from previous literature that there is a lack of **experimental studies on the interaction of TS waves with FFS that provide detailed flowfield measurements at the step location such that the relevant disturbance quantities can be compared with numerical simulations.**

## 1.6. Research questions and objectives

The literature review of the previous sections frames the research questions of this work. With that in mind, four research questions can be formulated:

1. **What is the effect of the FFS height on TS-dominated transition?**
  - (a) On the transition location.
  - (b) On the TS waves growth and related harmonics.
  - (c) On the distortion experienced by the TS waves at the step.
2. **What are the mechanisms responsible for the growth/decay of TS waves immediately downstream?**
3. **Is there any additional flow feature/structure close to the step, similar to the ones reported in the literature? More specifically:**
  - (a) Is there any other relevant unsteady phenomena present at some step heights? If there is, can it be related to any of the characteristic frequencies found in the main literature (e.g. the vortex shedding noticed by Eppink (2020); Eppink and Casper (2019) or the global oscillator frequency from an LSB as described in Rodríguez et al. (2021))?
  - (b) Is there any secondary near-wall structure present at the step, similar to what Shahzad (2020) and Casacuberta et al. (2021) report?
4. **What is the agreement between experiments and 2D DNS results?<sup>11</sup>**
5. **Are acoustic waves a suitable approach towards forcing TS waves?**
  - (a) Does LE receptivity provide fully developed TS waves at the step location?
  - (b) Is the pulsing technique a suitable approach towards decoupling TS and Stokes waves amplitudes?

The previous questions frame the main objective of this work:

**To characterize the main flow features and growth mechanisms present in the interaction of Tollmien-Schlichting waves with Forward-Facing Steps by means of experiments performed at TU Delft and 2D DNS conducted at DLR.**

To do so, this work is structured as follows. Chapter 2 describes the methodology used to design the experimental test matrix, the numerical tools (LST and 2D DNS) used throughout this work, and the main experimental and corresponding post-processing techniques employed. Chapter 3 presents the experimental set-up. Chapter 4 presents the no-step (smooth-surface), verifying a Blasius flowdevelopment, the stability of the model, the turbulence intensity and the background acoustic noise sources. In chapter 5 the main experimental and numerical results for different step heights are discussed. Finally, chapter 6 summarizes the main findings from this work and provides future recommendations.

---

<sup>11</sup>This work consists also of a collaboration with DLR. They performed DNS simulations resembling this work's experimental set-up. The collaboration aims to answer whether FFS-induced transition can be simulated using 2D DNS simulations.



# 2

## Methodology

### 2.1. Design of the experimental test matrix

This section describes the different stages followed to determine the relevant parameters to design the experimental test matrix. First, cases from literature are unified under the same non-dimensional parameters to establish which range of step heights avoids immediate transition but provides enough destabilization to show interesting features at the step. Secondly, Linear Stability Theory (LST) is used to determine the stability limits of the current set-up and decide which frequencies are of relevance for this work.

#### 2.1.1. Step heights

The choice of step heights to study in this work is motivated by two different requirements. First, the step should not trip the boundary layer at the step. Second, the steps chosen should present different destabilizing effects on the flow such that sufficiently different behaviors can be analyzed. Based on the level of destabilization of the flow, the steps can be categorized as subcritical, critical, and supercritical. All previous literature on FFS transition (e.g. Casacuberta et al. (2021); Eppink (2020); Rius-Vidales and Kotsonis (2021); Shahzad (2020)) shares a common point: the second recirculating region appears to be linked to a large destabilizing effect of the disturbances at the step. Based on this, the presence of a second recirculating region is here used to distinguish subcritical steps from critical ones. Finally, supercritical steps are defined as those which trigger transition immediately after the step.

#### Step parameters that trip the boundary layer

Experimental works on FFS-transition are used to find which step parameters represent supercritical conditions, i.e. trip the boundary layer at the step.

Figure 2.1 shows the relative transition location  $s = (x_T - x_s) / (x_{T0} - x_s)$ , as a function of two different parameters characterising the step: the relative thickness  $h/\delta^*$  and the Reynolds number based on the step height  $Re_{hh} = u_h h/\nu$ . The first parameter ( $h/\delta^*$ ) isolates the effect of the step location and height. The second parameter ( $Re_{hh} = u_h h/\nu$ ) adds information on the freestream conditions ( $\nu$ ).

The data plotted in figure 2.1 was digitized from Perraud and Seraudie (2000) and Wang and Gaster (2005) experimental works based on the resemblance to the present study. Other experimental works such as the one of Drake et al. (2010) or Crouch et al. (2006) were omitted due to insufficient information and differences in the pressure gradient, respectively. Beware that Perraud and Seraudie (2000) experiments were performed at  $M = 0.26$ . In this regard, the experimental data of Wang and Gaster (2005) are performed on a flat plate at  $M = 0.05 - 0.1$  and low turbulence levels, similar to the conditions of these experiments. It is important to recall that the experimental data of these authors concerns natural transition while in this work TS waves are forced at individual frequencies.

From the plots, it is established that the experiments of this work should be performed at  $h/\delta^* \leq 2$  and  $Re_{hh} \leq 2500$  to avoid the BL tripping at the step. Since there is no unique parameter describing the transition behavior in the presence of FFS, two parameters ( $h/\delta^*$  and  $Re_{hh}$ ) are taken here to define a tripping criteria.

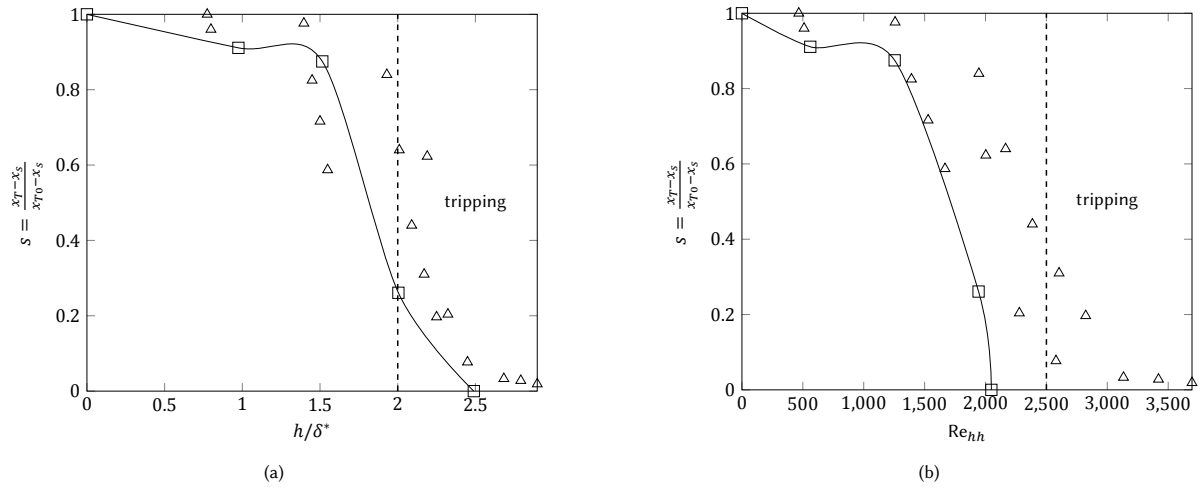


Figure 2.1: Change of transition location for different FFS heights. Data from experiments of Perraud and Seraudie (2000) ( $\square$ ) and Wang and Gaster (2005) ( $\Delta$ ). The dashline (---) indicates the critical  $h/\delta^*$  and  $Re_{hh}$  where the boundary layer trips.

### Selected step heights

Numerical literature results are useful to determine for which steps the secondary separation bubble is present. This information, together with the supercritical (tripping) step parameters previously found from experimental data (figure 2.1) shape the plot in figure 2.2.  $Re_{hh}$  is obtained from each data-set based on the step location ( $Re_s$ ) and relative step height ( $h/\delta^*$ ), which make it possible to compute  $U_h$  assuming a Blasius boundary layer.

The area of interest is bounded by dotted lines. Those numerical cases which report the presence of a secondary recirculating region are indicated by filled symbols. Note that Edelmann and Rist (2015) data includes one case where the step is moved upstream (lower  $Re_x$ ), which explains the outlier point ( $\bullet$ ) observed in the plot.

Red and blue squares in figure 2.2 show where the step heights tested during Campaign I and Campaign II, respectively, lie among the typical parameters used in literature. The non-filled blue and red squares indicate the steps for which no secondary recirculating region is expected, based on the observations from previous numerical literature.

Three different step cases can be identified<sup>1</sup>:

- **Subcritical steps.** Characterized by the absence of a secondary recirculating region and transition location close to the clean case. In the test matrix:  $h/\delta^* = \{0.5, 0.8\}$ .
- **Critical steps.** Characterized by the presence of a secondary recirculating region and a large destabilization of the boundary layer, i.e. a large movement of the transition point is expected. In the test matrix:  $h/\delta^* = \{1.1, 1.3, 1.5, 1.7\}$ .
- **Supercritical steps.** Characterized by transition taking place immediately after the step. In the test matrix:  $h/\delta^* = 2$ .

From now on, this nomenclature will be used to denote different steps. The step heights tested during the experiments are later presented in table 2.1 and table 2.2.

### 2.1.2. Disturbance frequencies and amplitudes

From figure 2.3 (a) the frequencies of interest for this work can be derived. Three different TS wave frequencies have been selected based on the different stability behavior that they present at the step.

Figure 2.3 (b) shows the N-factor development of the three different frequencies along the streamwise direction (computed with the OS solver fed with the DNS baseflow). First,  $f = 300$  Hz concerns a frequency that keeps amplifying after the step. A TS wave with frequency  $f = 450$  Hz would achieve maximum growth at the step and decay afterward. Finally, a  $f = 550$  Hz TS wave already achieved maximum growth before

<sup>1</sup>Note that the definition used in this work for subcritical, critical, and supercritical steps differs from the one presented within FFS literature.

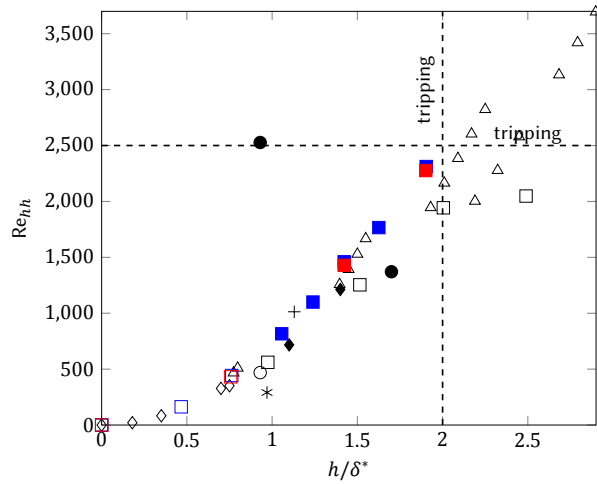


Figure 2.2: Step parameters used in different works from literature. ( $\diamond$ ) Shahzad (2020), ( $*$ ) Zh and Fu (2017), ( $\Delta$ ) Wang and Gaster (2005), ( $\circ$ ) Edelmann and Rist (2015), ( $\square$ ) Perraud and Seraudie (2000), ( $\blacksquare$ ) Campaign I and ( $\blacksquare$ ) Campaign II test cases. Filled symbols indicate the step cases for which a second recirculating region is expected during the experiments based on the numerical results from Edelmann and Rist (2015) ( $\bullet$ ) and Shahzad (2020) ( $\blacksquare$ ). The dashlines (---) indicate the critical  $h/\delta^*$  and  $Re_{\rho h}$  where the boundary layer might trip.

reaching the step and is decaying when it approaches it. Another interesting feature distinguishing all frequencies selected is the height of their amplitude peak. While for low frequencies the peak is located at a higher  $y$  coordinate, high frequencies present it closer to the wall, being the latter more vulnerable to regions of high mean shear (recall production term in equation (1.3)). All these differences could imply different instability behaviors for each frequency in the presence of a step.

The TS wave amplitudes were decided during the experiments. An acoustic calibration was performed using HWA to determine how the TS wave amplitude scales with acoustic forcing. Previous experimental literature on TS waves (Kotsonis et al., 2015) points to values of 0.01% of the freestream velocity as common TS wave amplitudes observed during the linear growth regime, being amplitudes of 1% enough to trigger non-linear mechanisms and hence breakdown to turbulence. The acoustic forcing was chosen based on a compromise between obtaining a sufficiently high microphone Signal-to-Noise Ratio (SNR) and TS waves amplitudes low enough to remain in the linear regime. The TS wave amplitudes achieved at the step location are indicated in table 2.1 and table 2.2.

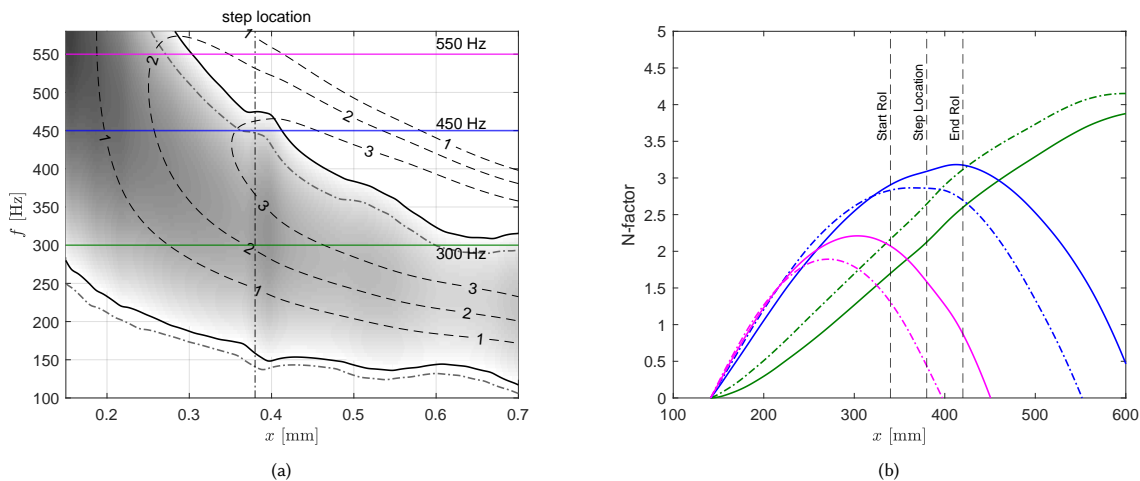


Figure 2.3: (a) Stability diagram from OS solver showing the growth rate (—) and N-factor isolines (---) with conditions from Campaign I and growth rate from Campaign II (-.-). (b) N-factor development in streamwise direction for frequencies  $f = 300$  Hz (green),  $f = 450$  Hz (blue) and  $f = 550$  Hz (magenta) at Campaign I conditions (—) and Campaign II (-.-).

Parameters	Symbols (units)	H0	H1	H2	H3
Reference velocity	$U_{ref}^*$ (m/s)	22.5	22.6	22.7	22.6
Kinematic viscosity	$\nu$ (m <sup>2</sup> /s)	$1.62 \times 10^{-5}$	$1.58 \times 10^{-5}$	$1.59 \times 10^{-5}$	$1.61 \times 10^{-5}$
Reynolds number	$Re_c$ (-)	$1.32 \times 10^6$	$1.36 \times 10^6$	$1.36 \times 10^6$	$1.33 \times 10^6$
Type of acoustic forcing		Continuous			
Microphone amplitude	$A_{mic}^\ddagger$ (Pa)	0.1			
Frequency	$f$ (Hz)	(300, 450, 550)			
Reduced frequency	$F$ (-)	(60, 90, 110)	(58, 87, 106)	(58, 87, 106)	(59, 89, 109)
Step type		Clean	Subcritical	Critical	Supercritical
Step height	$\bar{h}$ ( $\mu\text{m}$ )	-8	732	1380	1840
Relative step height	$(h/\delta^*)^\dagger$ (-)	-0.008	0.763	1.423	1.904
Reynolds step height number	$Re_{hh}$ (-)	0	443	1460	2311
Step location	$x_s$ (m)	0.38			
Reynolds number based on step location	$Re_s$ (-)	$5.30 \times 10^5$	$5.44 \times 10^5$	$5.43 \times 10^5$	$5.43 \times 10^5$

\*: External velocity  $U_e$  extracted at  $x = 0.2$  m.

†: displacement thickness extracted from boundary layer solver at the step location in clean conditions, i.e.  $h = 0$ .

‡: the TS wave amplitudes achieved at the step location with this acoustic forcing amplitude were  $u_{max} = (0.02, 0.22, 0.05) \%$  of  $U_e$  for  $f = (300, 450, 550)$  Hz, respectively.

Table 2.1: Test cases using Hot-Wire Anemometry (HWA).

Parameters	Symbols (units)	P0	P1	P2	P3
Reference velocity	$U_{ref}^*$ (m/s)	20.9	20.8	21.1	21.1
Kinematic viscosity	$\nu$ (m <sup>2</sup> /s)	$1.49 \times 10^{-5}$	$1.48 \times 10^{-5}$	$1.50 \times 10^{-5}$	$1.49 \times 10^{-5}$
Reynolds number	$Re_c$ (-)	$1.33 \times 10^6$	$1.34 \times 10^6$	$1.34 \times 10^6$	$1.34 \times 10^6$
Type of acoustic forcing		Pulsed			
Microphone amplitude	$A_{mic}^\ddagger$ (Pa)	0.17			
Frequency	$f$ (Hz)	(300, 450, 550)			
Reduced frequency	$F$ (-)	(64, 96, 118)	(64, 96, 118)	(63, 95, 116)	(63, 95, 116)
Step type		Clean	Subcritical	Critical	Supercritical
Step height	$\bar{h}$ ( $\mu\text{m}$ )	-8	732	1380	1840
Relative step height	$(h/\delta^*)^\dagger$ (-)	-0.008	0.756	1.423	1.901
Reynolds step height number	$Re_{hh}$ (-)	0	431	1428	2277
Step location	$x_s$ (m)	0.38			
Reynolds number based on step location	$Re_s$ (-)	$5.31 \times 10^5$	$5.34 \times 10^5$	$5.34 \times 10^5$	$5.36 \times 10^5$

\*: External velocity  $U_e$  extracted at  $x = 0.2$  m.

†: displacement thickness extracted from boundary layer solver at the step location in clean conditions, i.e.  $h = 0$ .

‡: the TS wave amplitudes achieved at the step location with this acoustic forcing amplitude were  $u_{max} = (0.1, 0.2, 0.15) \%$  of  $U_e$  for  $f = (300, 450, 550)$  Hz, respectively.

Table 2.2: Test cases using Particle Image Velocimetry (PIV).

### 2.1.3. Test cases

Two sets of campaigns were performed in this work. The first campaign comprised HWA and IR measurements while in the second PIV measurements were performed. Continuous acoustic forcing was employed during HWA and IR measurements whereas a pulsed technique was used during PIV. This strategy is later described and justified in section 3.2.

Due to temperature differences between Campaign I and Campaign II, there are slight differences between the reduced frequencies ( $\Delta F \approx 5$ ) studied in each campaign. Figure 2.3 (b) shows the different N-factors obtained during Campaign II compared to Campaign I. Since the velocity was slightly decreased in Campaign II<sup>2</sup>, all reduced frequencies increased the same ratio (table 2.1) when the dimensional frequency was kept constant. Although this barely changed the stability characteristics of all frequencies, it affected the acoustic forcing levels in Campaign II needed to trigger similar amplitude levels to Campaign I.

## 2.2. Numerical methods

This section describes the main numerical method used throughout this work. First, a boundary layer and the OS solver developed by the Aerodynamics Section in TU Delft are used. These numerical tools have been used to compute the smooth-surface conditions to design the experimental test matrix (presented in the previous section). Secondly, Direct Numerical Simulations (DNS) results on TS-FFS performed at the German Aerospace Center (DLR) are included in this work to gain insight very close to the step, where it is very challenging to

<sup>2</sup>This was performed to match the Reynolds number in both campaigns due to temperature differences.

Parameters	Symbols (units)	I0	I1	I2	I3	I4	I5	I6	I7
Mean reference velocity	$\bar{U}_{ref}$ (m/s)						22.1		
Mean kinematic viscosity	$\bar{\nu}$ (m <sup>2</sup> /s)						$1.58 \times 10^{-5}$		
Mean Reynolds number	$Re_c$ (-)						$1.34 \times 10^6$		
Type of acoustic forcing	(-)						Continuous		
Microphone amplitude	$A_{mic}$ (Pa)						0.1 and 0.2		
Frequency	$f$ (Hz)						(300, 450, 550)		
Step type	(-)	Clean	Subcritical		Critical				Supercritical
Step height	$\bar{h}$ ( $\mu\text{m}$ )	-8	448	732	1014	1190	1380	1561	1840
Relative step height	$(h/\delta^*)$ (-)	-0.008	0.467	0.763	1.056	1.240	1.423	1.626	1.904
Reynolds step height number	$Re_{hh}$ (-)	0	163	443	816	1100	1460	1766	2312

Table 2.3: Test cases using Infrared Thermography (IR).

measure with experiments. The link between DNS and experimental results can improve the understanding of the flow mechanisms close to the step.

### 2.2.1. Boundary layer and Orr-Sommerfeld solver

The stability of a flat plate boundary layer has an analytical solution described by the Orr-Sommerfeld equation (equation (1.9)). In this work, the result of the OS problem was used in the first stage to design the experimental test matrix and later to compare with experimental results in clean case conditions,  $h = 0$ .

The solution of the boundary layer in a flat plate can be described with the boundary layer equations (White and Corfield, 2006). The steady, two-dimensional, incompressible, and non-similar boundary layer equations (BL) are expressed as

$$\frac{\partial u}{\partial x} + \frac{\partial v}{\partial y} = 0, \quad (2.1)$$

$$u \frac{\partial u}{\partial x} + v \frac{\partial u}{\partial y} = U_e \frac{\partial U_e}{\partial x} + \nu \frac{\partial^2 u}{\partial y^2}, \quad (2.2)$$

with boundary conditions  $u(x, 0) = v(x, 0) = 0$  and  $u(x, \infty) = U_e(x)$ . The external velocity ( $U_e$ ) input in this work is obtained from the static pressure read by the pressure taps of the model as

$$U_e = \left( \sqrt{1 - C_p} \right) U_\infty \quad \text{where} \quad C_p = \frac{p_{st, tap} - p_{st, pitot}}{1/2 \rho U_\infty^2}. \quad (2.3)$$

Given that the pressure change in the  $y$  direction is small in no-step conditions, it can be assumed that  $U_e$  can be obtained from the pressure read at the wall.

The system of partial differential equations (PDEs) in equation (2.1) is parabolic, i.e. can be solved marching in the streamwise direction. An implicit finite difference scheme (second order accurate) is therefore used in the  $x$ -direction and Chebyshev polynomials ( $n^{\text{th}}$  order accurate) in wall-normal direction. Malik's transformation is used to map the Chebyshev grid points from  $[-1, 0, 1]$  to  $[0, y_i, y_{max}]$ , where  $y_i$  represents the wall-normal location where half of the nodes are placed. The wall-normal median coordinate ( $y_i$ ) is usually set to 3 to 10 Blasius length scales ( $\ell = \sqrt{\nu x_{ref}/U_{ref}}$ ) to properly resolve the modes inside the boundary layer (Groot, 2018). The inflow boundary condition consists on a Falkner-Skan-Cooke profile at equivalent Hartree parameter to the measured external velocity (Groot, 2018). The Orr-Sommerfeld equation was previously presented in equation (1.9) in chapter 1.

The input of the OS solver can be the boundary layer solution or the baseflow provided by the DNS. Once the eigenproblem is solved, a filter is applied to discard nonphysical solutions. To identify the physical disturbance, its shape function is verified to decay exponentially as  $\hat{v}(y) \approx e^{-i(\sqrt{\alpha^2 + \beta^2})y}$  in the freestream (Groot, 2018). The input parameters used for the BL and OS code are presented in table 2.4.

### 2.2.2. Direct numerical simulations

This work presents an experimental and numerical investigation jointly conducted by TU Delft and DLR on TS-FFS interaction. Direct Numerical Simulations (DNS) are performed at DLR using the Nek5000 code by Fischer et al. (2008) which is based on the Spectral Element Method (SEM). The SEM decomposes the physical domain into (spectral) elements where the flow field solution is given by a sum of Lagrange interpolants defined by

Parameters	Symbols (units)		Values
Domain start	S	(m)	0.15
Domain end	c	(m)	0.95
Domain height	H	(m)	0.1
Chebyshev node coordinate median	$y_i$	(-)	$(3-10)\ell$
Number of points in streamwise direction	$n_x$	(-)	500
Number of points in wall-normal direction	$n_y$	(-)	300
Number of Chebyshev Polynomials	$N_C$	(-)	100

Table 2.4: Numerical parameters used for the BL and OS solvers.

an orthogonal basis of Legendre polynomials up to degree  $N$  within each element, see table 2.5. The reader is referred to the work of Pau (2021) for further details on the numerical characteristics of the DNS code.

The DNS investigations focus on the onset of the transition process and therefore are limited to 2D domains to reduce the computational costs. The calculations consisted of a DNS of the steady laminar 2D baseflow and succeeding unsteady DNS for the disturbances' propagation. For the latter, a harmonic blowing and suction strip centered at  $x = 200$  mm is applied at the wall to introduce periodic TS waves. The blowing and suction strip introduces a wall-normal velocity component at a selected frequency with zero net-mass flow. Its amplitude is prescribed such that the developing TS wave matches the amplitude measured with HWA at  $x = 340$  mm. The external velocity and inflow velocity profile computed by the BL solver are inputs for the DNS inflow and top boundary conditions.

During experiments, a small geometrical suction slot was unintentionally created in front of the step. In order to faithfully represent the effects that this suction slot would have on the incoming disturbances, a non-zero wall-normal component is imposed from  $379.7 \leq x \leq 380$  mm. It is imposed following a Gaussian distribution along  $x$  to achieve smooth velocity transitions at the wall. The maximum suction velocity within the slot is  $v/U_{\text{ref}} \leq -1.4$  %.

Comparison between DNS and experiments is mainly focused on HWA measurements. This is so because PIV measurements aimed to study the flow topology at a region very close to the step, making it difficult to accurately track the TS wave growth along  $x$ , with barely two wavelengths being captured within the FoV. In addition, slight differences in the reduced frequencies between Campaign I and Campaign II impede the exact match between PIV and DNS results since DNS parameters were set to match the HWA conditions indicated in table 2.1. Moreover, 2D DNS results at critical and supercritical step conditions were not computed given the importance of non-linear effects in these cases, leading to three-dimensional flow development after the step.

Results obtained using the BL+OS solver are expected to show differences with DNS results due to the implicit approximations that the BL solver holds. In figure 2.4 results from BL solver+OS and DNS are shown. Figure 2.4 (a) shows that the BL solver predicts lower values of the displacement thickness compared to DNS. If the velocity profiles are compared, one can observe that this mismatch is due to differences in the inviscid region of the boundary layer. This happens because close to the freestream, if there is a pressure gradient different than zero,  $\partial u/\partial x$  is no longer much smaller than  $\partial u/\partial y$ , which makes the BL solver less accurate than DNS in the outer region of the boundary layer.

The mismatch in the boundary layer propagates to the OS solver. This can be observed in figure 2.4 (b), where the N-factors obtained from the OS solver fed with the DNS baseflow lie on top of the DNS results, with small differences probably being due to the parallel flow assumption in the OS equation. Conversely, when the OS solver is fed with the baseflow computed by the BL solver, the results show larger discrepancies. The OS results presented in this work will be computed with the DNS solution (when available) given the better agreement with the N-factor values measured during experiments (see figure 2.4 (b)).

## 2.3. Flow diagnostics

The following section explains the working principle of the measurement techniques used during these experiments. In addition, the relevance of their results towards answering the main research questions presented in section 1.6 is also discussed.

Parameters	Symbols (units)		Values
Domain start	S	(m)	0.15
Domain end	c	(m)	0.7
Domain height	H	(m)	0.1
Points in streamwise direction	$n_x$	(-)	1171
Points in wall-normal direction	$n_y$	(-)	334
Degree of Legendre polynomials	$N_p$	(-)	9

Table 2.5: Numerical parameters used for DNS.

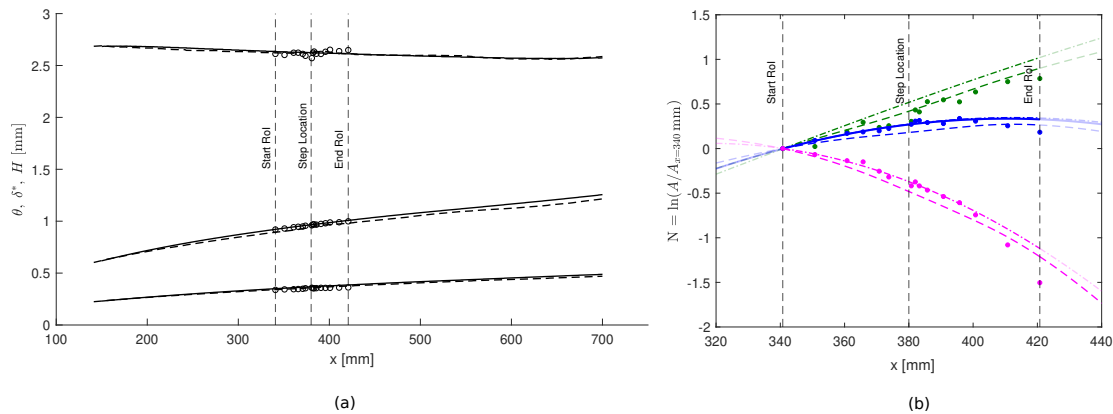


Figure 2.4: (a) Integral parameters from DNS (—), BL solver (---) and experiments (◦). (b) N-factor development along  $x$  for the three different frequencies tested:  $f = 300$  Hz (green),  $f = 450$  Hz (blue) and  $f = 550$  Hz (magenta). Results from DNS (—), OS solver fed with baseflow from BL solver (---), OS solver fed with DNS baseflow (-·-·) and experimental results (◦). All results presented are in clean conditions,  $h = 0 \mu\text{m}$ .

### 2.3.1. Infrared thermography

Infrared thermography makes use of the Reynolds analogy to measure the transition location. The Reynolds analogy states that a linear relationship exists between the shear stress  $C_f$  and the heat transfer coefficient  $\alpha$  experienced in a fluid that reads

$$\alpha = \frac{1}{2} C_f U_\infty \frac{k}{\nu} Pr^{1/3}, \quad (2.4)$$

where  $Pr$  is the Prandtl number and  $k$  is the thermal conductivity of the surface material. This relation turns out to be very useful since one can indirectly measure the skin friction, which is a very challenging quantity to measure, from the heat transfer distribution along a surface. Hence, transition can be identified from the large heat transfer gradient experienced between laminar and turbulent flow (Tropea et al., 2007).

To measure the heat transfer over the model's surface, in low-speed experiments an active heating technique is usually performed. It consists of heating a surface uniformly in space and time such that the model surface reaches thermal equilibrium. The heat transfer equilibrium taking place can be expressed as

$$q_j = q_{conv} + q_{rad} + q_{cond}, \quad (2.5)$$

where  $q_j$  is the energy generated by the heating element,  $q_{rad}$  is the radiation emitted by the surface material due to its temperature change,  $q_{cond}$  is the energy conducted through the model<sup>3</sup> and  $q_{conv}$  is the convective heat transfer between the air and the model:

$$\dot{q}_{conv} = \alpha (T_w - T_{aw}), \quad (2.6)$$

where  $T_w$  is the wall temperature,  $T_{aw}$  is the adiabatic wall temperature, and  $\alpha$  is the heat transfer coefficient.

The movement of the transition front for different step heights, TS wave amplitudes, and frequencies is tracked using Infrared Thermography (IR). This technique stands out among other transition front detection

<sup>3</sup>Usually an insulator is placed below the model surface to minimize the conduction losses on the opposite side of the measured plane.

methods for its superior accuracy and non-intrusiveness<sup>4</sup>. In addition, the use of an active heating technique allows for capturing averages in time which helps to increase the SNR. Finally, IR provides the transition front topology across the entire plate, which might reveal additional wall structures such as streaks.

### 2.3.2. Hot-wire anemometry

Thermal anemometry is a methodology that measures the fluctuations in the fluid velocity from the changes in heat transfer experienced by a hot wire. The wire is made out of a conductive material (e.g. tungsten) with a small diameter (around 5  $\mu\text{m}$ ) to reduce as much as possible its thermal inertia. This makes it possible to have both high temporal and spatial resolution (due to the small probe diameter) which results very convenient to measure linear disturbances since these are usually much smaller than the meanflow, i.e.  $\leq 0.01U_\infty$  (Tropea et al., 2007).

The main sources of heat transfer taking place at the wire can be described with the following expression

$$m_w c_w \frac{dT_w}{dt} = W_{\text{joule}} - (Q_{\text{conv}} - Q_{\text{cond}} - Q_{\text{rad}}), \quad (2.7)$$

where  $m_w$  is the mass of the wire and  $c_w$  is the specific heat of the wire material. Assuming that the wire is under equilibrium (the temporal change of the flow is slower than the rate at which the wire reaches thermal equilibrium), the previous equation can be simplified. If it is further assumed that conduction and radiation heat transfer contributions are low, equation (2.7) reads

$$W_{\text{joule}} - Q_{\text{conv}} = 0, \quad (2.8)$$

$$I_w^2 R_w - \alpha A (T_w - T_a) = 0, \quad (2.9)$$

where  $R_w$  is the wire resistance,  $I_w$  is the current through the wire,  $T_w$  is the temperature of the wire when is heated,  $T_a$  is the temperature of the fluid,  $\alpha$  is the convective heat transfer coefficient and  $A$  is the area of the wire exposed to forced convection.

There are different strategies to measure the velocity of the fluid from the changes in the wire's circuit. In these experiments, Constant Temperature Anemometry (CTA) is used. In CTA the wire constitutes one of the resistances,  $R_w$ , of a Wheatstone bridge. The bridge is kept in balance by changing the current,  $I_w$ , that goes through the wire such that the resistance is kept constant (and thus also its temperature). The voltage of the bridge,  $E_w$ , ends up being a direct indicator of the heat transfer at the wire.

#### Calibration procedure

A calibration law is necessary in HWA to convert the bridge voltage,  $E_w$ , to velocity. An expression relating  $U$  and  $E_w$  can be extracted from equation (2.8) when it is rewritten in terms of the Nusselt number,  $Nu = \alpha d/k_f$  where  $k_f$  is the thermal conductivity of the fluid,

$$\frac{E_w^2}{R_w} = \frac{k_f Nu}{d} A (T_w - T_a). \quad (2.10)$$

The Nusselt number  $Nu$  depends on the Reynolds number  $Re$  and the Prandtl number  $Pr$ . However, since the Prandtl number changes very weakly with the temperature, it can be assumed that  $Nu \approx f(Re)$ . Then, since  $A$  and  $d$  are constants, the previous equation can be expressed as

$$E^2 = f_1(Re) k_f (T_w - T_a), \quad (2.11)$$

which can also be written as

$$\frac{U}{\nu} = f_3 \left( \frac{E^2}{k_f (T_w - T_a)} \right). \quad (2.12)$$

Conventional calibration involves isolating  $U$  from the equation to end up with the so-called King's law,  $E^2 = A + BU^n$ , where  $A$  and  $B$  are coefficients found during the calibration procedure. However, these coefficients are dependent on the system properties and therefore also on the ambient temperature at the

<sup>4</sup>IR is non-intrusive as long as the temperature difference between the air and the surface remains low.

time of the calibration. One of the main inconveniences of CTA is that proper corrections for a change in the ambient temperature need to be performed before the post-processing. Thus, separate measurements of the fluid temperature need to be performed. A recent paper by Hultmark and Smits (2010) presents an effective calibration procedure to account for temperature changes.

Hultmark and Smits (2010) suggest that if instead the calibration is performed in non-dimensional terms such as on  $U/\nu$  with respect to  $E^2/k_f(T_w - T_a)$ , it is possible to know  $U$  independently of the change on the fluid temperature. To do so,  $\nu$  and  $k_f$  dependence on  $T$  should be known. This method is the one used in this work since it makes it possible to avoid corrections for changes in the ambient temperature and pressure during the post-processing.

Besides the high temporal and spatial resolution, HWA measurements cannot discern between different velocity components and directions. This, together with the fact that measuring the full field of interest using HWA is usually very time-consuming, makes PIV a perfect alternative to cover the limitations of HWA measurements.

### 2.3.3. Planar particle image velocimetry

Low-speed Planar Particle Image Velocimetry (2C-2DPIV) consists of quantifying the flow velocity and direction by measuring the displacement of particles immersed in the fluid. In double frame mode, a light source illuminates the field of view twice within a small-time interval separating each light shot, i.e.  $t$  and  $t + \delta t$ . A camera records both frames and finally, the velocity vector field can be solved by tracking the mean displacement of the particles within a small region of the image (interrogation window). The basic working principle of PIV is illustrated in figure 2.5 (a).

The success of PIV measurements relies on the correct choice of the tracer particles. The particles should follow the displacement of the flow and not alter their properties. In addition, their diameter should be large enough to not hinder the scattering of light. In air, since it is not possible to satisfy the buoyancy neutral condition ( $\rho_p - \rho_f/\rho_f$ ), the particle time response becomes a key parameter,  $\tau_p = d_p^2 \rho_p / 18\mu$ . One criterion to determine whether the particles follow faithfully the flow motion is to check whether the particle time response is lower than the smallest time scale in the flow. The Stokes number defines this criterion:

$$S_k = \frac{\tau_p}{\tau_f}. \quad (2.13)$$

As an example, in this work the smallest time scale in the flow is assumed to correspond to the highest frequency TS wave forced, which corresponds to  $f = 550$  Hz. In this case  $\tau_f = 1/550 = 1.82$  ms. In these experiments, water-glycol droplets are used. They have an average particle diameter of  $1 \mu\text{m}$ , a density of  $\rho_p = 10^3 \text{ kg/m}^3$  and  $\mu \approx 1.5 \times 10^{-3} \text{ Pa}\cdot\text{s}$ , which gives a Stokes number  $S_k \ll 0.1$ . Then, the uncertainty in the velocity due to the particle time response can be neglected.

The tracer particles are usually illuminated by a laser light due to its short pulse duration. This is of major importance to avoid particles showing in the frames as streaks. To avoid this, the distance covered by the particle during the pulse duration should be smaller than its diameter. Furthermore, only the particles lying inside the illuminated sheet should be in focus.

Proper pre-processing of the raw images can highly increase the SNR of the cross-correlation operation. The main goal of this phase is to reduce reflections and other artifacts which could corrupt the final result by showing up as fake particles to the algorithm. The final result of the pre-processing phase should look like a (very) low-intensity background with neat high-intensity particles on top. Figure 2.5 (b) shows a schematic of this procedure in terms of the intensity diagram of particles with respect to the background. First, a sliding filter is applied with a filter length of 9 pixels (this is representative of the average distance between seeding particles). Then, the minimum within the filter window is selected and subtracted from every pixel. This will highly reduce the counts of the background, leading to an intensity plot similar to  $I_2$  in figure 2.5 (b). Secondly, all the resulting frames from the sliding filter are averaged ( $\bar{I}_2$ ). Given that the distance between particles is larger than their diameter, this average value should lie way below the maximum intensity counts of the particles as illustrated in figure 2.5 (b) by the dotted dashed line crossing  $I_2$ . Hence, when the resulting filtered images are divided by this value, the intensity difference between the background and the particles is largely increased, making it easier to distinguish the particles from the background. The latter phase is indicated by  $I_3$  in figure 2.5 (b) with  $\kappa$  being a tuning constant to increase the count value.

To evaluate the velocity vectors, the image is partitioned in so-called interrogation windows. The intensity of the two frames separated by  $\delta t$  is cross-correlated:

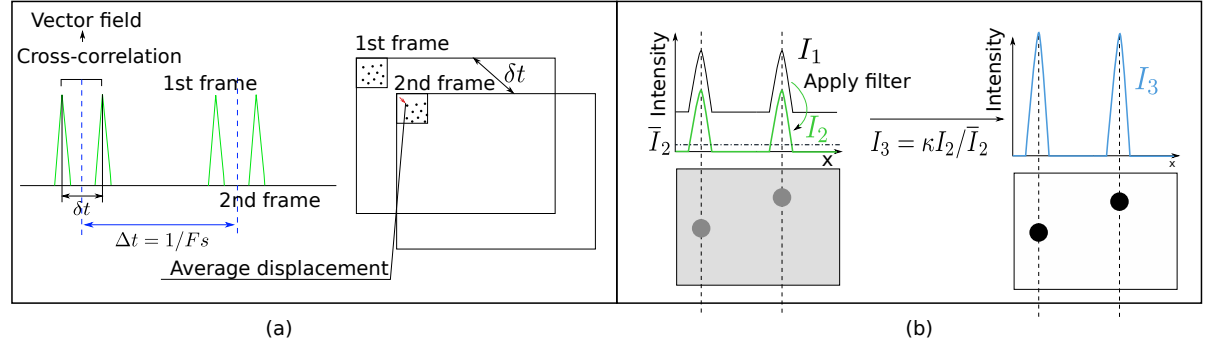


Figure 2.5: (a) Schematic of double-frame mode with later cross-correlation of the interrogation windows from both frames. (b) Pre-processing of the raw frame.

$$C(\delta_x, \delta_y) = \frac{\sum_j \sum_i F_1(i, j) \cdot F_2(i + m, j + n)}{\sqrt{\sum_j \sum_i F_1^2(i, j) \cdot \sum_j \sum_i F_2^2(i, j)}}, \quad (2.14)$$

where  $F_1$  and  $F_2$  denote the two different frames. Assuming that the size of the interrogation window is representative of the particle displacement, the result of this operation should depict a correlation peak at the average pixel displacement ( $m$  and  $n$ ) of the particles (or flow) within the window. A later Gaussian fit around the peak allows calculating the sub-pixel displacement of the particle. The velocity of the particle can be calculated as

$$\Delta U = \Delta p x_x \frac{M \times \text{px size}}{\delta t} \quad (2.15)$$

where the magnification factor ( $M$ ) and the pixel size (px size) are automatically retrieved from the geometrical mapping of the calibration image.

In principle, small interrogation windows are desired to increase the spatial resolution. However, this deteriorates the cross-correlation since very few particles will be common to the two frames. General rules for a proper window size include a minimum of 10 particles within the window and the average displacement of the particles to be less than  $1/4$  of the window size. In practice, the average displacement of the particles is larger than the window size. This could be solved by reducing the time pulse,  $\delta t$ , but this would also reduce the SNR (smaller displacements are more susceptible to noise, i.e. higher measurement uncertainty).

To achieve higher spatial resolution without worsening the cross-correlation results, multi-pass and multi-size cross-correlation is used in this work. Initially, the images are partitioned in large windows and cross-correlated. Then, the windows of each double-frame pair are shifted half the displacement computed in the initial pass,  $(\delta_x, \delta_y)$ , the first frame is shifted  $(\delta_x/2, \delta_y/2)$  and the second frame  $(-\delta_x/2, -\delta_y/2)$ . This increases the number of common particles found between the first frame and the second, improving the cross-correlation. In this work, a set of 4 passes are performed, excluding the initial pass, with a final window size of  $12 \times 12$  px and 75% overlap. In addition, an elliptic weighting can be applied to the interrogation windows, encompassing more pixels in the direction of largest shear (if known). This can help to increase the SNR of the cross-correlation peak since the compared windows are more likely to share particles if they are deformed in the dominant flow direction.

Low-speed Planar Particle Image Velocimetry (2C-2DPIV) is used in this work to characterize the TS waves and mean flow distortion around an FFS. 2C-2DPIV has been chosen since TS waves are two-dimensional disturbances. High temporal resolution is not required since the measurements are focused on capturing the topology of the disturbances and the meanflow close to the step, but not the temporal dynamics which are anyway measured with HWA. PIV allows the measurement of two different velocity components at the step. This will enable the visualization of the perturbation streamlines, the computation of the spanwise vorticity, etc.

## 2.4. Data analysis

This section covers the main post-processing methodologies used to extract this work results from experimental data.

### 2.4.1. Differential infrared thermography

In practice, IR measurements are affected by different sources of background noise. One clear example is the air between the emissivity body and the IR camera which also absorbs radiation and contaminates the signal. A relatively new approach to increase the signal-to-noise ratio of IR measurements is Differential Infrared Thermography (DIT), first introduced by Raffel and Merz (2014). The authors subtract two sets of IR measurements performed at different transition regimes to increase the SNR (assuming the background noise remains similar) and identify the largest intensity gradients as transition locations. The superior performance that several authors report (Gardner et al., 2017; Rius-Vidales and Kotsonis, 2020) compared to conventional IR, motivated the use of DIT during these experiments.

In these experiments, two consecutive measurements at different Reynolds numbers are used to perform DIT. Enough time separation is left between each acquisition set to ensure a steady thermal heat exchange between the surface and the fluid. For each Reynolds number, a set of 80 frames is averaged in time. Figure 2.6 illustrates the post-processing methodology used to track the transition fronts. Every phase represented in the figure is further explained in the remaining of this section.

A physical calibration is used to dewarp the image to account for the lens distortion and any misalignment between the measurement plane and the camera's focal plane. This calibration object is built using an image consisting of a uniform grid of 60 mm spaced points which are captured by the IR camera due to the high emissivity of the black paint. A geometric transformation in the form of two polynomials in  $x$  and  $y$  direction is calculated based on the distribution of points from the dewarped image and the one from the physical grid (60 mm spaced points). This object will dewarp the image and at the same time scale the pixels to the corresponding millimeters at the plate (Gonzalez and Woods, 2018). In addition, since the calibration image is placed strategically at the step edges, the coordinates of the calibration points within the model reference frame are known. This allows to track the transition front location with respect to the model's LE.

Once the two different IR sets are dewarped, DIT is applied. The resulting image presents a region of high intensity between the two transition fronts. The challenge remains in establishing a criterion to binarize the image (i.e. to find the boundary constituting the transition front). In this case, the criterion proposed by Otsu (Otsu, 1979) is used to define the pixel intensity threshold. This method searches for a threshold that minimizes the intra-class variance of the pixel intensity histogram. To do so, the histogram needs to exhibit bimodality, i.e. the valley that separates high from low-intensity pixels needs to remain low. Therefore, it is very important to avoid noisy DIT frames which can increase the gray valley and corrupt the threshold identification.

Subsequently, a Gaussian filter is applied to the binarized image and the intensity to compute the gradient across  $x$  and  $y$ . The first gradient peak along  $x$  (starting from the left) is identified as the transition front location for the lowest Reynolds number case (the flow comes from the right in these images). Finally, to determine the transition front, a linear fit of the identified peaks is performed and the standard deviation of the error is used as an estimate of the transition front uniformity along the span. The final transition front reported in this work consists of the intersection of the linear fit with the centerline of the model, i.e.  $y = 0$ .

### 2.4.2. Wall-finding in HWA velocity profiles

During the experiments, the last measuring point with HWA is usually taken at  $U/U_e \approx 10\%$  to avoid contact of the HWA sensor with the wall. The distance from the HWA sensor (i.e. wire) to the wall is then measured with a Taylor-Hubson micro-alignment telescope and later this value is refined during the post-processing.

In the clean case, the velocity profile is interpolated towards the wall using a least-squares fit, following the approach employed in White and Ergin (2004). Since the pressure gradient is nearly zero in the no-step case, it follows from the NS equations that  $\partial^2 U / \partial y^2 \approx 0$  and a linear fit near the wall holds. To do so, the last points of the velocity profile where  $U/U_e \leq 35\%$  are used to perform the linear least-squares fit. The distance to the wall ( $y_{wall}$ ) is given by the intersection of the linear fit with the  $y$ -axis. Finally, all the points in the profile are shifted in wall-normal direction  $y_{wall}$  mm such that the no-slip conditions is satisfied,  $U = 0$  at the wall.

The previous method suffers from large systematic errors when there is a step since the pressure gradient is no longer negligible. In this case, DNS results at the same test conditions are used to estimate the wall distance using again a least-squares approach. However, since the data does no longer satisfy a linear fit towards the wall, an iterative algorithm needs to be used where the objective function to minimize is

$$\epsilon(k) = \frac{1}{N_y} \sum_{i=1}^{N_y} \left( \frac{U_{\text{HWA}}(y + k\Delta y) - U_{\text{DNS}}(y)}{U_{\text{DNS}}(y)} \right)^2, \quad (2.16)$$

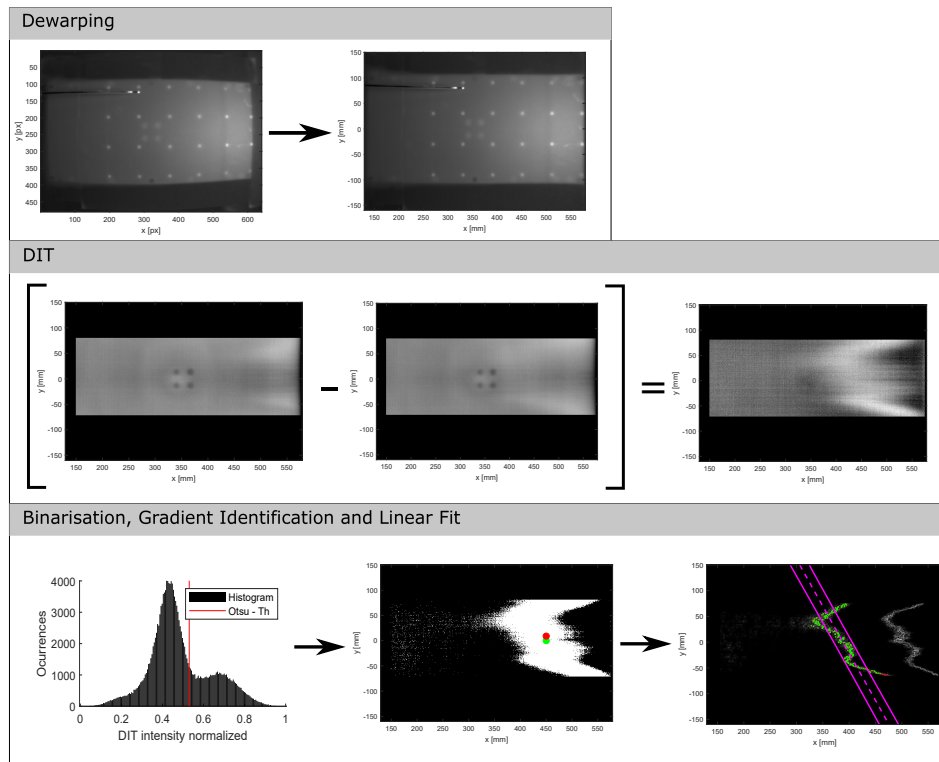


Figure 2.6: Schematic of the post-processing procedure used to extract the transition front location from the IR images.

where  $k$  is the iteration number and  $\Delta y$  are the wall-normal increments.

### 2.4.3. Welch's modified periodogram

In this work, disturbances are forced using acoustic waves at the same frequency. When the temporal readings of the HWA are transformed to the frequency domain using Fast Fourier Transformed (FFT), a distinct amplitude peak is observed at the forced frequency and also possibly at its harmonics. The amplitude distribution of the forced disturbance along the wall-normal direction is directly evaluated from the FFT peak at the forced frequency. The same procedure is used to quantify the acoustic amplitude peak from microphone readings.

However, in cases where the disturbance energy is not strictly focused on one frequency, the Power Spectral Density (PSD) appears very useful to study the distribution of the perturbation energy along the frequency domain. The Welch's Modified Periodogram method (i.e. Welch's method) is used herein to compute the PSD and reduce the noise of the signal (Proakis and Manolakis, 2006). This approach consists of a first split of the signal in segments of length  $L$  overlapped by a certain percentage of the signal. To reduce the contribution of possible non-periodic extremes in the FFT, a Hanning window (Eq. 5.4.9 in Proakis and Manolakis (2006)) is applied to give more influence to the center of each segment. The subsequent window overlapping mitigates the loss of information at the segment margins produced by the Hanning window. Each signal segment is Fourier transformed and later squared to compute the corresponding periodogram. Finally, the periodograms are averaged to reduce the variance of the power spectrum.

A trade-off solution needs to be found between noise reduction and frequency resolution when using Welch's method. To reduce the noise on the final PSD one can increase the number of windows or the overlap. The first would dramatically reduce the frequency resolution while the second, despite not affecting the latter, will deteriorate the result of the FFT due to the large correlation between samples.

### 2.4.4. Proper orthogonal decomposition

Most experimental and numerical fluid dynamic applications deal with large amounts of data that are difficult to interpret. In these cases, Proper Orthogonal Decomposition (POD) appears as a very powerful post-processing technique to reduce all this information to a synthetic representation of the most energetic coherent structures constituting the flow. From a mathematical point of view, POD creates an orthonormal basis constituted by functions that correlate best on average with the input velocity field. In practice, POD is an

approximation method where the velocity field  $u(x, t)$  is represented as the finite sum of  $N$  spatial modes multiplied by temporal coefficients:

$$u^n(x, t) \approx \sum_{i=1}^N a_i^n(t) \Phi^i(x), \quad (2.17)$$

where  $i$  denotes the number of modes used to reconstruct the field and  $n$  is the input snapshot.

The classic way to approach this approximation problem is to use a priori known basis functions,  $\Phi_i^{(n)}(x)$ , such as Legendre or Chebyshev polynomials. However, in POD these functions are obtained such that their projection is maximum onto the original velocity field, i.e. one seeks for functions that represent coherent structures. Mathematically, this is formulated as an optimization problem where the kinetic energy of the problem is best captured by the first  $N$  modes. The reader is referred to Section 22.4.6 in Tropea et al. (2007) for further details on the mathematical steps used to convert an optimization problem in energy terms to the final eigenvalue problem, which in matrix form is written as:

$$CA^i = \lambda^i A^i, \quad (2.18)$$

where  $C$  is the autocovariance matrix,  $\lambda_i$  are the eigenvalues and  $A^i$  are the eigenvectors. The original POD problem is usually formulated as in equation (2.17), the so-called direct POD. However, in fluid mechanic applications, the Snapshot POD formulation is more convenient (Weiss, 2019). In this case, the coefficients in equation (2.17) are spatial and the basis functions are temporal. The reason why this method is more convenient when dealing with experimental data (where the number of spatial points is larger than the number of snapshots,  $N > M$ ) is because the dimensions of the autocovariance matrix are highly reduced and the eigenvalue problem is much faster to solve. In Snapshot POD the autocovariance matrix is defined as

$$C = \frac{1}{N-1} U^T U, \quad (2.19)$$

where  $U$  is the matrix of fluctuating velocity components with dimensions  $M \times N$ ,  $N$  is the number of snapshots, and  $M$  is the number of vectors in the snapshot. Hence,  $C$  has dimensions  $N \times N$  (usually  $M \gg N$  in experimental data). The final solutions to the eigenvalue problem are ordered from larger to lower eigenvalues. The corresponding POD modes can be computed from the eigenvalue problem as (Weiss, 2019)

$$\Phi^i = \frac{\sum_{n=1}^N A_n^i u^n}{\left\| \sum_{n=1}^N A_n^i u^n \right\|}, \quad i = 1, \dots, N \quad (2.20)$$

and the temporal coefficients as

$$a^n = \Psi^T u^n, \quad (2.21)$$

where  $\Psi = [\phi^1 \ \phi^2 \ \dots \ \phi^N]$ . Then, a snapshot  $n$  can be reconstructed from the POD modes and coefficients as

$$u^n = \sum_{i=1}^N a_i^n \phi^i. \quad (2.22)$$

In practice, the only difference between the Snapshot and the Direct POD methods is that in Snapshot POD the optimal POD modes are obtained by correlating the points in time and averaging in space while in Direct POD the opposite is performed (Tropea et al., 2007).

## 2.5. Uncertainty analysis

This section presents the main sources of uncertainty from these experiments and an estimate of their value in the percentage of the measured quantity. This would allow to quantify the limitations of the measurement techniques used in this work.

Two main types of uncertainties are commonly identified. First, random uncertainty is linked to the existence of fluctuations in the measured quantities. This source of uncertainty can be quantified using statistical analysis and can be reduced by increasing the number of samples:

$$\varepsilon_r = \pm \frac{k\sigma}{\sqrt{N}}, \quad (2.23)$$

where  $N$  is the number of samples,  $k$  determines the confidence level and  $\sigma$  is the standard deviation. Secondly, systematic uncertainty is related to instrumentation resolution or errors from the wind tunnel user. Unlike random errors, they remain unchanged with the number of sample points but can be reduced or removed if correctly identified. The total uncertainty can be expressed as the sum of systematic and random errors

$$\varepsilon_T = \sqrt{\varepsilon_r^2 + \varepsilon_s^2}, \quad (2.24)$$

being  $\varepsilon_s$  the systematic uncertainty.

### 2.5.1. Pressure coefficient

The pressure coefficient  $C_p$  is expressed as

$$C_p = \frac{p_{\text{stat, tap}} - p_{\text{stat, pitot}}}{p_{\text{tot, pitot}} - p_{\text{stat, pitot}}} = \frac{p_{\text{scanner}}}{p_{\text{dyn}}}. \quad (2.25)$$

The uncertainty on the pressure coefficient ( $\Delta C_p$ ) is mainly governed by systematic errors and can be written as (Methel et al., 2021)

$$\Delta C_p = \sqrt{\left(\frac{\partial C_p}{\partial p_{\text{scanner}}} \Delta p_{\text{scanner}}\right)^2 + \left(\frac{\partial C_p}{\partial p_{\text{dyn}}} \Delta p_{\text{dyn}}\right)^2} = \gamma C_p, \quad (2.26)$$

and  $\gamma$  is

$$\gamma = \sqrt{\left(\frac{\Delta p_{\text{scanner}}}{p_{\text{scanner}}}\right)^2 + \left(\frac{\Delta p_{\text{dyn}}}{p_{\text{dyn}}}\right)^2}, \quad (2.27)$$

where  $\Delta p_{\text{scanner}}$  and  $\Delta p_{\text{dyn}}$  denote the systematic uncertainty on the pressure difference read by the pressure modules and the dynamic pressure read in the pitot, respectively. These values are specified in table 2.6. Figure 2.7 (b) shows the calculated uncertainty on the pressure coefficient with confidence bands.

### 2.5.2. IR transition fronts

The uncertainty on the transition front is mainly driven by systematic errors. The main sources of uncertainty on the transition front identification come from the calibration procedure due to, for instance, a misalignment of the calibration sheet with the step edge; from high levels of noise in the resulting DIT image (this hinders the correct estimation of a threshold using the Otsu method); or from the presence of turbulent wedges triggered by the test section walls.

A large number of tests should be performed to quantify the contribution of each error source to the final uncertainty. For instance, different calibrations should be performed, different temperatures in the heating element should be tested to verify the changes on the Otsu's threshold and consequent transition front identification, etc. However, given the time constraints associated with this thesis, these tests are outside the scope of this work.

The thermal sensitivity of the IR camera is usually denoted as Noise Equivalent Temperature Difference (NETD). This value indicates the minimum temperature difference that can be distinguished by the IR camera.

The results presented in this work will indicate the uncertainty on the transition location as the standard deviation of the error provided by the linear fit to the transition front. This represents the variance of the transition front due to its waviness or non-uniformity in span. Given the small NETD values of the IR camera (75 mK) compared to the uncertainty on the transition front non-uniformity, the latter dominates the total uncertainty.

### 2.5.3. HWA profiles

The uncertainty in the HWA measurements comes from the velocity and the estimate on the wall location. The velocity measurements are subject to random and systematic errors while the uncertainty on the wall location is mainly governed by systematic errors.

Systematic errors in the velocity measurements are accounted for in the calibration procedure. Random uncertainty, on the other end, needs to be computed based on an effective number of samples since these are not statistically independent, i.e.  $\Delta t \ll T_u$  (Sciacchitano and Wieneke, 2016):

$$\varepsilon_r = \pm \frac{k\sigma}{\sqrt{N_{\text{eff}}}} \quad \text{where} \quad N_{\text{eff}} = \frac{N}{2T_u/\Delta t}, \quad (2.28)$$

where the confidence level is set to  $k = 1$  and the integral time scale is expressed as

$$T_u = \frac{1}{2}\Delta t \sum_{i=-\infty}^{\infty} \rho_i(\tau) d\tau \quad (2.29)$$

in discrete form, with  $\Delta t$  being the sampling interval. The previous summation is usually stopped when  $\rho_i$  crosses zero (Sciacchitano and Wieneke, 2016). Since the measurement size (3 seconds) is greater than  $10T_u$ , it can be assumed that  $\rho$  is correctly computed when accounting for the total sample size (Smith et al., 2018). From equation (2.28) it becomes clear that, when the samples are highly correlated  $N_{\text{eff}} < N$ , the uncertainty on the mean value increases. This takes place when the ratio of  $2T_u/\Delta t \geq 1$ . In HWA this is particularly dangerous since, due to the high-frequency sampling,  $\Delta t$  is usually very small. In a boundary layer, the largest integral time scales are found in the freestream. Hence, in this work results, the random error is computed based on the integral time scale at the last point measured by the HWA in the velocity profile. As an example, in clean case conditions (no step) the integral time scale in the freestream reaches values as large as 0.18 sec, being the number of effective samples in this region  $N_{\text{eff}} = 53$  ( $N = 153600$ ). It can be observed that the number of effective samples has dangerously dropped in the freestream, dramatically increasing the uncertainty in the mean in this region. Sciacchitano and Wieneke (2016) recommend to increase the recording time in these regions in case  $T_{int}$  is unknown.

The maximum total uncertainty on the velocity (systematic uncertainty given by the HWA calibration together with the random uncertainty) is represented in figure 2.7 using confidence bands for a profile taken at  $x = 420$  mm in clean case conditions. Note that the uncertainty in the mean increases in the freestream due to the above-mentioned phenomenon.

The uncertainty in the wall-normal coordinate is mainly driven by systematic errors. Its correct quantification is important to determine the uncertainty of the integral boundary layer parameters. As mentioned previously in section 2.4.2, the  $y$ -coordinate is corrected according to the wall location estimate. This can be expressed as

$$y^* = y + y_{\text{wall}}, \quad (2.30)$$

which yields the uncertainty on  $y^*$  to be

$$\Delta y^* = \sqrt{\Delta y^2 + (\Delta y_{\text{wall}})^2} \approx \Delta y_{\text{wall}}, \quad (2.31)$$

where  $\Delta y$  is mainly associated with the resolution of the HWA traverse system (see table 2.6) which is almost negligible compared to  $\Delta y_{\text{wall}}$ . The uncertainty on the wall correction ( $\Delta y_{\text{wall}}$ ) depends on the presence of the step. On the one hand, in the clean case, the uncertainty on  $\Delta y_{\text{wall}}$  comes mainly from the error produced when assuming  $\partial p/\partial x = 0$  to interpolate linearly towards the wall. This error can be estimated by comparing the error on the  $y$ -coordinate between the wall-corrected profile and the corresponding Blasius profile. On the other hand, in the step case, the main contribution to  $\Delta y_{\text{wall}}$  comes from the error on the wire position, which is used to select the DNS profile from which to refine the wall location. The error on the wire position is mainly subject to the telescope resolution, which is the instrument with which the traverse coordinate system was referred to the step location, i.e.  $x = 380$  mm. To estimate  $\Delta y_{\text{wall}}$ ,  $y_{\text{wall}}$  is now found using the DNS profiles placed at  $x \pm \Delta x_{\text{telescope}}$ . The difference between these values and the previously computed  $y_{\text{wall}}$  determines  $\Delta y_{\text{wall}}$  in the presence of a step.

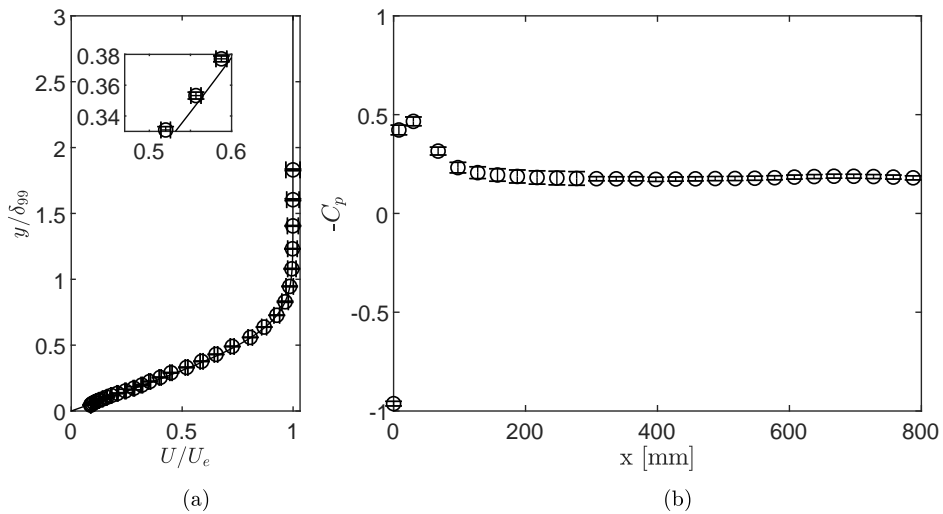
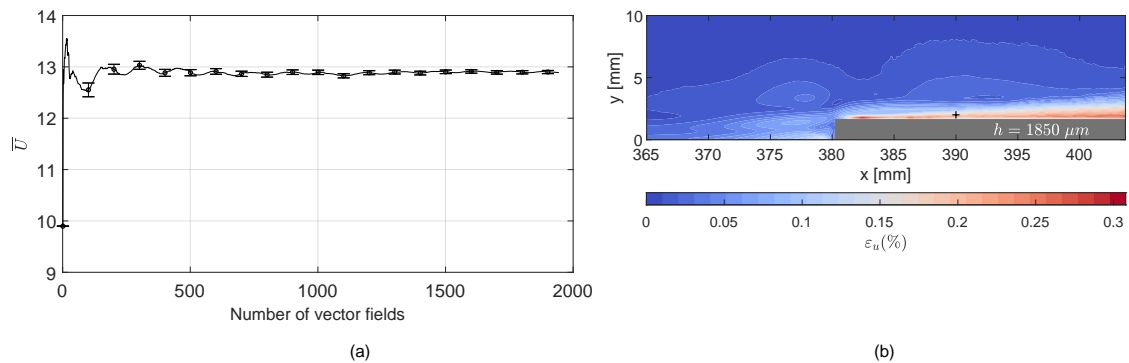
If otherwise not stated, the symbol size serves as an indicator of the maximum measurement error in the results plotted hereafter.

Instrument	Symbol	Systematic Uncertainty
Differential Pressure Sensor (range $\pm 1245.45$ Pa)	$\Delta p_{\text{dyn}}$	$\pm 1.25$ Pa
Pressure Scanners (range $\pm 160$ Pa)	$\Delta p_{\text{scanner}}$	$\pm 0.4$ Pa
Error from calibration curve fit	$\beta$	0.004
Telescope	$\Delta x_{\text{telescope}}$	$\pm 20$ $\mu\text{m}$
Zaber Traverse System	$\Delta y$	$\pm 2.5$ $\mu\text{m}$

Table 2.6: Uncertainties from experimental instrumentation and calibration.

Systematic uncertainty	Value
Clean case, $\Delta y_{\text{wall}}$	$\pm 1.75\%$
Step case, $\Delta y_{\text{wall}}$	$\pm 2.4\%$

Table 2.7: Maximum systematic uncertainty in velocity and wall-normal coordinate found amongst all HW profiles.

Figure 2.7: (a) Blasius profile (—) and mean velocity profile from HW measurements (o) with error bars indicating uncertainty in velocity and wall-normal direction. (b) Pressure coefficient  $C_p$  with uncertainties.Figure 2.8: (a) Convergence of meanflow U-component at point (+) with errorbars denoting standard deviation. (b) Contours of  $\epsilon_u$  with  $N = 1944$  averaged vector fields.

### 2.5.4. PIV flowfields

PIV measurements are subject to several systematic errors which establish the accuracy of the PIV results. These errors can come from installation and alignment of the set-up, incorrect levels of seeding concentration, reflections, out-of-plane motion, camera noise, particle size, etc. Usually, a large number of errors (such as

Region	$\varepsilon_u/U$
Freestream (clean case)	$\pm 0.005\%$
High-shear region (clean case)	$\pm 0.01\%$
High-shear region (highest step case) $\Delta y_{wall}$	$\pm 0.25\%$
Recirculating region (highest step case) $\Delta y_{wall}$	$\pm 0.15\%$

Table 2.8: Uncertainty of the  $U$  meanflow component in PIV.

the previously mentioned) can be quantified from the recorded image. However, other sources of systematic errors coming from, for instance, the calibration procedure or the poor synchronization between devices, are not manifested in the final image and cannot be quantified.

In recent years a number of efforts have been focused to quantify the uncertainty of every single PIV frame. The methodology discussed herein is the one used in DaVis, the software used to run the PIV algorithm, and firstly developed by Wieneke (2015). The so-called correlation statistics (CS) method uses the estimated displacement from PIV to dewarp the first and second image by half the displacement (similar to the multi-pass procedure previously explained). In an ideal noise-free scenario, the particles from both displaced images should perfectly lie on top of each other. The underlying uncertainties on each PIV frame cause non-overlapping particles which are translated into a non-symmetric correlation peak. This disparity in the correlation peak is used to estimate the uncertainty of the displacement field.

The uncertainty in the mean velocity fields is dominated by random errors. Hence, the uncertainty in the mean can be directly computed from the standard deviation, i.e. it is not necessary to know the uncertainty of every instantaneous frame. This can be expressed as

$$\varepsilon_U = \pm \frac{\sigma_U}{\sqrt{N}}. \quad (2.32)$$

Figure 2.8 (a) shows the convergence of  $U$  and  $V$  for different number of averaging fields,  $N = 1944^5$ . The point chosen for the convergence analysis is taken at a region of high shear for the largest step ( $x = 390$  mm and  $y = 2$  mm indicated in Figure 2.8 (b) with a + symbol) where the uncertainty is expected to be larger than in other regions of the flow. If convergence is achieved at this point, convergence everywhere else is likely to happen. Figure 2.8 (b) shows the standard deviation field for the largest step. As expected, regions of high uncertainty take place where the flow either starts to break down, is already turbulent, or is subject to large wall reflections. The uncertainty on  $U$  for a zero-step and the highest step case is indicated in table 2.8.

<sup>5</sup>Since the samples are statistically independent ( $\Delta t \geq 2T_u$ )  $N_{\text{eff}} = N$  in this case.



# Experimental Protocol

## 3.1. Experimental set-up

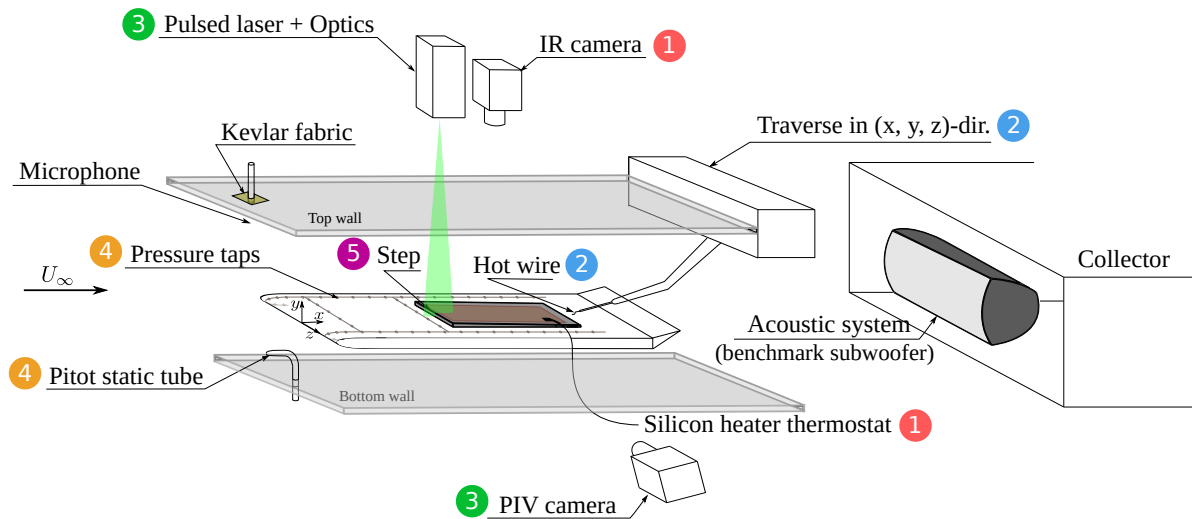


Figure 3.1: Sketch of the experimental set-up featuring the unswept flat plate, the FFS mechanism, the acoustic forcing system and the different measurement techniques used. Numbers indicate the subsections within this section where the details of the different measurement techniques are presented.

This section aims to describe the experimental set-up used during the present work. Figure 3.1 shows a schematic of the test section, the flat plate model, and the measurement techniques used. The numbers in the figure denote the subsections within this section where the indicated set-up instruments are described (except for the acoustic instrumentation which will be discussed separately in section 3.2).

The experiments were performed in the A-tunnel, an open-jet, anechoic, closed-circuit, subsonic, and vertical wind tunnel. The test section features acoustic absorbing foam which reduces sound reflections. This creates a suitable environment to force and study TS waves since these are highly responsive to acoustic reflections. A nozzle is used to adapt the circular inlet test section of diameter 600 mm to a rectangular one with dimensions  $500 \times 500 \text{ mm}^2$  where the flat plate model can rest at zero angle-of-attack. Ambient temperature and barometric pressure are measured using a PT100 RTD probe and NPA-201 sensor, respectively, both within the test section. For more details regarding the technical specifications of the A-tunnel, the reader is referred to Merino-Martínez et al. (2020).

The tests are performed with an unswept flat model of 950 mm chord and 20 mm thickness. The model features a Modified Super Ellipse (MSE) at the LE with  $\mathcal{R} = 6$ . This design moves the suction peak towards the LE and reduces the adverse pressure gradient in the LE region (Lin et al., 1992). All of this ensures rapid development towards a Blasius BL solution. The stagnation point and the LE pressure distribution can be adjusted with a TE flap. A rectangular cavity of dimensions  $428 \times 208 \text{ mm}^2$  starting at  $x = 380 \text{ mm}$  allows

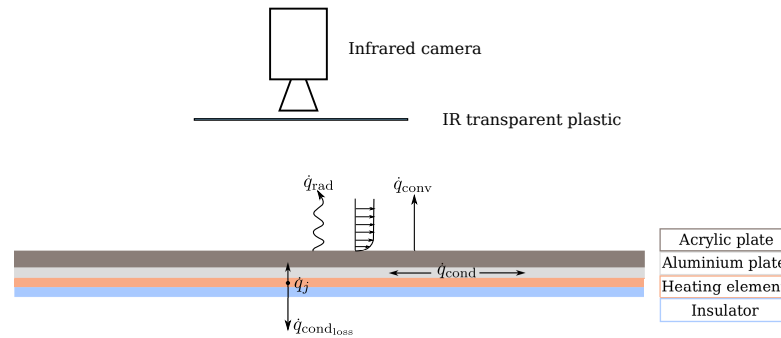


Figure 3.2: Sketch of the IR system illustrating the materials used and the flux of the different heat transfer mechanisms across the layout.

an insert to be placed in the model. During these experiments, a mechanism to create FFS is placed in this cavity. Finally, the boundary layer over the bottom side is forced to turbulent using a trip strip to avoid flow separation.

### 3.1.1. Infrared thermography

IR can provide a temperature map along the model surface from which the transition front pattern and location are determined (section 2.3.1).

In figure 3.2, the layout used for the IR measurements performed in this work is shown. The heating element consists of a printed copper circuit covered by a silicon insulator which supplies heat by Joule effect,  $\dot{q}_j$  (custom made silicon heater from *Kracht*). An additional insulator is placed on top of the heating element to reduce heat losses,  $\dot{q}_{cond,loss}$ . The non-insulated side of the heating element is in contact with an aluminum tooling plate (*Salplan 5000* from *Salomon's Metalen B.V.*) which constitutes the base for the step mechanism. The choice of aluminum for this layer is made based on its high thermal conductivity, which enhances uniform temperature distribution along the entire plate. A black mate acrylic plate is placed on top of the aluminum one. The high emissivity of this material ( $\varepsilon \approx 0.96$ ) makes it ideal for infrared detection.

Different heat transfer convection is experienced along the plate based on the wall-shear stress of the fluid, which relates to the heat transfer via the Reynolds analogy, as discussed in section 2.3.1. This causes different equilibrium temperatures along the plate which can be recorded with an infrared camera. Finally, a window made of IR transparent material ( $6'' \times 6''$  translucent IR material from *Edmund Optics*) is placed in front of the camera to allow it to see through the test section walls. The surface temperature difference was kept below half a degree to avoid interfering with the transition process (Costantini, 2016).

The field of view encompasses the region surrounding the insert<sup>1</sup>, with dimensions of  $500 \times 300$  mm. The IR camera used is an *Optris PI640* which has a sensor size of  $640 \times 480$  pixels, a spectral range between  $7.5$  to  $13 \mu\text{m}$  and thermal sensitivity (NETD) of  $70$  mK. The thermal detector uses an array of thin-film bolometers placed on the un-cooled focal plane which constitute a pixel size of  $17 \times 17 \mu\text{m}$  and therefore a sensor size of  $10.88 \times 8.16$  mm. A wide-angle lens,  $f = 10.5$  mm, is used to capture the entire heated plate. The camera is placed at  $40$  cm from the model, giving a magnification factor of  $M = 0.03$ . The number of frames recorded was  $100$  at a frequency rate of  $3.5$  Hz for each Reynolds number condition to later perform DIT following the methodology described in section 2.4.1.

### 3.1.2. Hot-wire anemometry

HWA measurements were taken to inspect the temporal dynamics of the flow close to the step. For that, a *55P15* Dantec Dynamics hot-wire probe is used to measure boundary layer velocity profiles. Figure 3.3 shows the geometry of this probe. Note that the sting holding the probe is above the wire location which highly reduces the blockage effect on the measurement and allows for velocity measurements near the wall. In addition, the inclination of the probe prongs with respect to the wall makes it easier to measure upstream of an FFS. In these experiments, the closest position where the wire could be set upstream of the (highest) step in order to avoid touching the prongs with the step edge was  $7$  mm (see figure 3.3).

A three degrees-of-freedom (DoF) traverse system positions the probe with a step resolution of  $2.5 \mu\text{m}$ . Fifteen velocity profiles were taken, distributed as indicated in figure 3.4. The choice for a higher number of profiles in the downstream direction was made based on the indications from literature pointing to the

<sup>1</sup>The insert is the only region being actively heated.

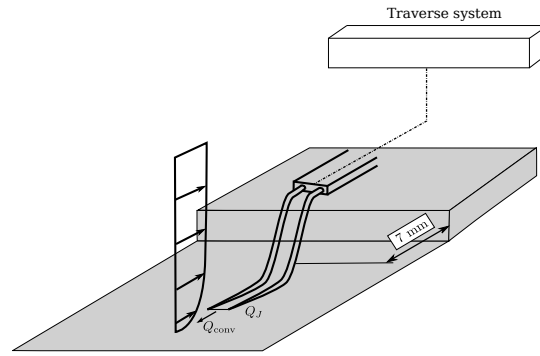


Figure 3.3: Sketch of the 55P15 Dantec hot-wire probe with predominant heat transfer exchange terms indicated. The annotation indicates the minimum distance to which the wire could be placed upstream of the step to avoid the wire prongs touching the step edge.

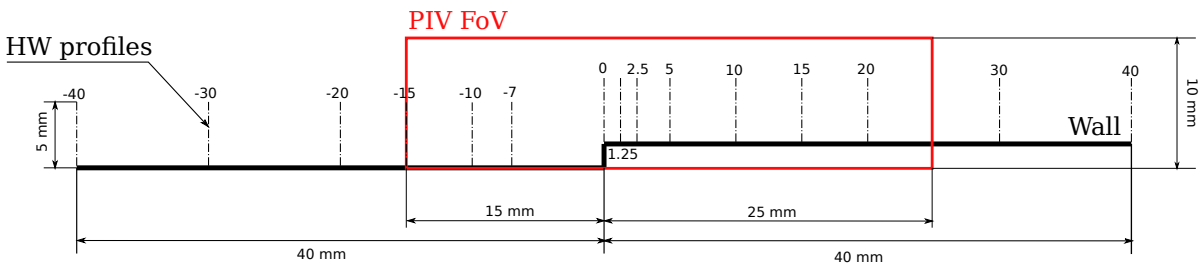


Figure 3.4: Location of HWA profiles and PIV field of view (FoV) with respect to the FFS location. Drawing has scale 2:1.

interesting flow features after the step edge. Each boundary-layer profile consists of 60 measurement points logarithmically distributed to increase the spatial resolution near the wall ( $\Delta y_{\min} = 0.007$  mm and  $\Delta y_{\max} = 0.32$  mm). In addition, the logarithmic spacing leads to a higher resolution around the TS maximum and a better characterization of the large velocity gradients taking place just after the FFS edge, where the boundary layer thickness is very small. The HWA sampling frequency was set to 51.2 kHz and the total measuring time per point was set to 3 seconds to ensure statistical convergence of the mean velocity.

The HWA calibration is performed by placing the wire at the freestream (approximately 10 cm away from the wall), close to a pressure tap in the midspan, indicated in figure 3.6. The dynamic pressure is computed by subtracting the static pressure of this tap from the total pressure read by the Pitot static tube.

### 3.1.3. Particle image velocimetry

Low-speed planar PIV (2C-2DPIV) measurements are performed to characterize the topology of both meanflow and instabilities across an FFS. Figure 3.4 shows the inspected FoV, focused on a region very close to the step, spanning 40 mm in  $x$  (15 mm upstream and 25 mm downstream the step), 10 mm in  $y$  and located along the midspan of the model,  $z = 0$ .

Figure 3.5 shows a schematic of the PIV set-up. Both camera and laser are placed on a linear traverse system. This enables their simultaneous displacement when taking measurements at different spanwise locations such that the particles remain in focus and the geometrical calibration at the midspan remains valid. The illuminated particles were recorded by one LaVision Imager sCMOS camera ( $2560 \times 2160$  pixels, 16 bit, and  $6.5 \times 6.5 \mu\text{m}^2$  pixel size) placed outside the test section, orthogonal to the light sheet and aligned to the model surface. The camera was placed as close to the inspected plane as possible (approximately 70 cm away from the midspan plane) to achieve high spatial resolution. During the acquisition, the image sensor was cropped to  $2560 \times 1000$  pixels to lower the memory requirements.

To closely examine the boundary layer at the step, a  $f = 200$  mm telephoto lens is placed on the camera to achieve large optical magnification,  $M = 0.4$ . During calibration,  $f\# = 4$  is used to focus on the measurement plane. However, during the measurements, the f-stop was set to 11 to capture more particles within the laser sheet. With these settings, the resulting particle image is  $d_{\tau} = 20 \mu\text{m}$ . Therefore, each particle spans 3 pixels, which is an acceptable ratio (given that there is no over-seeding for particle overlapping to take place) to avoid the so-called *pixel locking*. Finally, the inter-frame time  $\Delta t$  is set to  $19 \mu\text{s}$  such that the maximum displacement in the freestream is roughly 25 pixels. Accounting for a typical uncertainty on the particle image

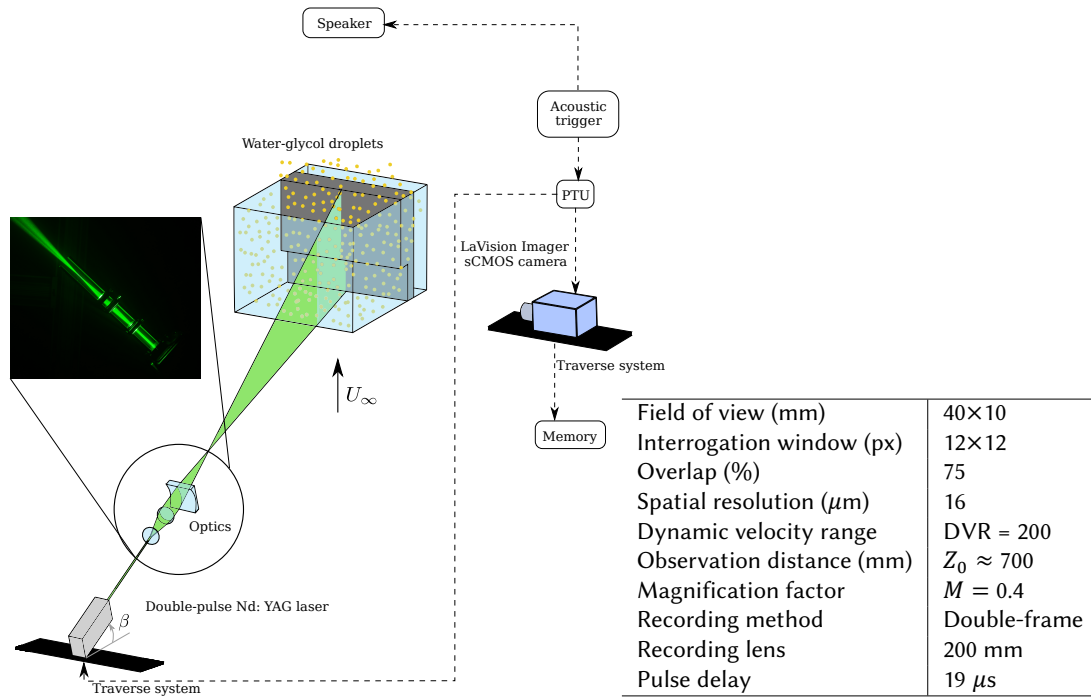


Figure 3.5: Schematic of the PIV set-up used during Campaign II. The sketch includes a realistic layout of optics, gadgets used (laser, camera, etc.), and the signal path (acoustic and laser trigger, etc.).

Table 3.1: Main PIV parameters during the experiments.

displacement of 0.1 pixels, the minimum velocity that could be measured was  $\min(|U|) \approx 0.08$  m/s (if the freestream velocity is  $U = 21$  m/s), i.e. the dynamic velocity range (DVR) is 200. Even though the maximum particle displacement (25 pixels) is larger than the recommended one ( $\leq 12$  pixels) in this specific problem this was a trade-off solution necessary to be able to capture the slow flow regions in front of the step.

Synchronization between laser and camera was performed through *LaVision Davis Programmable Unit PTU X*. The trigger was generated with an in-house LabView program aimed to design the acoustic pulse and locate the trigger with a specific time delay after the pulse. The images were captured at a frequency rate of 5 Hz and 15 Hz when the acoustic pulsed and continuous forcing techniques were used, respectively. Phase-locked images (1000 frames) were recorded at 6 different phases of the TS wave ( $\Delta\phi = [0, 60, 120, 180, 240, 300]$  deg). In addition, high-resolution phase-locked images (the phase difference between images was set to  $\Delta\phi = 5$  degrees) were recorded to build an ensemble of 1944 images from which to compute statistical quantities of the flow. This set of images is from now on denoted as *random*.

The number of images recorded in phase-lock mode was  $N = 1000$  while  $N = 1944$  in random mode. Later post-processing of the images was performed using *LaVision Davis 10.2.0: FlowMaser* software where the final interrogation windows were set to  $12 \times 12$  px with 75% overlap after applying the multi-pass procedure described in section 2.3.3.

A Quantel Evergreen dual-pulse Nd:YAG laser (200 mJ) is used to illuminate the particles during a very short pulse duration ( $\Delta t_{pulse} \leq 10$  ns) with a monochromatic light beam,  $\lambda = 532$  nm (green light). Two spherical ( $f = -50$  and  $f = 80$ ) and one cylindrical ( $f = 75$ ) lens were used to create a variable width laser sheet of thickness 1 mm centered at the midspan of the model, see figure 3.5. The light sheet was sent with an inclination angle with respect to the model surface to mitigate as much as possible the reflections at the step edge. Water-glycol particles were created using a *Safex* fog generator located in the wind tunnel collector to not perturb the flow and achieve a homogeneous seeding in the test section of approximately 0.018 PPI.

### 3.1.4. Static pressure measurements

Static pressure taps are distributed on the model sides, the LE, and in front of the step, as illustrated in figure 3.6. The aim of the static pressure taps close to the LE is to find the stagnation point. The pressure taps on the sides and along the span help to determine the spanwise modulation of the pressure due to the test section sidewalls. Streamwise taps appear shifted in  $x$  to increase the spatial resolution in this direction. Three ranges

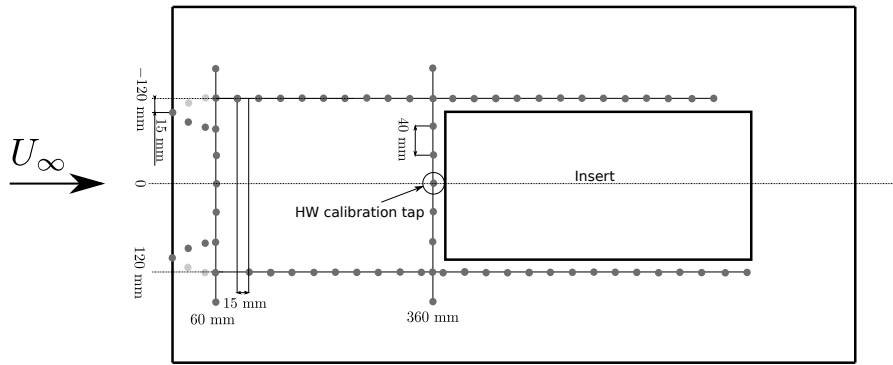


Figure 3.6: Sketch of pressure taps distribution along the model and insert (not to scale). Horizontal direction is  $x$  and vertical direction is  $z$ .

of differential pressure sensors were used based on the location of the pressure taps along the flat plate model.

The pressure imposed in the DNS at the top boundary condition ( $H = 0.1$  m) is set to match the pressure developing at the wall during experiments in no-step conditions (obtained from averaging right and left pressure tap rows) assuming that the variation of the pressure in wall-normal direction remains negligible, i.e.  $\partial p / \partial y \approx 0$ . The wall pressure in step conditions could not be measured during the experiments since the available pressure taps were located outside the step region (figure 3.6).

The freestream velocity ( $U_\infty$ ) is measured with a pitot-static tube located at the centerline of the model and approximately 10 cm upstream of the LE, i.e. at the entrance of the test section. The dynamic pressure read from the pitot-static tube is used to normalize the pressure coefficient,  $C_p$ .

### 3.1.5. FFS height adjustment

The model used for these experiments exhibits a rectangular cavity at  $380 \leq x \leq 808$  mm and  $-104 \leq z \leq 104$  mm (see figure 3.6). In this experiment, an insert is placed in this gap to create FFS and BFS at  $x = 380$  mm. The working principle of the mechanism is simplified in figure 3.7 (c) while in figures 3.7 (a) and (b) the final manufactured mechanism is presented together with the corresponding 3D CAD design.

The mechanism works as follows: two aluminum plates at the front and back of the insert (plate A and B in figure 3.7 (b) respectively) support the pulling micrometer and the pivoting adjusting screw, respectively. A floating aluminum plate (plate C) is subjected by two springs fixed on plates A and B. These springs hold the plate and at the same time ensure an equilibrium of forces with the pulling force of the micrometer and adjusting screws. Plate C is designed with a spherical cavity at the back which allows rotation compared to the pivoting adjusting screw. This screw can also adjust the height of the pivoting point such that the upstream and downstream edges of the insert can be set at the same  $y$ -level. Due to the large streamwise dimension of the insert, when the micrometer pushes the plate, small inclination angles are achieved for the desired step heights, e.g.  $\alpha \approx 0.25^\circ$  for the highest step of the test matrix. This ensures negligible pressure gradients across the inclined plate, i.e. the flow still behaves as a ZPG flow downstream of the step location.

The step heights were characterized using a Micro-Epsilon 2950-25 laser profilometer (resolution of  $2 \mu\text{m}$ ) which was traversed along the span ( $-80 \leq z \leq 80$  mm) to evaluate the spanwise uniformity. The resulting step height is computed using an in-house Matlab code that calculates the average  $y$ -discontinuity measured along the laser profiles. Results in section 4.1 will show the uniformity of the step height in spanwise direction as obtained from the laser profilometer.

## 3.2. Pulsed and continuous acoustic excitation of TS waves

This section introduces the pulsed acoustic forcing strategy, inspired by the method developed by Saric et al. (1995); White et al. (2000a), and used in the present work to decouple the Stokes wave amplitude from the TS wave one (refer to section 1.4 in this work). Later, the instrumentation and methodology used to force acoustic waves are presented.

### 3.2.1. Working principle of the pulsed acoustic forcing

The literature presented in section 1.4 explains that the appearance of a Stokes wave within the boundary layer is an immediate consequence of forcing TS instabilities using acoustic waves. White et al. (2000b) suggested

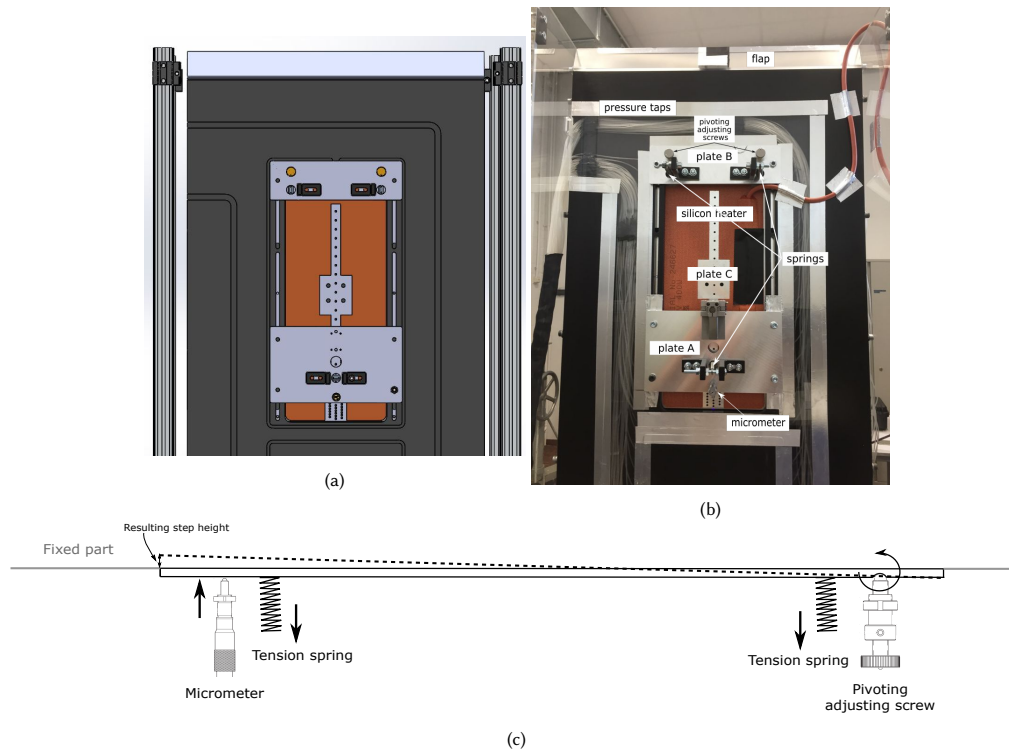


Figure 3.7: FFS mechanism: (a) CAD model, (b) real model and (c) sketch of the working principle.

the use of intermittent acoustic pulses (denoted as *pulsed acoustic forcing* in this work) to decouple the Stokes and TS waves during HWA measurements. In this work, the pulsed acoustic forcing is instead used during the PIV measurements.

The working principle of the pulsed acoustic forcing using PIV is illustrated in figure 3.8. The direction of propagation of acoustic and instability waves is indicated based on the location of the speaker with respect to the LE. When the upstream traveling acoustic waves (red lines in figure 3.8) reach the TE, the first Stokes waves start to be generated at the streamwise locations influenced by the acoustic front. Finally, acoustic waves will reach the LE, where TS waves will be generated through receptivity and convected downstream (green line), in the opposite direction to the (rapidly) traveling acoustic waves. After the final acoustic front of the pulse, there will be a time region where no acoustic waves will be propagating on top of the model (assuming there are no reflections) and therefore no Stokes wave will be present. This is the time region where one would be interested in measuring since only TS waves will be present.

In the example shown in figure 3.8 the signal duration is 200 ms and the pulse duration 100 ms. Using PIV, one would set the double-frame trigger at  $t \approx 131.2$  ms such that only TS waves are measured within the FoV. Since the pulse duration is larger (100 ms) compared to the laser pulse separation ( $9 \mu\text{s}$ ), one can ensure that TS waves will be present in both frames during the measurement. It is also convenient to force a long acoustic pulse to ensure proper characteristics of the forced TS waves at the center of the pulse signal<sup>2</sup>. According to the pulse configuration presented herein, a PIV frequency of  $f_s \approx 1/0.2 \approx 5$  Hz would be required. However, this frequency is three times lower than the maximum frequency rate of a 2C-2DPIV system ( $f_s = 15$  Hz), i.e. the measurements become three times slower than when using continuous acoustic forcing.

Similar to PIV, HWA measurements would also become slower. However, HWA will in addition require much more memory than in continuous forcing mode and an additional post-processing phase. From figure 3.8<sup>3</sup> it can be noticed that the available time to measure only TS waves is  $t \approx 50$  ms out of the 200 ms signal duration, i.e. decoupled TS wave measurements account for just 25% of the measurement time. Hence, if 3 seconds are necessary to ensure statistical convergence of the HWA signal, the total measurement time in pulsing mode should be approximately 4 times larger, so 12 seconds. This not only means that the mea-

<sup>2</sup>Due to the impossibility of the speaker to reproduce a step response, noise is produced at the edges of the speaker's output pulse. Here noise is understood as the excitation of multiple frequencies with similar energy levels, i.e. white noise.

<sup>3</sup>These values are computed assuming that the acoustic wave propagates at  $U_{ac} = 340$  m/s and the TS wave at  $U_{TS} \approx 0.36U_\infty \approx 7.5$  m/s.

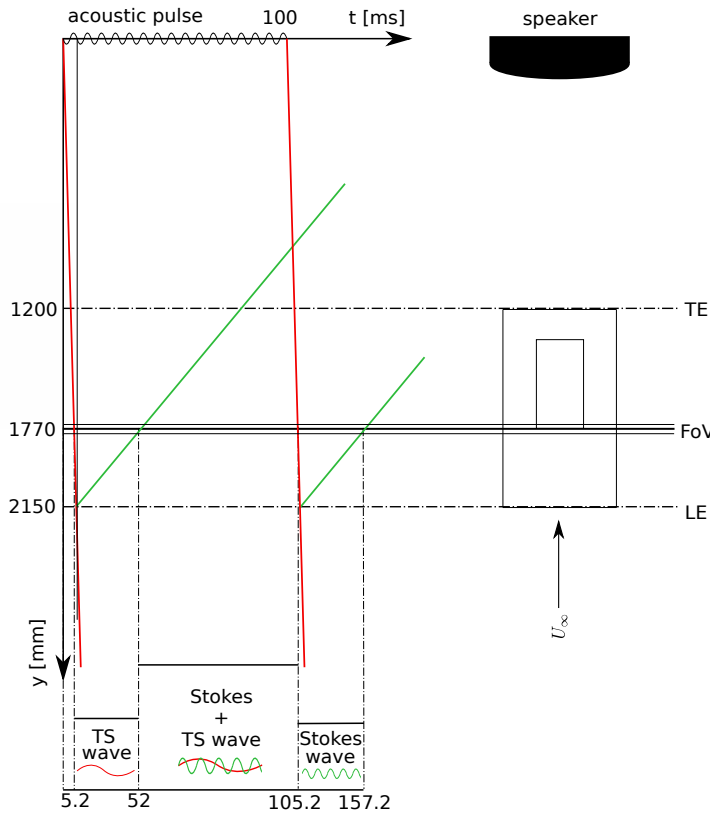


Figure 3.8: Schematic of the working principle of the *pulsing technique*. The right figure illustrates the position of the speaker w.r.t the A-tunnel cross-section. The left figure is a space-time diagram illustrating the propagation of the acoustic and TS waves during the pulse duration. Below the diagram, the time intervals where one would find an individual or combined Stokes and TS waves within the RoI are indicated.

measurements will take 4 times longer but that the memory requirements will also become 4 times larger. Adding up the measurement time required for one point to all the profiles needed, using the pulsed acoustic forcing with HWA becomes very expensive and time-consuming. This was also noticed by Saric and White (1998). Finally, an additional post-processing phase is needed to separate the TS wave signal from the rest. This hinders the analysis of results on-the-fly in the wind tunnel and makes it difficult to detect possible anomalies in the measurements.

Given the reasoning presented above, in this work, the pulsed acoustic forcing is tested using PIV. During HWA measurements continuous acoustic forcing is used, prioritizing the number of cases performed to understand the nature of the problem rather than acquiring a smaller set of cases without the Stokes wave (if present). Later in section 4.5, it will be determined from PIV measurements to which extent the Stokes wave affects the TS waves amplitude measured with HWA (if it does affect).

### 3.2.2. Acoustic set-up

Acoustic waves are generated using a 140W subwoofer with a frequency response of 60-19000 Hz. The speaker is placed on the wind tunnel collector (2.15 m downstream of the model's LE) with the driver placed parallel to the test section such that the acoustic wavefront reaching the LE hits every  $z$ -location as uniformly as possible.

Proper characterization of the wavefront was not performed on the assumption of a planar wave reaching the LE. If the speaker is represented as a point source, the resulting phase delay between the wavefront reaching the midspan of the LE model and one reaching the edge of it (the LE spans 0.5 m) is  $\approx 0.24^\circ$  (assuming a wave frequency of 450 Hz and the speed of sound to be 340 m/s). Another possible phenomenon taking place is the diffraction of the acoustic wave when meeting the test section walls. Due to the small thickness of the test section walls compared to the wavelength of acoustic waves,  $\lambda/t \leq 0.005$ , the wavefront will bend around these, distorting the wavefront immediately near the walls. This can increase the phase delay experienced by the wavefront reaching the edges of the LE compared to the wavefront region reaching the midspan of the model. In addition, the way the acoustic wave convects through the test section could also

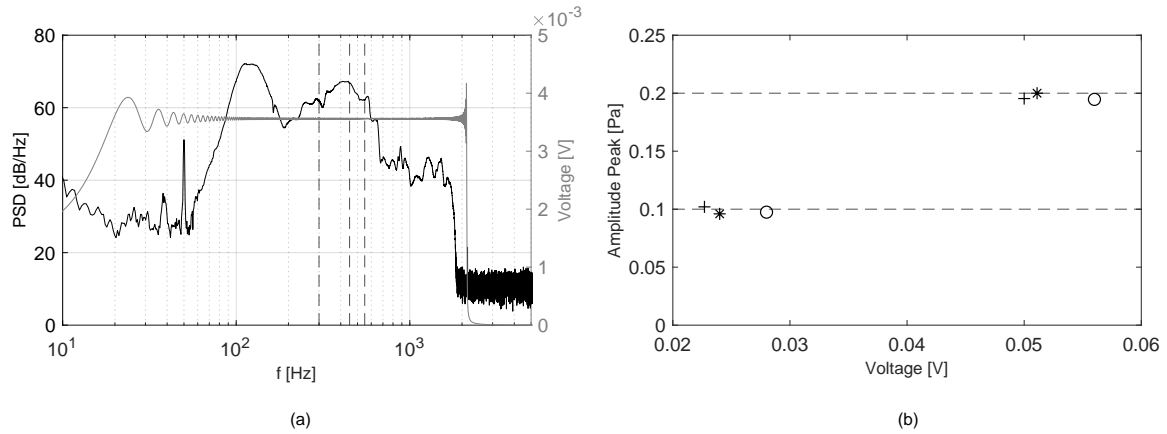


Figure 3.9: (a) Frequency response of speaker (black plot), ideal frequency response (gray plot) and frequencies of interest (dash-lines). (b) Correlation of input voltage to acoustic amplitude measured by the microphone at the LE for frequencies 550 Hz (\*), 450 Hz (+) and 300 Hz (o).

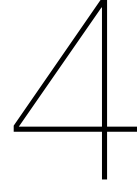
modify the uniformity of the incident wave front. All this phenomena could contribute to the receptivity to oblique waves in the LE region due to a non-planar acoustic wavefront hitting the LE. Therefore, in future experiments careful characterization of the acoustic wave reaching the LE is necessary if the point source is set far from the triggering point, i.e. LE.

The acoustic wave amplitude reaching the model's LE was characterized using a single flush-mounted GRAS 46AE free-field microphone. Based on the successful performance reported in several works (Li et al., 2017; Mayer et al., 2019), the microphone side facing the flow was covered with Kevlar fabric to achieve impermeability to hydrodynamic pressure fluctuations. Microphone readings were performed simultaneously with HW readings with a total measuring time of 3 sec to achieve statistical convergence. The resulting microphone measurements represent a reference point from which to reconstruct the wavefronts reaching the HW probe. During PIV, microphone readings were also taken to measure the acoustic amplitude.

An in-house LabView program was created to generate a sinusoidal acoustic pulse given the pulse amplitude, frequency, width, and phase shift. In addition, the PIV trigger signal is created given a pulse delay (w.r.t to the start of the acoustic pulse) and the PIV frequency which in this case was set to equal the acoustic pulse frequency. Random PIV measurements were achieved by phase-shifting the acoustic pulse by 5 degrees in each PIV acquisition. Hence, the resulting frames were not explicitly random but *high-resolution phase-locked* to reconstruct a large portion of the wave.

The frequency of the acoustic wave is not expected to change from the input to the output signal since it is uniquely determined by the speaker driver. By contrast, temperature changes will affect the speed of sound and wave attenuation. However, a report from Harris (1966) shows that the changes in the attenuation coefficient due to temperature drifts when the humidity is high ( $\geq 50\%$ , similar to this experiment) and the acoustic frequency is lower than 2000 Hz are minimum.

Figure 3.9 (a) shows the speaker frequency response obtained when a sinusoidal sweep signal is input. This test was performed inside the wind tunnel test section (anechoic chamber) to reduce the effect of reflections on the frequency response. Conversely to the spectral plateau obtained when the sweep signal is Fourier transformed, the speaker presents a modulated amplitude response in the frequency range 60-19000 Hz, as specified by the manufacturer. Figure 3.9 (b) represents the different voltage levels required for each frequency to obtain similar acoustic amplitudes at the LE. As also observed from figure 3.9 (a), the voltage requirements for frequencies 300 Hz and 550 Hz are higher than for 450 Hz if the same acoustic amplitude is desired at all frequencies.



## Baseline Results: Clean Case

This chapter presents the main results obtained during clean case conditions, i.e. no step. The following results aim to determine the spanwise uniformity of the model, the flow quality, and the noise levels in the test section. In addition, the stability characteristics of the model in clean case conditions are compared with OS and DNS results to verify agreement with numerical data. Finally, the receptivity of the LE under unforced conditions is characterized and the performance of the acoustic forcing is discussed, together with the existence of a possible Stokes wave in the set-up.

### 4.1. Spanwise flow uniformity

In this section the spanwise uniformity of the model and the step is assessed from the pressure readings at the wall, the step heights read with the laser scanner, and the PIV fields. Excellent agreement is observed in figure 4.1 (a) between the pressure readings from the two rows of pressure taps at 120 mm from the midspan (outside the insert region). In addition, the pressure readings from taps distributed along the span (see figure 4.1 (b)) show small changes in the velocity along  $z$ . For instance, at  $x = 360$  mm the pressure taps at  $z = -120$  will present approximately an external velocity 0.4% larger than the one read at the centerline. Based on these results, a two-dimensional flow assumption along the flat plate model span is valid within the measurement region with HWA and PIV.

Figure 4.2 (a) shows a series of surface profiles measured by the laser scanner at different  $z$ -stations along the step insert. Although special care was taken to avoid irregularities at the junction between the aluminum flat-plate and the acrylic insert, a small gap just before the step with dimensions  $\Delta x_{\text{gap}} = 0.26 \mu\text{m}$  was measured (figure 4.2 (a)). PIV measurements reveal that the maximum wall-normal velocity measured within the cavity is  $V_{\text{slot}}/U_{\text{ref}} \approx -1.4$  (figure 4.3 (c)).

The step height is computed using a MATLAB code developed by the Aerodynamics Section in TU Delft to extract the step height from the laser scanner profiles. First, a linear fit to the laser scanner measurements upstream and downstream of the step is performed. Secondly, both data fits are rotated to remove the inclination of the laser scanner sensor from the measurements. Finally, the wall-normal distance between the upstream and downstream linear fits is computed to extract the step height as

$$\Delta h = \bar{y}(x \geq 0) - \bar{y}(x \leq 0), \quad (4.1)$$

where  $\bar{y}$  denotes the points from the linear fit once rotated accordingly. The spanwise change of  $\Delta h$  in the clean case is shown in figure 4.2 (b). Similar spanwise modulation is observed in the presence of an FFS. A larger variance of  $\Delta h$  is observed for  $z \leq 0$  (left from the model midspan). This could eventually have an effect on the transition front modulation in spanwise direction. Finally, the average height measured is  $\bar{h} = -8 \mu\text{m}$  and the standard deviation is  $\sigma = 7.7 \mu\text{m}$  when the step height measured at the centerline is  $h = 0 \mu\text{m}$ .

Figure 4.3 (a) shows the displacement thickness from  $xy$  planes captured with PIV at  $z = (-40, 0, 40)$  mm. The maximum  $\delta^*$  difference between planes is  $\pm 2.1\%$  of  $\delta^*$  at the midspan. This difference is not due to the small variations in the external velocity at different  $z$ -locations (as shown in figure 4.1 (b)). If this was the case, the expected differences would be on the order of  $\pm 0.1\%$ . Instead, they could be related to the different suction rates observed from figure 4.3 (c) at different  $z$ -coordinates. Larger suction levels at  $z = 40$  mm could explain the larger deviation between  $\delta^*$  measured at this  $z$ -location with respect to the reference

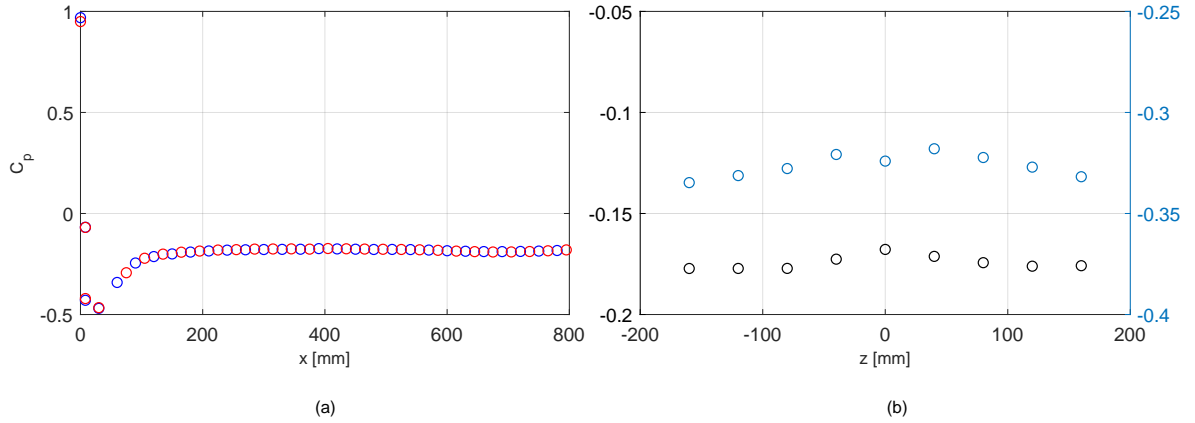


Figure 4.1: (a) Chordwise pressure coefficient distribution  $C_p$  from pressure taps at  $z = 120$  mm (red) and  $z = -120$  mm (blue). (b) Spanwise pressure coefficient distribution from taps at  $x = 60$  mm (blue) and  $x = 360$  mm (black).

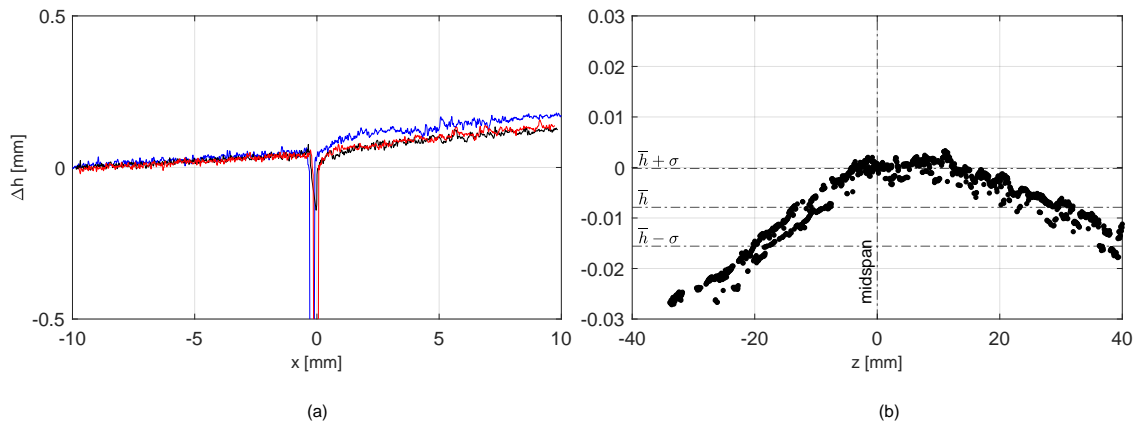


Figure 4.2: (a) Surface profiles in  $xy$  as read from laser scanner at  $z = -40$  mm (blue),  $z = 0$  mm (black) and  $z = 40$  mm (red) in no-step case. (b) Spanwise variation of the step height in no-step case.

Blasius  $\delta^*$ , as observed in figure 4.3 (a). Finally, figure 4.3 (b) shows negligible differences in the streamwise velocity component along the span. Similar conclusions can be drawn when acoustic forcing is applied at the amplitudes of interest.

## 4.2. Freestream turbulence and background noise

The turbulence levels present in a wind tunnel determine the transition scenario of the experiments. It is therefore important to verify that the testing environment features low levels of turbulence (approx.  $Tu \leq 0.18\%$ ) before any experiment to establish whether the flow will experience a *natural* transition path, which is usually the one taking place in flight conditions. The turbulence intensity,  $Tu$ , was determined by measuring the streamwise velocity fluctuations taking place at 10 cm from the model surface with a single hot-wire probe.  $Tu$  was computed as

$$Tu = \frac{1}{U_\infty} \sqrt{\int_5^{20k} PSD_{u'}(f) df}, \quad (4.2)$$

which overall resulted in  $Tu \leq 0.06\%$  at the test conditions of the experiments and with the model inside the test section. For this value of  $Tu$ , Mack's relation ( $N_T = -8.43 - 2.4 \ln(Tu)$ ) gives a transition N-factor of  $N_T = 9.37$ .

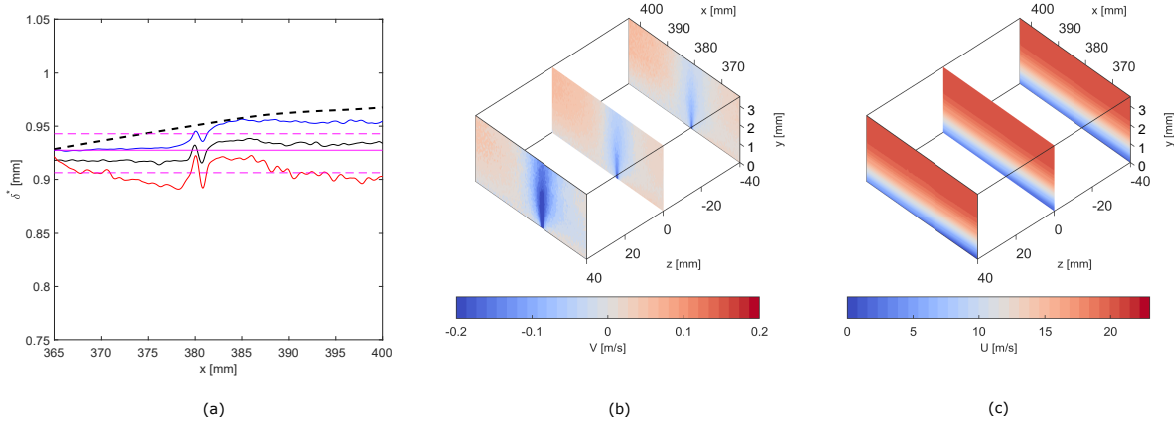


Figure 4.3: (a) Displacement thickness ( $\delta^*$ ) measured with PIV at different spanwise locations,  $z = -40$  mm (blue),  $z = 0$  mm (black) and  $z = 40$  mm (red) in no-step conditions. Black-dashed line (---) is  $\delta^*$  as predicted from the BL solver at PIV conditions. Magenta lines indicate  $\delta^*$  at the centerline and the deviation from this value at  $z = \pm 40$  mm. XY contour planes of the streamwise (b) and wall-normal (c) meanflow velocity components measured by PIV at different spanwise locations.

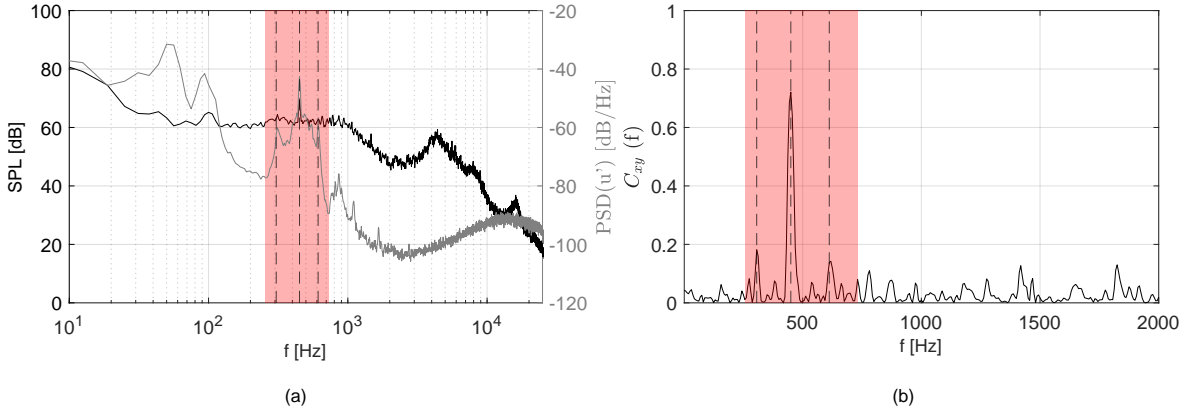


Figure 4.4: (a) Frequency spectrum of pressure fluctuations read by microphone in SPL (black plot) and velocity fluctuations of the HWA at  $y = 0.5$  mm away from the wall (gray plot). (b) Coherence between pressure and velocity fluctuations. Red patch denotes the frequency band of amplified TS waves in clean case conditions.

Figure 4.4 (a) shows the Power Spectral Density (PSD) results of the velocity fluctuations measured using a HWA probe placed inside the boundary layer ( $y = 0.5$  mm) and the SPL spectra of the pressure fluctuations read by a microphone near the LE (using acoustic forcing at  $f = 450$  Hz). The relation between these two signals is relevant to identifying which acoustic contributions are exciting instabilities within the boundary layer. To quantify the relationship between these two signals the magnitude-squared coherence is computed

$$C_{xy}(f) = \frac{|G_{xy}(f)|^2}{G_{xx}(f)G_{yy}(f)}, \quad (4.3)$$

where  $G_{xy}$  is the cross-spectral density and  $G_{xx}$  is the auto-spectral density, defined as the Fourier transform of the cross-correlation and auto-correlation, respectively, i.e.

$$G_{xy} = \int_{-\infty}^{\infty} R_{xy}(\tau) e^{-i2\pi f\tau} d\tau, \quad (4.4)$$

where  $R_{xy}$  is the cross-correlation of  $u'$  and  $p'$ :

$$R_{xy}(\tau) = \int_{-\infty}^{\infty} u'(t)p'(t + \tau) dt. \quad (4.5)$$

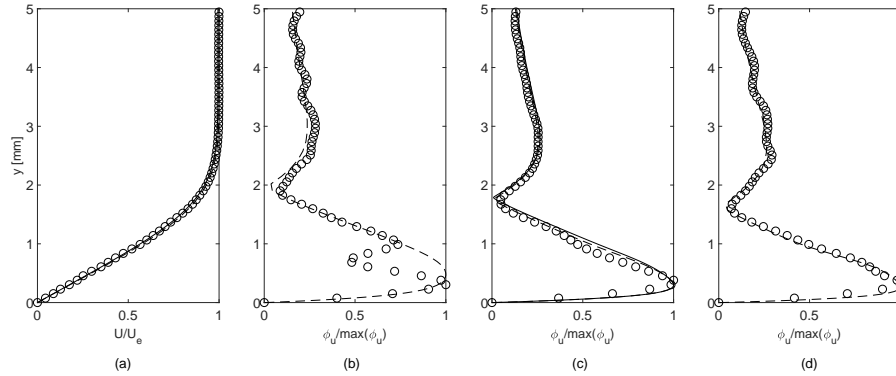


Figure 4.5: Flow diagnostics without step at  $x = 0.38$  m as computed with DNS (—), BL solver + OS (- -) and measured with HWA (o). (a) BL velocity profile. TS wave shape at forcing frequency  $f = 300$  Hz (a),  $f = 450$  Hz (b) and  $f = 550$  Hz (c).

The coherence between these two signals is shown in figure 4.4 (b). The frequency band where disturbances get amplified within the boundary layer (as predicted from LST) is represented with a red patch. It can be observed that three main frequencies present a high correlation (indicated with dashed lines). First, a large correlation peak is observed at 306 Hz, exciting TS waves within the boundary layer. This peak was also observed in Merino-Martínez et al. (2020) from their microphone array measurements, placed outside the test section, which indicated that the source was coming from the upper floor. The second and largest peak corresponds to the frequency at which the acoustic tone is being forced. Finally, a third peak is observed at 612 Hz whose source could not be identified from Merino-Martínez et al. (2020) work or during these experiments.

Changes on the SPL spectrum in the presence and absence of a step remain negligible, as expected. Similar observations apply for the background noise levels when the cooling system of the PIV laser and camera are on, thus having almost no effect on the forcing of TS waves. In addition, the SNR measured for the minimum acoustic amplitude forcing used ( $A_{ac} = 0.1$  Pa) is  $SNR \geq 10$ , which is an acceptable level to properly track the acoustic forcing amplitude.

### 4.3. Boundary layer stability

Stability results in clean case conditions are important to establish that a reference Blasius boundary layer develops along the measurement region. To validate this, the experimental measurement is compared with reference solutions obtained using an in-house boundary-layer solver and the DNS results from DLR. In chapter 2 it was shown in figure 2.4 that integral parameters and N-factor results from DNS and BL-OS solver showed very good agreement with experimental data, verifying Blasius flow in clean case conditions during the experiments.

Figure 4.5 (b), (c) and (d) present the no-step TS shape profiles measured with HWA when acoustic forcing at  $f = 300$  Hz,  $f = 450$  Hz and  $f = 550$  Hz is applied. A very good agreement is observed between experimental and numerical results at  $f = 450$  Hz and  $f = 550$  Hz frequencies. In contrast, HWA results at  $f = 300$  Hz show a double-peak modulation while DNS and OS predict a one-peak structure. One can find the explanation for this double-peak modulation by looking at figure 4.6 (a), where an uncontrolled forcing excites the TS wave frequency at  $f \approx 310$  Hz when no acoustic forcing is applied. A high coherence value was also predicted at this frequency (see figure 4.4 (b)). This points out to an overlapping TS wave at  $f \approx 310$  Hz forced by an unintentional acoustic wave present already in the test section. As already mentioned, Merino-Martínez et al. (2020) found this source coming from the upper floor of the wind tunnel. As a result of this unforeseen excitation, when the acoustic forcing is set at  $f = 300$  Hz, both the forced and unintended TS waves interfere due to their similar energy levels, creating this unusual peak modulation when  $f \approx 300$  Hz is reconstructed from FFT. This undesired interference corrupts the comparison between DNS and experiments and also makes it difficult to accurately predict the wave amplification along  $x$ . Nevertheless, it is still interesting to analyze the amplification behavior of this low-frequency TS wave across an FFS which is why the results at  $f = 300$  Hz are also presented in this work.

Finally, the stability bounds predicted from OS are compared in figure 4.6 with the range of unstable TS waves being naturally forced in the present experimental set-up. It is observed that the instability frequency

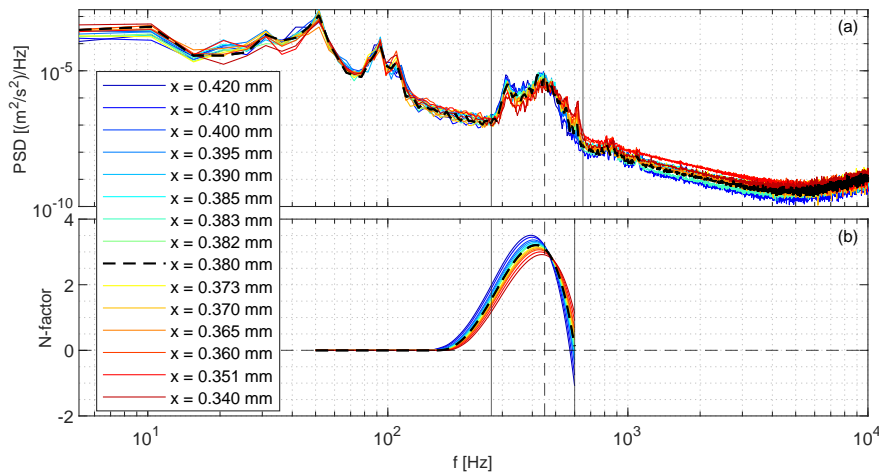


Figure 4.6: (a) PSD of HWA velocity fluctuations measured at the TS wave maximum. (b) N-factor spectrum from OS solver. Note how OS instability bounds agree with experimental results.

band captured from HWA ( $260 \leq f \leq 600$  Hz) matches the instability bounds predicted from OS, as expected. It remains unclear which background source could be exciting multiple frequencies in the test section such that an entire band of TS waves is forced. From the microphone spectra, it is observed that the noise levels in the test section are very low. Thus being receptivity to wind tunnel background noise unlikely. Moreover, the A-tunnel has very low turbulence levels. Another possibility could be the presence of high roughness at the LE or the existence of shedding at the TE. The latter would cause the stagnation point to move according to the shedding frequency, changing the receptivity characteristics of the model.

#### 4.4. Laminar-to-turbulent transition

Figure 4.7 (b) shows a DIT image in clean conditions with no acoustic forcing. While one can identify the high Reynolds number transition front within the heating plate, the low Reynolds one lies outside the same, making it impossible to measure the transition location in clean case conditions. In the present work, when clean case transition data is provided, it has been computed using the high Reynolds number and LST: the N-factor at the high Re transition location is taken to obtain the streamwise position at which transition would take place given the N-factor curve at lower Re (see blue lines in figure 4.7 (a)).

From figure 4.7 (b) it can be observed that well-established turbulent wedges dominate the transition scenario far downstream of the measurement region ( $340 \leq x \leq 420$  mm). These wedges are generated by the sidewalls of the test section. If the span of the model was longer, these wedges would not prevail over *natural* (TS waves-dominated) transition and, given the test conditions, transition would not take place along the flat plate model, as predicted by LST and the  $e^N$  model (see figure 4.7 (a)) for the low-turbulence intensity and noise levels inside the test section.

The observed wedges difficult correct identification of the transition front movement driven uniquely by TS waves in the presence of an FFS. The observed limitations are especially significant in the case of small FFS, where wedge-dominated transition still prevails over the influence of the step amplification. Hence, to properly quantify the effect of FFS on transition, appropriate identification criteria are required to establish whether the location of the transition front read by the IR camera can be attributed to TS- or wedges-dominated transition. This will be further discussed in section 5.1.

#### 4.5. Forced and unforced disturbances

As already discussed in the previous sections, this work uses acoustic waves to force single-frequency TS waves. Two types of acoustic forcing are tested: a continuous and a pulsed signal. The last strategy aims to decouple the contribution that a possible Stokes wave could have on the TS wave amplitude measurements. To investigate whether a Stokes wave is present or has a noticeable effect in this set-up, three cases are analyzed in this section (all in clean case conditions, i.e.  $h = 0$ ): (1) no acoustic forcing, (2) pulsed, and (3) continuous forcing at equivalent acoustic amplitudes.

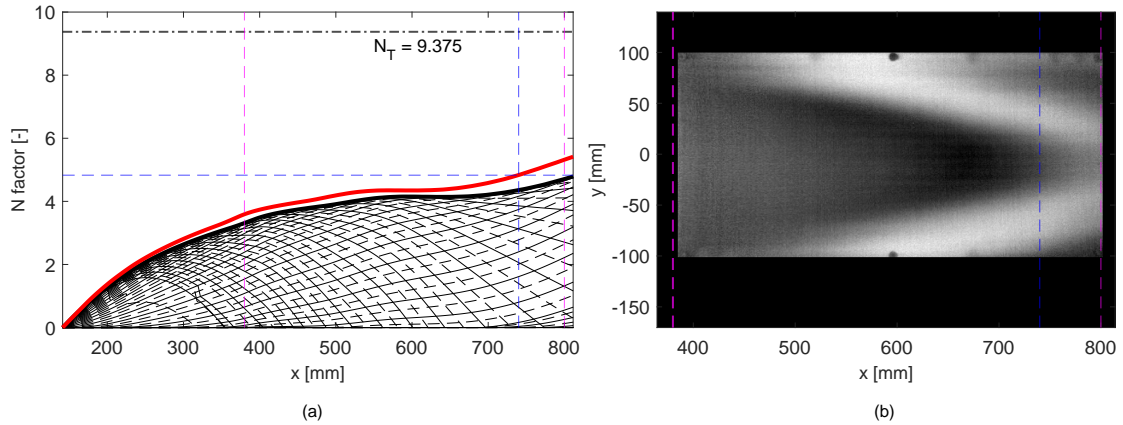


Figure 4.7: (a) N-factor envelope from OS solver at the test conditions specified in table 2.1 (low-Reynolds, thick black line) and at high Reynolds number (thick red line) for which the transition front is observed in (b).  $N_T$  denotes the N-factor where laminar-to-turbulent transition is expected to happen based on the freestream turbulence,  $Tu \leq 0.06$ . (b) DIT image in no-step and no-forcing conditions at low-Reynolds,  $Re = 1.32 \times 10^6$  and high-Reynolds number,  $Re = 1.45 \times 10^6$ . Dashed magenta lines in (a) and (b) indicate the IR FoV. Blue lines indicate the transition location and corresponding N-factor at high Re conditions.

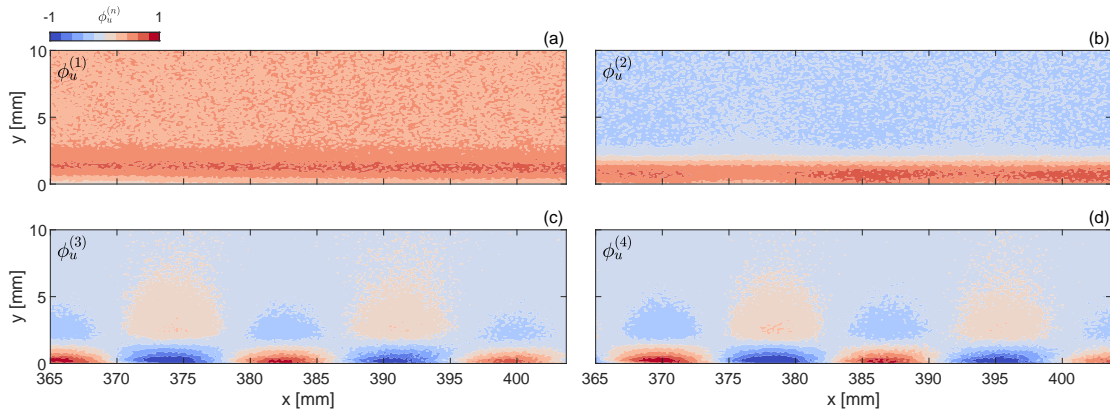


Figure 4.8: Normalized POD modes from  $u$ -component under pulsed acoustic forcing conditions.

Snapshot POD is used to identify the topological differences of the most energetic modes. Using POD it is possible to decouple the TS waves from the rest of background disturbances, including the Stokes wave which, given their higher phase velocity and thus longer wavelengths, can be topologically separated from the TS waves.

Figure 4.8 shows the four most energetic POD modes when using a pulsed acoustic forcing strategy. Equivalent modes are observed in continuous acoustic mode. In the absence of acoustic forcing, mode  $\phi_u^{(1)}$  and  $\phi_u^{(2)}$  are the only ones with relevant energy levels, see black bars in figure 4.9 (a). Therefore, these modes must be linked to other phenomena intrinsic to the wind tunnel background, e.g. a standing wave.

Figure 4.9 (a) shows the energy fraction of the first 10 modes obtained under pulsed (blue), continuous (red) and no forcing (black). Both continuous and pulsed cases show an energy increase in modes 1 and 2. As expected, two new modes emerge with high energy contribution, corresponding to a convective instability with a characteristic wavelength (see figure 4.8 (c) and (d)) proportional to the forced frequency: the forced TS waves.

Multiplication of each POD mode by its corresponding temporal coefficients allows to reconstruct the flow-field of individual modes. In this work, for each reconstructed mode, the root mean square of its  $u$  component in time is computed and the resulting RMS field is averaged in streamwise direction. Figure 4.9 (b)-(e) presents the wall-normal profiles of  $RMS(u)$  for each POD reconstructed field. Figure 4.9 (d) shows the results from

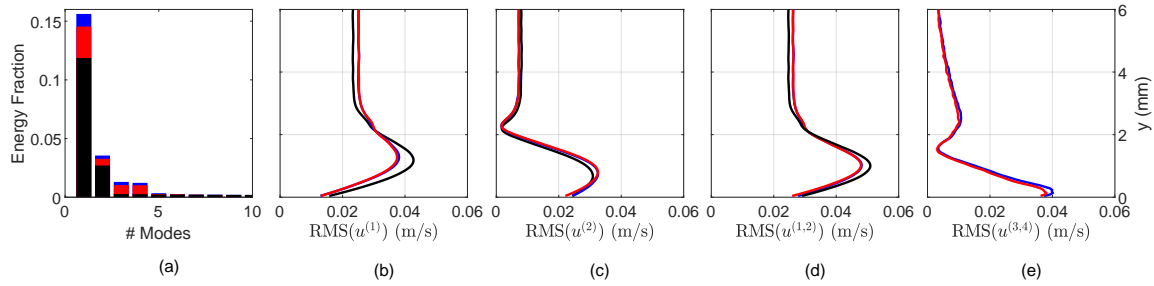


Figure 4.9: (a) Energy fraction per mode from POD cases. (b) Root mean square of reconstructed flowfield of  $u$ -component from POD modes (b) 1, (c) 2, (d) {1, 2} and (e) {3, 4}. No acoustic forcing case (black), pulsed forcing (blue) and continuous forcing (red).

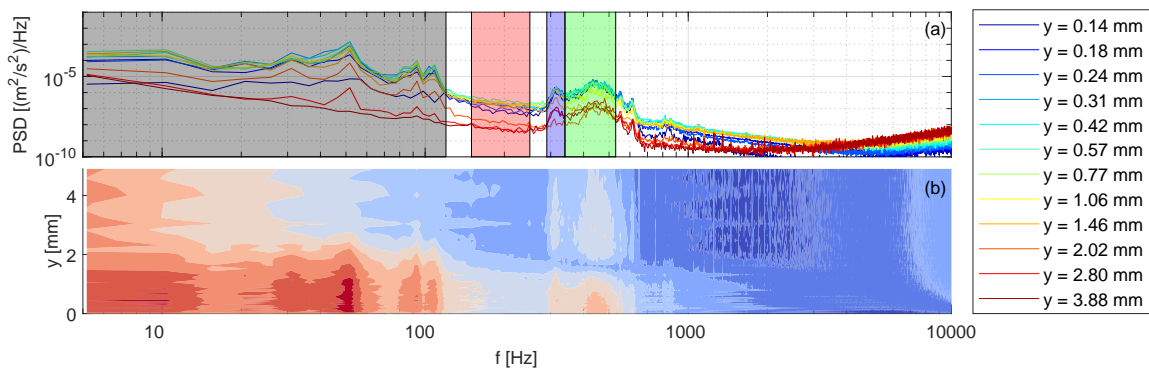


Figure 4.10: (a) PSD from HWA signal in no-step and no-forcing conditions at  $x = 420$  mm at different  $y$  stations. Colored areas indicate the frequency bands where the signal was bandpass to retrieve the disturbance profiles in figure 4.11. (b) Contours of PSD at same conditions and streamwise location as (a).

reconstructing the flowfield with modes 1 and 2. Both modes are identified as background disturbances due to their long wavelengths and their non-zero velocity components in the freestream, which clearly distinguishes them from TS waves.

From figure 4.9 it becomes evident that there are no noticeable differences between using continuous and pulsed acoustic forcing. If there was a strong Stokes wave dominating the continuous forcing scenario, one would expect large differences in the RMS levels between continuous and pulsed/non-forced cases. Instead, all three cases show similar RMS levels for the two dominant POD reconstructed disturbances ( $u^{1,2}$  and  $u^{3,4}$ ). Hence, it could be argued that if there is a Stokes wave in this set-up, its effect is so mild that it is probably overshadowed by the large background disturbances present in the facility. In the remaining of this section, the origin of the background disturbances observed from POD is investigated making use of the PSD results from HWA measurements.

Spectral data from HWA in no-step and no-forcing conditions can help to identify the characteristic frequencies of the observed background disturbances and verify whether the microphone also reads them, i.e. if they are due to external noise sources. Figure 4.10 (a) and (b) show the PSD measured at  $x = 420$  mm along  $y$ . From contours in figure 4.10 (b) one can identify the TS waves due to their characteristic dual-lobe structure. The rest of contours show large energy content close to the wall with no second maximum present, similar to POD modes 1 and 2. Bandpassing the HWA spectral data within these frequency ranges could help to determine whether the wall-normal profiles retrieved from POD resemble the low-frequency content in the HWA spectra.

Figure 4.11 shows the wall-normal profiles obtained when the HWA spectra is bandpass at the frequency bands specified in figure 4.10 (a) by colored patches. Figure 4.11 (a) shows that the boundary layer gradient ( $\partial U/\partial y$ ) presents good agreement with the HWA fluctuations between  $25 \leq f \leq 100$  Hz. Thus, the peaks

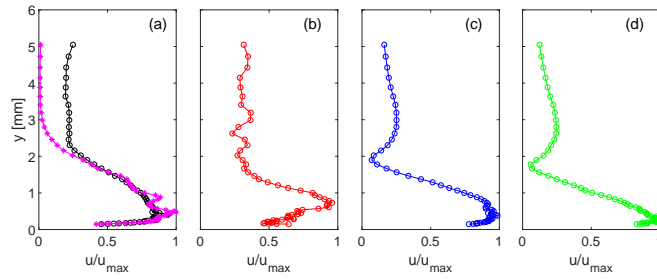


Figure 4.11: Wall-normal profiles of the resulting disturbances from bandpassing the PSD signal at the frequency bands indicated in figure 4.10 (a) with the same color notation used herein for the profiles. In (a) the magenta line represents the mean shear ( $\partial U/\partial y$ ) obtained from derivating the HWA meanflow velocity profile along  $y$ .

registered across that frequency band are oscillations (natural frequency plus harmonics) of the sting holding the HWA probe (Eppink, 2020). On the other hand, figure 4.11 (b) shows the wall-normal profile of the subharmonics. The existence of subharmonic modes in the set-up is further explored in section 5.6. Figure 4.11 (c) and (d) clearly correspond to TS waves, as previously predicted. None of the profiles shown in figure 4.11 presents good correlation with the  $u$ -RMS profiles from POD. Thus, it is unclear the origin of POD modes 1 and 2. However, it can be noticed from figure 4.11 (a) that the value of the bandpass data is different than zero in the freestream, similar to the wall-normal profiles from POD modes 1 and 2 shown in figure 4.9 (d). This indicates that the HWA probe oscillations could be masking other underlying unsteady behavior taking place also at low frequencies (which would be in accordance with the observed long wavelengths of these background modes from POD). This would explain why they become visible in the PIV measurements.

In future experiments using the same model and facility, it is highly recommended to identify the origin of these background disturbances and remove them (if possible) before starting the measurements.

# 5

## Results with Forward-Facing Steps

This chapter presents a detailed analysis of how different step heights affect the growth and topology of the fundamental mode and its harmonics in the vicinity of the step. First, section 5.1 provides an overview of how laminar-turbulent transition is modified with different step heights. In addition, previous experimental results on TS-FFS transition are compared with the present experiments. The meanflow modulation caused by different step heights is analyzed in section 5.2. In section 5.3, section 5.4 and section 5.5 and section 5.6 a comprehensive analysis of the effect of the step height on the growth, distortion, energy production, and spectral content of the perturbation field at a fixed forcing frequency,  $F = 90$ , is presented. Later, section 5.7 briefly discusses the effect of modifying the disturbance frequency on the growth experienced over the step.

2D DNS results are shown in clean ( $h/\delta^* = 0$ ) and subcritical ( $h/\delta^* = 0.775$ ) step conditions. 2D DNS in critical ( $h/\delta^* = 1.462$ ) and supercritical ( $h/\delta^* = 1.950$ ) step conditions could not be performed given the large non-linear effects present in these cases, which give rise to three-dimensional flow in the vicinity of the step. Nevertheless, HWA and PIV results are presented in critical and supercritical step cases. Hence, experimental and numerical comparison is only available in subcritical step conditions. Finally, note that, if otherwise not indicated, the step location is at  $x = 380$  mm in the following plots.

### 5.1. Transition front movement

Previous literature on TS waves dominated transition with FFS report that the transition location moves upstream for higher steps, i.e. increasing the step height has always a destabilizing effect. However, while all previous authors (concerned with experimental works) agree on the latter, their data do not show agreement with respect to *how* the transition moves upstream when the step height is increased. More specifically, while Wang and Gaster (2005) and Perraud et al. (2014) observe a rather abrupt movement of the transition front for critical step heights ( $h/\delta^* \geq 1.5$ ) Costantini (2016) and Crouch and Kosorygin (2020) results point towards a gradual movement of transition with  $h/\delta^*$ .

In the present experiments, seven step heights and a clean configuration have been tested at a fixed Reynolds number under forced and unforced conditions, as indicated in table 2.3 from section 2.1.

Figure 5.1 shows the transition front as retrieved from the IR thermal maps after applying DIT. Note that the flow comes from left to right so that the low Reynolds transition front (marked with green dots) is at the right of the image and the high Re one at the left. For the smallest step case,  $h/\delta^* = 0.475$ , the transition scenario is dominated by two turbulent wedges originating from the intersection of the flat plate model and the side walls of the test section. Thus, this case has been discarded from the analysis since the BL transition is not uniquely attributed to the interaction of TS waves with the step. Step cases at  $h/\delta^* \geq 0.475$  present a more uniform front distribution (note that the front variance diminishes) at the center of the insert, indicating that transition is most likely driven by TS waves in these regions. The transition location for step cases  $h/\delta^* \geq 0.475$  is estimated from the intersection of the linear fit (solid magenta line) with the model centerline,  $y = 0$ , following the procedure of Rius-Vidales and Kotsonis (2021).

Other features observed from figure 5.1 include the tilting of the transition front, with transition taking place upstream at  $y > 0$ . This tilting might come from the misalignment of the test section side walls, affecting the inclination of the wedges, or by different roughness, levels left and right of the LE. This is not triggered by any spanwise non-uniformity of the step geometry since in chapter 4 it was observed from figure 4.2 (b)

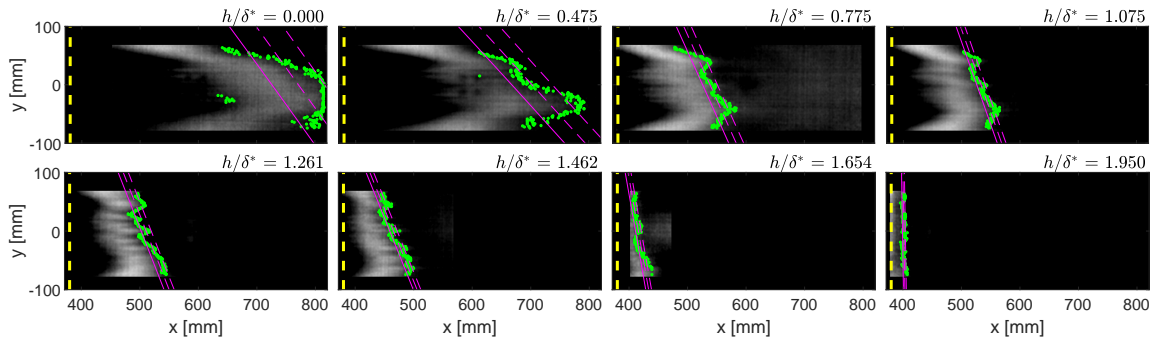


Figure 5.1: Transition front identification using DIT for different step heights with forcing frequency  $F = 90$ . Green dots indicate the transition front, dashed and solid magenta lines illustrate the variance and the linear fit to the front, respectively. Yellow dashed lines indicate the location of the step edge,  $x = 380$  mm. Flow comes from left to right.

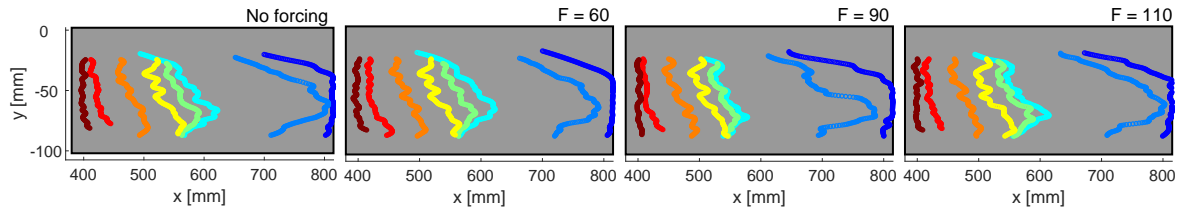


Figure 5.2: Transition front movement along the heating plate for increasing step height at different forcing conditions, as specified in table 2.3. Flow comes from left to right. Increasing color intensity indicates increasing step height, i.e. blue denotes clean case while brown indicates the highest step case ( $h/\delta^* = 1.950$ ).

that an opposite effect on the transition front tilting would be otherwise observed. Moreover, the transition front would not appear parallel to the step edge when it approaches the step location, as observed for  $h/\delta^* \geq 1.654$  in figure 5.1. Finally, from the IR thermal maps, it can be observed that the transition front features a streaky pattern uncommon in TS-dominated transition scenarios. This can be spotted both on the high and low Reynolds transition fronts. However, given the low turbulence levels on the A-tunnel, no streaks are expected to take place since in this type of configuration an H- or K-type transition scenario (Kachanov, 1994) is usually reported. Spectral data from HWA measurements in section 5.6 will provide further details into which type of transition scenario could be taking place after the step to explain the onset of such a streaky pattern in the transition front.

Figure 5.2 shows the transition front movement with different step heights at the three acoustic frequencies tested and in unforced conditions. The results show that transition is mainly driven by the breakdown of instabilities already present in unforced conditions, i.e. band of natural<sup>1</sup> TS waves. This indicates that the acoustic amplitudes used during the experiments were sufficiently small to not alter the natural transition scenario but sufficiently large to identify them when performing an FFT.

Figure 5.3 (a) shows the Reynolds number based on the transition location ( $Re_{x_T}$ ) obtained in the present experiments under forced and unforced conditions. In addition, the experimental data from Wang and Gaster (2005) is included based on the similarities that their set-up (unswept flat plate and similar relative step heights) and freestream conditions (zero pressure gradient and low turbulence intensity) have with the present experiments.

Large differences are observed between the  $Re_{x_T}$  values of Wang and Gaster (2005) and the present work. This was also observed in chapter 4 when it was noticed that the N-factor obtained from OS (in clean case conditions) at the transition location obtained from experiments was lower than predictions from the  $e^N$ -method. There are two plausible reasons for which the transition location in clean case conditions takes place further upstream than expected. First, the turbulent wedges of the test section side-walls (clearly noticeable from the thermal IR maps in figure 5.1) could be interfering with the *natural* transition front, promoting early transition. Secondly, high roughness present at the LE. Finally, receptivity at the LE could be affected by other acoustic sources coming from resonance effects in the open-jet facility, e.g. standing waves (Sec. 16.1.4 in

<sup>1</sup>Natural is used to denote TS waves which have been forced by the receptivity of the LE to background disturbances, e.g. wind tunnel noise combined with minute roughness at the LE.

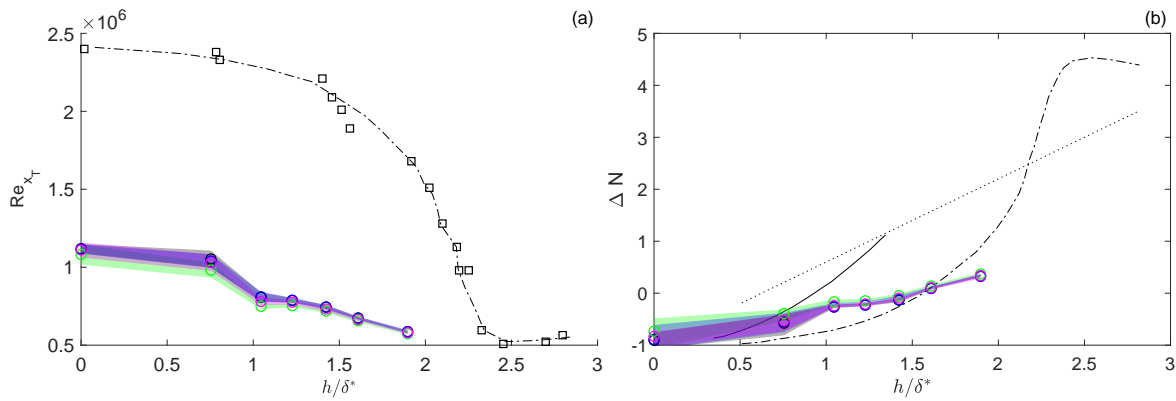


Figure 5.3: (a) Reynolds transition ( $Re_{x_T}$ ) as a function of the relative step height ( $h/\delta^*$ ). Data digitized from Fig.4 in Wang and Gaster (2005) ( $\square$ ) and these experiments ( $\circ$ ). (b) N-factor decrease at transition,  $\Delta N$ , as a function of the relative step height. Data fit digitized from Fig. 7 in Wang and Gaster (2005) (---), Fig. 6.4.2.1 (d) in Costantini (2016) (—),  $\Delta N = 1.6h/\delta^*$  model from Crouch et al. (2006) (.....) and the present experiments ( $\circ$ ). Unforced (black) and forced conditions at  $F = 60$  (blue),  $F = 90$  (green) and  $F = 110$  (magenta). Confidence bands indicate uncertainty on the transition front measurements.

Tropea et al. (2007)), or from a global feedback loop generated by vortex shedding at the TE. This could explain why, under such low levels of turbulence intensity, the range of naturally excited TS waves has a rather high amplitude, as observed from spectral HWA results under unforced conditions (see figure 4.6 in chapter 4).

In FFS-TS transition-related literature,  $\Delta N$  is used to isolate the effect of the step on transition from the freestream conditions, enabling proper comparison between different experimental works. This parameter represents the decrease of the N-factor at transition with respect to the clean case N-factor due to the presence of a roughness element, i.e.  $\Delta N = N_{T_0} - N$ . The clean transition front takes place outside of the heating plate in these experiments (see the location of the silicon heater in figure 3.1). Hence, to compute  $N_{T_0}$ , the clean case transition has been estimated using linear stability theory (LST) based on the transition location at a higher Reynolds number.

Figure 5.3 (b) shows the  $\Delta N$  results from this work compared to the different models and fits for  $\Delta N$  from Wang and Gaster (2005), Crouch et al. (2006) and Costantini (2016). The present results show a nearly linear dependence of  $\Delta N$  with the relative step height ( $h/\delta^*$ ), similar to the model proposed by Crouch et al. (2006) but with a lower slope, i.e. the FFS appears more detrimental for laminar-turbulent transition in Crouch et al. (2006) experiments.

From figure 5.3 (b) it can be observed that neither of the models presented nor this experiment's results present good correlation. For instance, while the model of Crouch et al. (2006) predicts a gradual movement of the transition front with  $h/\delta^*$ , the data fit of Wang and Gaster (2005) depicts an exponential-like increase of  $\Delta N$ , indicating that higher steps quickly advance transition towards the step location compared to smaller steps. Other authors (Costantini, 2016; Edelmann and Rist, 2015) have already noticed the large differences in  $\Delta N$  from different experimental works. Costantini (2016) argued that possible explanations for this could comprise the different measurement techniques used to identify transition location or the effect of the step location on the increase in  $\Delta N$ . Moreover, an additional source of discrepancy between the experimental data could be related to the different types of mechanisms governing transition in the clean case from each experimental set-up, which could be also modifying the onset of transition in the presence of steps. In this sense, the most optimal experimental set-up to study the influence of FFS on transition driven *uniquely* by TS waves under zero pressure gradient is the one of Wang and Gaster (2005). The rest of experimental works also include the effect of the pressure gradient (Crouch et al., 2006), the Mach number (Costantini, 2016; Perraud et al., 2014), the wall-temperature (Costantini, 2016), and the side-wall wedges (present experiments). The latter makes it very difficult to ascertain what is the individual effect of the step on transition since, from the given comparison (figure 5.3 (b)), it becomes unclear whether these effects are effectively being removed from the effect of the step when they are plotted in terms of  $\Delta N$ .

Finally, it is also important to notice that none of the previous literature accounts for the amplitude of the TS wave at the step location. Even though  $N_{T_0}$  would be (presumably) effectively isolating the smooth-surface transition from the effect of the step, one is inherently assuming that the amplitude of the incoming instability will not affect the N-factor increase provoked by the step. If the step was sensitive to the amplitude of the incoming instability, this would explain why the different experimental data do not show good correlation

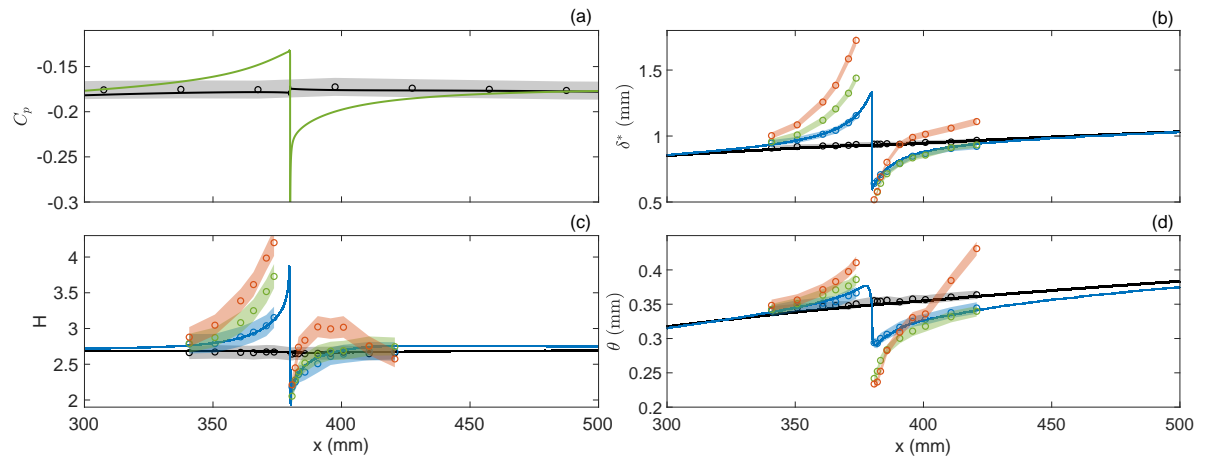


Figure 5.4: (a) Pressure coefficient at the wall, (b) displacement thickness ( $\delta^*$ ), (c) shape factor ( $H$ ) and (d) momentum thickness ( $\theta$ ). Symbols denote experimental data and full lines DNS. Clean (black), subcritical (blue), critical (green) and supercritical (orange) step cases. Confidence bands for experimental data are included. Note that DNS data is only provided in clean and subcritical step cases. Step is at  $x = 380$  mm.

in terms of  $\Delta N$ . Future attempts to compare experimental data on laminar-turbulent transition with TS-FFS should provide information on the amplitude of the TS wave upstream of the step when comparing  $\Delta N$  values.

## 5.2. Meanflow modulation at the step

How the meanflow is modified close to the step can be largely described by the change of the pressure gradient. figure 5.4 (a) shows the pressure coefficient at the wall from DNS results in clean and subcritical step case conditions. The pressure imposed in the DNS at the top boundary condition is set to match the pressure developing at the wall during experiments in no-step conditions. However, since the pressure exhibits a weak variation in wall-normal direction ( $\partial p/\partial y \approx 0$ ), small differences are observed in figure 5.4 (a) when comparing pressure tap measurements (indicated by black circles) and wall pressure from DNS at  $h/\delta^* = 0$ . Wall pressure in step conditions could not be measured during the experiments since the available pressure taps were located outside of the step region (see the set-up sketch in figure 3.1).

Figure 5.4 (b), (c), and (d) show the effect that the pressure gradient build-up by the step has on the integral boundary layer parameters (displacement thickness, shape factor, and momentum thickness, respectively). Furthermore, figure 5.5 shows the change of the velocity profiles at different streamwise locations for different steps. Note that, given the impossibility of measuring with HWA the velocity in the near-wall, the integral boundary layer parameters are computed assuming a linear fit towards the wall in the experimental velocity profiles. While this is valid in the case of zero pressure gradient, in the presence of a step this approximation becomes increasingly inaccurate. Therefore, higher errors are expected between DNS (if available) and HWA measurements with increasing step height. Nevertheless, DNS results in subcritical step conditions show very good agreement with experiments.

From figure 5.4 (a) it can be observed that the boundary layer is subject to a progressively growing adverse pressure gradient as it approaches the step. Regions of low momentum close to the wall are subject to large curvature ( $\partial^2 U/\partial y^2$ ) changes due to the pressure gradient (figure 5.5). This creates an inflection point within the boundary layer which moves away from the wall as the adverse pressure gradient increases (note maxima of  $\partial U/\partial y$  in figure 5.5). The loss of streamwise momentum close to the wall forces the boundary layer to expand in  $y$ , increasing its thickness, as observed from figure 5.4 (b), (c), and (d).

Right at the step edge, an infinitely large favorable pressure gradient takes place followed by a gradual adverse pressure gradient which recovers the no-step pressure levels further downstream (figure 5.4 (a)). A direct consequence of such a strong favorable pressure gradient is that the boundary layer becomes extremely thin at the step edge (see figure 5.4 (b), (c), and (d)). This has large consequences on the velocity profile curvature as observed in figure 5.5. Information about the boundary layer curvature in the near-wall can be directly retrieved from the pressure gradient as (from the  $x$ -momentum equation for a two-dimensional, incompressible flow, neglecting  $\mu \partial^2 U/\partial x^2$  and assuming  $U \gg V$ ):

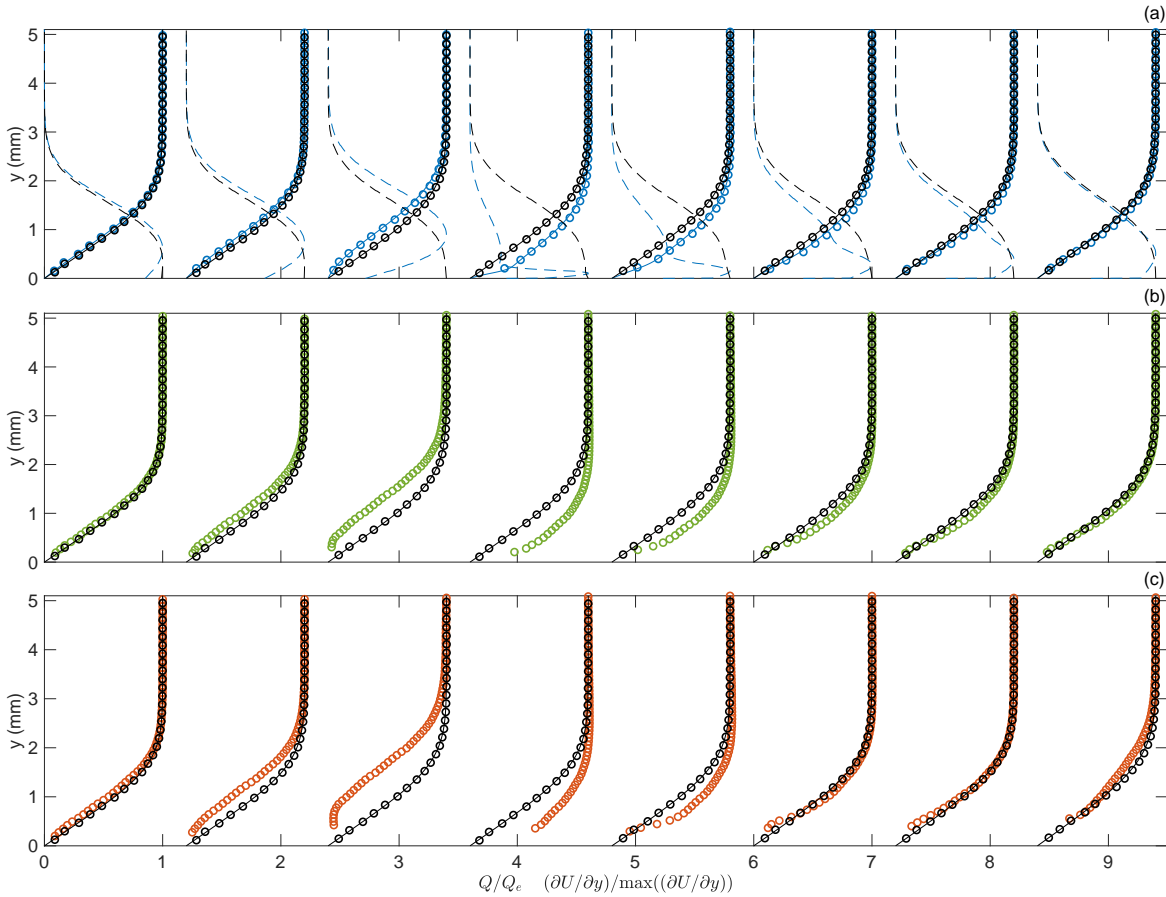


Figure 5.5: Normalized wall-normal velocity profiles of  $Q$  (with  $Q = \sqrt{U^2 + V^2}$ ) (—) and  $\partial U/\partial y$  (---). Lines denote DNS data and symbols (o) HWA results. Subcritical (a), critical (b) and supercritical (c) step cases, represented in colors. Clean case results are included in all step cases and represented in black. The streamwise locations plotted are at (from left to right)  $x = [341, 361, 374, 381, 383, 391, 401, 421]$  mm with the step at  $x = 380$  mm. The horizontal spacing between profiles is set to  $\Delta = 1.2$  for legibility.

$$\mu \frac{\partial^2 U}{\partial y^2} = \rho U \frac{\partial U}{\partial x} + \frac{\partial p}{\partial y}. \quad (5.1)$$

The work of Stratford (1959) provides a very intuitive derivation that revolves around equation (5.1) to explain how the pressure gradient affects different parts of the boundary layer. equation (5.1) shows that the curvature change of the boundary layer is governed by a balance between the pressure gradient (second term on the right-hand side) and its streamwise momentum (first term on the right-hand side). Stratford claims that, close to the wall, the flow has very low momentum and all the burden of an adverse pressure gradient must be balanced by a change of the profile curvature. In practice, this is reflected as a defect or reversal of velocity in the near-wall depending on how large is  $\partial p/\partial y$ . Conversely, in the outer layer, the adverse pressure gradient is mainly balanced by the high momentum in this region, being  $\partial^2 U/\partial y^2 \approx 0$  in this region. The large curvature differences between the outer and inner layers need to merge smoothly somewhere along  $y$ . This explains the onset of an inflection point in flows presenting large pressure gradients.

The idea described by Stratford (1959) results useful to reason the emergence of the two inflection points (note mean shear profiles in figure 5.5 (a) at  $x = 380$  mm) observed in the boundary layer after the step edge. This modular composition of the boundary layer is the result of the curvature change undergone due to the presence of two quasi-simultaneous opposite pressure gradients at the step (figure 5.4 (a)). It would appear that the effect of such a strong and delimited favorable pressure gradient persists after the step imprinted in the boundary layer curvature. Further downstream this is suppressed and the adverse pressure gradient prevails: note the merging of the two peaks in  $\partial U/\partial y$  (i.e. inflection points) from figure 5.5 (a) and the dashed

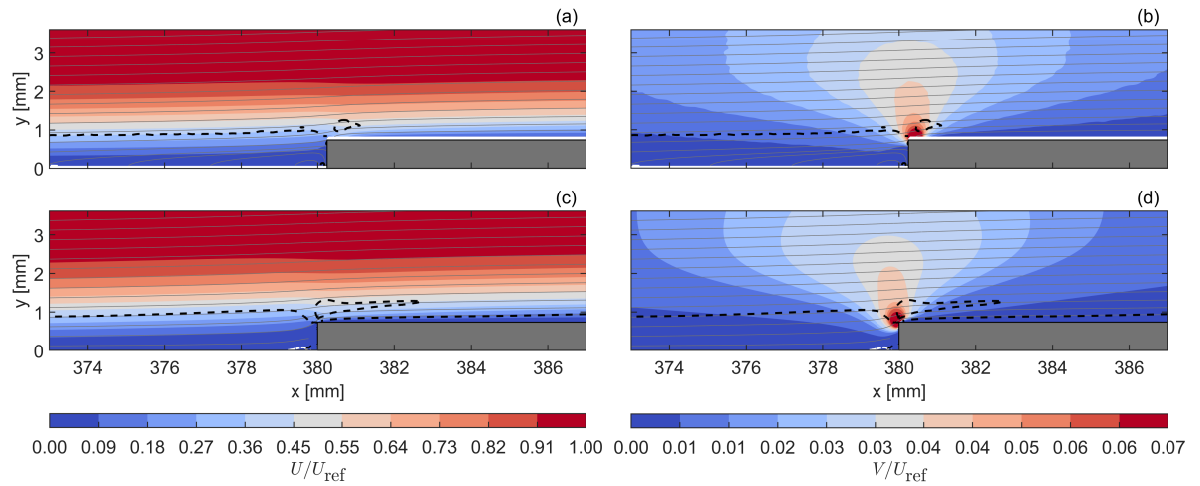


Figure 5.6: Contours of meanflow U ((a) and (c)) and V ((b) and (d)) components from PIV ((a) and (b)) and DNS ((c) and (d)) for  $h/\delta^* = 0.775$ . Streamlines (gray —), recirculating regions (white - - -) and inflection points (- - -) are also indicated.

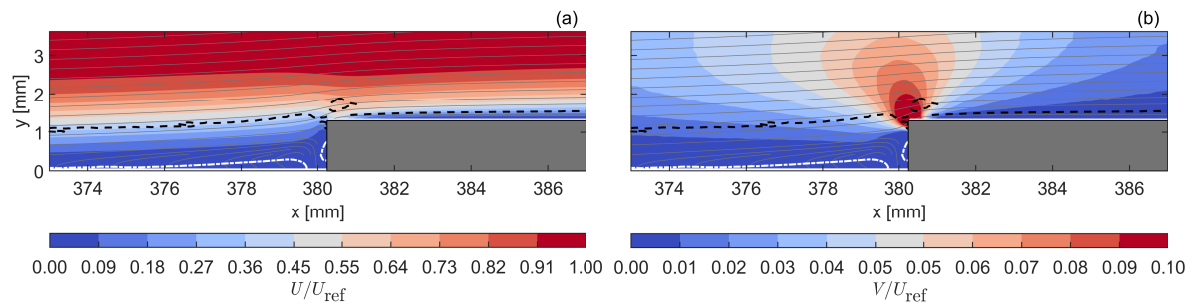


Figure 5.7: Contours of meanflow U ((a) and (c)) and V ((b) and (d)) components from PIV ((a) and (b)) and DNS ((c) and (d)) for  $h/\delta^* = 1.462$ . Streamlines (gray —), recirculating regions (white - - -) and inflection points (- - -) are also indicated.

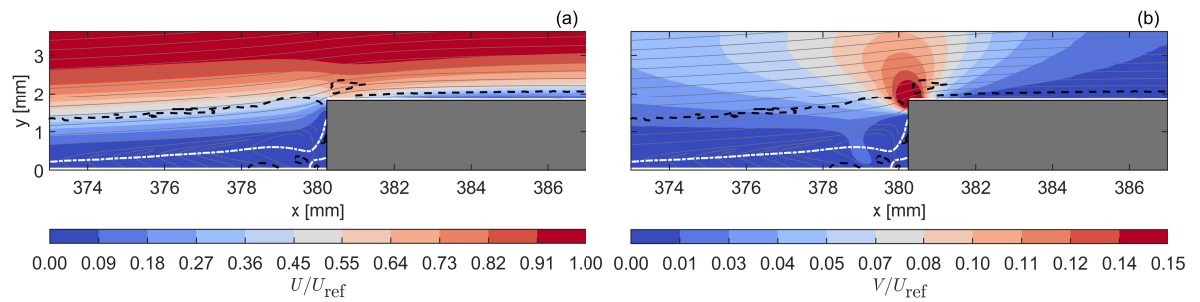


Figure 5.8: Contours of meanflow U (a) and V (b) components from PIV for  $h/\delta^* = 1.950$ . Streamlines (gray —), recirculating regions (white - - -) and inflection points (- - -) are also indicated.

contour lines in figures 5.6, 5.7 and 5.8 (a), indicating the location of the inflection points.

Figure 5.6 shows the streamwise and wall-normal meanflow velocity contours as obtained from PIV and DNS for a subcritical step. PIV results at critical and supercritical steps are shown in figure 5.7 and figure 5.8. Upstream of the subcritical step case (figure 5.6) there is a very small region of recirculating flow which is interrupted by the geometrical suction slot present in front of the step in both experiments and DNS. Downstream of the step there is no recirculating flow, as expected from the preliminary test matrix design performed in section 2.1. Upstream of both critical and supercritical steps (figures 5.7 and 5.8) the recirculating region is also modulated or directly broken due to the effect of the geometrical suction slot.

In line with experiments from Eppink and Casper (2019) and Rius-Vidales and Kotsonis (2021), and DNS

results from Shahzad (2020) and Casacuberta et al. (2021), a kink in the  $U$  meanflow component just at the step edge is also observed herein at all step heights, see figures 5.6 (a), 5.7 (a) and 5.8 (a). This effect seems to become stronger for higher steps. Eppink and Casper (2019) argue that this phenomenon can be explained by resorting to continuity. In short, the rapid displacement of wall-normal momentum away from the wall (see figures 5.6, 5.7 and 5.8 (b)) needs to be compensated by an also rapid streamwise momentum injected close to the wall. The reader is referred to Eppink and Casper (2019) for further details on the relationship established by the authors between these observations and the continuity equation.

Finally, while the baseflow distortion experienced upstream of the step can be widely observed in a number of well-studied stability problems (upstream of LSBs, in regions of mild adverse pressure gradient, etc.), the one observed immediately downstream (note the double inflection point in the boundary layer) is rarely found in the literature. Therefore, the direct implications that this complex modulation of the baseflow will have on the stability of the perturbation field are difficult to foresee.

### 5.3. Growth of the fundamental mode and harmonics over the step

As observed in the previous section, the step strongly distorts the meanflow within a very short streamwise extent. This abrupt change in the flow is immediately perceived by the perturbation field, which distorts and grows accordingly. This section is concerned with the growth of the fundamental mode and its harmonics for the most amplified TS wave at the step ( $F = 90$ ) with different step heights. Later, in section 5.7 a similar analysis will be performed for the rest of frequency cases, i.e.  $F = 60$  and  $F = 110$ .

Figure 5.9 shows HWA and DNS results of the  $N$ -factor evolution, defined based on the maximum of  $|\hat{u}|$ , for the fundamental mode and its harmonics at different step heights. Note that in figure 5.9 (d) no experimental data is given for the third harmonic from neither clean nor subcritical cases. This is so because these quantities were below the SNR of the HWA measurements, being their values non-conclusive for comparison with DNS. In addition, figure 5.10 shows the absolute amplitude of the fundamental mode and harmonics for every step to gain insight into the importance of non-linear effects in each case.

Figure 5.9 (a) shows very good agreement between DNS and experimental data in terms of the fundamental mode amplitude and its growth in clean and subcritical step conditions. In all step cases the fundamental mode (figure 5.9 (a)) undergoes exponential growth upstream of the step due to the presence of an adverse pressure gradient. However, downstream of the step, the amplification trends differ for every step. On the one hand, in the subcritical step case, the fundamental mode initially exhibits decay, trying to converge to clean case  $N$ -factor levels. However, at  $x = 420$  mm it destabilizes again. On the other hand, the critical step case exhibits a short region of decay right after the step (figures 5.9 and 5.10 (a)) but immediately downstream it undergoes an exponential-like amplification. Something similar is observed in the supercritical step case. However, in that case, the fundamental mode saturates and the transition regime starts within the HWA measurement domain (at around  $x = 400$  mm).

The harmonic behavior in the presence of a step largely varies from each harmonic (figure 5.9 (b)-(d)). While the subharmonic content (figure 5.9 (b)) grows exponentially in streamwise direction even after the step, the second harmonic (figure 5.9 (c)) presents irregular growth after the step, similar to the first harmonic. The third harmonic (figure 5.9 (d)) shows similar behavior to the second and first harmonics for the subcritical step case but depicts continuous growth in the case of critical and supercritical steps.

Examination on figure 5.10 (a)-(d) shows that the subharmonic content is particularly dangerous given its comparable amplitude with the fundamental mode, indicating that the subharmonic regime is likely growing due to non-linear interaction with the fundamental mode. In addition, its growth is enhanced for higher steps, being it even larger than the fundamental mode in the supercritical step case (see figure 5.10 (d)). Note that the subharmonic mode is not obtained from DNS. This indicates that this mode is not generated from non-linear interaction when only the fundamental mode is excited. Therefore, it must come from the non-linear interaction between the fundamental mode and other modes excited in the experimental set-up due to background disturbances. The origin of the subharmonic regime during the experiments and its growth in the presence of an FFS will be later discussed in more detail in section 5.6.

Profiles of the fundamental mode shape function and the mean shear are shown in figure 5.11 for different step heights. Very good agreement is observed between DNS and experimental results in clean and subcritical step conditions (figure 5.11 (a) and (b)). Although experiments do not reach to measure the near-wall peak after the step observed in figure 5.11 (b), they accurately capture the highly distorted TS shape at  $x = 420$  mm, which, interestingly, takes place in a region where the meanflow has already recovered to clean case

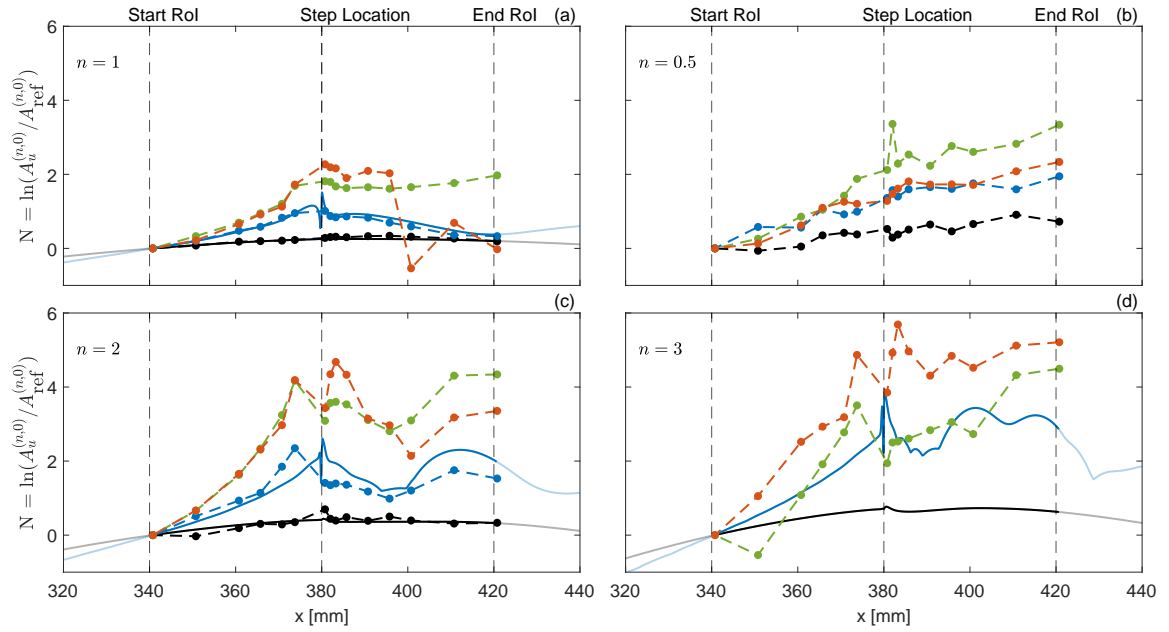


Figure 5.9: N-factor evolution of the  $|\hat{u}|$  maximum from the fundamental mode (a), subharmonic mode (b), second (c) and third (d) harmonics. Full lines denote DNS data (in clean and subcritical step cases) and symbols HWA measurements. Clean case ( $h = 0$  mm, black), subcritical ( $h = 0.775$  mm, blue), critical ( $h = 1.462$  mm, green) and supercritical ( $h = 1.950$  mm, orange) step cases. The frequency of the fundamental mode is  $F = 90$ . Note that dashed lines are not numerical data but just have the purpose of tracing the HWA points.

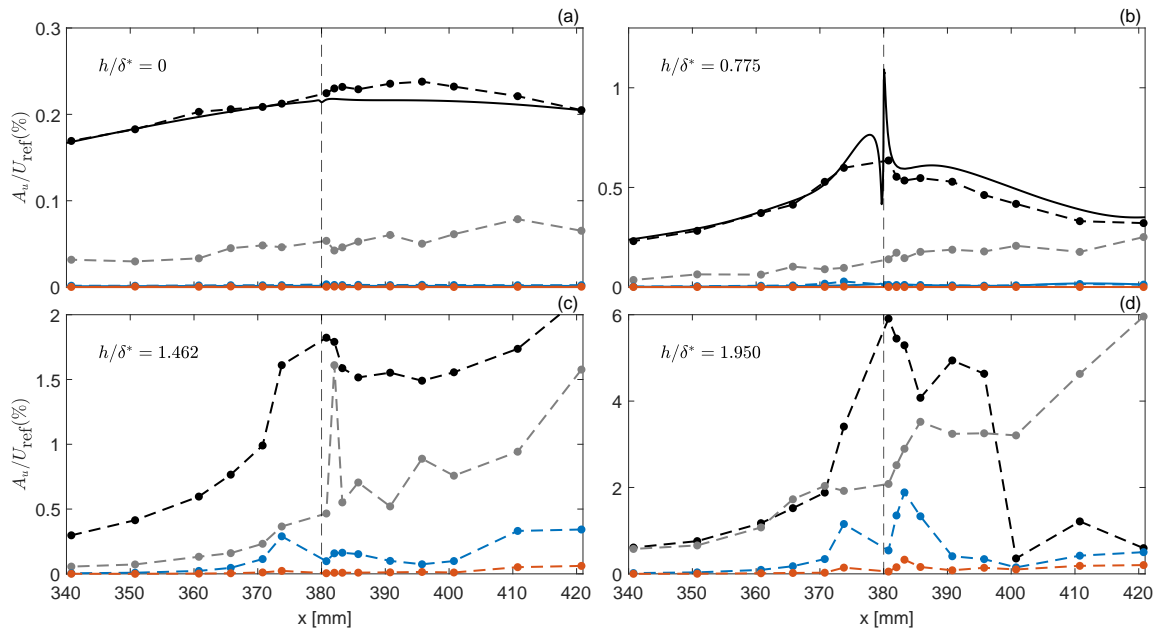


Figure 5.10: Absolute amplitude for different step heights: clean case (a), subcritical (b), critical (c) and supercritical (d) step conditions. Full lines denote DNS data (in clean and subcritical step cases) and symbols HWA measurements. Fundamental mode ( $F = 90$ , black), subharmonic mode ( $n = 0.5$ , gray), second harmonic ( $n = 2$ , blue) and third harmonic ( $n = 3$ , orange). Note that lines between experimental points are only for indicative purposes on the data trend.

conditions (note figure 5.4 (c) and figure 5.5 (a)).

From figure 5.11 (b)-(d) it can be observed that upstream of the step, the TS wave becomes thicker in regions where the maximum of  $\partial U / \partial y$  grows in wall-normal direction, as a consequence of the stronger adverse pressure gradient close to the step. At some point, this effect becomes so strong (note the supercritical step case in figure 5.11 (c)) that the TS wave exhibits an M-like modulation, characterized by an additional peak

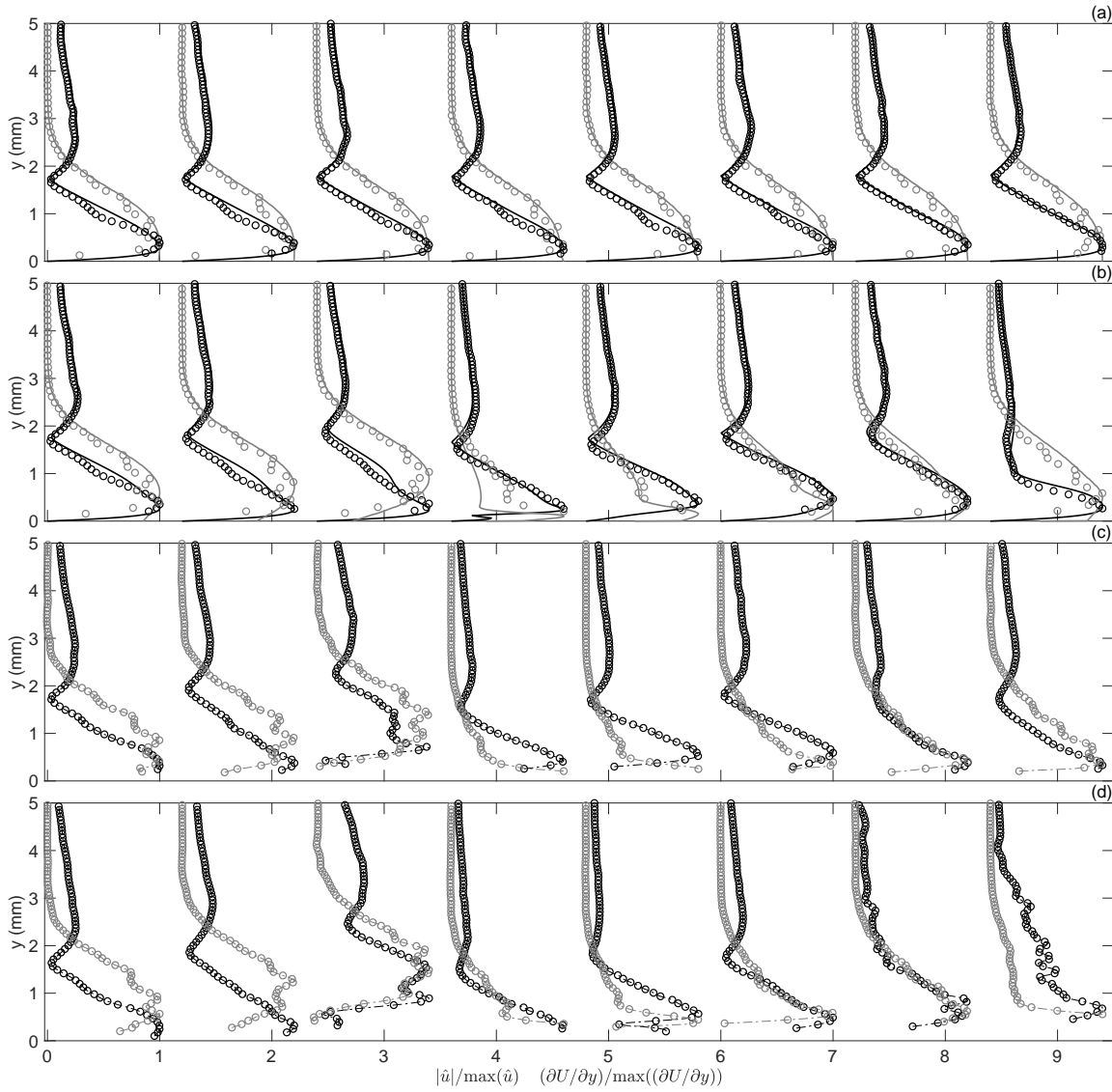


Figure 5.11: Wall-normal profiles of the fundamental mode ( $F = 90$ ) in terms of  $|\hat{u}|$  (black) and  $\partial U / \partial y$  (gray). Full lines denote DNS data and symbols (o) HWA results. Clean (a), subcritical (b), critical (c) and supercritical (d) step cases. The streamwise locations plotted are at (from left to right)  $x = [341, 361, 374, 381, 383, 391, 401, 421]$  mm with the step at  $x = 380$  mm. The horizontal spacing between profiles is set to  $\Delta = 1.2$  for legibility. Note that the dashed-dotted lines in (c) and (d) are not numerical data but just intend to trace the experimental data points for easier interpretability.

above the original lobe. Downstream of the step an additional peak is seen to emerge in the near-wall in the subcritical step case DNS results (figure 5.11 (b)), taking place in a region where  $\partial U / \partial y$  also exhibits a pronounced increase. Although hardly visible, HWA measurements also present an emergent near-wall lobe in the TS shape function in the supercritical step case (figure 5.11 (b)) which also correlates with a peak in  $\partial U / \partial y$ . The observed correlation between the different peaks in the TS shape function and the mean shear indicates that these features could be related to the growth of the fundamental mode driven by the production term in the Orr-Reynolds equation, which is proportional to  $\partial U / \partial y$ . Interestingly, the same link cannot be established in the case of the distorted TS shape observed at  $x = 420$  mm in the subcritical step case (figure 5.11 (b)), which takes place in a region where the mean shear is similar to clean case conditions.

Casacuberta et al. (2021) also observed a similar near-wall peak in the crossflow profile after the step edge. The authors attributed this peak to the insurgence of a secondary perturbation with equivalent wavelength to the primary crossflow mode. Evident differences (three-dimensional and steady problem) between their work and this one make it impossible to establish a link between them. However, it is nevertheless interesting to

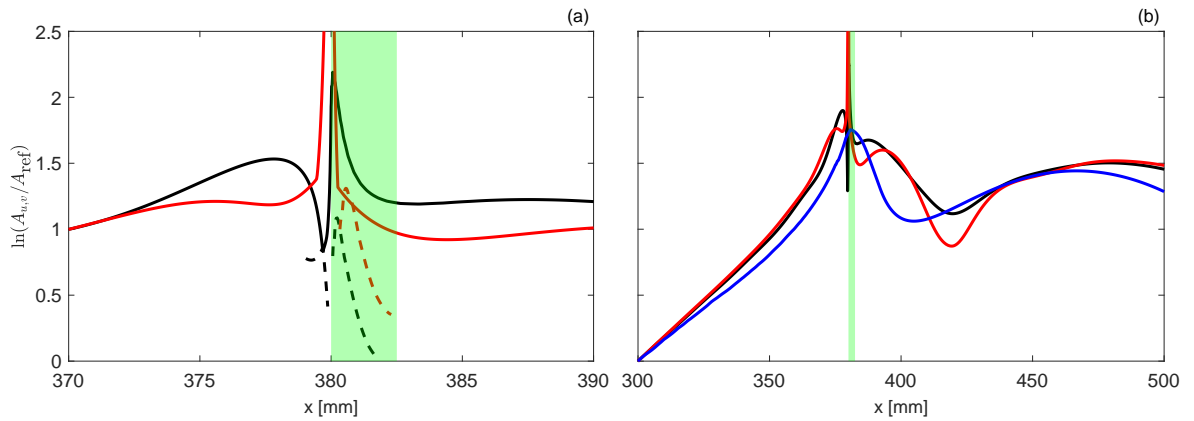


Figure 5.12: (a) N-factor of the different peaks in the fundamental mode ( $F = 90$ ) shape function from DNS in subcritical step case conditions. Full lines indicate the maxima of  $|\hat{u}|$  (black) and  $|\hat{v}|$  (red) while dashed lines indicate the secondary peaks different from the maxima. (b) N-factor based on the maxima of  $|\hat{u}|$  (black) and  $|\hat{v}|$  (red) from DNS for the fundamental mode ( $F = 90$ ) in subcritical step case conditions. Equivalent results from the OS solver computed with the DNS baseflow are indicated in blue. The green patch indicates the maximum streamwise extent of the secondary peak.

observe that a similar baseflow subject to different incoming instabilities shares similar flow features in the vicinity of the step.

The evolution of different peaks observed from the TS wave shape function have been tracked in streamwise direction to gain insight into their extent and amplification. Full lines in figure 5.12 (a) represent the N-factor based on the maxima of  $|\hat{u}|$  and  $|\hat{v}|$  from DNS results. In turn, dashed lines indicate additional peaks emerging in the TS shape which are different from the TS maxima and take place inside the boundary layer region<sup>2</sup>. The green patch in figure 5.12 (a) represents the streamwise extent of the secondary near-wall peak.

From figure 5.12 (a) it is observed that approximately 10 mm upstream of the step both  $|\hat{u}|$  and  $|\hat{v}|$  TS wave maxima start to present very different amplification trends. Immediately in front of the step, the maximum in  $|\hat{v}|$  experiences rapid growth while  $|\hat{u}|$  decays. This uncoupled growth trends between  $|\hat{u}|$  and  $|\hat{v}|$  can be explained by the distortion that the step geometry induces on the perturbation streamlines, making all the perturbation streamwise momentum to be transferred to the wall-normal direction. This will be clearly illustrated in section 5.5 when examining the disturbance streamline results (see figure 5.20). After the step edge, all wall-normal momentum is again transferred to the streamwise component of the disturbance, making  $|\hat{u}|$  and  $|\hat{v}|$  to experience a sharp growth and decay, respectively (note the immediate region after  $x = 380$  mm in figure 5.12 (a)). Right at this region a near-wall peak develops in the TS shape function, as observed from figure 5.11 (a), in both  $|\hat{u}|$  and  $|\hat{v}|$  components. The amplitude of this peak is normalized with its initial amplitude in figure 5.12 (a) (the amplitude measured at the position where it is first identified). Interestingly, the near-wall structure grows in the region where there is strong transfer of disturbance momentum from the wall-normal to the streamwise component, i.e. where  $|\hat{u}|$  and  $|\hat{v}|$  exhibit decoupled growth. Afterwards, it decays and merges with the original TS maxima, as observed from the disturbance profiles in figure 5.11 (a).

Linear Stability Theory (LST) results are computed and compared with the DNS results for a subcritical step case. LST assumes parallel flow, i.e. the growth of disturbances depends uniquely on the baseflow profile at a particular  $x$  location. In the vicinity of the step, due to the existence of a strong pressure gradient, the flow becomes highly non-parallel, which makes LST results highly inaccurate in this region. However, far upstream and downstream of the step, where the baseflow recovers to clean case conditions, LST should provide similar growth rates and shape functions as DNS since non-parallel effects are no longer important.

Figure 5.12 (b) shows the N-factor obtained from the Orr-Sommerfeld (OS) solver using the DNS baseflow for a subcritical step case. The median  $y$  coordinate ( $y_i$ ) has been adapted according to the change in the boundary layer thickness along  $x$  to properly resolve the modes inside the boundary layer (Groot, 2018). An additional modification has been necessary downstream of the step, where the EV filter (explained in section 2.2.1) predicted two eigenvectors with very low and similar errors, i.e. two plausible solutions to the problem. In light of this, the eigenvector displaying the highest growth rate ( $\alpha_i$ ) has been selected in every

<sup>2</sup>This avoid accounting for the lobe above the critical layer that the TS wave presents in the streamwise component.

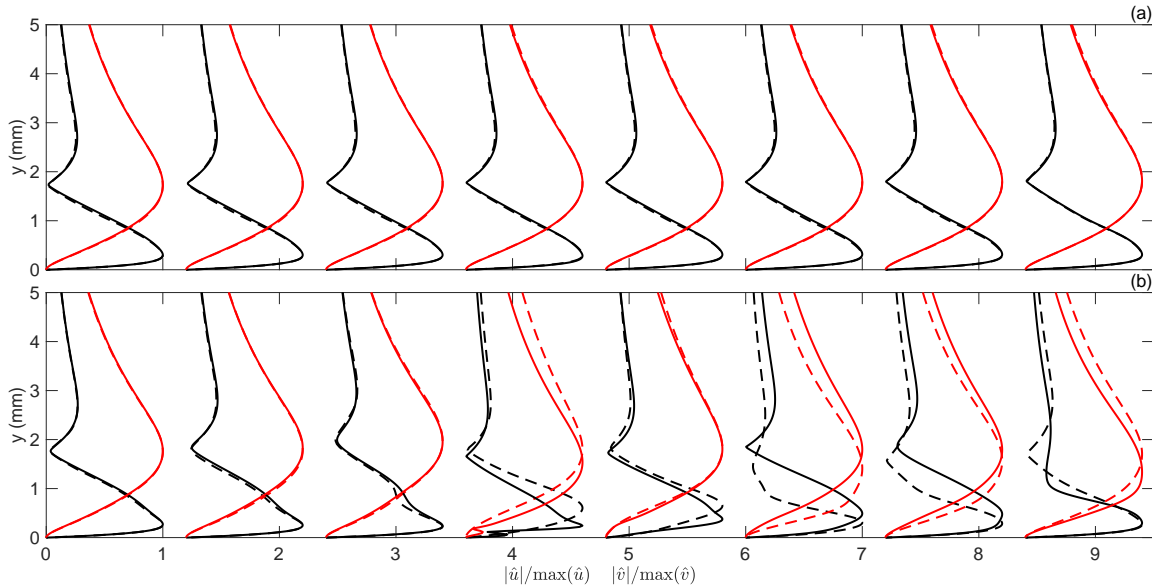


Figure 5.13: Shape function of the fundamental mode from DNS (full lines) and OS (dashed lines) results in clean (a) and subcritical (b) step conditions. Shape function of  $|\hat{u}|$  in black and  $|\hat{v}|$  in red.

streamwise location after  $x = 380$  mm, i.e. the resulting  $(\alpha_i)$  represents the envelope of the growth rate of the two possible modes found from the OS solver. Furthermore, figure 5.13 shows the shape functions of  $|\hat{u}|$  and  $|\hat{v}|$  from the resulting OS modes compared to DNS results.

Upstream of the step, results from OS predict exponential growth, similar to DNS results. The observed differences in this region are related to the parallel flow assumption made in OS, which leads to a larger disagreement between both methods as the step is approached. Downstream of the step OS fails to capture the N-factor decay in the vicinity of the step mainly due to the large non-parallel effects in this region. However, even farther from the step region, where non-parallel effects become negligible (for  $x \geq 395$  mm as indicated by the shape factor recovery to  $H = 2.59$  in figure 5.4 (a)), OS shows large discrepancy with DNS results in terms of both N-factor and TS shape functions (figures 5.12 and 5.13).

Edelmann (2014) also observed a large discrepancy between LST and DNS results in regions where non-parallel effects are not relevant. The author argued that the disagreement between LST and DNS in these regions could not be explained by non-linear effects given the small amplitudes of the harmonics compared to the fundamental mode, similar to the present work (note the low amplitude of the harmonics in figure 5.10 (b)). In light of this, Edelmann (2014) suggests that the existence of spatial transient growth in these regions could explain the large discrepancy between LST and DNS. Transient growth (sometimes denoted as non-modal growth) has been previously described in chapter 1, section 1.2.2.

Examination of figure 5.12 (b) reveals yet another hint pointing towards the plausibility of regions governed by spatial transient (or non-modal) growth. The different growth trends observed when the N-factor is defined based on  $|\hat{u}|$  or  $|\hat{v}|$  maximum indicate that the growth of the disturbance cannot be exclusively described in exponential form, i.e.  $q = \hat{q}(x, y)e^{i\Theta(x, t)}$ . Marxen et al. (2009) claims that to assert the existence of spatial transient growth one needs to verify that  $|\hat{u}_{||}|$  and  $|\hat{v}_{\perp}|$  (perturbation field components orthogonal to the baseflow direction) exhibit different growth behavior in  $x$ .

In the present work, the disturbance components orthogonal to the baseflow are computed as follows using the DNS data (Marxen et al., 2009):

$$\begin{bmatrix} \hat{u}_{||} \\ \hat{v}_{\perp} \end{bmatrix} = \frac{1}{\sqrt{U^2 + V^2}} \begin{bmatrix} U & V \\ -V & U \end{bmatrix} \begin{bmatrix} \hat{u} \\ \hat{v} \end{bmatrix}. \quad (5.2)$$

Figure 5.14 (a) and (b) shows the orthogonal disturbance components in terms of wall-normal integral energy (integrating  $|\hat{u}_{||}|^2$  and  $|\hat{v}_{\perp}|^2$  along  $y$ ) and maximum amplitude, respectively. Note that depending on the parameter chosen to plot in the  $y$ -axis, the conclusions are different. Marxen et al. (2009) analyze

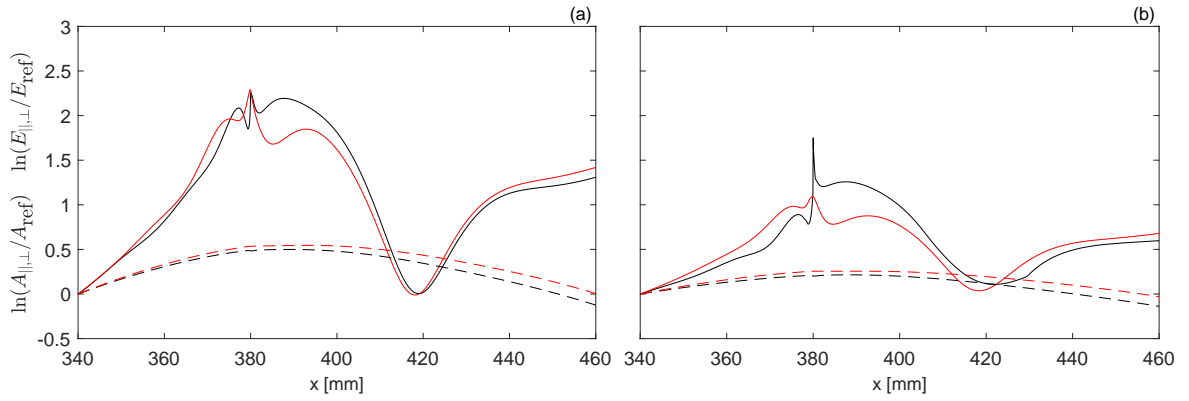


Figure 5.14: N-factor evolution of the disturbance components orthogonal to the baseflow,  $|\hat{u}_{\parallel}|$  (black) and  $|\hat{v}_{\perp}|$  (red), as obtained from equation (5.2). Clean case (dashed lines) and subcritical step case (full lines) from DNS results. (a) N-factor defined in terms of the disturbance energy integrated along  $y$ , i.e.  $\int_0^{h_{\text{DNS}}} |\hat{u}_{\parallel}|^2 dy$ . (b) N-factor defined based on the maxima of  $|\hat{u}_{\parallel}|$  and  $|\hat{v}_{\perp}|$ .

the evolution of the different peaks on the disturbance shape function. Note that when the integral-energy definition is chosen, all peaks are taken into account in the description. The analysis of Marxen et al. (2009) suggests that this could lead to misleading conclusions since different regions of the disturbance can present modal or non-modal behavior. Therefore, results from figure 5.14 (b) should be addressed herein.

Figure 5.14 (b) shows that the disturbance presents mainly two regions in which the growth trends between  $|\hat{u}_{\parallel}|$  and  $|\hat{v}_{\perp}|$  are not different by an offset, indicating that in these regions non-modal growth is plausible. These two regions correspond to an area immediately in front of the step ( $375 \leq x \leq 380$  mm) and far downstream ( $380 \leq x \leq 430$  mm). It will be later observed in section 5.5 that the disturbance presents large topological differences compared to a conventional TS wave in these regions, particularly around  $x \approx 420$  mm.

## 5.4. The perturbation field at the step

The previous section covered the growth of the TS wave over the step in terms of the N-factor. This section will present results over the entire perturbation field at the step to visualize how the main stability features (growth, phase, and production term) change within the field of view. First, section 5.4.1 will analyze the change of the disturbance amplitude and phase for different step heights. Later, in section 5.4.2, the evolution of the production term in the vicinity of the step will be presented. Similar to the previous section, the analysis of the perturbation field is restricted to one fundamental mode frequency,  $F = 90$ . DNS results are also included in clean and subcritical step conditions.

### 5.4.1. Amplitude and phase modification of the fundamental mode

The disturbance amplitude field of the fundamental mode ( $F = 90$ ) is shown in figure 5.15 for all step heights. Figure 5.15 (a)-(d) show results from DNS while figure 5.15 (e)-(j) present the amplitude of the TS wave extracted from PIV measurements by performing a (temporal) FFT on the set of high-resolution phase-locked frames. Contour lines show the inflection points on the meanflow  $U$  component and on  $|\hat{u}|$  and  $|\hat{v}|$  from the perturbation. Tracking the inflection points of the disturbance profile results useful to visualize in which regions the disturbance experiences large distortion, which is sometimes in accordance with high modulation in the meanflow curvature. It is important to keep in mind that DNS simulations were set to match HWA conditions. Thus, only qualitative comparison is possible between PIV and DNS for a subcritical step case since the perturbation parameters (non-dimensional frequency, amplitude, etc.) are slightly different (note table 2.1 and table 2.2 in chapter 2). Despite the acknowledged differences, the agreement between DNS and PIV in terms of  $|\hat{u}|$  and  $|\hat{v}|$  amplitude fields is very satisfactory.

DNS and PIV results in figure 5.15 (c)-(f) show that the lobes (indicated by the yellow and black contour lines in the plot) of the  $|\hat{u}|$  and  $|\hat{v}|$  components of the TS wave take place at a similar  $y$  location as in the clean case (see figure 5.15 (a)-(b)) both far upstream and downstream within the FoV. This is modified in front of the step, where the  $|\hat{u}|$  maximum lifts over the step, decaying in magnitude, while the peak in  $|\hat{v}|$  is abruptly moved towards the wall, rapidly increasing its amplitude. This is in accordance with observations in the amplification

rates close to the step from Figure 5.12 (a) in the previous section. Bearing in mind the vortical nature of a TS wave, one could visualize this process as the distortion that the TS vortex undergoes when it meets a wall.

Downstream of the subcritical step the disturbance seems to recover its clean case configuration, with the maximum of  $|\hat{u}|$  and  $|\hat{v}|$  returning to its characteristic wall-normal locations, see figure 5.15 (c)-(f). However, close to the wall, one new peak is originated both in  $|\hat{u}|$  and  $|\hat{v}|$  (these peaks are not retrieved from PIV due to wall reflections), similar to what happens also to the mean shear ( $\partial U/\partial y$ ). In the previous section, it was observed when examining the TS shape functions that the wall-normal location of this new peak was in agreement with the emerging peak in  $\partial U/\partial y$ . As explained in section 5.2, the good spatial correlation presented between the emerging peaks in the disturbance and the ones in the mean shear might indicate the importance of the production term towards modifying the perturbation energy in these regions. In the next section (section 5.5) it will be shown that the emergence of this near-wall peak is related to the presence of a vortex in the disturbance field with the same frequency as the fundamental mode.

Figure 5.15 (g)-(h) present the amplitude evolution of the fundamental mode for a critical step from PIV results. Upstream of the step the TS wave develops an M-peak structure. The secondary lobe emerges in wall-normal locations where the mean shear is maximum, meaning that the disturbance is effectively extracting energy from the baseflow in these locations (note production term in the Reynolds-Orr equations and the linear dependence with  $\partial U/\partial y$ ). This M-peak structure has previously been reported by several authors when a TS wave approaches a region of reverse flow (Dovgal et al., 1994; Kurelek et al., 2019; Park and Park, 2013). Right in front of the step the TS wave amplitude exhibits opposite growth trends in  $|\hat{u}|$  and  $|\hat{v}|$  (decay versus growth), as previously noticed in the subcritical step case, due to the distortion that the TS vortex experiences at the step edge.

Downstream of the critical step case (figure 5.15 (g)-(h)) the amplitude fields of  $|\hat{u}|$  and  $|\hat{v}|$  resemble the subcritical step case results. However, immediately after the step edge, although hardly perceptible, one can observe that there are two different regions of maximum growth in the wall-normal direction. First, a region very close to the wall that seems to either decays in streamwise direction or merge with the above maximum. Secondly, the above maximum, which continues to grow in streamwise direction. Finally, note that slightly downstream of the step there is a stabilizing region around  $383 \leq x \leq 386$  mm (well-noticed in figure 5.15 (h)), in agreement with the stabilization also observed from the N-factor evolution in figure 5.9. Later, this stabilizing effect will be observed to come from a negative contribution in the production term.

Amplitude fields in supercritical step case conditions (figure 5.15 (i)-(j)) show that the upstream growth behavior of the fundamental mode resembles subcritical and critical step cases, with higher amplification due to the stronger mean shear in front of the step. Although this observation could seem trivial, it is of major importance since it might indicate that the TS growth upstream increases in proportion with the step height, in line with the underlying assumptions in the  $\Delta N$  methods, which claim that the main effect of the step height is towards increasing the TS growth. However, downstream of the supercritical step case, it is observed that the amplitude contours of the TS wave exhibit large differences with respect to other step cases. Particularly in terms of  $|\hat{v}|$  where, from figure 5.15 (j) one can observe that the disturbance undergoes such a large distortion that two clear lobes appear in the  $|\hat{v}|$  component.

The amplitude field of  $|\hat{u}|$  (figure 5.15 (i)) shows that after the step the TS wave also exhibits two different regions of maximum growth, as previously noticed in critical step case conditions. However, in this case, the near-wall peak experiences large growth in streamwise direction, merging with the upper lobe further downstream at  $x \approx 388$  mm, contrary to what happened in critical step conditions where both peaks were merging close after the step edge. Interestingly, the amplitude of  $|\hat{v}|$  depicts a region of large stabilization right before both peaks in  $|\hat{u}|$  merge.

Figure 5.16 show the phase contours of  $\hat{u}$  and  $\hat{v}$  for the fundamental mode at different step heights. The phase information will reveal extremely important later in this section to understand how the production of disturbance energy changes over the step.

Figure 5.16 (c)-(f) show numerical and experimental phase contours results in subcritical step case conditions. Once more, excellent agreement is observed between experiments and DNS results, indicating that the problem remains fully two-dimensional in subcritical step conditions with the present TS wave amplitude. Upstream of the step DNS and PIV results show the phase contours of  $\hat{u}$  slightly tilted compared to the phase contours in clean case conditions (figure 5.16 (a)-(b)). This indicates that the TS wave might appear tilted in this region, with the vortex head pointing towards upstream  $x$  positions<sup>3</sup>. In turn, at the end of the FoV the

<sup>3</sup>Hereafter, this type of tilting will be denoted as *tilting against the mean shear direction* and vice-versa for the opposite.

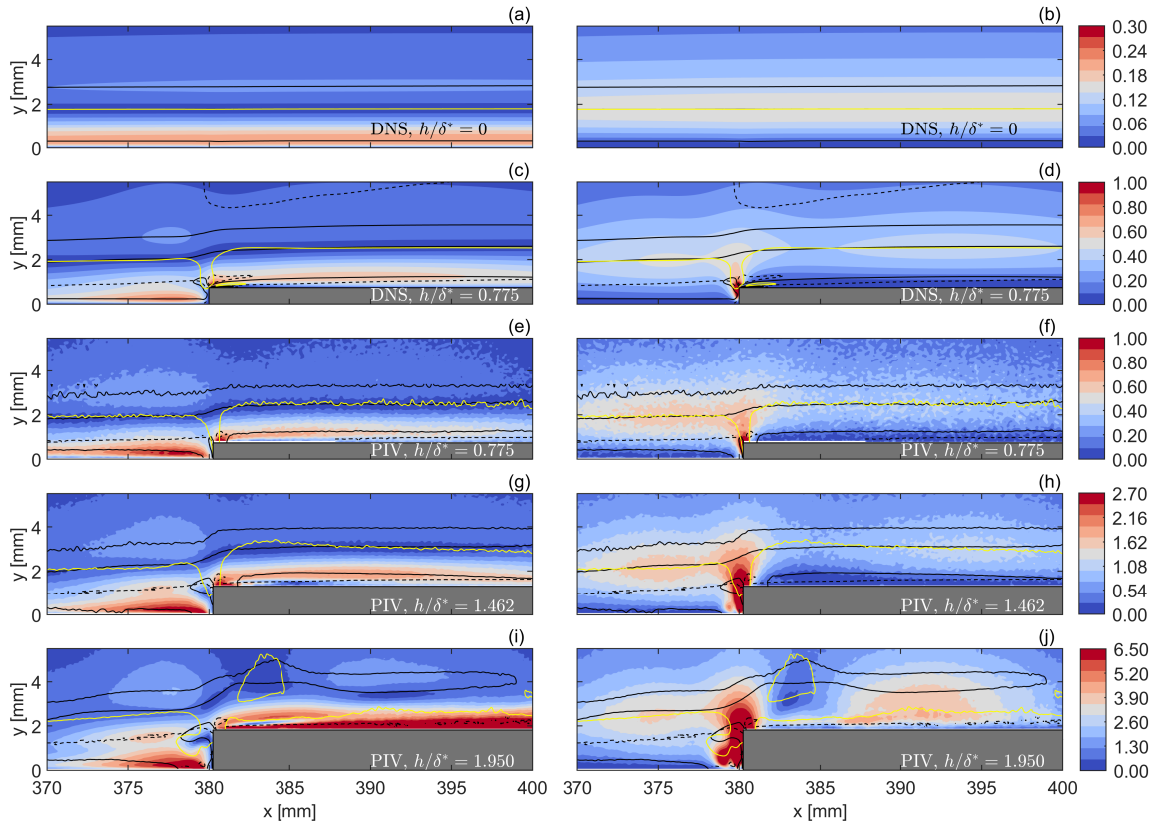


Figure 5.15: Contours of the fundamental mode ( $F = 90$ ) amplitude in terms of  $|\hat{u}|$  (a, c, e, g, i) and  $|\hat{v}|$  (b, d, f, h, j) components from DNS (a)-(d) and PIV (e)-(j) results. Contour lines of the inflection points from  $\partial U/\partial y$  (---),  $|\hat{u}|$  (black —) and  $|\hat{v}|$  (yellow —) are also shown. Clean case (a)-(b), subcritical step (c)-(f), critical step (g)-(h) and supercritical step case (i)-(j). The colorbar legend corresponds to  $|\hat{u}|/U_{ref}(\%)$ . Note:  $|\hat{v}|$  is multiplied by two to fit it within the colorbar of  $|\hat{u}|$ . The wall-normal coordinate has been scaled by 1.35 for visualization purposes.

opposite takes place, with the vortex head tilted downstream, i.e. tilting in the mean shear direction. Later in this section, it will be discussed the implications that the tilting direction has on the production term.

In the freestream of the phase contours shown in figure 5.16 (c)-(f) it can be observed that  $\hat{u}$  and  $\hat{v}$  keep a phase shift of approximately  $\pm\pi/2$ , similar to what is observed in clean case conditions. However, inside the boundary layer, the phase of the TS wave is highly modified, with the phase shift of  $\pm\pi/2$  between  $\hat{u}$  and  $\hat{v}$  being largely broken in this region. This could be related to the large modifications undergone by the boundary layer in the vicinity of the step, which at the same time modify the way viscosity acts towards shifting the phase of  $\hat{u}$  and  $\hat{v}$ . The reader can refer to the early works of Lin (1945); Mack (1984); Prandtl (1921); Taylor (1915) to understand how does viscosity affect the phase shift between  $\hat{u}$  and  $\hat{v}$  to enhance the growth of the disturbance inside the boundary layer. This was briefly discussed in chapter 1, section 1.2.

Unfortunately, PIV does not reach to capture the near-wall phase behavior of the disturbance. However, zooming close to the near-wall region after the step edge in DNS results (figure 5.16 (d)) one can observe a small region where the phase contours of  $\hat{u}$  and  $\hat{v}$  become opposite to the phase contours of the original disturbance. In the next section, the streamline results in that region will manifest the presence of an independent vortical structure coexisting with the original TS wave on top but counterrotating it, as the phase contours shown herein indicate.

Figure 5.16 (g)-(h) present the phase contours in critical step conditions. Similar features are observed upstream and downstream of the step as in subcritical step conditions. However, now the phase contours exhibit more pronounced tilting of the disturbance. Close to the step,  $\hat{u}$  and  $\hat{v}$  phases are largely distorted, presenting regions where  $\hat{u}$  and  $\hat{v}$  are largely out of quadrature. The latter will be later seen to dramatically increase the Reynolds stresses ( $u'v'$ ), highly stabilizing or destabilizing the flow. In this case, even from PIV results it can be observed that there is a near-wall region after the step edge, similar to the one observed in subcritical step case conditions, where phase contours opposite to the ones on top (coming from the original

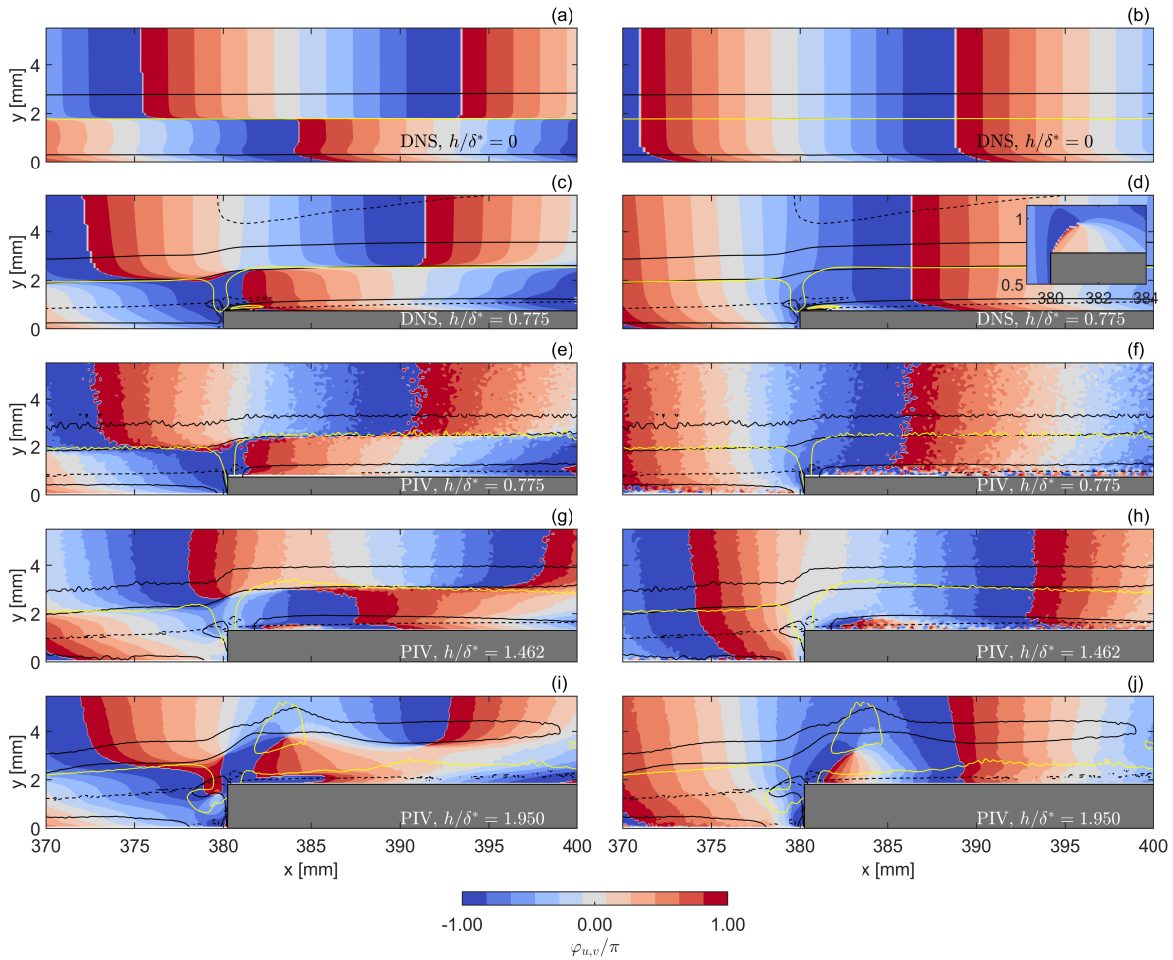


Figure 5.16: Contours of the fundamental mode ( $F = 90$ ) phase in terms of  $\varphi_{\hat{u}}$  (a, c, e, g, i) and  $\varphi_{\hat{v}}$  (b, d, f, h, j) components from DNS (a)-(d) and PIV (e)-(j) results. Contour lines of the inflection points from  $\partial U/\partial y$  (---),  $|\hat{u}|$  (black —) and  $|\hat{v}|$  (yellow —) are also shown. Clean case (a)-(b), subcritical step (c)-(f), critical step (g)-(h) and supercritical step case (i)-(j). The wall-normal coordinate has been scaled by 1.35 for visualization purposes.

disturbance, i.e. TS waves) are observed.

In supercritical step case conditions (figure 5.16 (i)-(j)) the phase is highly distorted in the vicinity of the step both in terms of  $\hat{u}$  and  $\hat{v}$ . Now the distortion created by the step on the disturbance field is so strong that it is even felt in the inviscid region of the disturbance, i.e. outside of the boundary layer. Similar to observations in the critical step case, after the supercritical step a region with opposite phase to the disturbance on top is also observed (note figure 5.16 (j)). However, in this case, the influence of this region is highly expanded in wall-normal direction. In the next section, section 5.5, it will be shown that this corresponds to a region where a secondary counterrotating vortical structure is also observed, similar to subcritical and critical step cases, but this time it will exhibit a much higher wall-normal extent.

### 5.4.2. Production of perturbation energy

The results presented in the previous section show that the growth of TS waves upstream of the step follows exponential-like behavior, related to the progressive meanflow distortion caused by the effect of an upstream adverse pressure gradient. However, in the step vicinity and downstream of it, the TS wave growth becomes highly complex. Some indicators of this higher complexity include the emergence of secondary lobes in the TS shape function and the different amplification trends observed between not only  $|\hat{u}|$  and  $|\hat{v}|$  but also between the disturbance components orthogonal to the baseflow, i.e.  $|\hat{u}_{||}|$  and  $|\hat{v}_{\perp}|$  (Marxen et al., 2009). At this point, what remains to be understood is *how* and *which* are the mechanisms behind the complex growth experienced by the disturbance downstream of the step. Examination of the disturbance stability from an

energetic point of view can provide an intuitive interpretation of the underlying physics. This section focuses on one of the terms present in the Reynolds-Orr equation (see equation (1.3) in chapter 1): the production term. This term represents how the disturbance absorbs (positive production, increase of disturbance energy) or returns (negative production, decrease of disturbance energy) energy to the baseflow through the action of the Reynolds stresses.

Examination of the production term is well-suited to analyze the linear growth mechanisms that contribute to stabilizing or destabilizing the disturbance. The production term from the energy balance of the fundamental mode (see mathematical development in Section C of Jin et al. (2021)) is expressed as

$$\hat{\mathcal{P}} = -(\hat{u}_i^* \hat{u}_j + \hat{u}_i \hat{u}_j^*) \frac{\partial U_i}{\partial x_j}, \quad (5.3)$$

where the superscript \* denotes complex conjugate. Other terms from the energy balance equation (non-linear, pressure, dissipation, and advection contributions) and the energy budget of other harmonics are not considered in this analysis given the higher complexity that it would entail. Nevertheless, if a complete picture of the underlying physical problem is desired, then this study should be extended to account for higher harmonics and all energy contributions. For now, to understand the linear growth mechanisms in play after the step, the production term is most useful.

First of all, the subcritical step case is examined in detail given the larger size of the field of view available from DNS results with respect to PIV. Figure 5.17 (a) shows the contours of the production term over the step. In addition, the streamlines of the fundamental mode at a given phase are also represented to visualize how the disturbance topology relates to the changes in the production term. Figure 5.17 (b) shows the four different contributions to the production term and the total value integrated in wall-normal direction, i.e.  $\tilde{\mathcal{P}} = \int_0^{h_{\text{DNS}}} \hat{\mathcal{P}} dy$  with  $h_{\text{DNS}}$  being the DNS domain height. From figure 5.17 (b) it is observed that the dominant term is  $\hat{\mathcal{P}}_{12}$ , which can be expressed in terms of the disturbances amplitude and phase as

$$\hat{\mathcal{P}}_{12} = -2 |\hat{u}| |\hat{v}| \cos(\varphi_{\hat{u}} - \varphi_{\hat{v}}) \frac{\partial U}{\partial y}. \quad (5.4)$$

This last expression indicates that the increase or decrease on production takes place in regions of high shear where  $\hat{u}$  and  $\hat{v}$  are not in quadrature, i.e.  $(\varphi_{\hat{u}} - \varphi_{\hat{v}}) \neq \pm\pi/2$ . Finally, figure 5.17 (c) presents the kinetic energy of the fundamental mode integrated in wall-normal direction, i.e.  $\tilde{E} = \int_0^{h_{\text{DNS}}} \hat{E} dy$ , with wall-normal and streamwise contributions to  $\tilde{E}$  also represented separately (note dashed lines).

From figure 5.17 (a) and (b) it can be observed that upstream of the step the production term is positive and increases as it approaches the step. Consequently, the energy of the disturbance (figure 5.17 (b)) grows in this region. At the step region, there is a very pronounced negative peak in production, followed by a sudden positive peak at the step edge which immediately returns to negative values after (figure 5.17 (b)). In terms of the energy of the disturbance (figure 5.17 (c)) this is translated into a first decay in front of the step, sudden growth at the step edge, and right after a pronounced decay. Downstream of the step, production undergoes several changes of sign. After the stabilizing effect at the step edge, the production term becomes positive and the disturbance starts to grow mildly. As of  $x = 390$  mm production becomes negative again and the disturbance energy decays until  $x = 420$  mm, where production goes back to positive values and the disturbance starts to grow. Further downstream the production term recovers to clean case values (not shown here) and the evolution of the disturbance energy goes back to clean case trends but at higher energy levels, similar to observations from figure 5.12 (b) when LST results were compared with DNS. The good correlation presented between production and energy indicates that for this step case the evolution of the disturbance energy can be largely described by resorting uniquely to the production term.

Figure 5.17 (a) shows how the topology of the fundamental mode relates to the sign of the production term. Overall, it is observed that regions where the disturbance tilts against the shear (note stations  $360 \leq x \leq 380$  mm and  $420 \leq x \leq 440$  mm) seem to correlate with locations of high positive production where the disturbance is amplified (figure 5.17 (b)-(c)). In turn, locations where production becomes largely negative (e.g.  $390 \leq x \leq 420$ ) exhibit the disturbance tilted in the mean shear direction. Interestingly, in a region around  $x \approx 420$  mm, the disturbance energy undergoes an inflection in growth, production changes sign and the disturbances abruptly change their tilting direction (figure 5.17 (a)). Further downstream the TS waves recover its upright position (i.e.  $(\varphi_{\hat{u}} - \varphi_{\hat{v}}) \approx \pm\pi/2$ ) followed by the recovery of production to clean case values.

Based on previous works, the growth of disturbances as a result of their tilting against the shear can be associated with a particular non-modal growth mechanism: the Orr-mechanism (refer to section 1.2.2). Åkervik

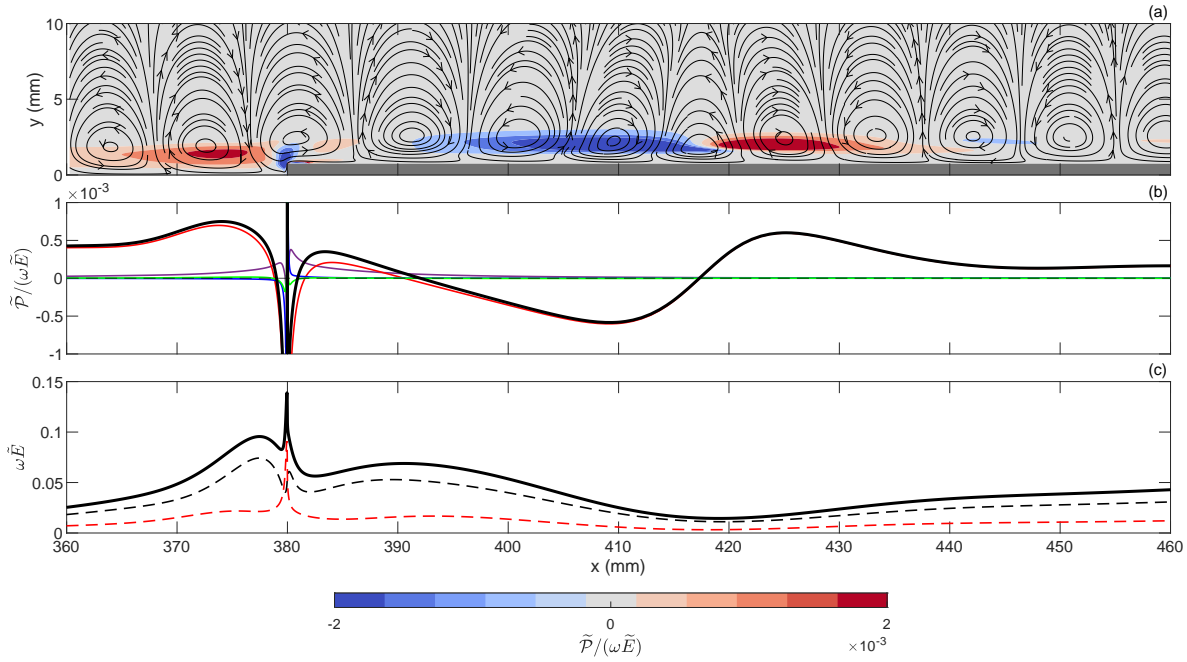


Figure 5.17: (a) Contours of the production term ( $\tilde{\mathcal{P}}$ ) as defined in equation (5.3). In addition, streamlines from DNS for the fundamental mode ( $F = 90$ ) at phase  $\phi = \pi$  rad are shown. (b) Streamwise evolution of the production term and its different contributions:  $\tilde{\mathcal{P}}_{11}$  (magenta),  $\tilde{\mathcal{P}}_{12}$  (red),  $\tilde{\mathcal{P}}_{22}$  (blue),  $\tilde{\mathcal{P}}_{21}$  (green) and total production (black). A dashed line indicates the zero in the  $y$ -axis. (c) Streamwise evolution of the disturbance kinetic energy ( $\tilde{E} = |\hat{u}|^2 + |\hat{v}|^2$ ) integrated in wall-normal direction and multiplied by the TS frequency ( $\omega = 2\pi f$ ). Contributions of  $|\hat{u}|$  (black-dashed line) and  $|\hat{v}|$  (red-dashed line) to the energy are also represented. The wall-normal coordinate has been scaled by 1.35 for visualization purposes.

et al. (2008) studied the stability of a Blasius boundary layer subject to 2D disturbances by means of non-modal analysis and observed that the Orr mechanism is the most optimal condition to initiate TS waves. Their results show the evolution of a wavepacket tilted against the shear which effectively amplifies the disturbance linearly until it forms a well-developed TS wave which switches to exponential growth downstream. The authors observe that when only TS type modes are considered, the predicted maximum growth is much lower. Despite the differences with the present results, where the incoming disturbance is already a well-developed TS wave, Åkervik et al. (2008) findings manifest the importance of accounting for non-modal growth to correctly evaluate the energy of the disturbance further downstream.

Figure 5.18 (a)-(d) shows the contours of production obtained at different step heights from PIV results. DNS results are also included for the subcritical step case to validate their good agreement, see figure 5.18 (a). Figure 5.18 (c) and (d) show the production term contours for a critical and a supercritical step. It can be observed that the evolution of production over the step is very similar for all step cases. The main difference between steps is the magnitude of the production term, which seems to increase in proportion to the step height.

It is important to emphasize that for higher step cases a description of the disturbance energy growth resorting uniquely to the production term might not be sufficient given the large amplitude that higher harmonics achieve in these cases. The contribution of non-linear effects to the energy budget of the fundamental mode can become very important and surpass the contribution of the production term in these cases. A clear example of this can be established from the results of the production term in critical step conditions (figure 5.18 (c)) and the corresponding  $N$ -factor curves presented in a previous section in figure 5.9 (a). While looking at the downstream region of figure 5.18 (c) one would be tempted to say that the disturbance is being stabilized, the amplification rate for the fundamental mode in figure 5.9 (a) and figure 5.10 (c) presents an uninterrupted growth in streamwise direction, indicating that the observed growth is likely linked to non-linear effects. In supercritical step conditions, non-linear effects become so strong that transition takes place within the measurement region (see figure 5.10 (d)). Therefore, the decay observed in the fundamental mode as of  $x \geq 400$  mm is not related to the negative value of production in this region but to immediate flow breakdown.

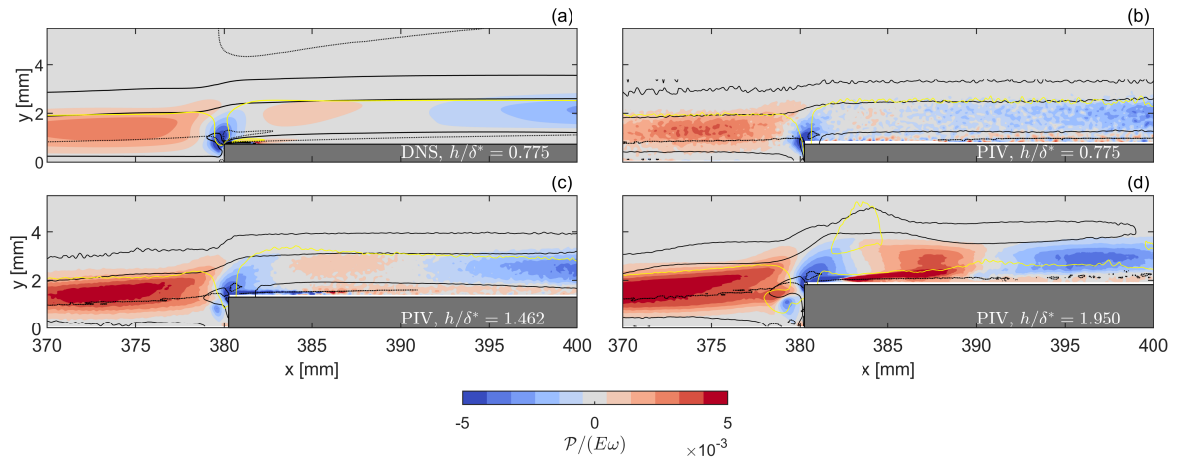


Figure 5.18: Contours of the production term ( $\tilde{\mathcal{P}}$ ) as defined in equation (5.3) at different step heights. Contour lines represent the inflection points from  $\partial U/\partial y$  (---),  $|\hat{u}|$  (black —) and  $|\hat{v}|$  (yellow —). Subcritical step (a)-(b), critical step (c) and supercritical step case (d). Results in (a) correspond to DNS. The wall-normal coordinate has been scaled by 1.35 for visualization purposes.

## 5.5. Phase-locked fields: TS waves motion over the step

Results from previous sections suggested the presence of a secondary structure coexisting with the original TS wave in the near-wall region after the step edge. A secondary lobe in the TS shape function profiles (figure 5.11) and different phase contours (figure 5.16) constitute some examples of results pointing towards an additional structure present in the near-wall. In this section the topology of the TS wave and this near-wall structure will be characterized, together with their evolution at the step within one TS wave cycle. In this section the disturbance streamlines are used to identify vortical regions and their direction of rotation.

Figure 5.19 shows the evolution of the TS wave over a subcritical step at three different phases of its cycle from DNS results. Dotted-dashed green lines indicate locations where production changes sign. As previously discussed, these regions present a high correlation with changes in the tilting direction on the disturbance streamlines. At first sight, one could be tempted to explain the distortion on the disturbance field around  $390 \leq x \leq 440$  mm by resorting to non-parallel effects. However, in these regions, the baseflow has already recovered to clean case values, as indicated by the shape factor results in figure 5.4 (c) which converge to Blasius flow values,  $H = 2.59$ . This, together with the low amplitude of the harmonics in this step case (20 times lower than the fundamental mode amplitude), discards any explanation implying non-parallel effects or non-linear mechanisms. All this makes a description based on non-modal growth mechanisms in this region increasingly compelling.

Figure 5.20 shows the zoomed contours of the spanwise vorticity and streamlines at the step edge. A clear vortical structure can be observed in the near-wall, counterrotating (note different colors from vorticity contours) the incoming TS wave, as also observed from the phase contours shown in figure 5.16. It is important to note that no recirculating flow was identified from the DNS baseflow in the region where this vortical structure is observed. This secondary structure becomes more elongated when a TS wave goes over it (figure 5.20 (a)-(c)) and is almost vanished when the edge of the vortex is at the step edge (figure 5.20 (b)). Unfortunately, PIV phase-locked images could not capture this structure near the wall given the high reflections present in this region. Nevertheless, the reader can refer to figure A.1 in appendix A to observe the evolution of the disturbances close to the step from PIV compared to DNS results in subcritical step case conditions. The origin of this near-wall vortical structure remains unknown. However, further analysis concerned with the different energy contributions governing this region could shed light on the mechanisms giving rise to it.

Figure 5.21 shows the  $u$  contours and streamlines of the fundamental mode in critical step case conditions as obtained from phase-locked PIV frames. Upstream of the step the disturbance appears slightly tilted against the shear, as also observed in the subcritical step case. Downstream of the step it exhibits tilting in the opposite direction, in agreement with the negative production values observed in the previous section in figure 5.18 (c). However, in the step region, the TS wave is highly distorted compared to the subcritical step case. Indeed, one can even identify from PIV frames two secondary regions with apparently vortical motion upstream (figure 5.21 (e)) and downstream (figure 5.21 (f)) of the step. These are in agreement with regions presenting opposite phase contours, as observed from figure 5.16 (e)-(f) in section 5.4.

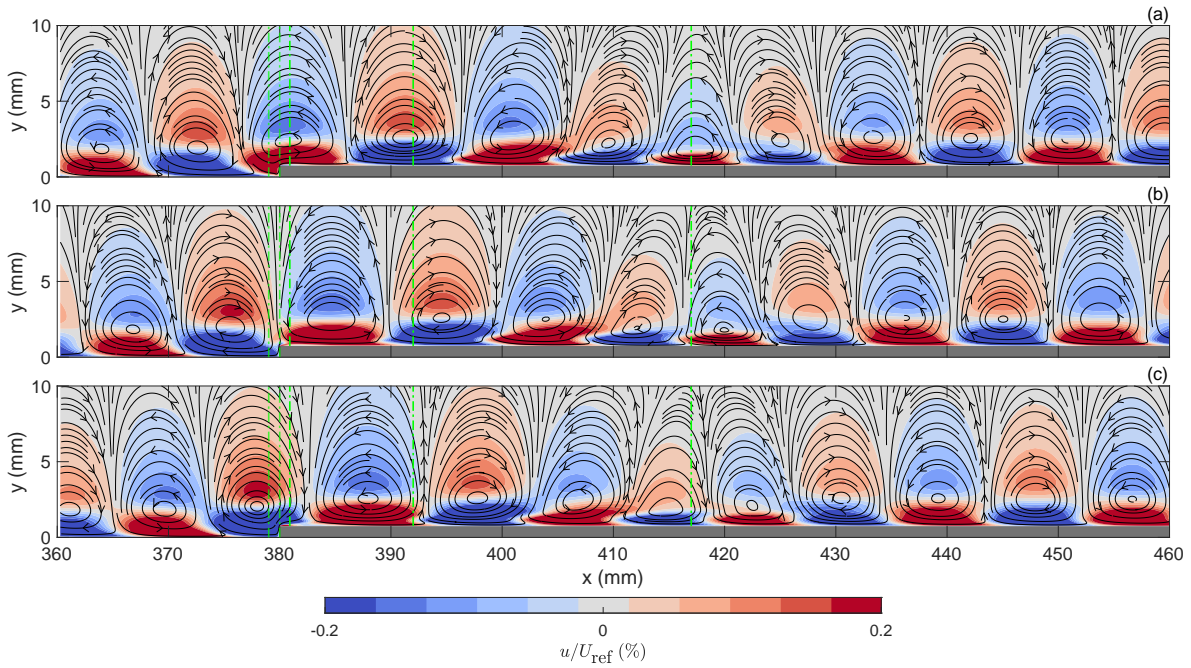


Figure 5.19: Contour fields of the disturbance  $u$  component from DNS results at three different phases of the TS wave cycle:  $\phi = 0^\circ$  (a),  $\phi = 60^\circ$  (b) and  $\phi = 120^\circ$  (c). Subcritical step conditions ( $h/\delta^* = 0.775$ ) with fundamental mode frequency being  $F = 90$ . Disturbance streamlines are also included at the corresponding phase. Green dash-dotted lines indicate the streamwise positions where production changes sign in figure 5.18 (b). The wall-normal coordinate has been scaled by 1.35 for visualization purposes.

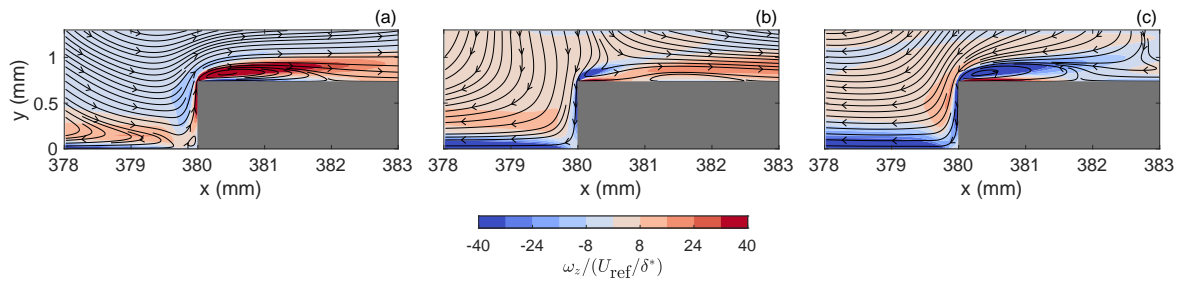


Figure 5.20: Contours of the normalized spanwise vorticity ( $\omega_z$ ) and disturbance streamlines around the step corner from DNS results at three different phases of the TS wave cycle:  $\phi = 0^\circ$  (a),  $\phi = 60^\circ$  (b) and  $\phi = 120^\circ$  (c). Subcritical step conditions and forcing frequency at  $F = 90$ . Wall-normal axis is scaled by 1.35 for visualization purposes.

Supercritical step results in figure 5.22 exhibit upstream tilting of the disturbance against the mean shear before reaching the step, in line with subcritical and critical step results. However, in this case, at the step region, the TS wave undergoes even stronger distortion. From the phase contours shown in the previous section, (section 5.4 in figure 5.16 (j)-(i)), it was shown that the secondary structure (also observed in subcritical and critical step case conditions) presented much larger wall-normal extent in supercritical step cases. Despite being difficult to ascertain the exact evolution of the TS wave at the step, one could speculate that, because of the larger wall-normal extent of this counterrotating structure at the step edge, the TS wave now becomes isolated from the disturbances downstream of this secondary vortex (note figure 5.22 (d)). This could explain the merging observed in figure 5.22 (e) between the incoming TS wave and the disturbance downstream of the secondary structure. Finally, downstream of the step the disturbance tilts in the mean shear direction and highly distorts due to non-linear effects, reshaping into structures characterized by an approximately  $45^\circ$  inclination that precedes the onset of breakdown to turbulent flow. The flow is highly three-dimensional downstream of this step case.

It becomes clear from the previous results that the topological features of the disturbance become increasingly complex with higher steps. Two characteristic vortical structures have been observed upstream and downstream of the step. On the one hand, an upstream vortical motion could be detected in front of the critical

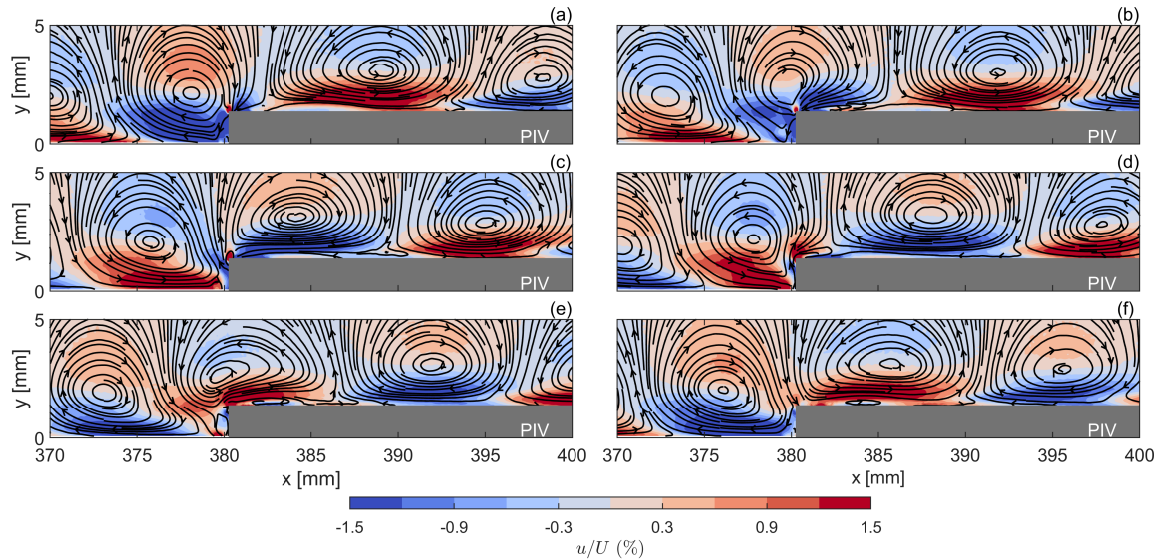


Figure 5.21: Velocity contours ( $u$ ) and disturbance streamlines for a critical step,  $h/\delta^* = 1.462$  from PIV phase-locked frames. The different images correspond to the different phases measured:  $\phi = 0^\circ$  (a),  $\phi = 60^\circ$  (b),  $\phi = 120^\circ$  (c),  $\phi = 180^\circ$  (d),  $\phi = 240^\circ$  (e) and  $\phi = 300^\circ$  (f). Wall-normal axis is scaled by 1.35 for visualization purposes.

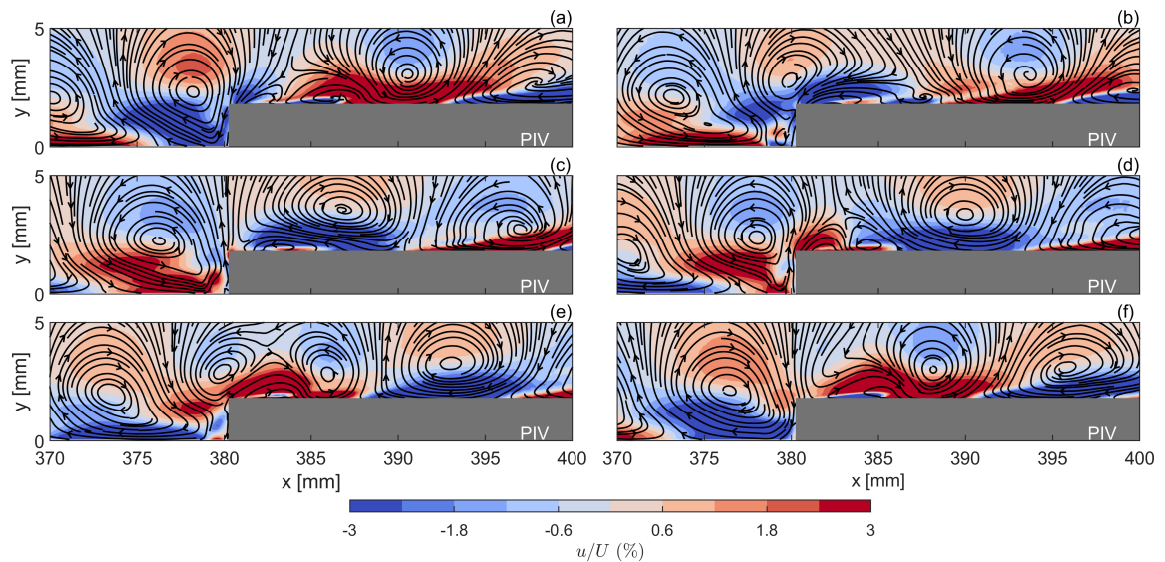


Figure 5.22: Velocity contours ( $u$ ) and disturbance streamlines for a supercritical step,  $h/\delta^* = 1.950$  from PIV phase-locked frames. The different images correspond to the different phases measured:  $\phi = 0^\circ$  (a),  $\phi = 60^\circ$  (b),  $\phi = 120^\circ$  (c),  $\phi = 180^\circ$  (d),  $\phi = 240^\circ$  (e) and  $\phi = 300^\circ$  (f). Wall-normal axis is scaled by 1.35 for visualization purposes.

and supercritical step cases. This could be linked to the presence of a geometrical suction slot in this region. On the other hand, the downstream vortical structure is present in all step cases and its wall-normal extent is largely modified with the step height, assuming considerable dimensions in the supercritical step case. The mechanisms giving rise to this near-wall vortical structure could not be established from these results. However, its dimensions could be related to the onset of breakdown immediately downstream given that, from the present results, its wall-normal extent appears to have dramatic effects on the TS wave distortion at the step.

## 5.6. Disturbance energy spectra over an FFS

All the results presented so far were mainly concerned with the growth and topological features of the fundamental mode and its harmonics at the step. However, the presence of the step could be forcing other types of

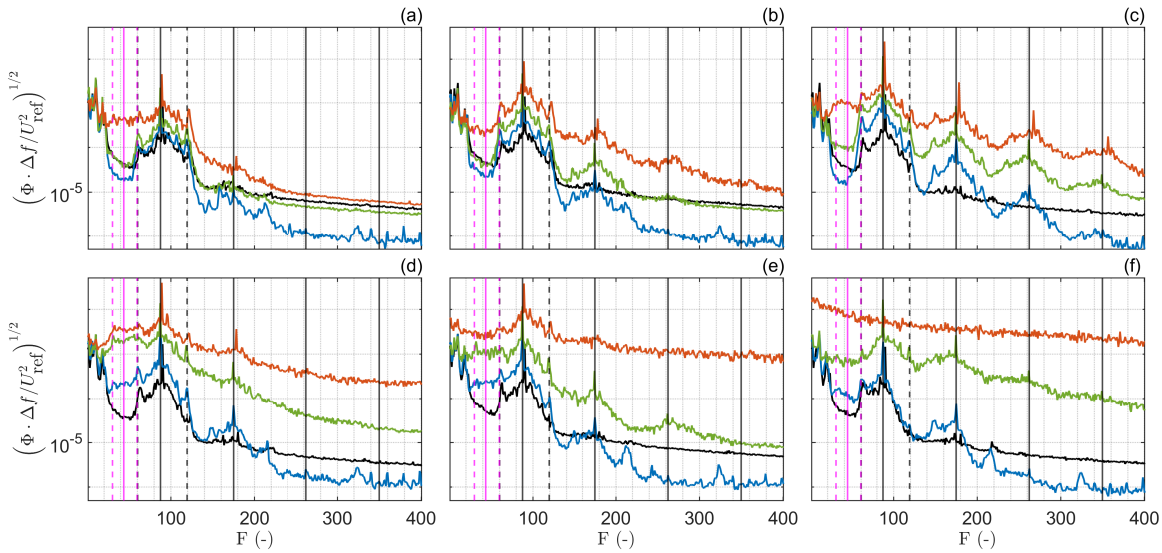


Figure 5.23: Power Spectral Density results from HWA measurements for different step heights with acoustic forcing at  $F = 90$ . Streamwise locations shown:  $x = 341$  mm (a),  $x = 361$  mm (b),  $x = 374$  mm (c),  $x = 383$  mm (d),  $x = 396$  mm (e) and  $x = 421$  mm (f). Step is located at  $x = 380$  mm. Clean case ( $h/\delta^* = 0$ , black), subcritical step ( $h/\delta^* = 0.775$ , blue), critical step ( $h/\delta^* = 1.462$ , green) and supercritical step ( $h/\delta^* = 1.950$ , orange). The x-axis corresponds to reduced frequency,  $F = (2\pi f U_{ref}^2 / \nu) \times 10^6$ . Full vertical lines denote fundamental and higher harmonics (black) and subharmonic (magenta) of the forced frequency. Dashed black lines indicate the limits of the naturally forced TS waves. Dashed magenta lines denote the subharmonic corresponding to the band of unstable TS waves.

unsteadiness on the flow (e.g. Kelvin-Helmholtz instability, shedding coming from the recirculating regions, etc.) which could also play an important role in the onset of transition. To retrieve such information, the spectral results from HWA measurements over the step result are most useful given their high-frequency resolution. Figure 5.23 shows the Welch's Power Spectral Density (PSD) results retrieved from HWA measurements at different streamwise stations for the different step heights tested (distinguished in colors). The spectral data is taken at the wall-normal position ( $y$ ) where the disturbance at  $F = 90$  presents its maximum. Dotted black lines indicate the frequency band where natural TS waves are excited by receptivity to background wind tunnel disturbances. In addition, full black lines indicate the forced TS wave and its harmonics.

From figure 5.23 it can be observed that there is a regime of unstable TS waves in addition to the forced TS frequency. In chapter 4 (section 4.3) this frequency range was confirmed to match the range of unstable frequencies predicted from LST. This range of unstable TS waves (which is also observed in unforced conditions) is the result of the receptivity at the LE to background disturbances. It appears that there is an uncontrolled source (e.g. white noise, uncontrolled vibrations, etc.) exciting all frequencies at the same time (similar to the effect of introducing a wavepacket) which triggers the LE receptivity to multiple frequencies, leading to a wide range of possible modes becoming unstable in the present set-up. Note that this is very different from the forcing applied in DNS, where only one frequency is being excited through a blowing and suction strip.

From figure 5.23 (a)-(c) it can be observed that, upstream of all steps, higher harmonics are rapidly amplified due to the adverse pressure gradient. In line with observations from previous studies (Dovgal et al., 1994), as the wall-normal location of the inflection point gets farther from the wall the destabilizing effect becomes more detrimental (recall observations from previous section 5.3, figure 5.11). Interestingly, PSD results at critical and supercritical step conditions exhibit rapid growth on the subharmonic regime (enclosed by magenta dashed lines in figure 5.23) even upstream of the step. The growth of the subharmonic content with the step height will be further discussed later in section 5.6.1.

Downstream of the subcritical step case higher harmonics exhibit lower amplitude, indicating that the flow is stabilized. However, the subharmonic growth is still present, growing in streamwise direction, in accordance with observations in section 5.3, where the maximum amplitude of the subharmonic was seen to surpass the amplitude of the TS wave in critical and supercritical step conditions (see figure 5.10 (b) and (c)). Conversely to the subcritical step case, both critical and supercritical steps show the energy being homogeneously distributed all over the spectral domain, representing the flow randomization and the breakdown to turbulence (see full turbulent spectra in figure 5.23 (f) at a supercritical step).

Figure 5.24 shows how the spectral content changes in wall-normal direction for the different streamwise

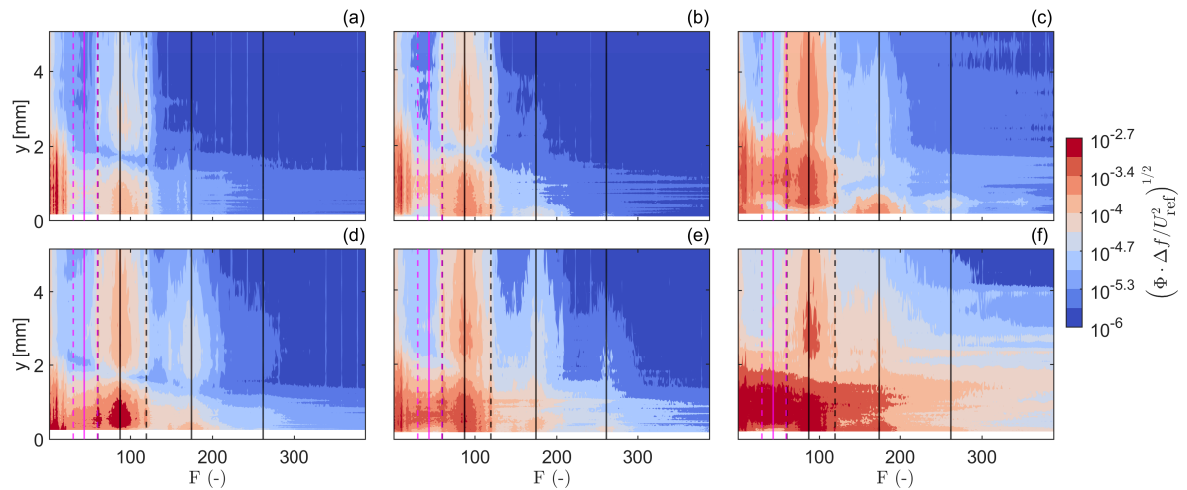


Figure 5.24: PSD contours from HWA measurements in critical step case conditions ( $h/\delta^* = 1.462$ ) with acoustic forcing at  $F = 90$ . Streamwise locations shown:  $x = 341$  mm (a),  $x = 361$  mm (b),  $x = 374$  mm (c),  $x = 383$  mm (d),  $x = 396$  mm (e) and  $x = 421$  mm (f). Step is located at  $x = 380$  mm. The x-axis corresponds to reduced frequency,  $F = (2\pi f U_{\text{ref}}^2 / \nu) \times 10^6$ . Full vertical lines denote fundamental and higher harmonics (black) and subharmonic (magenta) of the forced frequency. Dashed black lines indicate the limits of the naturally forced TS waves. Dashed magenta lines denote the subharmonic corresponding to the band of unstable TS waves.

locations measured with HWA shown in the figure above (figure 5.23). From this figure the topology of the different unstable frequencies can be retrieved. The range of TS waves and harmonics can be easily identified from the second lobe that they exhibit in the freestream. In turn, the subharmonic regime only exhibits one maximum located in the near-wall. From figure 5.24 (c) it can be observed that the disturbances maxima (for subharmonic, TS waves and harmonics) lift in the wall-normal direction in front of the step but suddenly moves towards the step once it goes over it (figure 5.24 (d)). Similar observations were made from the amplitude results from PIV and DNS fields presented in section 5.3. However, in this case, it is remarkable to observe that the subharmonic content also features similar behavior to the fundamental mode over the step, becoming highly destabilized in regions where the TS waves also do.

Eppink (2020) experimentally studied the unsteady flow behavior when a CFI goes over an FFS. The author could identify shedding and flapping frequency ranges from their spectral results. In addition, they also speculated the presence of a K-H type instability leading to the shedding observed at high frequencies. However, from the present spectral results (figure 5.23), the high energy content that both naturally unstable TS waves and their harmonics have, make the identification of flapping and shedding challenging. Indeed, it could be the case that these phenomena were indeed taking place in the flow but became overshadowed by the high energy content of the rest of the instability waves. Moreover, due to reflections near the wall in PIV measurements, it is not possible to retrieve accurate data regarding the geometry and reversed velocity in the recirculating regions, which makes it even more difficult to identify the characteristic frequencies of shedding and flapping from the Strouhal numbers reported in the literature (Strouhal numbers for LSB flapping and shedding are usually given as a function of the LSB length and external velocity). Nevertheless, it is important to emphasize that if shedding and flapping were present in this problem, one would expect these phenomena to take place at very different frequency ranges for different step heights due to the dependence of the recirculating region length on the step height. However, from figure 5.23 it is observed that all spectral *humps* take place within the same frequency range for different steps.

### 5.6.1. The subharmonic content

The previous PSD results from HWA measurements (figure 5.23 and figure 5.24) present significant growth in the subharmonic content (denoted with magenta dashed lines in the figures) with increasing step height. However, DNS results do not predict the growth of the subharmonic modes when only the fundamental mode is excited. This indicates that the subharmonic mode must come from the non-linear interaction between other modes originated in the set-up due to the LE receptivity to background disturbances.

Subharmonic growth has previously been reported by several authors to generate from non-linear interaction. The amplification of the subharmonic content is usually attributed to a symmetric three-wave resonance, as proposed by (Craik, 1971). The experiments of Kachanov and Levchenko (1984b) and Medeiros and

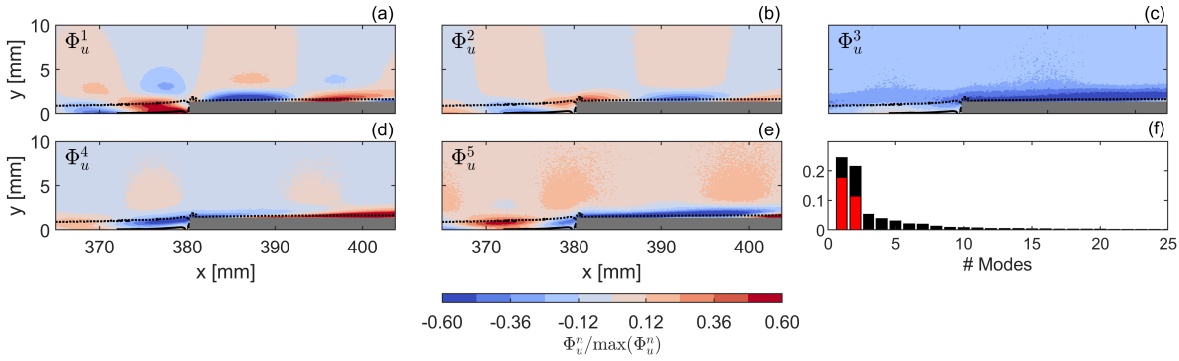


Figure 5.25: POD results for a critical step ( $h/\delta^* = 1.462$ ) with acoustic forcing at  $F = 90$ . First five normalized POD modes from the  $u$ -component of the disturbance (a, b, c, d, e) and energy fraction per mode from both  $u$ - (black bars) and  $v$ - (red bars) components.

Gaster (1999) concern two different examples where subharmonic resonance was observed. On the one hand, Kachanov and Levchenko (1984b) forced single-frequency disturbances using a vibrating ribbon and observed the onset of a packet of low-frequency oscillations growing along with the subharmonic. It was later observed that the instabilities associated with this subharmonic regime correspond to 3D oblique TS waves with half the streamwise TS wavenumber. On the other hand, Medeiros and Gaster (1999) also observed the emergence of subharmonic behavior when a wave packet exciting all unstable frequencies was introduced in the experiments. The author also signals the emergence of oblique waves in the process. In the present experiments, selective amplification (as in Gaster's experiments) from background fluctuations is also observed. This can be noticed from the hump of TS waves excited between  $60 \leq F \leq 119$ , corresponding to the unstable regime of the BL (recall section 4.3). This subharmonic growth is perceived both under forced and unforced conditions, indicating that it is not related to acoustic forcing.

The work of Park and Park (2013) further confirms that the growth of the subharmonic is present in laminar-turbulent transition with two-dimensional roughness elements. The authors studied the effect of two-dimensional humps with incoming two-dimensional TS wave instabilities using LST, linear and non-linear Parabolic Stability Equations (PSE). From their non-linear PSE results, the authors observe that even small initial disturbance amplitudes can lead to large subharmonic growth in the presence of a hump, exciting modes with different spanwise wavelengths (similar to the oblique modes reported in Kachanov and Levchenko (1984b)). The results of these authors further confirm that the step enhances the growth of the subharmonic through non-linear interaction, in line with the results presented in this work.

In order to observe whether oblique waves related to the subharmonic content could be present in the current experiments, POD results are examined. Figure 5.25 shows the first POD modes of  $u$  obtained for a critical step in forced conditions. Forced TS waves at  $F = 90$  can be identified from modes 1 and 2 due to their wavelength being close to the one observed from phase-locked images,  $\lambda_x \approx 16$  mm. In addition, given the topology of mode 3, this mode is likely to be triggered by some background wind tunnel noise source, as previously speculated from clean case results shown in section 4.5. However, the growth that this mode exhibits over the step corroborates that its exact nature remains unclear<sup>4</sup>. Modes 4 and 5 depict long wavelengths being about twice the TS wavelength. These modes could be the cross-section of oblique TS waves giving rise to the subharmonic resonance observed from the spectra.

To confirm the relationship between modes 4 and 5 and the subharmonic regime, the resulting wall-normal profile obtained from bandpassing HWA spectral results between  $30 \leq F \leq 61$  (subharmonic range) is compared with the obtained RMS from reconstructing  $\Phi_u^4$  and  $\Phi_u^5$  in figure 5.26. Reconstruction from POD modes has only been possible for a subcritical (modes 5 and 6) and a critical step (modes 4 and 5). In the supercritical step case, given the large energy that the high-frequency content acquires, discerning these oblique modes from the rest of the modes becomes more challenging<sup>5</sup>. From figure 5.26 it can be observed that very good agreement is found between reconstructed POD modes and subharmonic modes. The latter sustains that the subharmonic content in the spectra is associated with modes featuring twice the TS wavelength, in line with

<sup>4</sup>Since PIV results are not time-resolved it is not possible to identify this mode with any peak from the HWA spectra. In addition, the lack of spanwise measurements makes it also challenging to determine its nature.

<sup>5</sup>The reader is referred to figure A.2 and figure A.3 in appendix A for POD results at subcritical and supercritical step heights.

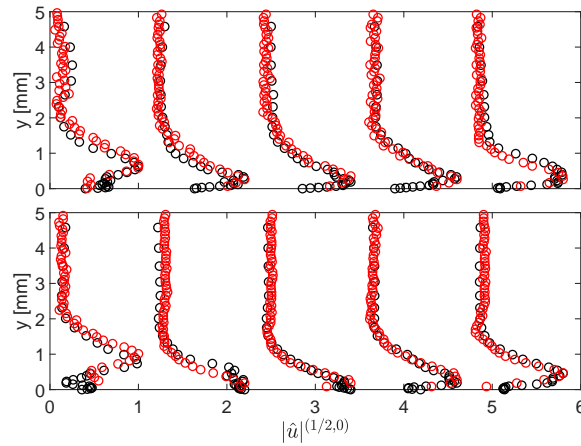


Figure 5.26: Wall-normal profiles of the subharmonic modes as extracted from HWA spectral data bandpass at  $30 \leq F \leq 57$  (black symbols) and from the RMS of the reconstructed flow from POD modes 5-6 for a subcritical step and 4-5 for a critical step (red symbols). Subcritical step results (top figure) and critical step results (bottom figure). Streamwise locations shown (from left to right):  $x = [371, 382, 386, 391, 401]$  mm.

Kachanov (1994) claims. Unfortunately, given the lack of spanwise measurement planes, it is not possible to confirm the three-dimensionality (obliqueness) of these modes.

The emergence of subharmonic resonance before laminar flow breakdown is usually associated with an H-type (Herbert, 1984) transition scenario. However, the appearance of streaky patterns in the transition fronts from IR images calls into question whether an H-type transition takes place in the present experiments (see figure 5.1 in section 5.1). Throughout this subsection, it has been shown that the existence of oblique waves in the set-up might be related to the growth of the subharmonic regime. If this is true, the onset of streaks further downstream (as observed from IR results) could be explained through the non-linear interaction of oblique waves, as already reported in other experiments (Schmid and Henningson, 2012). Nevertheless, high spatial resolution and detailed time-resolved measurements would be necessary in the transition region to confirm which type of transition scenario dominates these experiments.

## 5.7. Effect of disturbance frequency

Previous sections focused on the detailed analysis of the flow features in the vicinity of the step at one frequency,  $F = 90$ . However, it is important to also understand how the step affects the amplification of other disturbance frequencies to investigate the onset of transition. To do so, in this section a step back will be taken to discuss how the results presented in section 5.1, concerned with the movement of transition, relate to the amplification observed herein for different frequencies. Finally, the TS wave shape function at different forcing frequencies will be presented to show that the growth dynamics governing the step are expected to be overall very similar to the ones presented before ( $F = 90$ ) for  $F = 60$  and  $F = 110$ .

Figure 5.27 shows the N-factor at different step heights for the different forcing frequencies tested. DNS and experimental data are included in clean and subcritical step case conditions (figure 5.27 (a)-(b)). Agreement between experimental and numerical data is very good for the fundamental mode frequencies  $F = 90$  and  $F = 110$ . As previously discussed in chapter 4 (section 4.3), the results at  $F = 60$  are disrupted by an additional source of noise in the wind tunnel background, as observed from the results of the coherence between the HWA and the microphone signals in figure 4.4 from chapter 4. This additional source of noise at a frequency very close to  $F = 60$  interacts with the fundamental mode forced with acoustics and creates the modulated TS shape. This explains the larger discrepancy between experimental and DNS results at  $F = 60$  compared to the other two forcing frequencies.

Figure 5.27 (b) shows the effect of a subcritical step for different fundamental mode frequencies. Upstream of the step all frequencies exhibit growth. Downstream of the step, similar to the discussion reported in all previous sections for  $F = 90$ , all frequencies depict a region of complex growth behavior. All modes depict a region of a pronounced initial decay that ends at around  $x \approx 420$  mm. From that location onwards, the TS wave converges to the growth rates observed in clean case conditions, i.e.  $F = 110$  and  $F = 90$  decay while  $F = 60$  grows after the step. However, compared to smooth-surface results, the final N-factor increase is

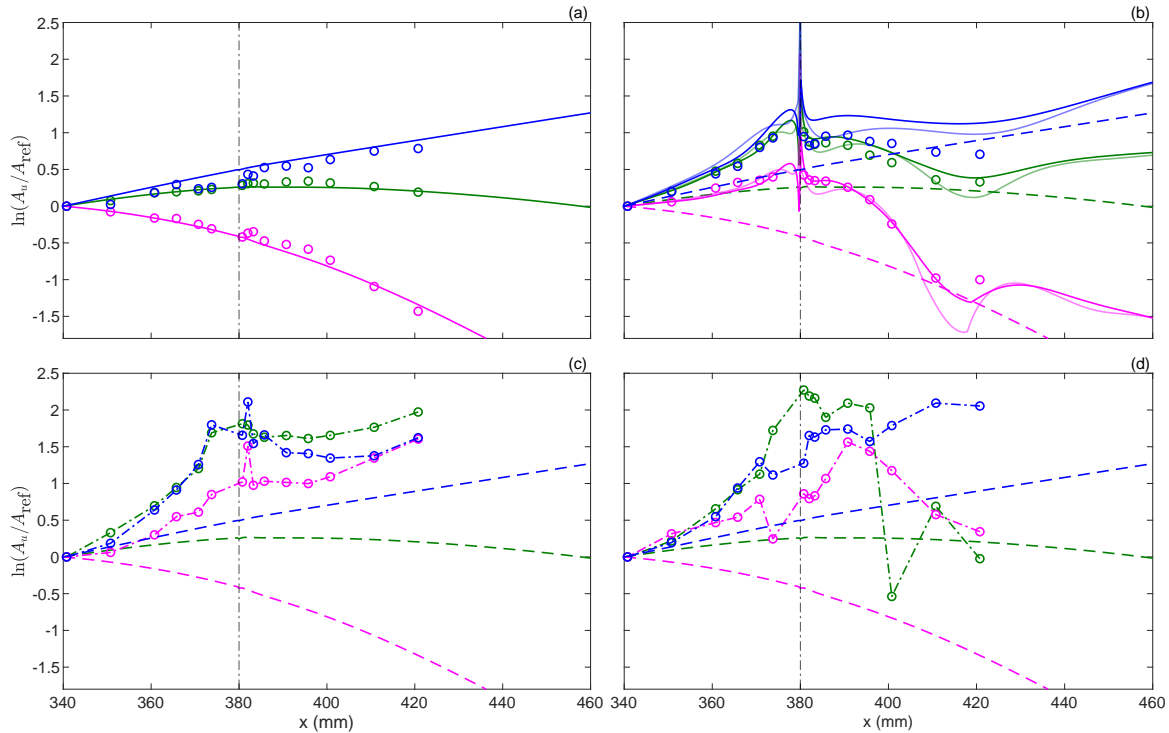


Figure 5.27: N-factor of the fundamental mode for different forcing frequencies:  $F = 60$  (blue),  $F = 90$  (green) and  $F = 110$  (magenta). Clean case (a), subcritical step (b), critical step (c) and supercritical step (d) conditions. Symbols denote HWA measurements, full lines represent DNS results in clean (a) and subcritical step conditions (b). Dashed lines in (a), (b) and (c) denote the clean case results from DNS. Note that the dashed-dotted lines between HWA data points are not numerical data but are just included for easier interpretability of the experimental data trend.

higher with the step (note the difference between  $N$  in clean case and step case conditions, i.e.  $\Delta N$ ), indicating that the step moves transition upstream. In general, from the results shown in figure 5.27 (b), one can observe that transition might be governed by lower frequencies in subcritical step case conditions, similar to the clean case. Therefore, in this case, despite having a region where the instability could undergo spatial transient growth in the vicinity of the step (note different amplification trends in  $|\hat{u}|$  and  $|\hat{v}|$ )<sup>6</sup>, transition might still be governed by lower frequencies downstream.

Figure 5.27 (c) shows the N-factor evolution for the different forcing frequencies tested in critical step conditions. Upstream of the step all frequencies grow, similar to the results shown in figure 5.27 (b) for a subcritical step. Downstream of the step, it can be observed that, conversely to the observations from figure 5.27 (a), now the trend of the different frequencies diverges from the one presented in smooth-surface conditions. More specifically,  $F = 90$  and  $F = 110$  continuously grow while in clean case conditions they experience decay after the step. From the N-factor levels after the step, it can be argued that the fundamental mode governing transition would be  $F = 90$  given the higher N-factors compared to the other frequencies. As expected from the sudden rise experienced immediately after the step, transition takes place close downstream of the step, as shown from figure 5.2 in section 5.1.

Interestingly, at  $x = 382$  mm, modes  $F = 110$  and  $F = 60$  present a peak in the N-factor (figure 5.27 (c)). Looking at the shape function profiles from HWA one cannot retrieve any additional peak in the TS wave corresponding to the equivalent peak observed in the N-factor. Instead, HWA measurements (not shown here) present a sudden increase of the TS wave maximum in this region. It remains unclear where does the sudden rise in the amplitude of the TS wave come from in these regions.

Figure 5.27 (d) shows the results in supercritical step conditions. Upstream of the step all frequencies experience similar growth as in critical step conditions (figure 5.27 (d)). However, both  $F = 110$  and  $F = 60$  present a sudden decay in front of the step. This could be related to the decay observed for the  $|\hat{u}|$  TS component at  $F = 90$ , which was triggered by the distortion of the TS vortex upstream of the step edge, resulting in

<sup>6</sup>The reader is referred to the end of section 5.3 for a more detailed discussion on this.

a transfer of streamwise disturbance momentum to the wall-normal direction (predicted from PIV results in figure 5.15 (i)-(j)). Downstream of the step it can be observed from figure 5.27 (d) that all modes saturate at a similar streamwise location ( $x \approx 400$  mm). From section 5.1 in figure 5.2 it was shown that transition takes place immediately after the step in supercritical step conditions, more specifically, at  $x \approx 400$ .

Figure 5.28 and 5.29 show the TS shape function from the fundamental mode when forcing at frequency  $F = 110$  and  $F = 60$ , respectively. The agreement observed from figure 5.28 (a)-(b) between DNS and HWA results is very satisfactory, both methods capturing the uncommon distortion observed from the TS wave after the subcritical step case at  $x = 420$  mm (already thoroughly analyzed for  $F = 90$  in section 5.4 and section 5.5). In turn, the disagreement between DNS and HWA observed from figure 5.29 (a)-(b) is attributed to the additional background disturbance at a similar frequency, as previously discussed.

Figures 5.28 and 5.29 (b)-(d) show that the distortion of the TS shape upstream and downstream of the step shares similar features with the results previously presented in figure 5.11 from section 5.3 at  $F = 90$ . In essence, upstream of the step the TS wave develops a secondary lobe due to the growth of the mean shear in higher wall-normal locations. Moreover, right after the step, the TS wave exhibits a secondary near-wall vortex which in the case of higher step cases prevails further downstream (see figures 5.28 and 5.29 (d)) while in subcritical step cases it vanishes (see figures 5.28 and 5.29 (b)). Further downstream it was observed for the case of  $F = 90$  that the TS wave presented large distortion in regions where non parallel effects were negligible, at  $x \approx 420$  mm. It is observed from figure 5.28 (b) that at  $F = 110$  an even stronger distortion at this location is observed. In turn, at  $F = 60$  (figure 5.29 (b)) this is not discernible. This indicates that higher frequencies might be more susceptible to large distortion in these regions, probably for their maxima being closer to the wall, i.e. in regions of high shear.

It is important to notice that, given the large amplitude of the harmonics after the critical step (not shown here for brevity), non-linear effects become relevant and three-dimensional flow might start to develop, i.e. the onset of breakdown, in figures 5.28 and 5.29 (c)-(d). Therefore, any modulation observed in the wall-normal TS shape profile (particularly after the step region in critical and supercritical step cases) is not representative of the actual perturbation shape, given the possible modulation experienced by the instability in the spanwise direction.

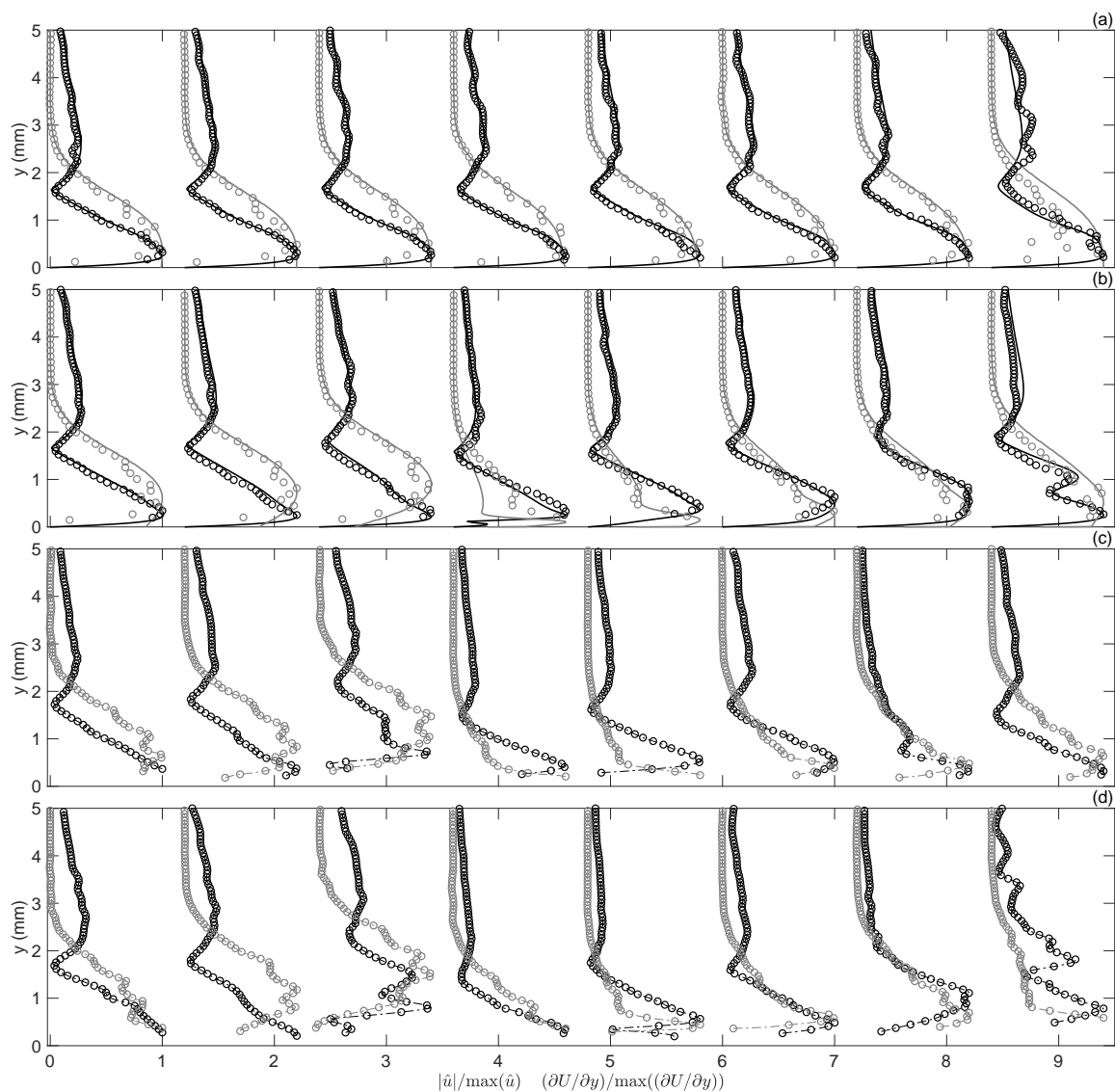


Figure 5.28: Wall-normal profiles of the fundamental mode ( $F = 110$ ) in terms of  $|\hat{u}|$  (black) and  $\partial U / \partial y$  (gray). Full lines denote DNS data and symbols (o) HWA results. Clean (a), subcritical (b), critical (c) and supercritical (d) step cases. The streamwise locations plotted are at (from left to right)  $x = [341, 361, 374, 381, 383, 391, 401, 421]$  mm with the step at  $x = 380$  mm. The horizontal spacing between profiles is set to  $\Delta = 1.2$  for legibility. Note that the dashed-dotted lines in (c) and (d) are not numerical data but just intend to trace the experimental data points for easier interpretability.

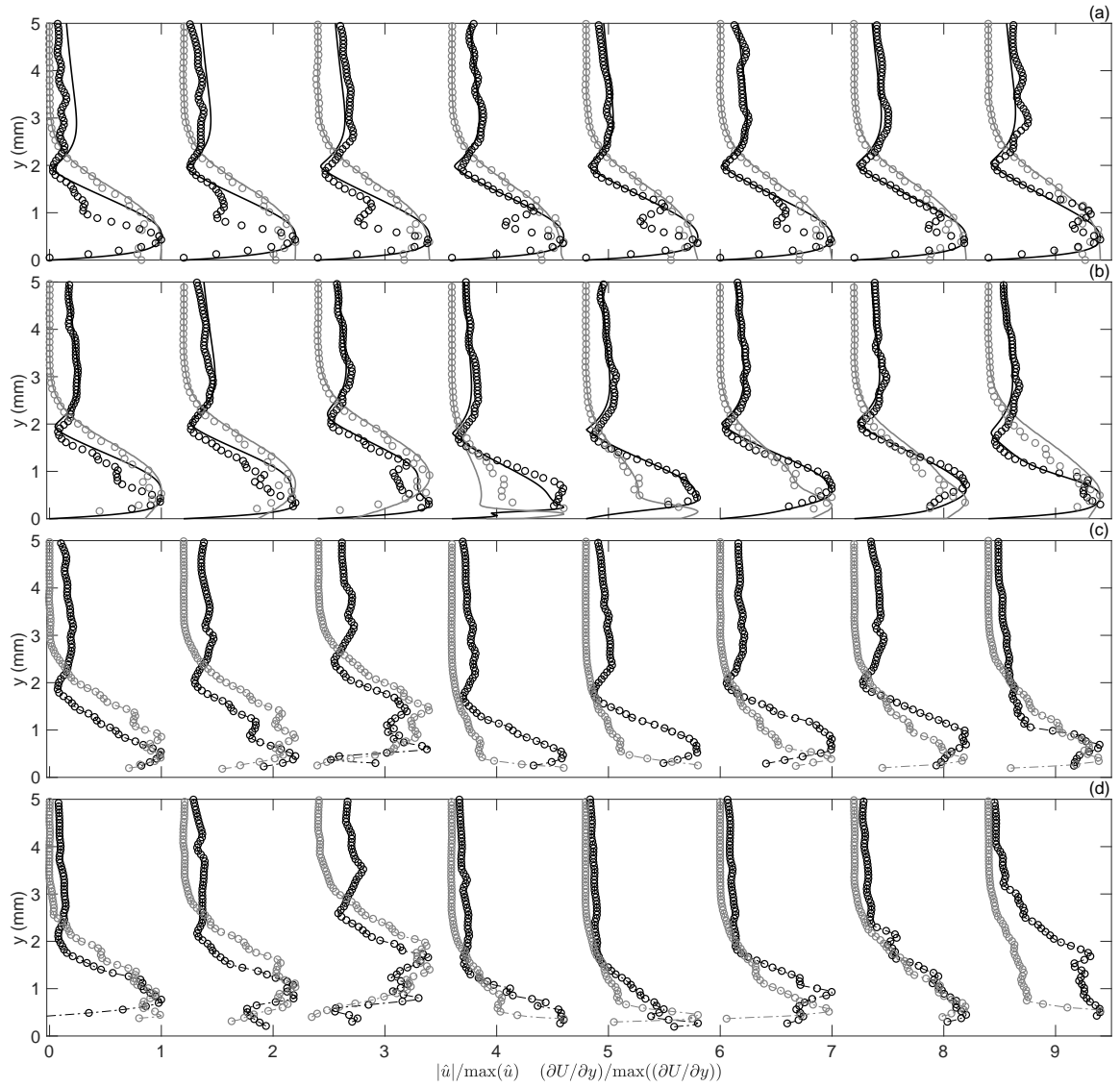


Figure 5.29: Wall-normal profiles of the fundamental mode ( $F = 60$ ) in terms of  $|\hat{u}|$  (black) and  $\partial U / \partial y$  (gray). Full lines denote DNS data and symbols (o) HWA results. Clean (a), subcritical (b), critical (c) and supercritical (d) step cases. The streamwise locations plotted are at (from left to right)  $x = [341, 361, 374, 381, 383, 391, 401, 421]$  mm with the step at  $x = 380$  mm. The horizontal spacing between profiles is set to  $\Delta = 1.2$  for legibility. Note that the dashed-dotted lines in (c) and (d) are not numerical data but just intend to trace the experimental data points for easier interpretability.

# Conclusions and Recommendations

## 6.1. Conclusions

The stability of Tollmien-Schlichting waves in the presence of Forward-Facing Steps has been studied by means of experiments in this work. In addition, results from two-dimensional Direct Numerical Simulations performed at DLR were also presented to gain further insight into the physics of the problem.

The global effect of FFS on transition has been studied using Infrared Thermography. Results show that, in line with the previous literature (Crouch et al., 2006; Perraud and Seraudie, 2000; Wang and Gaster, 2005), increasing the step height moves transition upstream. The present results on laminar-turbulent transition show poor correlation with the existing  $\Delta N$  models and fits found in literature, which in addition present large differences among the works of different authors. These observations indicate the difficulty of describing the effect of an FFS on transition with a few non-dimensional parameters. These findings suggest that the step could be highly dependent on the particular experimental conditions, ranging from the different measurement techniques used to identify transition (Costantini, 2016) to the different incoming disturbance amplitudes.

Close examination of the meanflow and disturbance features in the vicinity of the step has been possible by means of PIV and HWA measurements. Detailed measurements in the step region allowed for comparison with 2D DNS results in clean and subcritical step ( $h/\delta^* = 0.775$ ) conditions. Throughout this work, an excellent agreement has been observed between DNS and experimental data. Thus validating the study of subcritical step cases with 2D DNS. On the other hand, critical ( $h/\delta^* = 1.462$ ) and supercritical ( $h/\delta^* = 1.950$ ) step cases were studied only experimentally given the high non-linear interactions and subsequent three-dimensional flow after the step region.

Figure 6.1 is presented herein to summarize the most important observations made from experimental and numerical data close to the step region. These will be briefly explained in the remaining of this chapter.

Upstream of the step, the boundary layer thickness increases due to the adverse pressure gradient built by the step, and TS waves undergo large exponential growth. The destabilizing effect is observed to become stronger with higher steps, in line with the highly positive production term present in that region.

At the step location, the boundary layer presents a large curvature distortion as a combined effect of two quasi-simultaneous but opposite pressure gradients. In addition, the TS wave is highly distorted by the step geometry, with most of the streamwise momentum of the disturbance being transferred to the wall-normal direction. Immediately after the step edge, the opposite takes place. In this region  $|\hat{u}|$  and  $|\hat{v}|$  exhibit opposite growth trends and, interestingly, a near-wall vortical structure is originated which manifests in the TS shape functions as a secondary lobe, similar to observations in Shahzad (2020). Disturbance streamline results from DNS (for subcritical steps) show this near-wall vortex to counterrotate the incoming TS wave. In addition, PIV results present explosive growth of this secondary structure in wall-normal direction when the step height is increased, drastically distorting the incoming TS waves in the supercritical step case.

Downstream of the step, subcritical step cases exhibit large differences from critical and supercritical ones (figure 6.1).

On the one hand, results in subcritical step conditions show the secondary structure confined in the near-wall, decaying in streamwise direction and finally vanishing. After this region, the TS wave undergoes a complex growth behavior characterized by regions where the production term changes sign several times along the streamwise direction. Interestingly, despite non-parallel effects being negligible in this region, results from

the OS solver present a large discrepancy with DNS and experiments in that region. Following the work of Marxen et al. (2009), when the disturbance components orthogonal to the baseflow are computed, it is observed that the maximum of  $|\hat{u}_{||}|$  and  $|\hat{v}_{\perp}|$  present different growth trends, pointing towards non-modal growth mechanisms active in these regions. Examination of the DNS perturbation flowfield in this area exhibits the tilting direction of disturbances with respect to the mean shear to be closely related to a change of sign in the production term. These findings indicate that the Orr-mechanism could play a role in the non-modal growth of disturbances after the step. Further downstream, the amplification of the TS wave recovers the trends observed in clean case conditions but with higher disturbance amplitudes. Results at different forcing frequencies show that in subcritical step cases the onset of transition is governed by low frequencies, similar to clean case conditions.

On the other hand, critical and supercritical step cases exhibit destabilization immediately after the step for the three forcing frequencies tested. Downstream of the step the amplitude of the higher harmonics increases, with breakdown to turbulent flow taking place within the field of view in supercritical step conditions. Results at different forcing frequencies show that transition is governed by the disturbance presenting maximum amplification at the step, in this case,  $F = 90$ .

The aforementioned observations suggest that the dimensions of the near-wall structure observed at the step edge could be linked to or be the consequence of some alternative mechanism highly destabilizing the flow in that region. Nevertheless, in the context of the present work, it has not been possible to find out the origin of this near-wall vortex.

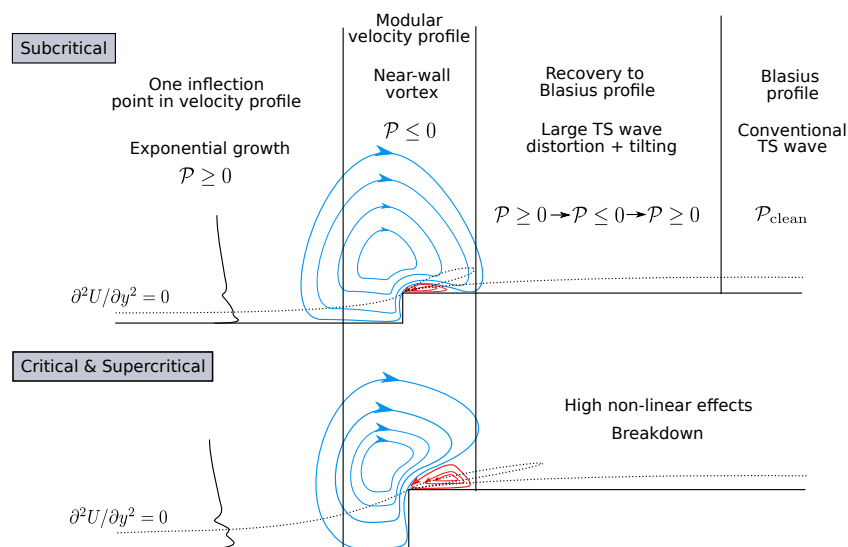


Figure 6.1: Schematic of main flow features and growth trends found in this work for a FFS with an incoming TS wave.

Finally, from spectral results during HWA measurements it has been observed that the subharmonic content is highly sensitive to the step height. This is in line with the work of Park and Park (2013), where the authors find that increasing the height of the roughness element (a hump in their work) enhances the growth of the subharmonic modes through non-linear interaction. The growth in the subharmonic content could be linked to the presence of oblique modes in the present experimental set-up, which originated through receptivity to background disturbances in the LE. These oblique modes amplify by a symmetric three-wave resonance mechanism (Craik, 1971). The presence of oblique modes in the present experiments could explain the observed streaky transition fronts identified from IR images.

## 6.2. Recommendations

In the present work, several interesting features have been observed downstream of a subcritical step case which could point to the presence of non-modal growth in these regions. To further understand and confirm the existence of such growth mechanisms, the present problem should be readdressed using non-modal tools. Furthermore, other contributions to the disturbance kinetic energy balance should be investigated following an approach similar to the one adopted in this work with the production term. Finally, following the work of Marxen et al. (2009), the streamwise evolution of distinct peaks within the TS wave (once projected into

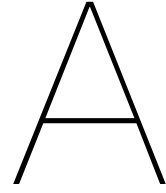
the baseflow components) should be studied to determine whether different peaks present different growth mechanisms.

In light of the results obtained for the three different step cases studied, it can be said that the one presenting more interesting features is the subcritical step. The latter presents a large streamwise extent where the disturbance exhibits tilting and continuous change in growth while, in critical and supercritical step cases, destabilization is immediate. Thus, in future experiments and numerical works it is highly recommended to further study the flow features originating in steps with heights laying in between the subcritical and the critical step heights presented in this work.

Future works concerned with the stability of TS-FFS transition should also explore how the initial TS wave amplitude changes the dynamics at the step. If the effect of the step becomes different based on the incoming TS wave amplitude, this could explain why the different  $\Delta N$  models present disagreement under different experimental conditions.

Finally, several features could be improved from the experimental set-up used in this work. First of all, the span of the present set-up should be increased to avoid the interference of the turbulent wedges with the TS-dominated transition front. This would improve the transition front measurements in this work and the consequent comparison with other experimental works as the one of Wang and Gaster (2005). Secondly, the receptivity at the model's LE should be revisited to understand the onset of such high-amplitude instabilities excited by uncontrolled background disturbances. In this regard, different TE configurations (or tripping strips) should be explored to discard any shedding at the TE. In addition, the acoustic excitation should be placed close to the LE in future experiments to remove possible sources of non-uniform receptivity (e.g. non-parallel wavefront) at the LE.





# Extra figures

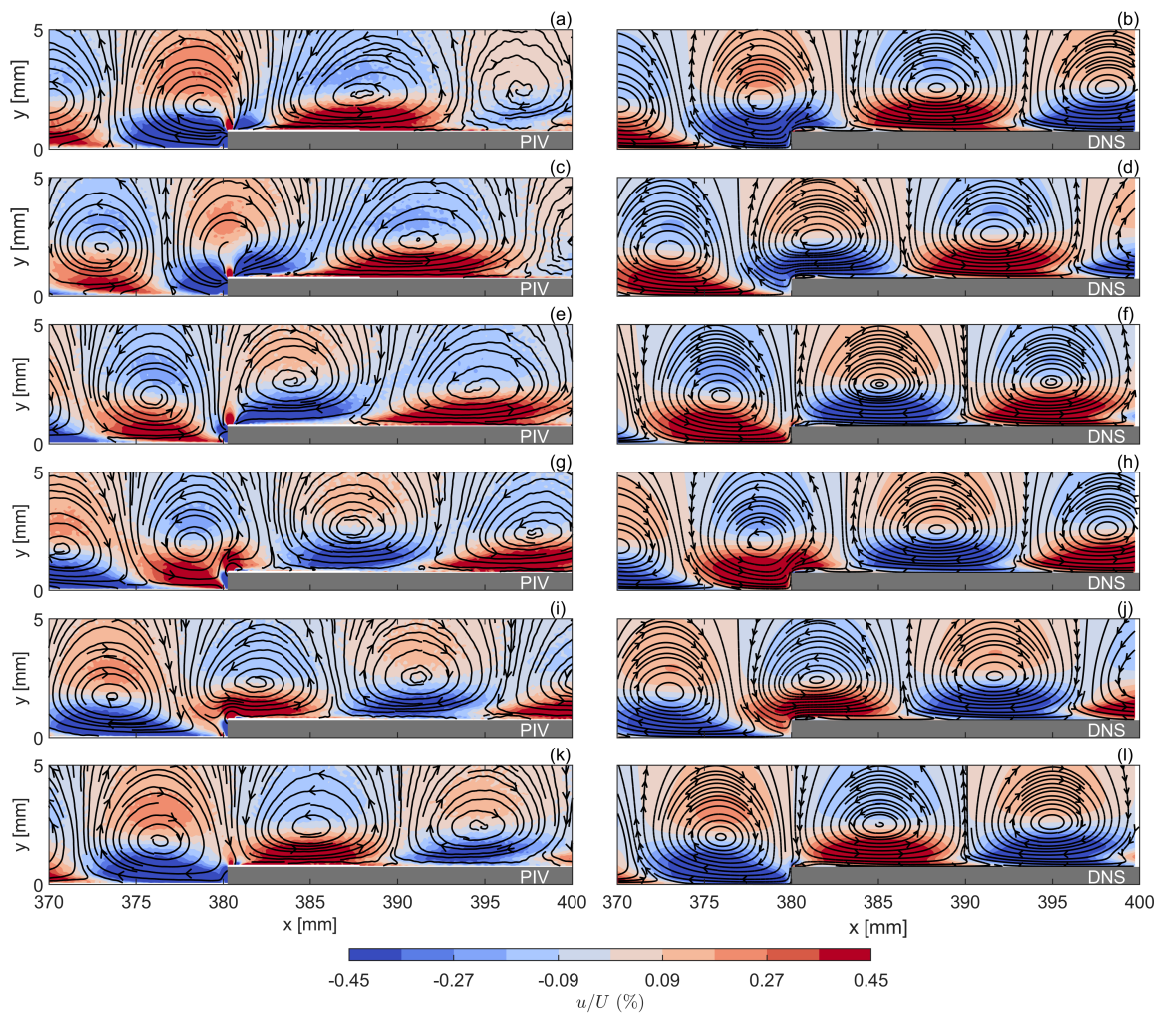


Figure A.1: Velocity contours ( $u$ ) and disturbance streamlines for a subcritical step,  $h/\delta^* = 0.775$  at forcing frequency  $F = 90$ . PIV (a, c, e, g, i, k) and DNS (b, d, f, h, j, l) results.  $\phi = 0^\circ$  (a, b),  $\phi = 60^\circ$  (c, d),  $\phi = 120^\circ$  (e, f),  $\phi = 180^\circ$  (g, h),  $\phi = 240^\circ$  (i, j) and  $\phi = 300^\circ$  (k, l). Wall-normal axis is scaled by 1.35 for visualization purposes.

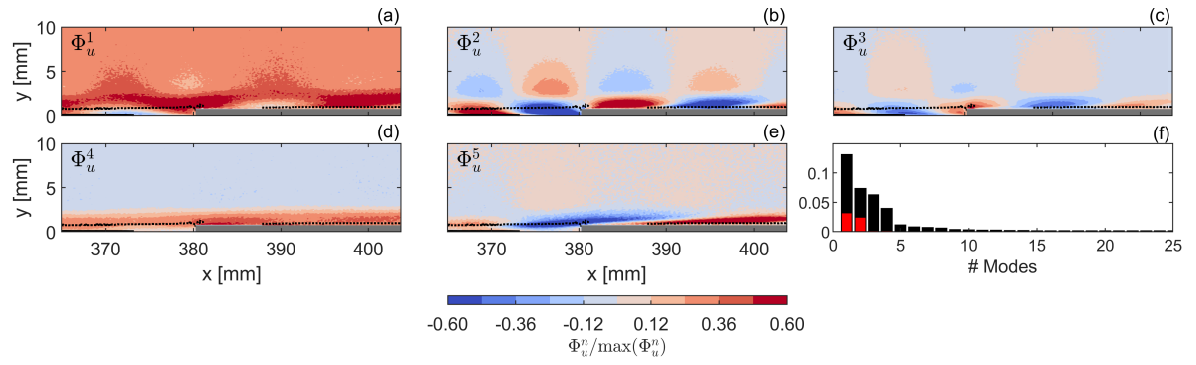


Figure A.2: POD results for a subcritical step ( $h/\delta^* = 0.775$ ) with acoustic forcing at  $F = 90$ . First five normalized POD modes from the  $u$ -component of the disturbance (a, b, c, d, e) and energy fraction per mode from both  $u$ - (black bars) and  $v$ - (red bars) components.

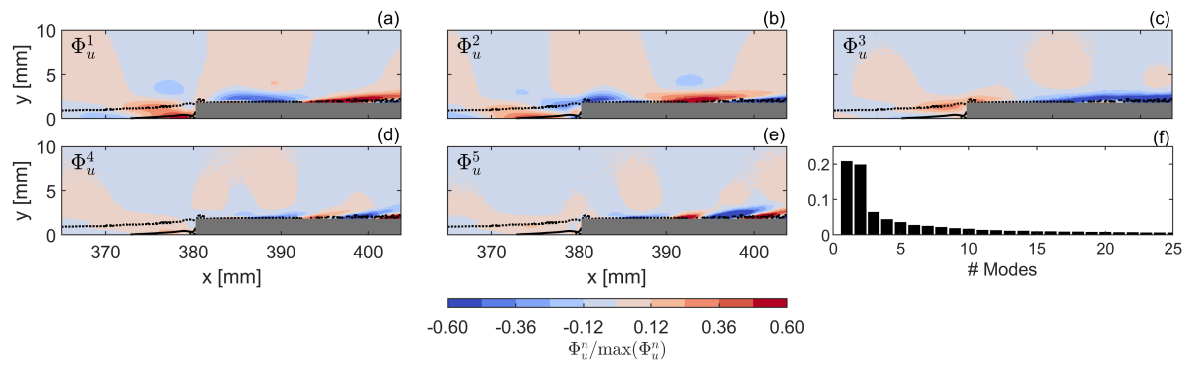


Figure A.3: POD results for a supercritical step ( $h/\delta^* = 1.950$ ) with acoustic forcing at  $F = 90$ . First five normalized POD modes from the  $u$ -component of the disturbance (a, b, c, d, e) and energy fraction per mode from both  $u$ - (black bars).

# Bibliography

- Direct numerical simulations of the impact of smooth humps on laminar-turbulent transition, 2021. Institut für Aerodynamik und Gasdynamik.
- E Åkervik, U Ehrenstein, F Gallaire, and DS Henningson. Global two-dimensional stability measures of the flat plate boundary-layer flow. *European Journal of Mechanics-B/Fluids*, 27(5):501–513, 2008.
- D Arnal and JP Archambaud. Laminar-turbulent transition control: Nlf, lfc, hlfc. *Advances in Laminar-Turbulent Transition Modeling*, 2008.
- PG Baines, SJ Majumdar, and H Mitsudera. The mechanics of the tollmien-schlichting wave. *Journal of fluid mechanics*, 312:107–124, 1996.
- HM Blackburn, D Barkley, and SJ Sherwin. Convective instability and transient growth in flow over a backward-facing step. *Journal of Fluid Mechanics*, 603:271, 2008.
- L Brandt. The lift-up effect: the linear mechanism behind transition and turbulence in shear flows. *European Journal of Mechanics-B/Fluids*, 47:80–96, 2014.
- L Brandt, D Sipp, JO Pralits, and O Marquet. Effect of base-flow variation in noise amplifiers: the flat-plate boundary layer. *Journal of Fluid Mechanics*, 687(503-528):15, 2011.
- J Casacuberta, S Hickel, and M Kotsonis. Mechanisms of interaction between stationary crossflow instabilities and forward-facing steps. In *AIAA Scitech 2021 Forum*, page 0854, 2021.
- G Chauvat. *Receptivity, Stability and Sensitivity analysis of two-and three-dimensional flows*. PhD thesis, KTH Royal Institute of Technology, 2020.
- JM Chomaz. Global instabilities in spatially developing flows: non-normality and nonlinearity. *Annu. Rev. Fluid Mech.*, 37:357–392, 2005.
- M Costantini. *Experimental Analysis of Geometrie, Pressure Gradient and Surface Temperature Effects on Boundary-Layer Transition in Compressible High Reynolds Number Flows*. PhD thesis, Rheinisch-Westfälische Technische Hochschule Aachen, 2016.
- A DD Craik. Non-linear resonant instability in boundary layers. *Journal of Fluid Mechanics*, 50(2):393–413, 1971.
- JD Crouch and VS Kosorygin. Surface step effects on boundary-layer transition dominated by tollmien-schlichting instability. *AIAA Journal*, 58(7):2943–2950, 2020.
- JD Crouch, VS Kosorygin, and LL Ng. Modeling the effects of steps on boundary-layer transition. In *IUTAM Symposium on Laminar-Turbulent Transition*, pages 37–44. Springer, 2006.
- AV Dovgal, VV Kozlov, and A Michalke. Laminar boundary layer separation: instability and associated phenomena. *Progress in Aerospace Sciences*, 30(1):61–94, 1994.
- A Drake, A Bender, and R Westphal. Transition due to surface steps in the presence of favorable pressure gradients. In *26th AIAA Applied Aerodynamics Conference*, page 7334, 2008a.
- A Drake, A Bender, and R Westphal. Transition due to surface steps in the presence of favorable pressure gradients. In *26th AIAA Applied Aerodynamics Conference*, page 7334, 2008b.
- A Drake, A Bender, A Korntheuer, R Westphal, W Rohe, G Dale, B McKeon, and S Geraschchenko. Step excrescence effects for manufacturing tolerances on laminar flow wings. In *48th AIAA Aerospace Sciences Meeting Including the New Horizons Forum and Aerospace Exposition*, page 375, 2010.

- PG Drazin. *Introduction to hydrodynamic stability*, volume 32. Cambridge university press, 2002.
- HL Dryden. Review of published data on the effect of roughness on transition from laminar to turbulent flow. *Journal of the Aeronautical Sciences*, 20(7):477–482, 1953.
- C Edelmann and U Rist. Impact of forward-facing steps on laminar-turbulent transition in subsonic flows. In *New Results in Numerical and Experimental Fluid Mechanics IX*, pages 155–162. Springer, 2014.
- CA Edelmann. Influence of forward-facing steps on laminar-turbulent transition. *Dissertation for the Doctoral Degree (University of Stuttgart, Stuttgart, 2014)*.
- CA Edelmann and U Rist. Impact of forward-facing steps on laminar-turbulent transition in transonic flows. *Aiaa Journal*, 53(9):2504–2511, 2015.
- T Ellingsen and E Palm. Stability of linear flow. *The Physics of Fluids*, 18(4):487–488, 1975.
- Jenna L Eppink. Mechanisms of stationary cross-flow instability growth and breakdown induced by forward-facing steps. *Journal of Fluid Mechanics*, 897, 2020.
- JL Eppink and C Casper. Effects of forward-facing step shape on stationary crossflow instability growth and breakdown. In *AIAA Aviation 2019 Forum*, page 3532, 2019.
- JA Franco, S Hein, and E Valero. On the influence of two-dimensional hump roughness on laminar–turbulent transition. *Physics of Fluids*, 32(3):034102, 2020.
- AD Gardner, C Eder, CC Wolf, and M Raffel. Analysis of differential infrared thermography for boundary layer transition detection. *Experiments in Fluids*, 58(9):1–14, 2017.
- G Gluyas and J Nenni. Aerodynamic design and analysis of an lfc surface(aerodynamic design criteria for maintaining laminar flow control including instability limit, surface roughness, acoustical environment, etc). *ASTRONAUTICS AND AERONAUTICS*, 4:52–57, 1966.
- ME Goldstein. The evolution of tollmien-schlichting waves near a leading edge. *Journal of Fluid Mechanics*, 127: 59–81, 1983.
- ME Goldstein. Scattering of acoustic waves into tollmien-schlichting waves by small streamwise variations in surface geometry. *Journal of Fluid Mechanics*, 154:509–529, 1985.
- RC Gonzalez and RE Woods. *Digital image processing*, hoboken, 2018.
- K Groot. *BiGlobal Stability of Shear Flows: Spanwise & Streamwise Analyses*. PhD thesis, Delft University of Technology, 2018.
- MJP Hack and P Moin. Algebraic disturbance growth by interaction of orr and lift-up mechanisms. *Journal of Fluid Mechanics*, 829:112, 2017.
- H Hansen. Laminar flow technology—the airbus view. In *27th International Congress of the Aeronautical Sciences (ICAS), Nice, France, 2010*.
- CM Harris. Absorption of sound in air versus humidity and temperature. *The Journal of the Acoustical Society of America*, 40(1):148–159, 1966.
- D Henningson. Comment on “transition in shear flows. nonlinear normality versus non-normal linearity”[phys. fluids 7, 3060 (1995)]. *Physics of Fluids*, 8(8):2257–2258, 1996.
- T Herbert. Analysis of the subharmonic route to transition in boundary layers. In *22nd Aerospace Sciences Meeting*, page 9, 1984.
- M Hultmark and AJ Smits. Temperature corrections for constant temperature and constant current hot-wire anemometers. *Measurement Science and Technology*, 21(10):105404, 2010.
- J Jiménez. How linear is wall-bounded turbulence? *Physics of Fluids*, 25(11):110814, 2013.

- B Jin, S Symon, and SJ Illingworth. Energy transfer mechanisms and resolvent analysis in the cylinder wake. *Physical Review Fluids*, 6(2):024702, 2021.
- YS Kachanov. Physical mechanisms of laminar-boundary-layer transition. *Annual review of fluid mechanics*, 26(1):411–482, 1994.
- YS Kachanov and VY Levchenko. The resonant interaction of disturbances at laminar-turbulent transition in a boundary layer. *Journal of Fluid Mechanics*, 138:209–247, 1984a.
- Yu S Kachanov and V Ya Levchenko. The resonant interaction of disturbances at laminar-turbulent transition in a boundary layer. *Journal of Fluid Mechanics*, 138:209–247, 1984b.
- J Kendall. Experimental study of disturbances produced in a pre-transitional laminar boundary layer by weak freestream turbulence. In *18th Fluid Dynamics and Plasmadynamics and Lasers Conference*, page 1695, 1985.
- PS Klebanoff. Effect of free-stream turbulence on a laminar boundary layer. In *Bulletin of the American Physical Society*, volume 16, pages 1323–+. Bull. Am. Phys. Soc., 1971.
- PS Klebanoff and KD Tidstrom. Mechanism by which a two-dimensional roughness element induces boundary-layer transition. *The Physics of Fluids*, 15(7):1173–1188, 1972.
- PS Klebanoff, KD Tidstrom, and LM Sargent. The three-dimensional nature of boundary-layer instability. *Journal of Fluid Mechanics*, 12(1):1–34, 1962.
- CF Knapp and PJ Roache. A combined visual and hot-wire anemometer investigation of boundary-layer transition. *AIAA Journal*, 6(1):29–36, 1968.
- M Kotsonis, RK Shukla, and S Pröbsting. Control of natural tollmien-schlichting waves using dielectric barrier discharge plasma actuators. *International Journal of Flow Control*, 7, 2015.
- A Krein and G Williams. Flightpath 2050: Europe’s vision for aeronautics. *Innovation for Sustainable Aviation in a Global Environment: Proceedings of the Sixth European Aeronautics Days, Madrid*, 30, 2012.
- JW Kurelek, S Yarusevych, and M Kotsonis. Vortex merging in a laminar separation bubble under natural and forced conditions. *Physical Review Fluids*, 4(6):063903, 2019.
- MT Landahl. A note on an algebraic instability of inviscid parallel shear flows. *Journal of Fluid Mechanics*, 98(2):243–251, 1980.
- D Lanzerstorfer and HC Kuhlmann. Three-dimensional instability of the flow over a forward-facing step. *Journal of fluid mechanics*, 695:390, 2012.
- L Li, P Liu, H Guo, Y Hou, X Geng, and J Wang. Aeroacoustic measurement of 30p30n high-lift configuration in the test section with kevlar cloth and perforated plate. *Aerospace Science and Technology*, 70:590–599, 2017.
- CC Lin. On the stability of two-dimensional parallel flows. ii. stability in an inviscid fluid. *Quarterly of Applied Mathematics*, 3(3):218–234, 1945.
- CC Lin. Some physical aspects of the stability of parallel flows. *Proceedings of the National Academy of Sciences of the United States of America*, 40(8):741, 1954.
- Nay Lin, Helen L Reed, and WS Saric. Effect of leading-edge geometry on boundary-layer receptivity to freestream sound. In *Instability, Transition, and Turbulence*, pages 421–440. Springer, 1992.
- JC Loiseau, JC Robinet, S Cherubini, and E Leriche. Investigation of the roughness-induced transition: global stability analyses and direct numerical simulations. 2014.
- LM Mack. Boundary-layer linear stability theory. Technical report, California Inst of Tech Pasadena Jet Propulsion Lab, 1984.
- O Marxen, M Lang, U Rist, O Levin, and DS Henningson. Mechanisms for spatial steady three-dimensional disturbance growth in a non-parallel and separating boundary layer. *Journal of Fluid Mechanics*, 634:165–189, 2009.

- M Matsubara and PH Alfredsson. Disturbance growth in boundary layers subjected to free-stream turbulence. *Journal of fluid mechanics*, 430:149–168, 2001.
- Y Mayer, B Zang, and M Azarpeyvand. Design of a kevlar-walled test section with dynamic turntable and aeroacoustic investigation of an oscillating airfoil. In *25th AIAA/CEAS Aeroacoustics Conference*, page 2464, 2019.
- M AF Medeiros and M Gaster. The production of subharmonic waves in the nonlinear evolution of wavepackets in boundary layers. *Journal of Fluid Mechanics*, 399:301–318, 1999.
- R Merino-Martínez, AR Carpio, LTL Pereira, S van Herk, F Avallone, D Ragni, and M Kotsonis. Aeroacoustic design and characterization of the 3d-printed, open-jet, anechoic wind tunnel of delft university of technology. *Applied Acoustics*, 170:107504, 2020.
- J Methel, M Forte, O Vermeersch, and G Casalis. Experimental study on the effects of two-dimensional surface defects on the transition of a sucked boundary-layer. In *Aero 2020+ 1-55th 3AF International Conference on Applied Aerodynamics*, pages FP82–AERO2020, 2021.
- MV Morkovin. Transition in open flow systems-a reassessment. *Bull. Am. Phys. Soc.*, 39:1882, 1994.
- WM Orr. The stability or instability of the steady motions of a perfect liquid and of a viscous liquid. part ii: A viscous liquid. In *Proceedings of the Royal Irish Academy. Section A: Mathematical and Physical Sciences*, volume 27, pages 69–138. JSTOR, 1907.
- N Otsu. A threshold selection method from gray-level histograms. *IEEE transactions on systems, man, and cybernetics*, 9(1):62–66, 1979.
- D Park and SO Park. Linear and non-linear stability analysis of incompressible boundary layer over a two-dimensional hump. *Computers & Fluids*, 73:80–96, 2013.
- J Perraud and A Seraudie. Effects of steps and gaps on 2d and 3d transition. In *European Congress on Computational Methods in Applied Science and Engineering*, pages 11–14. ECCOMAS Barcelona, Spain, 2000.
- J Perraud, D Arnal, and W Kuehn. Laminar-turbulent transition prediction in the presence of surface imperfections. *International Journal of Engineering Systems Modelling and Simulation* 48, 6(3-4):162–170, 2014.
- L Prandtl. Bemerkungen über die entstehung der turbulenz. *ZAMM-Journal of Applied Mathematics and Mechanics/Zeitschrift für Angewandte Mathematik und Mechanik*, 1(6):431–436, 1921.
- JG Proakis and DK Manolakis. *Digital Signal Processing (4th Edition)*. Prentice Hall, 4 edition, 2006. ISBN 0131873741.
- M Raffel and CB Merz. Differential infrared thermography for unsteady boundary-layer transition measurements. *AIAA journal*, 52(9):2090–2093, 2014.
- H Reed and WS Saric. Transition mechanisms for transport aircraft. In *38th fluid dynamics conference and exhibit*, page 3743, 2008.
- E Reshotko. Transition issues for atmospheric entry. *Journal of Spacecraft and Rockets*, 45(2):161–164, 2008.
- O Reynolds. Iv. on the dynamical theory of incompressible viscous fluids and the determination of the criterion. *Philosophical transactions of the royal society of london.(a.)*, (186):123–164, 1895.
- AF Rius-Vidales and M Kotsonis. Influence of a forward-facing step surface irregularity on swept wing transition. *AIAA Journal*, 58(12):5243–5253, 2020.
- AF Rius-Vidales and M Kotsonis. Impact of a forward-facing step on the development of crossflow instability. *Journal of Fluid Mechanics*, 924, 2021.
- D Rodríguez, EM Gennaro, and MP Juniper. The two classes of primary modal instability in laminar separation bubbles. *Journal of Fluid Mechanics*, 734, 2013.
- D Rodríguez, EM Gennaro, and LF Souza. Self-excited primary and secondary instability of laminar separation bubbles. *Journal of Fluid Mechanics*, 906, 2021.

- W Saric and E White. Influence of high-amplitude noise on boundary-layer transition to turbulence. In *29th AIAA, fluid dynamics conference*, page 2645, 1998.
- WS Saric. Introduction to linear stability.
- WS Saric and AH Nayfeh. Nonparallel stability of boundary-layer flows. *The physics of Fluids*, 18(8):945–950, 1975.
- WS Saric, W Wei, and BK Rasmussen. Effect of leading edge on sound receptivity. In *Laminar-Turbulent Transition*, pages 413–420. Springer, 1995.
- T Sayadi, CW Hamman, and P Moin. Direct numerical simulation of complete h-type and k-type transitions with implications for the dynamics of turbulent boundary layers. *Journal of Fluid Mechanics*, 724:480–509, 2013.
- H Schlichting. Berechnung der anfachung kleiner störungen bei der plattenströmung. volume 13, pages 171–174, 1933.
- H Schlichting and K Gersten. *Boundary-layer theory*. Springer, 2016.
- PJ Schmid and DS Henningson. *Stability and Transition in Shear Flows*. Applied Mathematical Sciences. Springer New York, 2012. ISBN 9781461301851.
- GB Schubauer and HK Skramstad. Laminar boundary-layer oscillations and transition on. *Journal of research of the National Bureau of Standards*, 38:251, 1947.
- A Sciacchitano and B Wieneke. Piv uncertainty propagation. *Measurement Science and Technology*, 27(8):084006, 2016.
- H Shahzad. Flow stability around forward facing steps in unswept incompressible boundary layers. Master’s thesis, TU Delft, 2020.
- A Smith and N Gamberoni. Transition, pressure gradient, and stability theory. report no. es. 26388, douglas aircraft co. Inc., *El Segundo, CA*, 1956.
- BL Smith, DR Neal, MA Feero, and G Richards. Assessing the limitations of effective number of samples for finding the uncertainty of the mean of correlated data. *Measurement Science and Technology*, 29(12):125304, 2018.
- A Sommerfeld. Ein beitrag zur hydrodynamischen erklärung der turbulenten fluessigkeitsbewegungen. pages 116–124. Atti del IV Congresso internazionale dei Matematici, 1908.
- BS Stratford. The prediction of separation of the turbulent boundary layer. *Journal of fluid mechanics*, 5(1):1–16, 1959.
- H Stüer, A Gyr, and W Kinzelbach. Laminar separation on a forward facing step. *European Journal of Mechanics-B/Fluids*, 18(4):675–692, 1999.
- I Tani. Effect of two-dimensional and isolated roughness on laminar flow. In *Boundary layer and flow control*, pages 637–656. Elsevier, 1961.
- GI Taylor. I. eddy motion in the atmosphere. *Philosophical Transactions of the Royal Society of London. Series A, Containing Papers of a Mathematical or Physical Character*, 215(523-537):1–26, 1915.
- F Tocci, JA Franco, S Hein, G Chauvat, and A Hanifi. The effect of 2-d surface irregularities on laminar-turbulent transition: A comparison of numerical methodologies. In *STAB/DGLR Symposium*, pages 246–256. Springer, 2020.
- W Tollmien. Über die entstehung der turbulenz. pages 21–44, 1929.
- C Tropea, AL Yarin, JF Foss, et al. *Springer handbook of experimental fluid mechanics*, volume 1. Springer, 2007.
- MW Tufts, HL Reed, BK Crawford, GT Duncan Jr, and WS Saric. Computational investigation of step excrescence sensitivity in a swept-wing boundary layer. *Journal of Aircraft*, 54(2):602–626, 2017.

- JL Van Ingen. A suggested semi-empirical method for the calculation of the boundary layer transition region. *Technische Hogeschool Delft, Vliegtuigbouwkunde, Rapport VTH-74*, 1956.
- JBV Wanderley and TC Corke. Boundary layer receptivity to free-stream sound on elliptic leading edges of flat plates. *Journal of Fluid Mechanics*, 429:1–21, 2001.
- YX Wang and M Gaster. Effect of surface steps on boundary layer transition. *Experiments in Fluids*, 39(4): 679–686, 2005.
- Julien Weiss. A tutorial on the proper orthogonal decomposition. In *AIAA Aviation 2019 Forum*, page 3333, 2019.
- EB White and FG Ergin. Using laminar-flow velocity profiles to locate the wall behind roughness elements. *Experiments in fluids*, 36(5):805–812, 2004.
- EB White, WS Saric, and RH Radeztsky. Leading-edge acoustic receptivity measurements using a pulsed-sound technique. In *Laminar-Turbulent Transition*, pages 103–108. Springer, 2000a.
- EB White, WS Saric, and RH Radeztsky. Leading-edge acoustic receptivity measurements using a pulsed-sound technique. In *Laminar-Turbulent Transition*, pages 103–108. Springer, 2000b.
- FM White and I Corfield. *Viscous fluid flow*, volume 3. McGraw-Hill New York, 2006.
- B Wieneke. Piv uncertainty quantification from correlation statistics. *Measurement Science and Technology*, 26(7):074002, 2015.
- Q Ye. *Mechanisms of boundary layer transition induced by isolated roughnes*. PhD thesis, Delft University of Technology, 2017.
- H Zh and S Fu. Forward-facing steps induced transition in a subsonic boundary layer. *SCIENCE CHINA Physics, Mechanics & Astronomy*, 60(10):1–11, 2017.